SCHOOL OF MECHANICAL ENGINEERING

DEVELOPMENT OF AN UNMANNED AERIAL VEHICLE (UAV) INTEGRATED INERTIAL STABILISATION PLATFORM (ISP) TARGETING DISASTER MANAGEMENT AND HUMANITARIAN AID SCENARIOS.

Matthew Adrian Swanepoel (BScEng, UKZN)

Supervisor:

Prof. Glen Bright

Co-Supervisor:

Ms. Ingrid Retha Botha

June 2024

Submitted in the fulfilment of the academic requirements for the degree of Master of Science in Engineering at the School of Mechanical Engineering, University of KwaZulu-Natal

DECLARATION 1 - SUBMISSION

As the candidate's Supervisor I agree to the submission of this dissertation.

Dissertation supervisor: Professor Glen Bright

Dissertation Co-Supervisor: Ms. Ingrid Botha

DECLARATION 2 - PLAGIARISM

I, Matthew Adrian Swanepoel, declare that

1. The research reported in this thesis, except where otherwise indicated, is my original research.

2. This thesis has not been submitted for any degree or examination at any other university.

3. This thesis does not contain other persons' data, pictures, graphs or other information, unless specifically acknowledged as being sourced from other persons.

4. This thesis does not contain other persons' writing, unless specifically acknowledged as being sourced from other researchers. Where other written sources have been quoted, then:
   a. Their words have been re-written but the general information attributed to them has been referenced
   b. Where their exact words have been used, then their writing has been placed in italics and inside quotation marks, and referenced.

5. This thesis does not contain text, graphics or tables copied and pasted from the Internet, unless specifically acknowledged, and the source being detailed in the thesis and in the References sections.

Signed: 

Date: 13 June 2024

DECLARATION 3 - PUBLICATIONS

DETAILS OF CONTRIBUTION TO PUBLICATIONS that form part and/or include research presented in this thesis (include publications in preparation, submitted, *in press* and published and give details of the contributions of each author to the experimental work and writing of each publication)

Publication 1 (Published): M2VIP 2022

Swanepoel, M; Bright, G; Botha, I, "Optimized Two-Axis Inertial Stabilization Platform Design for Unmanned Aerial Vehicle Integration", In the IEEE *28th International Conference on Mechatronics and Machine Vision in Practice 2022.*

The paper was published and presented in November 2022, in Shanghai, China

Matthew Swanepoel was the lead author of this paper and conducted all research and experimental investigations under the supervision of Professor Glen Bright and Ms. Ingrid Botha.

The paper received the Best Conference Paper Award.

Publication 2 (Accepted): PRASA-RobMech 2024

Swanepoel, M; Bright, G; Botha, I.R, "Fused Deposition Modelling Parameter Optimization for Aerial Robotic Applications", *17th International RAPDASA-RobMech-PRASA-AMI Conference 2024.*

The paper was accepted in April 2024, in Gqeberha, South Africa.

Matthew Swanepoel was the lead author of this paper and conducted all research and experimental investigations under the supervision of Professor Glen Bright and Ms. Ingrid Botha.

Signed:	[redacted]	Date: 13 June 2024	Mr Matthew Swanepoel
Signed:		Date:	Professor Glen Bright
Signed:		Date:	Ms. Ingrid Botha

ACKNOWLEDGEMENTS

I would like to take this opportunity to acknowledge the following people for their continuous support throughout this research project:

To my parents: thank you for your endless support and belief in me and thank you for all the sacrifices you made in order to provide me with the opportunities and education that you have. I am eternally grateful for all that you have done for me.

To my brother, Hennie: Thank you for always encouraging, inspiring, and pushing me to persevere in the face of adversity. You are a true role model.

To Professor Glen Bright: thank you for your constant support and guidance as project supervisor. Working under your supervision over the past three years, both as an undergraduate and as a postgraduate, has been an absolute privilege.

To Ms. Ingrid Botha, project co-supervisor: you have my eternal gratitude for your contributions of time and effort to this research project. Your contribution to my development as an engineer over the past three years is immeasurable.

"Work hard now and play hard later"

~Ted Arderne~

ABSTRACT

The integration of mechatronic devices in daily life and the commercial environment has undergone a profound transition in response to the advent of the Fourth Industrial Revolution (4IR). Included in 4IR, falling under the" intelligent devices" category, are Unmanned Aerial Vehicles (UAVs). 4IR has highlighted the potential of UAVs to assume tasks previously performed by humans or other less efficient production systems. Could this potential function of UAVs be extrapolated into the disaster management and humanitarian aid scenarios? More specifically, could the UAV be used to transport medical supplies and essential items such as food, water, vaccines, and blood samples? This dissertation details the research and design of a two-axis, roll-pitch Inertial Stabilization Platform (ISP), which is compatible with the DJI Matrice 300 (DM300) UAV for humanitarian applications.

The research aimed to assess the operational viability of the device within the disaster management and humanitarian aid scenarios. The intention was to assist current strategies, most notably during time-sensitive situations and when access to the region of interest was obstructed. The design was required to repetitively stabilize the load being transported by the UAV. This accounted for the transportation of fragile cargo, vaccines, and blood samples. Additionally, this enabled unbalanced loads to be transported without potentially destabilising the UAV.

Owing to the 2.7kg payload carrying capacity of the DM300 UAV, the design was required to be lightweight to maximise the operational payload capacity of the ISP. Subsequently, Fused Deposition Modelling (FDM) was proven applicable for the fabrication of the device. The research undertook an experimental investigation into the optimisation of the FDM process parameters to identify the most durable, lightweight parameter combinations. The outcomes thereof proved the most structurally resilient, lightweight, components to be produced with no infill and increased part wall thicknesses under the expected loading conditions. FDM fabrication of the ISP consisted of 19 individual components with a combined mass of 329.7g. The final design assembly featured an Arduino Nano microcontroller, an Adafruit BNO055 Inertial Measurement Unit (IMU), two DSSERVO 35kg.cm servo motors, and two 7.4V lithium-ion batteries in addition to the FDM components. Hinging on the final ISP assembly mass of 709.86g, the final operational payload capacity of the ISP was specified to be 1900g.

Evaluation of the ISP operational capabilities was achieved through a series of experimental testing procedures that logged the device's stabilisation responses in both static and dynamic environments, as well as loaded and unloaded states. Findings validated the prototypes functionality, with acceptable stabilisation capabilities being exhibited in both axes. Under fully loaded and kinematic conditions, the ISP roll and pitch axes were noted to settle in 1.89 seconds and 1.92 seconds, respectively. These figures represented a maximum 33.33% increase in settling time, resulting from UAV noise transferral and loading in comparison to baseline results.

TABLE OF CONTENTS

LIST OF FIGURES

LIST OF TABLES

ACRONYMS

4IR	4th Industrial Revolution
ABS	Acrylonitrile Butadiene Styrene
AM	Additive Manufacturing
ADR	Address
ADCs	Analog-to-Digital Converters
AI	Artificial Intelligence
AR	Aspect Ratio
AEDs	Automated External Defibrillators
B-VLOS	Beyond Visual Line of Sight
BLDC	Brushless Direct Current
CFRP	Carbon Fibre Reinforced Polymer
CPR	Cardio-Pulmonary Resuscitation
CoG	Centre of Gravity
CoM	Centre of Mass
CS	Chip Select
C.O.T. S	Commercial Off-The-Shelf
CFD	Computational Fluid Dynamic
DJI	Da-Jiang Innovations
DoF	Degree of Freedom
DFA	Design for Assembly
DFM	Design for Manufacture
DMP	Digital Motion Processor
DC	Direct Current
DM300	DJI Matrice 300 RTK
EMF	Electro-Motive Force
ESC	Electronic Speed Controller
FPV	First-Person View
GPIO	General Purpose Input/Output
IMU	Inertial Measurement Unit
ISP	Inertial Stabilisation Platform
IP45	Ingress Protection
IDE	Integrated Development Environment
I^2C	Inter-Integrated Circuit
ICAO	International Civil Aviation Organisations
ICINCO	International Conference on Informatics in Control, Automation, and Robotics

IoT	Internet of Things
LED	Light Emitting Diode
LOS	Line of Sight
Li-Ion	Lithium-Ion
Li-Po	Lithium-Polymer
MIT	Massachusetts Institute of Technology
MISO	Master Input/Slave Output
MOSI	Master Output/Slave Input
MTOM	Maximum Take-Off Mass
MR^2G	Mechatronics and Robotics Research Group
MEMS	Micro Electro-Mechanical System
MOI	Moment of Inertia
MR-RPL	Multi-Rotor Remote Pilot License
PETG	Polyethylene Terephthalate Glycol
PLA	Polylactic Acid
PTSD	Post-Traumatic Stress Disorder
PI	Proportional-Integral
PID	Proportional-Integral-Derivative
RTK	Real Time Kinematics
RPL	Remote Pilot License
RTO	Remote Training Organization
RPAS	Remotely Piloted Aircraft System
R-VLOS	Restricted Visual Line of Sight
RMS	Root Mean Square
RAE	Royal Aircraft Establishment
ROC	RPAS operators Certificate
R^2	R-Squared
SD	Secure Digital
SLM	Selective Laser Melting
SLS	Selective Laser Sintering
SCLK	Serial Clock
SPI	Serial Peripheral Interface
SACAA	South African Civil Aviation Authority
SA-CATS	South African Civil Aviation Technical Standards
SLA	Stereolithography
SWOT	Strengths, Weaknesses, Opportunities, Threats
TPU	Thermoplastic Polyurethane

3D	Three-Dimensional
2D	Two- Dimensional
UTS	Ultimate Tensile Strength
UAV	Unmanned Aerial Vehicle
UI	User Interface
VTOL	Vertical Take-Off and Landing
VLOS	Visual Line of Sight

NOMENCLATURE – UNITS

A	Ampere
°	Degree
°C	Degree Celsius
°/ms	Degree per Millisecond
°/s	Degree per Second
GHz	Gigahertz
g	Gram
H	Henry
Hz	Hertz
K	Kelvin
kg	Kilogram
kg.cm	Kilogram Centimetre
$kg.m^2$	Kilogram Metre Squared
kg/m^3	Kilogram per Cubic Metre
kg/m.s	Kilogram per Metre-Second
kJ	Kilojoule
km	Kilometre
km/h	Kilometre Per Hour
kPa	Kilopascal
[mxn]	Matrix
MPa	Megapascal
m	Metre
m/s	Metres Per Second
mkg.cm/A	Milli Kilogram Centimetre per Ampere
mkg.cm/(°/s)	Milli Kilogram-Centimetre per Degree per Second
mAh	Milliampere-Hour
mm^2	Millimetre Squared
ms	Millisecond
Nm	Newton-Metre
Ω	Ohm
%	Percent
P	Pixels
rad/s	Radian per Second
rad/s^2	Radian per Second Squared
s	Second
V	Volt
W	Watt
W/m.K	Watts per Metre-Kelvin

NOMENCLATURE – SYMBOLS

Chapter 2: ISP Mathematical Modelling

T	Nm	Torque
I	$kg.m^2$	Moment of Inertia
α	rad/s^2	Angular Acceleration
θ_P	°	Pitching Angle
θ_R	°	Rolling Angle
R_P^I	[mxn]	Inertial Reference Frame to Pitch Reference Frame Rotation Matrix
R_R^P	[mxn]	Pitch Reference Frame to Roll Reference Frame Rotation Matrix
R_R^I	[mxn]	Inertial Reference Frame to Roll Reference Frame Rotation Matrix
$\vec{L}$	$kg.m^2/s$	Angular Momentum Vector
L_x	$kg.m^2/s$	Angular Momentum Vector Component
$\vec{\omega}$	rad/s	Angular Velocity Vector
ω_x	rad/s	Angular Velocity Vector Component
M	Nm	Net External Moment
φ	rad/s	Arbitrary Angular Velocity
$\dot{\vec{\omega}}$	rad/s^2	Angular Velocity Vector Time Derivative
$\dot{\omega}_{x_R}$	rad/s^2	Angular Velocity Vector Time Derivative Component
I_P	$kg.m^2$	Pitch Axis Inertia Tensor
I_R	$kg.m^2$	Roll Axis Inertia Tensor
I_{xx}	$kg.m^2$	Inertia Tensor Component
D	-	Product of Inertia
α_P	°	Measured Pitch Angle of ISP Platform
$\alpha_{P,D}$	°	Desired Pitch Angle of ISP Platform
e	°	Attitude Control Error
R_e^R	[mxn]	Inertial Reference Frame to Roll Reference Frame Attitude Error Rotation Matrix

Chapter 4: Mechatronic Design and Optimisation

Actuator Calculations		
$F_{payload,allowed}$	kg	Allowed Payload Mass During Initial Calculations
T_{roll}	kg.cm	Roll Axis Required Motor Torque
T_{pitch}	kg.cm	Pitch Axis Required Motor Torque
RF_{torque}	-	Motor Torque Reserve Factor at Saturation
$T_{available}$	kg.cm	Available Motor Torque at Saturation
$F_{available,roll}$	kg	Maximum Available Roll Axis Payload Mass
$F_{available,pitch}$	kg	Maximum Available Pitch Axis Payload Mass
x	°/s	Motor Equivalent Rotational Speed
f_{servo}	Hz	Motor Operational Frequency at Saturation
T_{servo}	s	Servo Rotation Period
Battery Pack Calculations		
$T_{flight,\ total}$	min	Maximum Permissible UAV Loaded Flight Time
$I_{motor,stall}$	A	Stall Current of Chosen Motor
$B_{capacity,\ servo}$	mAh	Ideal Required Battery Capacity to Power Motors
$\eta_{electrical}$	-	Motor Electrical Efficiency
$B_{capacity,actual}$	mAh	Actual Required Battery Capacity to Power Motors
$B_{capacity,required}$	mAh	Final Required Battery Capacity to Power Motors
Aerodynamic Optimisation		
a	mm	Ellipse Minor Arc Radius
b	mm	Ellipse Major Arc Radius
C_D	-	Drag Coefficient
V_{eq}	m/s	Maximum Effective UAV Speed
ρ	kg/m^3	Atmospheric Density
μ	kg/m.s	Atmospheric Kinematic Viscosity
Re	-	Reynold's Number
c	m/s	Speed of Sound at Operational Height
M	-	Mach Number at Operational Height
P	kPa	Atmospheric Pressure at Operational Height
K	W/m.K	Thermal Conductivity at Operational Height
T	°C	Atmospheric Temperature at Operational Height

Chapter 5: FDM Optimisation

ASTM Test Sample Geometry		
W	mm	Width of Narrow Section
L	mm	Length of Narrow Section
WO	mm	Minimum Overall Width
LO	mm	Minimum Overall Length
G	mm	Gage Length
D	mm	Distance Between Grips
R	mm	Fillet Radius
RO	mm	Outer Radius
T	mm	Specimen Thickness
Testing Theory		
σ_F	MPa	Flexural Stress at Failure
F	N	Flexural Failure Load
l	mm	Support Span
σ_T	MPa	Tensile Stress at Failure
P	N	Tensile Failure Load
A_{cs}	mm^2	Cross- Sectional Area in Gage Length of Specimen
n	-	Number of Perimeter Layers
N	mm	Nozzle Diameter
$\%_i$	-	Infill Percentage, Expressed in Decimal Format

Chapter 6: Control System Implementation

Simulink Model Development

V_m	V	Motor Voltage
V_b	V	Motor Back EMF Voltage
V_{net}	V	Net Motor Voltage
L_a	H	Armature Inductance
R_a	Ω	Armature Resistance
i_a	A	Armature Current
K_m	mkg.cm/A	Motor Torque to Current Constant
T_m	kg.cm	Motor Torque
T_f	kg.cm	Friction Torque
T_d	kg.cm	Disturbance Torque
T_{net}	kg.cm	Net Motor Torque
I	$kg.m^2$	Motor Load Inertia
K_f	mkg.cm/(°/s)	Motor Friction Coefficient
ω_m	°/s	Motor Speed
K_s	-	Motor Speed to Gimbal Axis Speed Constant
ω_g	°/s	Gimbal Axis Speed
θ_g		Gimbal Axis Angular Position
m_{Roll}	g	Roll Axis Final Mass
$I_{Servo,Roll}$	$kg.m^2$	Roll Axis Servo Motor Load Inertia
d_{xr}	m	CoM Offset From Roll Servo Shaft
M_{xR}	Nm	Net External Torque Experienced by the Roll Axis
m_{Pitch}	g	Pitch Axis Final Mass
$I_{Servo,Pitch}$	$kg.m^2$	Pitch Axis Servo Motor Load Inertia
d_{yp}	m	CoM Offset From Pitch Servo Shaft
M_{yP}	Nm	Net External Torque Experienced by the Pitch Axis
ω_G	Hz	Gyro Bandwidth Frequency
ζ_G	-	Gyro Damping Factor
K_P	-	Proportional Gain
K_I	-	Integral Gain
K_D	-	Derivative Gain

Chapter 6: Control System Implementation Continued

ISP Software and Firmware Implementation

q	-	Quaternion
w,x,y,z	-	Real Coefficients of Quaternion Components
Q_0	-	IMU Quaternion Data w-Component Storage Variable
Q_1	-	IMU Quaternion Data x-Component Storage Variable
Q_2	-	IMU Quaternion Data y-Component Storage Variable
Q_3	-	IMU Quaternion Data z-Component Storage Variable
u(t)	ms	Control Signal
e(t)	ms	Error Signal
Grad Error	°/ms	Error Signal Derivative Approximation

Chapter 7: System Performance Verification

$\lvert T_D \rvert$	°/s	Disturbance Magnitude
a_x	s	Error Signal Initial Disturbance x-Coordinate
a_y	°	Error Signal Initial Disturbance y-Coordinate
b_x	s	Error Signal Maximum Disturbance x-Coordinate
b_y	°	Error Signal Maximum Disturbance y-Coordinate
c_x	s	Error Signal Settlement x-Coordinate
c_y	°	Error Signal Settlement y-Coordinate
T_s	s	Disturbance Settling Time

1 INTRODUCTION

1.1 Introduction

The following dissertation details the methodical Mechatronic engineering approach to design, manufacture, and test a DM300 UAV integrated ISP targeted at assisting current disaster management and humanitarian aid strategies. The mechatronic ISP aimed to provide a solution to the lack of commercially available payload transportation devices, which are compatible with consumer-grade UAVs such as the DM300. The proposed solution was required to transport fragile disaster relief cargo such as blood samples and vaccines, which are classified as dangerous goods. To make provisions for these substances, as well as unbalanced loads which could potentially destabilise the UAV, the mechatronic design was required to repetitively stabilise the cargo during transportation. A literature review was conducted to identify the components required to bring the proposed solution to fruition. Thereafter, system conceptualisation and component selections took place. The resulting ISP consisted of five subsystems: a mechanical aero frame with a payload cradle, an IMU, a microcontroller, actuators, and batteries. The literature review also identified FDM to be a suitable fabrication method for the device. Consequently, an experimental investigation into the optimal FDM parameter combinations to produce the most lightweight, structurally resilient prototype was required before the device could be manufactured. The ISP prototype was manufactured and its performance evaluated against the specifications derived from the literature review. Chapter 1.2, which follows, establishes the need for the device based on the current state of research in the field and assesses the viability of the proposed solution within the disaster management and humanitarian aid

1.2 Background

The onset of the Fourth Industrial Revolution (4IR) is characterized by the Internet of Things (IoT), Artificial Intelligence (AI), cyber-physical systems, and the automation of processes to produce smart factories. Included in 4IR, falling under the" intelligent devices" category, are UAVs. 4IR has highlighted the potential of UAVs to perform tasks previously performed by humans or other, more cumbersome production systems, in a more economical and efficient way. The technical assistance offered by these devices complements the focal point of 4IR; to substitute humans performing D^3 (Dull, Dirty, Dangerous) tasks with cyber-physical systems to perform these tasks autonomously [1].

Considering the tasks mentioned above, it would stand to reason that dangerous operations such as disaster relief, a function of the response phase of disaster management, would benefit from UAV integration [2]. The ability to provide emergency assistance to those in need, while mitigating the probability of additional casualties to those entering the disaster region alike, would be a logical further utilisation of UAVs, complimenting the aims of 4IR. The research project identified a complete lack of industrial- and consumer-grade UAV-compatible commercially available ISPs for these purposes. This finding then raised the question of why these operations are not conducted utilising UAVs such as the DM300, which was

available for utilisation within the research project. To answer this question, it was necessary to evaluate the suitability of the DM300 within disaster management strategies to identify any hindrances opposing the use of the UAV for the intended purpose. The evaluation focused on the functions, characteristics, and capabilities of the UAV, and the potential of the relevant UAV attributes to satisfy the requirements of disaster management strategies.

Firstly, disaster management was defined as a comprehensive approach to dealing with the four phases of a disaster. These phases being the response, recovery, mitigation, and the preparation [3]. These phases are dealt with by systematically organising and managing resources to lessen the impact of the disaster in the manner shown by Figure 1-1 below [4].

Figure 1-1: Disaster Management Cyclic Process [5]

Referring to the contents of Figure 1-1 above, both the mitigation and preparation phases are satisfied by taking action to reduce the possible adverse effects experienced by people and property during a disaster and by implementing procedures and plans to minimise effects [2] [6]. These phases take place prior to a disaster event occurring. The response and recovery phases are satisfied by taking action to decrease fatalities and prevent further damage to property, and thereafter, to take action to begin returning to normal after the disaster has occurred [2] [6]. Having analysed the general disaster management strategy in Figure 1-1 above, and elaborated on the general attribute on each phase, the DM300 was the next item to be considered when evaluating the UAV suitability for the intended use.

The DM300 UAV is one of the latest industrial-grade UAVs produced by DJI Enterprises, which are also available to the individual consumer. Through a thorough review of literature pertaining to the DM300, a summarised version of the UAV attributes relevant to the suitability assessment was derived. The DM300 features a maximum take-off weight of 9kg, including a 2.7kg payload. A maximum unloaded flight time of 55 minutes can be expected per charge of the batteries [4]. The UAV features a maximum, unobstructed, controllable transmission range of 15km. Additional features of the aircraft include a 6-directional obstacle sensing and positioning vision system, an infrared sensing system, and a First-Person View (FPV) camera [4]. Chapter 2.2 provides a full analysis of the DM300 before the pertinent UAV specifications are tabulated in Chapter 3 below.

Amalgamating the findings of the disaster management cycle review as well as those of the DM300 review, it was concluded that the DM300 was suitable for the disaster management resource transportation application proposed by the research project. With reference to the preparation for, and mitigation of disasters, these phases are satisfied by using the UAVs vision and FPV camera system to identify suitable land for development, and to survey land and plan evacuation routes. Similarly, in the response and the recovery phases the obstacle sensing vision system, infrared sensing system, and a FPV camera can be used for search and rescue response purposes, thus satisfying the requirements of the phase. In fact, the DM300 is advertised by DJI Enterprises as an "industrial grade mapping inspection device", who go as far as to state that "First responders are turning to DJI's aerial solutions to aid in search and rescue missions. Deployed at land or sea, drones can efficiently scan vast areas and help pinpoint individuals in distress thanks to high-resolution digital and thermal sensors" [7]. How, then, can the DM300 UAV be optimised to cater for the transportation and delivery of critical supplies within disaster management scenarios?

Through the abovementioned research it became evident to the author that the DM300 UAV possesses the required attributes to be further utilised within disaster management and humanitarian aid situations. Therefore, the research project aimed to develop a DM300-integrated ISP as a solution which promoted the additional use of the UAV apart from the standard provisional functions. The proposed solution intended to exploit the DM300's maximum speed of 23m/s for time-sensitive situations, and the UAVs 2.7kg payload capacity for the transportation of resources to and from disaster regions [8]. The DM300 integrated ISP proposed by this research project was intended to contribute to research a basis for commercially available UAVs to be further utilised for humanitarian aid on a global scale, with the goal of reducing disaster mortalities through assisted planning, prevention, and recovery operations.

1.3 Challenges

The information presented above identified a niche area within current research, being the lack of existing UAV-compatible devices available for the transportation of resources to and from disaster affected regions. Challenges associated with developing the ISP prototype included the specification of lightweight components and materials to be incorporated into the design. The design was required to be as lightweight as possible whilst remaining structurally resilient to facilitate the repetitive stabilisation of the maximum permissible payload mass. Due to the limited payload carrying capacity of the UAV, the FDM manufacturing parameters of the ISP needed to be optimised in order for the ISP mass to be minimised, thus maximising the final allowable ISP payload carrying capacity.

The research endeavoured to provide current disaster management strategies with an additional response and relief tool, being the DM300-ISP assembly. The applicability of the UAV for the intended application was established for time-sensitive, and obstructed land access situations. Under these conditions, the ISP would be required to facilitate the transportation and delivery of critical medical supplies. When considering the transportation of these critical medical supplies, the most influential items were determined to be blood, blood samples, and vaccines. These items are classified as dangerous goods, which require

high levels of care during transportation as they cannot be shaken. Therefore, the ISP was required to repeatedly stabilize the load being transported by the UAV in real time. This enabled the transportation of blood samples, vaccines, and fragile cargo. Additionally, this allowed for unbalanced loads to be transported without potentially destabilising the UAV. The influential payload items mentioned above were of a small enough form factor and mass to be transported by the limited payload carrying capacity of the DM300. However, achieving real time stabilisation of the items via the ISP proved to be a challenge.

Another challenge associated with the development of the DM300-specific ISP solution included the required roll-pitch configuration of the device. The most common ISP configurations found by this research were the roll-yaw and the pitch-yaw ISP configurations, as these are readily used for camera stabilisation as well as tracking and seeking operations. As such, the roll-pitch ISP for payload stabilisation proved to be a unique undertaking, with minimal literature surrounding the topic, most notably when developing the ISP Simulink model.

1.4 Research Questions

1. Is an ISP a viable solution to the lack of UAV-specific resource transportation devices utilised within disaster management and humanitarian aid scenarios?
2. Can a mechatronic design approach produce an ISP device with acceptable stabilisation capabilities?
3. How can an ISP prototype be manufactured to incorporate the necessary components while still remaining aerodynamically efficient and lightweight?

1.5 Research Objectives

The aim of the research project was to develop a lightweight, aerial DM300-specific ISP as a solution to the absence of available UAV-specific transportation devices for disaster management and humanitarian aid resources. For the aim to be fulfilled, the research objectives provided below were derived. The objectives attached to the research provided the structural outline to ensure the successful completion of both the project and the associated dissertation, whilst ensuring a comprehensive investigation was undertaken. In doing so, it was possible to conclude the project and answer the research questions with conviction. Each objective was structured to provide the necessary insight required to proceed onto the next objective until such time as the project was completed. The research objectives were as follows:

1. Research legislation governing the use of a UAV and assess the potential of using a UAV for the research purpose.
2. Identify commercially available ISPs and components commonly used to control their motion.
3. Identify and review manufacturing technologies applicable to the ISP design.
4. Design an optimised ISP prototype which integrates the necessary components to produce optimal stabilisation capabilities.
5. Manufacture the final prototype and perform tests to analyse performance characteristics.
6. Discuss findings, make recommendations, and conclude the project.

1.6 Project Scope and Limitations

As alluded to previously, the aim of the research project was to develop a lightweight, aerial ISP as a transportation device for disaster management and humanitarian aid resources. Therefore, the scope of the project covered the entire development phase of the optimised prototype, from conceptualisation to field testing. For the aim to be fulfilled, the research project undertook a thorough investigation into prevailing literature pertaining to the above-mentioned scenarios, which guided project development. Major focus areas of the research were limited to the legislation surrounding the use of the UAV for the purpose intended by this research, a viability assessment of using UAVs for the purposes, ISPs, and the applicability of using FDM technologies to manufacture the resultant prototype. Findings of the literature review saw the following scope and limitations attached to the research. Firstly, the ISP DOF requirements were reduced from three dimensions to two dimensions, with the required stabilisation axes being in the roll and pitch axes relative to the UAV. This discernment was made due to the yaw axis having no bearing on the platform stability relative to the inertial frame. Drawing on UAV legislation, the proposed operation was limited to a maximum service ceiling of 121.92m and associated environmental conditions. A maximum DM300 UAV wind resistance of 15m/s further refined the scope of environmental conditions to be considered by the design, with the wind direction being assumed to be a head or tail wind. Eventually, FDM was found to be an applicable fabrication method for the prototype, and the scope of further FDM part strength parameter investigation limited to infill density, infill pattern, wall thickness, and layer height.

1.7 Dissertation Structure

The dissertation conveys the findings of the research project, which answered the research questions through completion of the above objectives. The dissertation was structured as follows:

Chapter 2 conferred the literature review, which researched UAVs, the DM300, UAV legislation, and the potential integration of UAVs into the public health sector for the transportation of critical medical resources. Chapter 2 also researched ISPs and applicable manufacturing technologies for the research project design. The final subsection of the literature review was the mathematical modelling of the ISP.

Insight s and specifications gained from Chapter 2 were then utilised to produce Chapter 3, which tabulated the final design specifications. Chapter 3 provided the complete set of DM300 specifications, the ISP target specifications, and the final operational specifications of both the UAV and the ISP.

Chapter 4 detailed the mechatronic design of the ISP prototype. The chapter first detailed the conceptualisation of components to satisfy the requirements of each subsystem of the ISP. Thereafter, the final mechatronic design of the ISP was presented, consisting of both mechanical and electrical designs.

Chapter 5 presented the FDM optimisation experimentation undertaken to arrive at the final ISP component manufacturing FDM parameters. Contents included the experimental methodology, apparatus, testing procedure, individual test descriptions, and results analysis of each test. The chapter then provided the

experimental results verification, followed by the derivation of the final manufacturing parameters and fabrication particulars.

Chapter 6 was comprised of the systematic control system development for the ISP prototype. The chapter first detailed the development of the individual constituents of the ISP Simulink model. The complete ISP simulation model was then provided, and the results of system response tuning given. Chapter 4 then deciphered the final ISP firmware.

Chapter 7 detailed the initial experimental procedure adhered to during performance testing of the ISP prototype. The experimental results were then utilised to verify the system simulation model and the functionality of the prototype.

Chapter 8 provided a comprehensive evaluation of the ISP operational performance. Two tests were conducted to evaluate the operational performance of the prototype. The first test analysed the effect of external noise originating from the UAV on the ISP. The second test analysed the performance of the ISP under operational and kinematic conditions.

Chapter 9 included a detailed discussion of the findings of the research project in relation to the aim and objectives of the dissertation. A chapter-wise overview of the dissertation was provided, inclusive of insights gained throughout each chapter. The ISP performance evaluation chapters were summarised, and comparisons made to target specifications of the design. Thereafter, potential areas of future work in the context of the research project were identified.

Chapter 10 concluded the dissertation. The chapter conveyed research contributions made and challenges faced throughout the research project duration. Recommendations for future work in the field of study were provided.

1.8 Chapter Summary

The chapter introduced the research project to the reader and established the rationale behind the generation of the research topic. The chapter discussed the problem being addressed by the research, and anticipated the challenges associated with the proposed solution. Research questions were formulated and presented in response to the proposed solution. The resultant research aim was stated before the presentation of the objectives attached to the project to facilitate the aim being met. Thereafter, the chapter provided a brief overview of the dissertation structure.

2 LITERATURE REVIEW

2.1 Introduction

The function of the literature review was to identify and provide crucial information pertaining to the project, from which key design requirements and specifications can be derived. The pertinent information portrayed by the chapter is guided by, and aims to satisfy, the first three objectives detailed in Chapter 1.5 above. The general areas of interest for exploration being UAVs (with focus of the DM300), applicability of UAVs for the research project's intended purpose, ISPs (and the control thereof), applicable manufacturing technologies, and mathematical modelling of the ISP.

2.2 UAV Overview

The history of unmanned aviation dates back to 1804, when the first documented flight of an unmanned fixed wing glider took place in Yorkshire, England [9].Thereafter, slow progression and development in the field of unmanned aviation led to the first documented flight of a radio controlled unmanned aircraft on 3 September 1924. The flight was conducted successfully without an onboard safety pilot for a duration of 39 minutes by the British Royal Aircraft Establishment (RAE) [9].Originally made popular by militaries for combat purposes, UAVs are commonly used for purposes such as aerial photography, surveillance, military operations, and environmental and agricultural monitoring [10]. However, despite the positive contributions of UAVs across many fields thus far, concerns of privacy, security, collision avoidance and data protection have come to fore [10].

In an attempt to counteract scepticism surrounding the UAV industry as a whole, UAV regulations are constantly being developed, reviewed, and updated to ensure the safest possible operating conditions are being adhered to. The specific features of the UAV which are continuously monitored and controlled are the UAV type, the UAV service ceiling (maximum flying altitude), UAV speed, and the control spectrum of the UAV [10]. According to [11] and [12], the five main areas of focus explored when UAV regulations are developed are:

1. Application: Considers the role, weight, and type of UAV.
2. Operational limitations: Considers location of the UAV and ways to restrict free roaming.
3. Administration: Pertains to procedures and prerequisites to be attained by the UAV operator.
4. Technical capabilities: Considers the mechanical, control, and communication capabilities of the UAV.
5. Ethical considerations: Pertains to imposing privacy regulations on the UAV.

While the specifics of the UAV regulations vary between locations, countries, and settlement densities, the above-mentioned criterion of the UAV are commonly exploited when regulations are being amended and imposed. Chapter 2.5 explores the regulations which are pertinent to the UAV operation proposed by the research project in greater depth.

2.3 DJI Matrice 300 RTK UAV Review

The DM300 UAV is one of the latest models of UAV technology produced by Da-Jiang Innovations (DJI) Enterprises. The UAV is commonly used for surveying, surveillance, mapping, general aerial photography, and inspection [13] [14]. This research project aimed to evaluate the viability of the DM300 as a tool for disaster management and humanitarian aid purposes. As such, the UAVs capabilities, functions, and characteristics needed to be evaluated to assess its viability for the hypothesized application. This was done by researching the capabilities of the UAV which would make it suitable to deal with the response, recovery, prevention, and the preparedness phases of a disaster management scenario. Additionally, the determination of whether the UAVs abilities could be extended to the humanitarian aid scenario was of interest.

2.3.1 Obstacle Sensing

The DM300 possesses both infrared and vision sensors on all six sides of the UAV which can be customised to detect objects up to 39.93m away at a maximum of 16.99m/s [15]. The UAV also features built in LED lighting to enhance obstacle sensing in poor visibility and poor lighting conditions, thus enhancing its collision avoidance capabilities. In the disaster management scenario, having a 6-directional detection and observation system on board would prove exceptionally useful for search and rescue applications within a disaster region.

2.3.2 Durability and Reliability

The DM300 comes with an IP45 liquid and solids resistance rating. This means the UAV can be safely operated in the presence of objects exceeding a nominal size of 1mm, such as sand and dust and is water resistant against heavy rain [16]. The IP45 rating confirmed the UAV to be compatible with all weather conditions, except for winds stronger than 15m/s (54km/h), which earmarks the maximum wind resistance of the DM300 [8]. However, the ability to fly in adverse weather conditions proved the UAV to be reliable in the disaster management and humanitarian aid scenarios.

2.3.3 Flight Time

The inclusion of two TB60 batteries on the UAV allows for a maximum, unloaded, flight time of 55 minutes [17] [8] [18]. This is, however, heavily dependent on the loading for the UAV. As can be seen in Figure 2-1 below, the addition of a payload to the unloaded UAV rapidly decreases the available flight time to a maximum possible flight time of 31 minutes with both TB60 batteries and a maximum of 2.7kg payload on board.

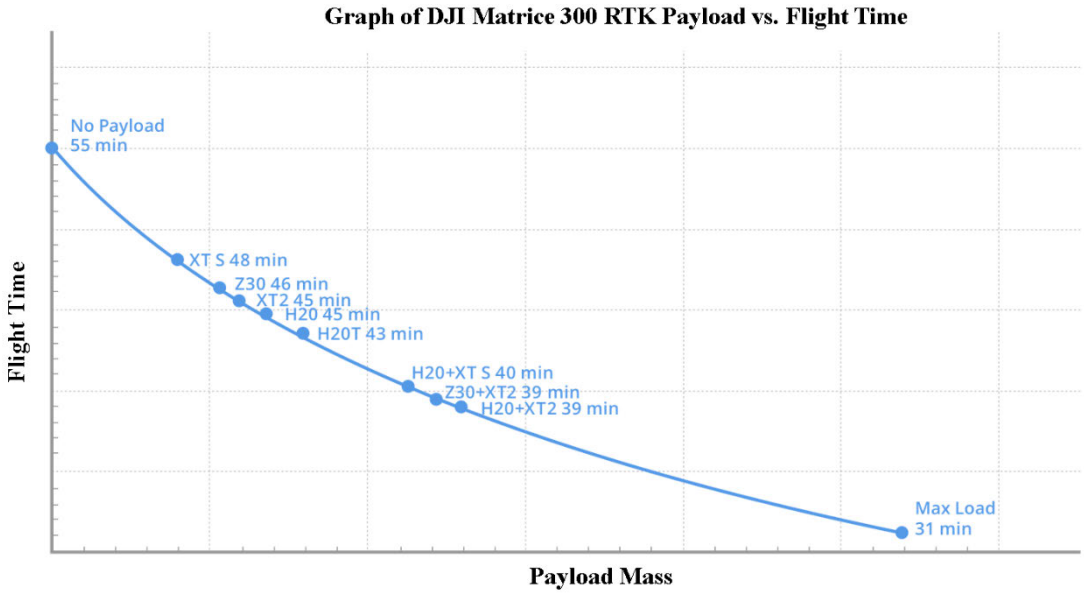

Figure 2-1: Effect of Loading On UAV Flight Time, Adapted From [17] [8]

Figure 2-1 above describes the effect of loading on the UAV flight time. At the DM300 maximum speed of 23m/s according to [8] and [17], 31 minutes of fully loaded travel time would translate to a maximum service radius of 21.39km, assuming a round trip to the destination and back. When one takes into consideration the time-sensitive nature of a disaster, whether it be natural or man-made, it is evident that the DM300 is extremely versatile in terms of transmission range, speed, and service radius, and would be an asset as a response vehicle.

2.3.4 Camera and Transmission Capabilities

The DM300 comprises a built-in First-Person View (FPV) camera which provides real-time video to the controller at 1080P. The FPV camera is mounted at a forward inclination and relays to the remote controller what is in front of the UAV in real time. The controller of the UAV has a built-in 5.5-inch 1080P resolution touch screen to the pilot to interact with the UAVs surroundings via the FPV system. The transmission of video data and control signals to the UAV is facilitated by the DJI "OcuSync" software at a frequency of 2.4GHz, for a maximum distance of 15km, whilst simultaneously supporting up to three 1080P video channels at 30 frames per second, should the user wish to include a DJI-approved camera gimbal to the UAV [15]. The DM300 is also capable of switching controllers when the UAV is in use. This gives the UAV the ability to depart and land under the command of multiple pilots, giving it an effective transmission range of 30km [15]. The high resolution of video transmission to the remote controller coupled with the high refresh rate of 30 fps justifies the DM300 as an attractive tool for landscape mapping, surveillance, and search and rescue. The effective transmission range of the UAV solidifies the viability of the UAV in terms of its search radius. As such, the DM300 was deemed applicable for the disaster management and humanitarian aid purposes proposed by the research project.

2.4 UAV Viability in Disaster Management

The DM300 was previously determined to be a suitable tool for the integration into disaster management and humanitarian aid scenarios. This evaluation was made based on the UAVs capabilities and functions in its standard form. UAVs, in general, are advantageous over other forms of transportation in these scenarios due to their unhindered ability to move into the affected area and extract real-time images and video data to disaster management officials [19]. This would enable the rapid assessment of damages and determination of response strategies to rescue civilians in need, address damages to critical infrastructure, and develop healthcare systems [20]. The combination of the aforementioned capabilities of the DM300 proved it to be a viable transportation resource for both disaster management and humanitarian aid situations. Additionally, the UAV possesses the necessary characteristics to be used for transportation of resources to and from disaster regions when other forms of transportation are obscured from entering the region, or when time is of the essence. Utilising the UAV for this purpose would complement current disaster management strategies by providing immediate relief when it is needed. However, according to current literature, no commercially available attachments have been developed to address this purpose. The lack of commercially available UAV load transportation devices for the purpose then raises the question of whether such a device, coupled with a UAV such as the DM300, could be substantive in disaster relief operations. Considering the disaster relief segment of disaster management falls within the response and recovery phases, this would mean the scope of goods the UAV would be required to transport would be emergency health supplies such as medications, first aid supplies, and blood samples. Therefore, the potential integration of UAVs into the public health sector at large must be assessed.

2.4.1 UAV Potential in Public Health

The probability of successful integration of UAVs into public health, and therefore disaster management, was assessed by Laksham, [21]. A Strengths, Weaknesses, Opportunities, and Threats (SWOT) analysis was undertaken to review the advantages and disadvantages of UAVs in the public health domain. The analysis culminated in the following criteria, which have been adapted to incorporate the DM300 UAV.

2.4.1.1 Strengths

UAVs have shown the potential to significantly reduce travel time to patients for diagnoses and treatments [22]. Using the DM300 UAV, patients within a 15km radius of the pilot could, theoretically, be reached in 11 minutes (approximated using the UAVs top flight speed), which would be significantly faster than conventional emergency services [21] [23]. UAVs have also been proven a cost-efficient alternative to conventional emergency services transportation vehicles and are more adept to difficult terrains. Due to legal restrictions, UAVs are required to fly closer to the ground than conventional air transport vehicles, thus ensuring better quality data being transmitted to the pilot. This comes as a result of reduced contamination of photographic data due to cloud cover at higher altitudes and sheltered flight conditions due to land formations at lower altitudes. Finally, UAVs can quickly reach desolate areas such as mountains

and valleys to assist in search, rescue, and recovery missions [24] . When one considers events such as the Covid-19 pandemic, UAV delivery of vaccinations would have greatly increased vaccine availability at a decreased cost, whilst mitigating human contact. As such, UAVs can be seen to possess optimal characteristics for public health integration.

2.4.1.2 Weaknesses

A weakness opposing the potential to integrate UAVs into the public health domain is that of infrastructure and manpower. According to [21], certain UAVs require a runway to become airborne as well as trained staff to assist with the take-off process. However, the DM300 is a Vertical Take-Off and Landing (VTOL) UAV, meaning that neither a runway nor runway officials are required for the take-off process. Therefore, using the DM300, specifically, for medical delivery purposes poses a potential risk of job loss for those involved as runway and take-off officials for non-VTOL UAVs.

In comparison to aerial vehicles such as aeroplanes and helicopters, UAVs can only offer a fraction of the payload capacity and flight time. In the case of the DM300 UAV, as previously specified, a maximum flight time and payload of 31 minutes and 2.7kg, respectively, can be expected [8]. However, as 4IR progresses, UAV technology has been making advancements, and their capabilities furthered with longer flight times and larger payload capacities [25]. With these advancements, however, concerns of privacy, security, collision avoidance and data protection have arisen as UAV capabilities evolve. The battery life of UAVs is of concern as they are rapidly drained during use and could pose a safety hazard should the UAV lose power during flight. However, UAVs are generally equipped with a hybrid power supply system architecture [26]. In the case of the DM300, the UAV has a built-in failsafe system which overrides the pilot when the batteries are discharged and returns the UAV home to its point of take-off [8]. As such, the only technical limitation which cannot be disregarded as a potential weakness of the UAV, is signal interference between the UAV and pilot, and extreme winds. However, weather reports and satellite data are readily available, and an educated decision can be made not to continue with the flight in adverse conditions [21] [14]. Concerning signal interference, the DM300 utilises advanced signal encryption standards to ensure safe, interference-free signal transfer between controller and UAV [17].

2.4.1.3 Opportunities

Developing countries such as South Africa often face shortages of blood safe for transfusion. This is critical in rural areas which are difficult to reach by conventional means of transport. UAVs could potentially be used to transport blood into these areas for general surgeries, as well as for emergencies, such as mass casualties. In these areas, access to blood storage facilities is not always possible, so having access to blood on demand from the closest medical centre could potentially save lives. This has become a common practice in Rwanda, where blood is being delivered by UAV around 30 minutes after it is requested, for approximately the same cost as a motorbike-facilitated delivery [27]. Critical medical supplies such as blood, vaccines, and medications often require refrigeration during transportation. Should access to the

disaster region by land be obscured, the DM300 was previously determined to be able to reach regions within 15km by air in a theoretical maximum time of 11 minutes. This delivery window would be advantageous, as supplies could potentially be delivered, unrefrigerated, within the required temperature range, by UAV [24]. The lack of access to proper healthcare facilities in rural areas delays disease diagnoses. This could be overcome by using UAVs to transport patients' samples to laboratories nearby for testing. Once testing is completed, the results could be sent back via UAV, along with medication should it be necessary. This practice has been successful in Madagascar, where blood samples from rural locations without medical laboratories are being transported by UAV to cities with laboratories for testing [28]. Whilst testing phases have been fairly limited to blood samples, there exists no reason as to why UAVs cannot be extended to transport vaccines or anti-venoms, into rural areas, where they can be distributed to the public through a central dispatch and receiving point.

UAVs can be readily used for disaster relief operations by identifying victims in damaged infrastructure and searching for vessels lost at sea. In these cases, they could be further utilised to deliver medication, food, and water to victims until such time as rescue workers are able to access the area. In severe cases, the UAV could be used to deliver medical devices such as Automated External Defibrillators (AEDs) to victims and provide visual feedback of the victim for healthcare officials to be able to assist a bystander provide the victims with Cardio-Pulmonary Resuscitation (CPR) [29].

Within the organ transplantation medical industry, time taken to transport organs from the donor to the recipient is critical to the success of the operation. Here, organs are usually transported from one hospital to another by motor vehicle which is escorted by traffic police to minimise transportation time, but transportation is still subject to traffic congestion. Using UAVs, organs can be quickly and safely transported between hospitals without the delay of traffic [30]. This method has shown promising results as a kidney was transported by UAV and reached its destination without damage related to transportation via UAV [31].

2.4.1.4 Threats

As previously mentioned, UAVs are a point of apprehension amongst the public due to their inherent threat to human safety should a UAV become dysfunctional in flight and fall to the ground. A falling UAV might land in a residential area and cause injury to people and property. This apprehension comes as a result of U.S military drones having crashed and caused damage globally, which is an annual occurrence according to the Washington Post, [32]. Additionally, the ever-looming threat of commercially available UAVs being weaponised for both military applications as well as terror attacks looms, and thus poses a threat to the integration of UAVs into public health. Therefore, fear of military drones is a global issue which has been seen to be a large contributor to mental health disorders such as Post Traumatic Stress Disorder (PTSD) and anxiety in Pakistan. Likewise, a screening of military personnel found that remote pilots of UAVs also have higher chances of suffering from PTSD [21] [33]. There also exists the possibility of a medical UAV

being misconceived and destroyed by the military or having its transmission signal intercepted and the UAV being hijacked for its payload.

2.4.2 Existing Disaster Management UAV Technologies

The above sections evaluated the pertinence of UAVs, and the DM300 UAV specifically, within disaster management and humanitarian aid scenarios. Findings of the evaluation showed that these technologies were not only applicable but possess the capabilities to function as crucial tools within these scenarios. Zipline, an American-owned company, too, identified the potential of UAVs within these scenarios and founded the company in 2014 in response. Currently, Zipline is at the forefront of disaster management and humanitarian aid relief operations in African countries to deliver medical supplies. These countries include Rwanda, Ghana, Nigeria, and Kenya. Contrary to the DM300 UAV, Zipline uses fixed-wing plane-like UAVs with a single propeller for propulsion, which encapsulates each pre-packaged parcel for delivery. Each UAV has a maximum allowable payload mass of 1.8kg per flight and has an 80km delivery radius at a maximum speed of approximately 100km/h. The company claims to have an average delivery time of 15-45 minutes with a 5–7-minute turnaround time from receiving an order to launch of the UAV [34]. Each Zipline delivery costs between $15-$45 (R274-R822) depending on payload weight, destination, and delivery urgency.

To put these values into perspective, a Massachusetts Institute of Technology (MIT) technology review by Lee [35] presented the findings of a study conducted on UAV vaccine delivery in Mozambique, South Africa. The objective of the study was to test the UAV delivery method in response to a range of challenging scenarios which the UAV could, realistically, encounter during commercial use. Even under varying conditions, the delivery method was shown to provide cost savings ranging from 20%-50% over traditional delivery methods. A pilot project conducted in Madagascar also successfully delivered medical supplies by UAV under similar conditions and yielded comparable results, potentially increasing vaccines availability by 94% to 96% [36].

In closing, Lee, who is an associate professor of international health at the Johns Hopkins Bloomberg school of public health, stated that the implementation of new technologies such as UAVs has the intrinsic potential to save both money and lives. However, these savings, both monetary and of human lives, are dependent on the reliability of UAVs and the willingness of people to accept them [35].

The findings of the technology review, as well as the ongoing success of Zipline corroborates the above research of UAV viability in disaster management. The DM300 can therefore be confirmed as a viable delivery vehicle for payloads consisting of blood samples, vaccines, and medical supplies, to aid current disaster management and humanitarian aid scenarios. An integrated attachment would still be required to facilitate the loading of payload items onto the UAV, owing to the gap in research identified previously, being the lack of available UAV-compatible load transportation attachments.

2.5 UAV Regulations in South Africa

As UAV technology progresses with the development of the 4th industrial revolution, so too do the capabilities of UAVs. This, in turn, requires strict monitoring of UAVs to ensure they are being used only for their intended use as industries continue to integrate them into the workplace. The imposing of regulations requires thorough assessments to be undertaken to identify all potential hazards which could be caused by the UAV to operating personnel, the immediate environment, its surroundings, and to the public at large.

In South Africa, the South African Civil Aviation Authority (SACAA) is responsible for the regulation of UAVs and is a signatory of the International Civil Aviation Organisations (ICAO). As such, the SACAA regulations comply with certain technical international standards (SA-CATS) [36]. The SACAA defines a UAV as a Remotely Piloted Aircraft System (RPAS). Under the authority, UAVs are allowed to be used for personal and private use, provided that the operator does not gain from its use commercially. All commercial operations are required to be registered and comply with the regulations of Part 101 of the SACAA act [37] [38]. When utilising the UAV for the operation proposed by the research project, the operator of the UAV would need to undergo theoretical and practical training to obtain a RPAS license through an organisation such as the Remote Training Organization (RTO) before a flight could commence. Should the process become commercialised, the UAV itself would also need to be thoroughly inspected and undergo testing before it can be approved for commercial use to ensure compliance with both the SACAA and SA-CATS regulations. The regulations further categorise UAVs based on capabilities and intended uses, and assigns additional regulations based on the UAVs category. Table 2-1 below describes the categories into which the SACAA groups UAVs based on their prospective applications.

Table 2-1: UAV Classification Categories Outlined by [37] [39]

Class	Line-of-sight	Energy (kJ)	Height (m)	MTOM (kg)
Class 1A	R-VLOS/VLOS	E<15	h<121.92	m<1.5
Class 1B	R-VLOS/VLOS	E<15	h<121.92	m<7
Class 1C	VLOS/E-VLOS	E<34	h<121.92	m<20
Class 2A	VLOS/E-VLOS	E<34	h<121.92	m<20
Class 2B	Experimental/Research			
Class 3A	BVLOS	E>34	h<121.92	m<150
Class 3B	VLOS/E-VLOS	Any	h>121.92	m<150
E -Refers to Energy at impact should there be a collision				
h – Refers to the UAVs flying height above the control surface				
***All operations remain restricted to radio line-of-sight**				
VLOS – Visual Line of Sight				
R-VLOS – Restricted Visual Line of Sight				
E-VLOS – Extended Visual Line of Sight				
BVLOS – Beyond Visual Line of Sight				

With reference to Table 2-1 above, it is evident that for the intended use of the UAV within this research project, the DM300 UAV would fall under category 3A. This categorisation was made on the assumption that the operation became commercialised and based on the UAVs unobstructed transmission range of 15km and unrestricted service ceiling placing the UAV in the BVLOS category. In this category, the pilot of the UAV is required to possess a Multi-rotor Remote Pilot Licence (MR-RPL). Additionally, due to the extended range of use, the pilot is required to possess a BVLOS endorsement on their RPL [38]. In addition to the above regulations, the SACAA has an imposed power reserve regulation on all VLOS and B-VLOS vehicles which requires the vehicle has enough battery life to complete the planned flight with a minimum of a 10% reserve in battery life. Finally, in accordance with subsection 101.05.4 of the regulations act, the SACAA prohibits the releasing, dispensing, dropping, delivering, and deploying of all objects from a RPAS unless the pilot is in possession of a RPAS operators Certificate (ROC) [40].

2.6 Inertial Stabilisation Platform Overview

Inertial stabilisation is applicable to systems which require line of sight (LOS) stabilisation relative to a specified target. These systems include missile guidance systems, auto-tracking telescopes, and camera systems [41]. Alternatively, inertial stabilisation can be used to eliminate disturbances and errors acting on a sensor, or a system as a whole. Inertially Stabilised Platforms (ISPs) are commonly integrated into systems to facilitate inertial stabilisation of a system component or assembly about, or relative to, a set point. An ISP is a device which controls the orientation of a payload, and commonly achieves this using structure synonymous to a gimbal. A single gimbal is a simple support system which allows rotation of an object about one Degree of Freedom (DOF), or axis. A common practice is to mount single gimbals in orthogonal orientations to one another to allow more DOFs of an object about the Centre of Gravity (CoG) of the system [41]. This practice is illustrated below in Figure 2-2, where the object can be seen to have the ability to rotate about the x-axis, the y-axis, and the z-axis due to the Roll gimbal, Pitch gimbal, and Azimuth gimbal, respectively.

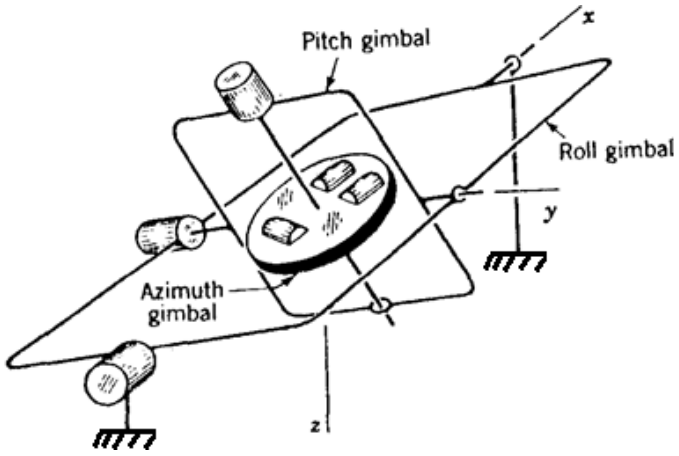

Figure 2-2: Orthogonal Gimbal Orientations, Adapted From [42]

Whilst ISPs are applicable to a vast array of applications, the general purpose of the ISP remains fixed: to maintain the orientation of an object. This applies to objects which require a set (commonly level) orientation in 3D space, as well as object which require a set orientation relative to another object (such as in a tracking operation) in 3D space. This is mostly done by stabilising the payload about two gimbal axes, however, stabilisation about three or more gimbal axes (redundancy) has shown better isolation of the ISP from its mounting platform, leading to better performance of the ISP [41]. Within the research project outlined by Chapter 1 above, the role of the ISP would be to allow for relative motion between the UAV and the gimbal assembly, whilst accurately stabilising the payload platform in real time. That is: the inertial rate sensor or Inertial Measurement Unit (IMU) is to be held steady in inertial space when intentional motion of the UAV and disturbances from the external environment occur.

2.6.1 Commercially Available ISPs

Due to advances made by the 4th industrial revolution, ISP technology has evolved rapidly due to the constant need to extend their uses. In aerial applications, ISP technology is readily called upon for rejection of noise and disturbances resonating from aircraft to attachments, external forces due to wind gusts, rain, and turbulence. As a result, there exists a plethora of commercially available ISP attachments for this purpose. Figure 2-3 provides examples of commercially available ISPs developed by DJI Enterprises.

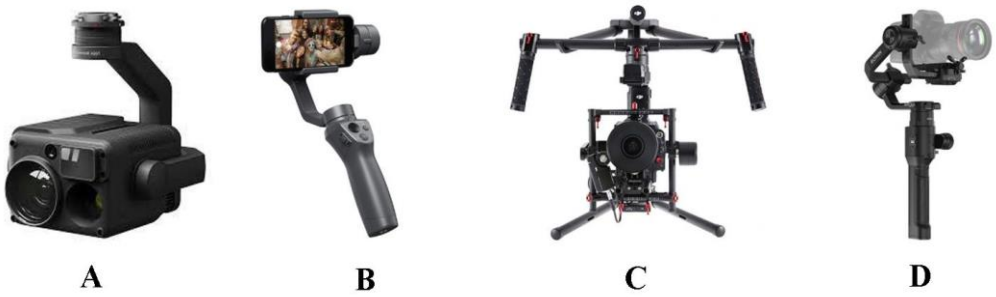

Figure 2-3: Commercially Available ISP Units, Adapted from [114] [115]

In Figure 2-3 above, a few of the commercially available ISPs from DJI Enterprises are shown. All of the displayed gimbals are 3-axis stabilisers. Their specific models are the Zenmuse H20T (A), the Osmo Mobile 2 (B), the Ronin-MX (C), and the Ronin-S (D). Of the illustrated ISPs, the Osmo Mobile 2, Ronin-MX, and the Ronin-S are handheld devices, whereas the Zenmuse H20T can be attached to the DM300. The Zenmuse H20T has an angular vibration range of ±0.01°, a mechanical range in the roll axis of 90° to +60°, in the pitch axis of -132.5° to +42.5°, and in the azimuth (yaw) axis of ±330°. The controllable range of the assembly in the pitch axis is -120° to +30°, and ±320° in the yaw axis. [43]. The compatibility of the Zenmuse H20T ISP with the DM300 meant that its specifications could be used as target specifications for the ISP resulting from this research project.

2.7 ISP Composition Theory

Typically, ISPs are comprised of three sub-systems; a payload to be stabilised, an electro-mechanical assembly to facilitate and limit the motion of the payload, and a control system which actuates the gimbal assembly and payload. These sub-systems are further elaborated on in the following subsections.

2.7.1 ISP Payload

The payload of the ISP is the overriding system which determines the system size, specifications, and constraints. There are many scenarios in which inertial stabilisation may be required. As such, it is not possible to fully categorise payloads and, hence, determine system specifications. Any scenario in which a degradation of system performance is observed due to external disturbances or torques are eligible for inertial stabilisation. The resulting electro-mechanical assembly is dependent on the payload being stabilised.

2.7.2 Electro-Mechanical Assembly

The electro-mechanical assembly of the ISP comprises of all the necessary mechanical and electrical components required for the system to function as required. The electro-mechanical assembly also provides a location through which the ISP can be affixed to the host vehicle. The complexity of the electro-mechanical assembly is directly linked to the intended purpose and payload of the ISP. These two factors determine the type of electro-mechanical assembly required. An ISP can be either mass stabilised or mirror stabilised [41]. Deciding under which category the intended purpose and payload of the ISP falls is intrinsic to the design of the electro-mechanical assembly.

2.7.2.1 Mass Stabilisation

In a mass stabilised system, the entire payload is stabilised through the rotation of gimbal axes. Here, the rotation of the host vehicle of the ISP is counteracted by the payload being rotated in the opposite direction to facilitate stabilisation of the payload. Hence, the gimbal rotates in such a way that the payload is directly controlled by the gimbal motion [41]. Within this configuration, the number of gimbal axes required is equal to the number of axes in which stabilisation is required. Relating back to the DM300 being utilised by the research project, only the tilting motion of the UAV when rolling or pitching posed a risk of destabilising the payload. Therefore, only two axes of stabilisation would be required, the roll axis and the pitch axis, to stabilise the payload in response to disturbances experienced by the platform resulting from UAV kinematics. With an anticipated rigid mounting of the ISP to the UAV, these disturbances would be experienced by the platform and payload in the form of a torque about one or both axes. A mathematical relationship between the UAV motion and the torques experienced by the ISP platform and payload was therefore required.

The ideal, frictionless mass stabilised ISP obeys Newton's 2nd Law for stabilisation. That is: the disturbance torque, T, acting on the system is equal to the product of the systems moment of inertia, I, and the systems angular acceleration, α, giving:

$$\sum T = I\alpha \tag{2-1}$$

The ideal system would be one that has balanced gimbals, yielding a negligible internal torque about each axis. This is done to minimise the net torque acting on the payload. As such, the ideal system would remain stable in its initial position. In a real system, however, internal disturbance torques cannot be avoided. Internal disturbances arise from friction in the system, physical flexure of the system, and dynamic and geometric coupling within the assembly [41]. When designing a mass stabilised ISP, a major design goal is to minimise the disturbance effects on the payload. This is done during the design phase of the electro-mechanical assembly, by iteratively designing the centre of mass of the system to coincide with one of the axes of rotation of the system [44] . In most cases, kinematic disturbances are present in the ISP. This can be due to physical coupling relationships between gimbal axes, meaning that the rotation of one axis induces involuntary rotation onto the other, due to system geometry. Disturbances can also arise from dynamic relationships between the rotation of the gimbals and the moment of inertia of the assembly. Reduction of these disturbances is possible through by suspending a gimbal from an axis which coincides with the CoG of the assembly [45]. The mathematical modelling of kinematic relationships between gimbals can be found in section 2.9 below.

In the case of the UAV integrated ISP for disaster management and humanitarian aid, it would not be sufficient to stabilise the system using a simple mechanical system such as springs due to the contribution of the ISP to research: the design, manufacture, and testing of a novel payload attachment for a "Universal" payload which can consist of blood samples, vaccines, and unbalanced loads. Here, it will not be uncommon for payloads of different geometries, weights, and distributions to be placed in the payload cradle of the ISP. Therefore, it is not possible to design a simple mechanical system to account for all payload variables; for a light payload, the spring would be too tough and essentially rigid on the payload, and for a payload approaching the maximum allowable weight, the response of the spring would be slower than required. Therefore, an electro-mechanical ISP is required to control the stabilisation of the payload. These systems are most commonly controlled using DC motors due to their high torque and precision capabilities in control applications. These DC motors directly control the gimbal, or make use of a gearing system, or a belt drive system. Hydraulic, pneumatic, and piezoelectric actuators have also been used, but these are uncommon options [46]. The most common form of actuator coupling is direct coupling where the DC motor approximates an ideal, direct torque on the gimbal.

2.7.2.2 Mirror Stabilisation

In a mirror stabilised system, components such as mirrors and prisms are controlled to maintain a LOS relative to a sensor mounted on the base vehicle. Mirror stabilisation is commonly employed on systems which have a large sensor and systems which have a mass distribution which makes them unsuitable for mass stabilisation [41]. Due to the kinematics of a mirror stabilised system, where only certain components move instead of the entire system, it is possible to make mirror stabilised system significantly more compact than mass stabilised systems. As such, these systems are more suitable to applications where there are physical or geometric design constraints imposed on the system design. The general consensus is that mass stabilised systems offer superior results over mirror stabilised systems with regards to LOS control precision, especially when dealing with small angles of rotation [47].

2.7.2.3 Alternative Stabilisation Techniques

An alternative stabilisation technique to both mass and mirror stabilised systems, is the use of a feedforward control system. In this system, a gyroscope is attached rigidly to the base vehicle, and the technique referred to as strapdown technology [48]. The feedforward system receives the LOS position or motion based on the strapdown data and estimates the relative motion between the base vehicle and the assembly controlling LOS motion. Subsequently, a closed control loop is formed about the LOS signal, and not the gyroscope signal [41]. The gyroscope is then required to continually provide accurate measurements to the control system. It is also essential to actively mitigate gyro drift within the ISP as feedforward gyroscopes generally desire greater accuracy and sensitivity than feedback gyroscopes. Certain feedforward techniques have also been shown to better deal with non-linearities such as friction within the ISP system, as well as to improve rejection of base vehicle motion disturbances [49].

Incorporating forms of redundancy into the ISP design can aid in stabilising of the system. Designing the gimbal to include redundant gimbals – more than one gimbal per axis of rotation – allows the ISP to have more DOF than required by the application. Redundant gimbals can be used to eliminate gimbal lock, where certain input commands cause a geometric lock within the assembly. This technique is often applied to cases in which a high aerodynamic disturbance is expected. The basic idea behind this technique is that the outer gimbal absorbs majority of the external disturbance, which allows the inner gimbal to perform its task of stabilisation more accurately [49].

2.7.3 Control System

The final subsystem of the ISP is the control system. Control system constituents include the hardware, software, algorithms, and any other architecture which facilitates the control of the ISP [50] .The main objective of the control system is to command rotations of the ISP axes in response to base vehicle movements, in order to maintain the desired payload orientation. The control system is required to do this whilst simultaneously accounting for, and thus rejecting, disturbances imposed on the ISP. The primary aims of the control system are to:

1. Stabilise the sensor and mitigate disturbance to the sensor, such that accurate sensor data may be obtained.
2. Keep track of the required platform orientation.
3. Measure the real time orientation of the platform.
4. Command actuators to rotate the platform in response to the actual position, to achieve the desired position.

Within the ISP configuration, the control system assumes the role of combining the dynamics of each individual system component. The efficiency and effectiveness of the control system is dependent on the system dynamics of components, as well as the derived control algorithm. According to [51], control systems which have been Proportional-Integral-Derivative (PID) tuned, or Proportional-Integral (PI) tuned, are most abundant amongst ISPs. However, remarkable results with regards to better disturbance rejection have been realised using more complex control methods such as internal model control, adaptive control, fuzzy PID, feedforward control, and H_∞ [50], [49] - [52]. For more complex scenarios where controller optimisation and robustness are of interest, these complex control methods are well equipped to deal with non-linearities present in the system. Non-linearities which commonly arise in ISPs include effects of friction in the assembly, structural resonances, unbalanced payloads, as well as actuators and Inertial Measurement Units (IMUs) reaching their physical limits (saturation) [44].

The purpose of the research being undertaken in this research project is two-fold; to develop an ISP compatible with the DM300 UAV, and to assess whether it is a viable solution to the lack of universal payload transportation devices for disaster management and humanitarian aid scenarios. Hence, a classical PI or PID controller will suffice as the emphasis of the project is not solely focused on the performance of the ISP. Osborne, [53], suggests that while these controllers are theoretically only appropriate for linear systems, they produce acceptable results in systems with small deviations from the required operating point. They do, however, lose accuracy as distance from the required operating point is increased [53]. The typical ISP control system is composed of two loops: a low bandwidth position tracking loop, and a high bandwidth rate loop. Figure 2-4 below depicts the typical control system block diagram for an ISP.

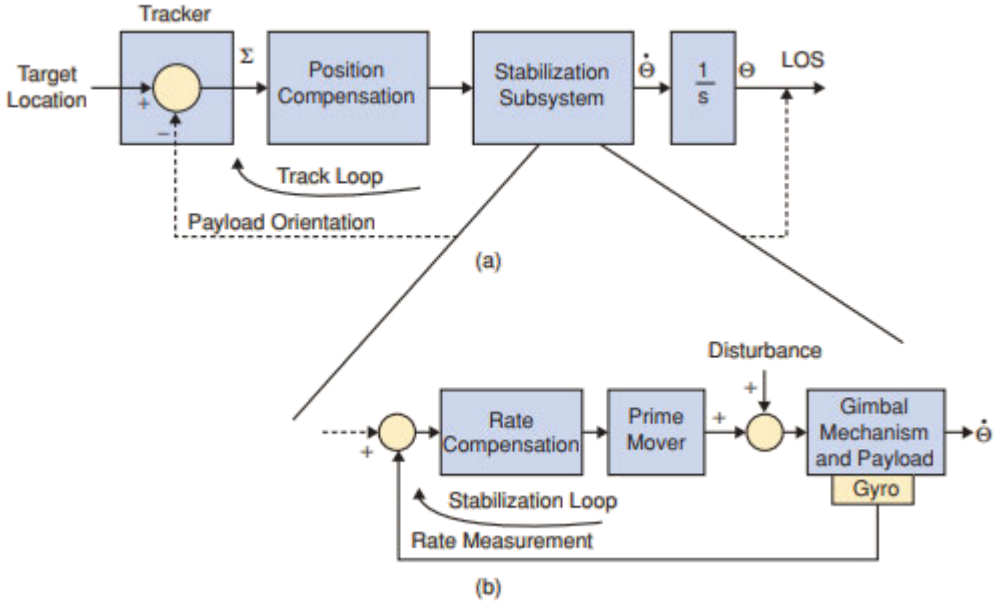

Figure 2-4: ISP Typical Control Architecture, Adapted From [49]

As can be seen in the above figure, the previously mentioned high bandwidth inner stabilization loop is shown by (b). Conversely, the position tracking loop is the low bandwidth closed loop represented by (a), which forms the outer control loop. Within the typical arrangement, the inner stabilisation loop is responsible for the mitigation of disturbances and involuntary motion within the electromechanical assembly. The outer tracking loop is responsible for ensuring that the LOS of the IMU remains fixed relative to the target value, and thus operates on the LOS angle of the platform [49].

The stabilisation loop in the typical ISP control system can be seen to receive its input commands from the outer tracking loop. Similarly, the tracking loop can be seen to receive its input commands via the outputs of the stabilisation loop, making the control loops mutually-dependant on each other. Classical compensation choices for the inner stabilisation loop include PI and PID controllers, as previously alluded to. P controllers have been found to be adequately responsive, however, their low-frequency disturbance rejection capabilities have been shown to be inferior to the PI and PID alternatives. While PID controllers' low-frequency disturbance rejection capabilities are superior to PI controllers, a stable design is often more difficult to achieve, and these controllers are prone to oscillating in response to input commands. The rate input to the stabilisation loop can be seen to be controlled by the gyroscope of the IMU. For simplicity sake, this research project will make use of a Micro Electro-Mechanical System (MEMS) gyroscope which is integrated into an IMU, due to its small form factor and miniscule mass in comparison to alternative gyroscopic sensors which are well documented in [41] [49].

One of the most convenient ways to predict how well the control system will be able to follow input commands to mitigate disturbance torques is to analyse the closed-loop bandwidth. The closed-loop bandwidth is a quantifiable measure of the control systems feedback response to its input command. At

low frequencies, the rate-command following error is reduced by a factor which is approximately proportional to the closed-loop bandwidth, according to [41]. The closed-loop bandwidth is dependent on the control system specifically designed for the application, the dynamic characteristics of the components of the system, which are present in the loop, as well as torsional structural interactions and dynamics. In smaller systems, however, the closed-loop bandwidth is more dependent on the dynamics of actuators and gyroscopes. Hence, the optimal control system would be designed to account for component dynamics, noise, and error. Figure 2-5. below provides a summarised version of the structural interactions and dynamic disturbances which are common to ISPs and are known to affect the closed loop bandwidth.

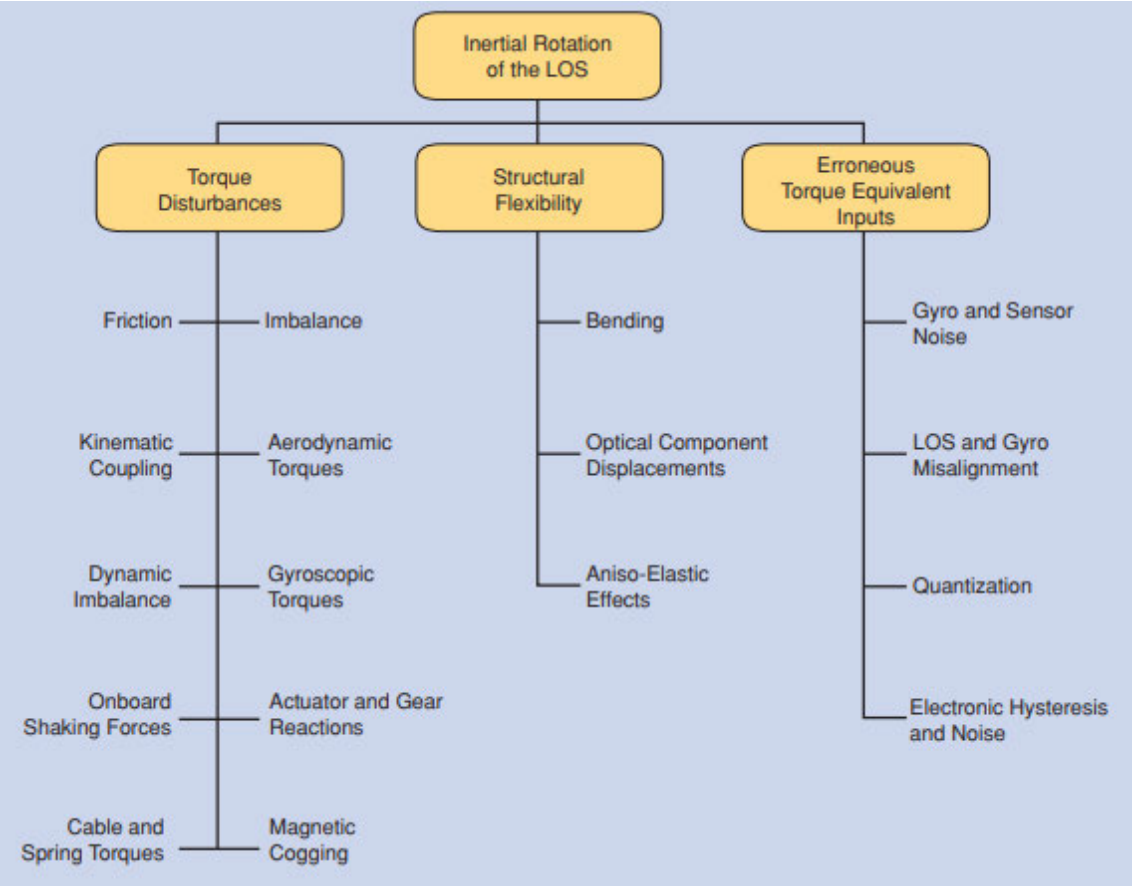

Figure 2-5: Summary of Common ISP Disturbances [41]

Another convenient method to analyse the ability of the control system to follow input commands and eliminate errors would be to analyse the step response of the system. A step response analysis elucidates the system response characteristics following a disruption of the initial equilibrium state of the system. The disruption of the system readily takes the form of a "step", which administers a rapid change in the system input command. In the case of the ISP, the step would disrupt the desired platform orientation, thus designating the desired platform orientation to be the control system input.

2.8 Additive Manufacturing Applicability

The aerial nature of the ISP resulting from this research project is an important consideration which plays a vital role in the determination of the manufacturing method to utilise during the manufacturing phase of the project. Conventionally, fabrication of UAVs and associated aerial prototypes has made use of technologies such as CNC cutting of foam materials using a hot wire, manual balsa wood fabrication, as well as manual hand fabrication using composites. Whilst these materials have fared well for their intended purpose, the use of manual, labour intensive, processes have proven disadvantageous in comparison to modern Additive Manufacturing (AM) methods. AM includes all manufacturing processes in which a 3D part is created from a Computer Aided Design (CAD) model, layer by layer. Characteristics of conventional methods such as high mould costs, long lead time on manufacturing, and complex manufacturing processes consisting of many steps cast modern AM methods in a very desirable light due to their ease of manufacture [54].

Arguably the biggest drawback of the conventional fabrication methods mentioned prior is the restriction they impose on the design of aerial vehicles. Due to the process-dependence of these manufacturing methods, designs are constrained by the limitations of manufacturing machinery and tools, which prohibits design innovation [54]. Recent advancements in the research on cell structures and topology optimisation have produced a basis for UAVs to be fabricated using lightweight structures, while still maintaining the required structural resilience for aerial applications [55]. However, conventional manufacturing methods cannot be used to create these structures. Hence, optimised, and innovative design of aerial vehicles necessitates the use of modern AM practices.

Some of the commonly exploited AM techniques for UAVs and aerospace applications are Fused Deposition Modelling (FDM), Stereolithography (SLA), Selective Laser Sintering (SLS), and Selective Laser Melting (SLM). Of these techniques, the most commonly used method to create UAVs and associated aerial vehicle parts are FDM, SLS, and SLA. Due to the applicability, affordability, and sustainability of FDM fabrication, this method will be exploited in this research project.

2.8.1 Fused Deposition Modelling

Under the influence of 4IR the global manufacturing industry is being revolutionised, with much emphasis being placed on research and development in the AM field. FDM is an additive manufacturing process wherein a thin 2D trace of molten, thermoplastic, polymer (known as filament) is deposited from a heated nozzle on a flat build surface in a given shape, before being hardened via convection – either forced or natural depending on the application. Thereafter, the nozzle is lifted by a small increment (usually equal to the desired layer height), and the process is repeated on top of the previous layer until such time as a complete 3D part is produced.

FDM has become an established technique for producing parts rapidly, with precision, from a CAD model. Initially, FDM parts could not be produced with an acceptable level of geometrical accuracy and surface finish which was required for engineering applications. However, development within the field has produced machines capable of producing parts with high accuracy, a uniform surface finish, and better structural integrity than ever before. The infinite repeatability capabilities of the new FDM machines, coupled with the part characteristic above, means that parts can now be produced such that the engineering criteria of FDM parts are being fulfilled [56].

Research and development of FDM technology has seen it become affordable and available to hobbyists, whilst still being used by businesses and professionals for commercial purposes. FDM often proves to be a superior manufacturing method over conventional fabrication techniques due to its customizability, accuracy, and sustainability. The most common FDM materials used are Polylactic Acid (PLA) and Acrylonitrile Butadiene Styrene (ABS) [57]. Due to their substituents being naturally sourced sugarcane and maize, these materials are affordable and abundant. ABS and PLA FDM parts will typically produce similar mechanical properties; however, PLA is generally the favoured material for use within the FDM industry due to its ease of use, biodegradability, and sustainability. Other commonly utilised FDM materials include Nylon and Polyethylene Terephthalate Glycol (PETG). However, these materials were not considered in the study as they are more difficult to print with (more prone to failure during printing), and have lower tensile and bending strengths than PLA [58].

2.8.2 FDM Sustainability

One of the major hinderances towards 4IR is environmental degradation associated with industry expansion, advanced machining abilities, and the increased number of machines being developed and introduced into the industry. In this regard, focus on sustainable strategies and techniques for manufacturing is being increased. Of relevance to this research project, is the relationship between FDM, 4IR, and sustainability. Benefits such as reduced demand on raw materials such as metals, weight savings in production parts, energy savings during manufacturing, reduced part production times, and minimisation of waste mean that the technique is intrinsic to the concepts that the 4IR is trying to instil [59]. However, for the technique to be of total relevance to 4IR, it must be deemed to be a sustainable method of manufacturing.

The sustainability of FDM technology can readily be assessed from two perspectives: the recyclability of its materials, and the reusability and reproduction of parts. The PLA FDM material is derived from the renewable resources of maize and sugarcane. This makes the PLA material abundant and easily attainable, whilst also being cost effective. Apart from FDM, PLA can be found in disposable food packaging and utensils. [60]. Whilst being sourced from the same resources, PLA is far more biodegradable than ABS – mainly due to processes followed during production and its chemical makeup [61]. In addition to biodegradability, the specific chemical makeup of the material renders PLA a thermoplastic, meaning that parts can be recycled and re-extruded as new filament for new parts. As such, the reusability and

recyclability of the FDM material proves to be a sustainable end-of-life process, rendering the FDM process itself sustainable.

2.8.3 FDM Potential in Aerial Applications

3D-printing techniques are introducing a paradigm shift by rapidly replacing the conventional subtractive techniques, where material is removed from a larger workpiece, with AM methods. This paradigm shift is backed by companies such as Boeing, Blue Origin, Airbus, SpaceX, and Rocket Lab, amongst others, who introduce increasing numbers of 3D-printed parts in their designs each year [62]. Major benefits of 3D-printing exploited by these companies are the reduced production costs and reduced production times. This is because the need for process preparation and tooling for production is eliminated by these techniques. Hence, the use of AM techniques has proven applicable to the aircraft, aerial vehicle, and UAV industry.

Within the AM envelope, [1] and [63] have proven FDM to be widely used in aircraft construction due to the development of high-temperature composite polymer filaments, such as Carbon Fibre Reinforced Polymer (CFRP), which is the most common filament used for FDM manufacturing of complete UAVs. Additionally, the techniques are readily used for production of parts and assemblies for UAVs and associated components. As such, it is evident that FDM is applicable to the nature of the prototype being developed by this research project. However, using FDM for the intended purpose of this research project does face certain shortfalls. These shortfalls are discussed in section 2.6.4 and section 2.6.5 which follow.

2.8.4 Impact of FDM Process Parameters

Within the FDM process is a fundamental step where the CAD model is transferred into a slicing program and broken down into individual layers before fabrication can occur. Within the slicing program, various parameters exist which directly impact part strength, mass, durability, flexibility, fabrication time, print direction, and surface finish. The parameters which have the most influence on the above part characteristics are the layer height, infill density, infill pattern, wall thickness, and print speed. These are of particular interest to this research project as the lightest, most resilient parts are required during production as a direct result of the aerial nature of the project.

The impact of FDM process parameters on aerodynamic surfaces and the structural integrity of produced parts is crucial to the functional capabilities of the developed prototype. Aerodynamic drag is of interest within this research project, and the effect of FDM parameters on the drag coefficient of the prototype is an important consideration. Another important consideration is the impact of FDM parameters on the structural integrity of parts. Therefore, it will be necessary to undertake an exercise in parameter optimisation to determine the set of printing parameters which will produce parts with the most desirable strength-to-mass ratio, whilst minimising the effect of FDM parameters on aerodynamic drag of the prototype.

2.8.5 Aerodynamic Surfaces

Aerodynamic surfaces produced by FDM techniques are susceptible to increased drag forces as a direct result of their surface finish. It is common for FDM parts to exhibit lines on the part surface due to each subsequent layer being printed – this is known as the stair stepping effect. The stair stepping effect leads to higher relative roughness values than what is desirable in aerial applications [64]. This effect can, however, be minimised through optimal parameter combinations of layer height and part cooling during printing to produce the best surface finish possible of the machine.

An additional method to reduce this effect is to align the layer deposition direction of the machine with the direction of the intended forward velocity of the part [65]. By reducing the stair stepping effect on a part, the aerodynamic drag force exerted on the part in operation is being decreased. Whilst this is a desirable outcome, it can induce further imperfections into the part by increasing the anisotropic nature of the part. This is known to cause a directional dependence in the mechanical properties of the part for different layers, which can lead to a brittle part in one or more directions. As such, the risk of delamination in the part is increased [54]. Therefore, the optimum surface finish for preserving part strength and minimising the drag force on the part is obtained by combining optimal parameter combinations of layer height and part cooling during printing, and manual post-processing techniques such as sanding and polishing [60].

2.8.6 Structural Integrity

The structural integrity of a FDM part is readily improved upon through the inclusion of lightweight internal structures, and the use of materials with high strength-to-weight ratios. FDM possesses the capability to produce complex topologies and associated complex internal structures, while fabricating these parts using robust materials such as ABS and PLA. Thus, the FDM fabrication technique is capable of producing parts with a structural integrity which meets engineering needs. However, a limitation of FDM which deteriorates structural integrity of larger parts is the small build volume of most commercially available machines. This means larger parts must be designed as smaller, modular parts for printing and connected post-printing using additional fasteners. This introduces extra fasteners, weight, and complexity into the assembly, and can only be avoided by using a machine with a bigger build volume.

The FDM parameters intrinsic to part strength include infill density, infill pattern, wall thickness, and layer height. This was proven by [66], which determined, experimentally, that the force required to deform test specimens was inversely proportional to layer height. Infill percentage was shown to alter the effect of deposition angle on the required deformation force, such that a lower infill percentage yields a greater influence of deposition angle on deformation force. These results held true for specimens of the same infill pattern.

The infill pattern of FDM fabricated parts is known to be a major contributor to mechanical strength and resilience. In the Cura slicing software, fourteen different infill patterns are available during slicing. Of

these patterns, six are appropriate for models, figurines, and non-functional FDM prints. The remaining eight patterns are applicable to functional parts (which require high strength in multiple directions), and flexible parts respectively. The infill patterns applicable to functional parts are known as Cubic, Cubic Subdivision, Honeycomb, Tetrahedral, Quarter Cubic, and Gyroid [67]. Through a review of empirical testing methods, [68] was able to determine that the Gyroid was the most stable infill pattern, withstanding a compressive force of 246kg along all axes, thus offering equal strength along all three axes. Similarly, [68] found that the Cubic infill pattern could withstand a uniaxial compressive force of approximatively 250kg, however, the strength of the z-axis was noticeably less than the x- and y- axes. Both of these infill patterns produced testing samples with a mass similar to that of the other infill patterns, but took around 125% longer than the average, normalized, time taken to produce a sample.

2.9 ISP Mathematical Modelling

As mentioned previously, there are many scenarios in which an ISP is required. Of these scenarios, there are exceptionally few which require stabilisation of only one axis. Almost all ISP systems in practice are required to stabilise an object about multiple axes. It is for this reason that the dynamics of the multi-axis ISP needs to be analysed. In [41], it can be seen that the kinematics of a multiple gimbal system inevitably introduces some nonintuitive effects, such as dynamic coupling and gimbal lock effects. As these effects are not present when analysing gimbals individually using *Equation 2-1*, it is necessary to analyse the system as a whole. Additionally, since not all multi-axis gimbal systems can be considered rigid, symmetrical, and homogenous (of constant density throughout) – especially when manufactured by FDM – *Equation 2-1* fails to produce an acceptable dynamic description of the system.

The following section of the chapter presents the equations of motion, and their derivations, for the roll-pitch ISP. Within this research project the main focus, with regards to the ISP, is attitude control – maintaining a constant, level position of the payload platform in real time. This requires that the dynamic relationships due to the geometry and mechanical coupling of the ISP system be derived. Using these relationships, a robust controller can be designed to further reduce errors in the attitude of the platform. The development of the following equations of motion was mainly based on existing theories in the works of Johansson [69] and Hepworth [50], however, Tas et. al [70] also aided in the development.

2.9.1 Orientation and Reference Frames

In Figure 2-6 below, the orientation and rotations of the DM300 UAV in inertial space are presented. As can be seen by the figure, the “Roll” function of the UAV is defined as a rotation orthogonal to the forward direction. Similarly, the “Pitch” function is defined as a rotation which is orthogonal to the roll direction.

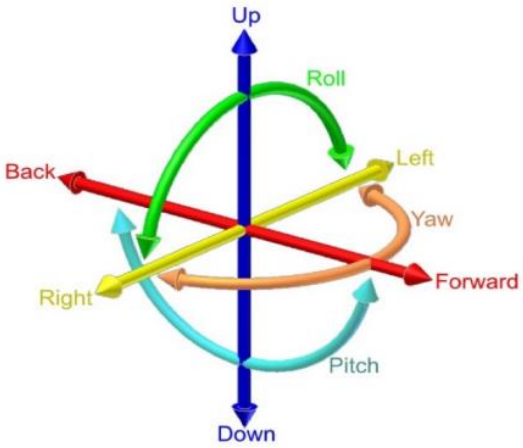

Figure 2-6: ISP Rotation Designation [123]

It is these rotations of the UAV which produce a change in attitude of the pitch platform, and thus induce a reaction rotation of either (or both) the roll and pitch gimbal within their respective reference frames, relative to the inertial reference frame. It is, therefore, imperative to derive a mathematical relationship for the rotation of the reference frames of the body of the UAV, and those of the roll and pitch axis of the ISP.

Consider the schematic shown in Figure 2-7 below. The schematic displays a triad of orthogonal vectors which primarily define the orientation of the inertial reference frame, I. The components of the inertial reference frame can be seen to be defined by the unit vectors $\{X_I,Y_I,Z_I\}$. For the purpose of this research project, the forward heading direction of the UAV will be aligned with the positive Y_I direction of the inertial reference frame. Therefore, the following designations were made:

i. Rotation about the X_I axis denotes a Pitching motion of the ISP, with the pitching angle being observed as θ_P.
ii. Rotation about the Y_I axis denotes a Rolling motion of the ISP, with the rolling angle being observed as θ_R.
iii. The Z_R and Z_P axes of the ISP gimbals are fixed and rotate with the UAV relative to the Z_I axis.
iv. An IMU is fixed to the pitch gimbal to measure the pitching and rolling angles, θ_P and θ_R , respectively.
v. The roll and the pitch gimbals are assumed to be rigid bodies.

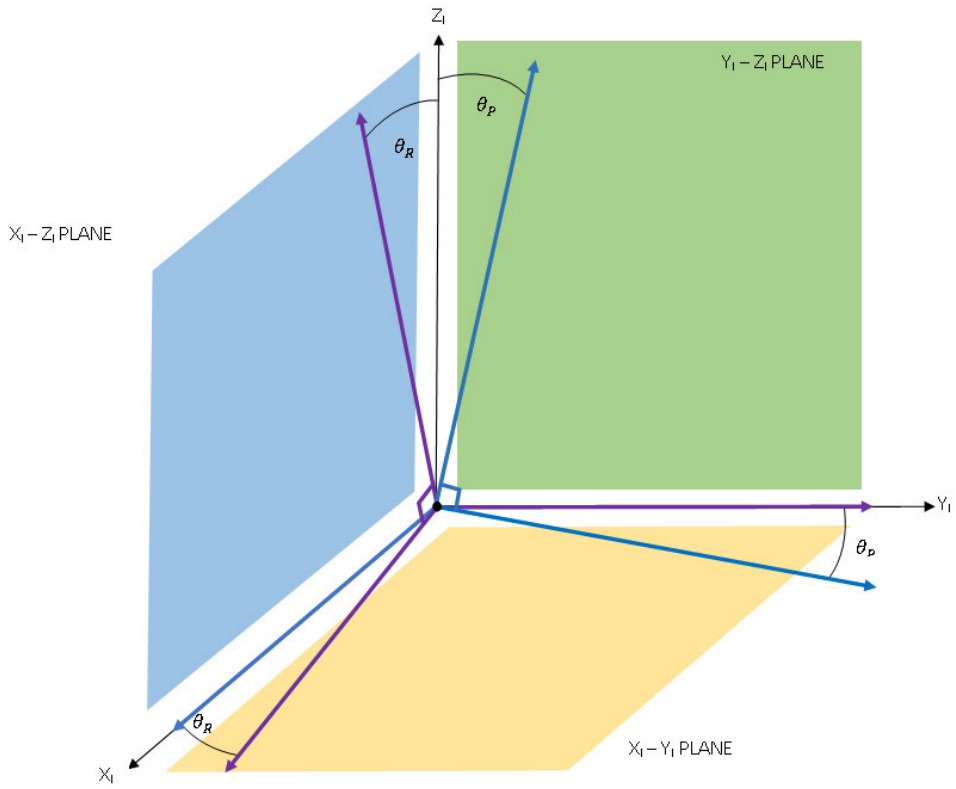

Figure 2-7: ISP Reference Frame Orientation Designations

Within the figure, two additional triads of orthogonal unit vectors can be seen. The purple triad represents the components of the motion of the roll gimbal of the ISP, thus defining the roll reference frame, R. The components of the roll reference frame can be seen to be defined by the unit vectors $\{X_R,Y_R,Z_R\}$. Similarly, the blue triad represents the components of the motion of the pitch gimbal of the ISP, and describes the pitch gimbal reference frame, P. The components of the pitch reference frame can be seen to be defined by the unit vectors $\{X_P,Y_P,Z_P\}$.

2.9.2 Euler Rotations

In order to produce an adequately descriptive mathematical model of the ISPs motion, it is necessary to derive a relationship between the rotation of each gimbal of the ISP and the body of the UAV. To do this, the triads of each of these components are projected into a single reference frame, and made to share a frame origin, as shown in Figure 2-7 above. Making use of Euler's 1st theorem, which states that "Any two independent orthonormal coordinate frames may be related by a minimum sequence of rotations (less than four) about coordinate axes, where no two successive rotations may be about the same axis" [71], the total rotation matrix of the ISP can be found relative to the inertial frame, I. This is done using Euler angles, where the sequence for calculations should be from the outermost axis to the innermost axis. Therefore, an Euler sequence of pitch-roll is used.

Firstly, the inertial frame I is translated into coincidence with the pitch frame, P, by a positive angle of rotation, θ_P, about the X_I axis. As such, a unit vector in I may be represented in P by the rotation matrix R_P^I, where:

$$R_P^I = \begin{bmatrix} 1 & 0 & 0 \\ 0 & cos\theta_P & sin\theta_P \\ 0 & -sin\theta_P & cos\theta_P \end{bmatrix}$$

Secondly, the pitch frame P is translated into coincidence with the roll frame, R, by a positive angle of rotation, θ_R, about the Y_I axis. As such, a unit vector in P may be represented in R by the rotation matrix R_R^P, where:

$$R_R^P = \begin{bmatrix} cos\theta_R & 0 & -sin\theta_R \\ 0 & 1 & 0 \\ sin\theta_R & 0 & cos\theta_P \end{bmatrix}$$

Finally, the total rotation matrix between the inertial frame, I, and the roll frame, R, can be determined by *Equation 2-2*:

$$R_R^I = R_P^I R_R^P \tag{2-2}$$

Giving:

$$R_R^I = \begin{bmatrix} cos\theta_R & 0 & -sin\theta_R \\ sin\theta_P sin\theta_R & cos\theta_P & sin\theta_P cos\theta_R \\ cos\theta_P sin\theta_R & -sin\theta_P & cos\theta_P cos\theta_R \end{bmatrix}$$

2.9.3 ISP Kinematics

The law of conservation of momentum provides a basis for the derivation of dynamic equations of the ISP, through the derivation of dynamic equations for each individual gimbal constituent of the ISP. The angular momentum of a gimbal can be found as follows in *Equation 2-3*:

$$\vec{L} = I \cdot \vec{\omega} \tag{2-3}$$

Where the angular momentum vector, given by $\vec{L}$, is defined as the dot product of the gimbal inertia, I, and the angular velocity vector, ω , of the gimbal. Now, the conservation of angular momentum can be defined as per *Equation 2-4*.

$$\sum M = \dot{\vec{L}} \tag{2-4}$$

Which states that the net external moment acting on the gimbal, M, is equivalent to the time derivative of the angular acceleration, $\vec{L}$, which is defined relative to a fixed coordinate system such as an inertial reference frame. However, when there is relative motion between the gimbal reference frame and the defined coordinate system, as is the case with the UAV ISP, it is necessary to adapt *Equation 2-4* above to include changes in the angular momentum due to Coriolis forces. Suppose the moving coordinate system has an arbitrary angular velocity, φ, then *Equation 2-4* becomes:

$$\sum M = \dot{\vec{L}} + \varphi \times \vec{L} \tag{2-5}$$

In the case that the moving coordinate system is attached to the gimbal body, as is the case with the UAV body being attached to the gimbal assembly in the research project, then $\omega = \varphi$, and *Equation 2-5* above simplifies to *Equation 2-6* below as follows:

$$\sum M = I \cdot \dot{\vec{\omega}} + \vec{\omega} \times \vec{L} \tag{2-6}$$

Using the above equations, the roll and the pitch gimbals of the ISP may be analysed to derive dynamic equations for the system as a whole. These dynamic equations will then be utilised later on in the project timeline for the control system design and tuning.

2.9.4 Pitch Axis Kinematics

Within the ISP configuration, the pitch axis has been assigned the responsibility of housing the payload platform. To model the 3D rotational motion of this axis, two kinematic properties are required. These properties are the axis' angular velocity, and its inertia. These properties are given by ω_P and I_P below, respectively. Here, the angular velocity matrix is given by:

$$\vec{\omega}_P = \begin{bmatrix} \omega_{x_P} \\ \omega_{y_P} \\ \omega_{zp} \end{bmatrix}$$

Similarly,

$$\dot{\vec{\omega}}_p = \begin{bmatrix} \dot{\omega}_{x_P} \\ \dot{\omega}_{y_P} \\ \dot{\omega}_{zp} \end{bmatrix}$$

And the inertia matrix, known as an inertia tensor, is given by:

$$I_P = \begin{bmatrix} I_{xxp} & D_{xyp} & I_{xzp} \\ D_{xyp} & I_{yyp} & D_{yzp} \\ D_{xzp} & D_{yzp} & I_{zzp} \end{bmatrix}$$

Where "I" denotes a moment of inertia and "D" denotes a product of inertia. Now, utilising *Equation 2-6* above, the net external disturbance moment imposed on the pitch gimbal can be found by *Equation 2-7* below.

$$M_P = I_P \cdot \dot{\vec{\omega}}_p \ + \vec{\omega}_P \ \text{x} \ \vec{L}_\text{P} \tag{2-7}$$

But first, $\vec{L}_\text{P}$, the angular momentum vector, is required. This is derived by:

$$\vec{L}_P = I_P \cdot \vec{\omega}_P$$

$$\vec{L}_P = \begin{bmatrix} L_{x_P} \\ L_{y_P} \\ L_{zp} \end{bmatrix} = \begin{bmatrix} I_{xxp} & D_{xyp} & I_{xzp} \\ D_{xyp} & I_{yyp} & D_{yzp} \\ D_{xzp} & D_{yzp} & I_{zzp} \end{bmatrix} \cdot \begin{bmatrix} \omega_{x_P} \\ \omega_{y_P} \\ \omega_{zp} \end{bmatrix}$$

$$\vec{L}_P = \begin{bmatrix} I_{xxp}\omega_{x_P} + D_{xyp}\omega_{y_P} + I_{xzp}\omega_{zp} \\ D_{xyp}\omega_{x_P} + I_{yyp}\omega_{y_P} + D_{yzp}\omega_{zp} \\ D_{xzp}\omega_{x_P} + D_{yzp}\omega_{y_P} + I_{zzp}\omega_{zp} \end{bmatrix}$$

Now,

$$M_P = \begin{bmatrix} M_{x_P} \\ M_{y_P} \\ M_{zp} \end{bmatrix} = \begin{bmatrix} I_{xxp} & D_{xyp} & I_{xzp} \\ D_{xyp} & I_{yyp} & D_{yzp} \\ D_{xzp} & D_{yzp} & I_{zzp} \end{bmatrix} \cdot \begin{bmatrix} \dot{\omega}_{x_P} \\ \dot{\omega}_{y_P} \\ \dot{\omega}_{zp} \end{bmatrix} + \begin{bmatrix} \omega_{x_P} \\ \omega_{y_P} \\ \omega_{zp} \end{bmatrix} \ \text{x} \ \begin{bmatrix} I_{xxp}\omega_{x_P} + D_{xyp}\omega_{y_P} + I_{xzp}\omega_{zp} \\ D_{xyp}\omega_{x_P} + I_{yyp}\omega_{y_P} + D_{yzp}\omega_{zp} \\ D_{xzp}\omega_{x_P} + D_{yzp}\omega_{y_P} + I_{zzp}\omega_{zp} \end{bmatrix}$$

Yielding:

$$M_P = \begin{bmatrix} I_{xxp}\dot{\omega}_{x_P} + D_{xyp}\dot{\omega}_{y_P} + I_{xzp}\dot{\omega}_{zp} \\ D_{xyp}\dot{\omega}_{x_P} + I_{yyp}\dot{\omega}_{y_P} + D_{yzp}\dot{\omega}_{zp} \\ D_{xzp}\dot{\omega}_{x_P} + D_{yzp}\dot{\omega}_{y_P} + I_{zzp}\dot{\omega}_{zp} \end{bmatrix}$$

$$+ \begin{bmatrix} \omega_{y_P}\left(D_{xzp}\omega_{x_P} + D_{yzp}\omega_{y_P} + I_{zzp}\omega_{zp}\right) - \omega_{zp}(D_{xyp}\omega_{x_P} + I_{yyp}\omega_{y_P} + D_{yzp}\omega_{zp}) \\ \omega_{zp}\left(I_{xxp}\omega_{x_P} + D_{xyp}\omega_{y_P} + I_{xzp}\omega_{zp}\right) - \omega_{x_P}(D_{xzp}\omega_{x_P} + D_{yzp}\omega_{y_P} + I_{zzp}\omega_{zp}) \\ \omega_{x_P}\left(D_{xyp}\omega_{x_P} + I_{yyp}\omega_{y_P} + D_{yzp}\omega_{zp}\right) - \omega_{y_P}(D_{xzp}\omega_{x_P} + D_{yzp}\omega_{y_P} + I_{zzp}\omega_{zp}) \end{bmatrix}$$

However, by suspending the gimbal from its principal axis, by design, the inertia tensor reduces to:

$$I_P = \begin{bmatrix} I_{xxp} & 0 & 0 \\ 0 & I_{yyp} & 0 \\ 0 & 0 & I_{zzp} \end{bmatrix}$$

And the pitch axis torque matrix above is simplified to:

$$M_P = \begin{bmatrix} I_{xxp}\dot{\omega}_{x_P} \\ I_{yyp}\dot{\omega}_{y_P} \\ I_{zzp}\dot{\omega}_{zp} \end{bmatrix} + \begin{bmatrix} \omega_{y_P}(I_{zzp}\omega_{zp}) - \omega_{zp}(I_{yyp}\omega_{y_P}) \\ \omega_{zp}(I_{xxp}\omega_{x_P}) - \omega_{x_P}(+I_{zzp}\omega_{zp}) \\ \omega_{x_P}(I_{yyp}\omega_{y_P}) - \omega_{y_P}(I_{zzp}\omega_{zp}) \end{bmatrix}$$

$$M_P = \begin{bmatrix} I_{xxp}\dot{\omega}_{x_P} + (I_{zzp} - I_{yyp})\omega_{y_P}\omega_{zp} \\ I_{yyp}\dot{\omega}_{y_P} + (I_{xxp} - I_{zzp})\omega_{zp}\omega_{x_P} \\ I_{zzp}\dot{\omega}_{zp} + (I_{yyp} - I_{zzp})\omega_{x_P}\omega_{y_P} \end{bmatrix}$$

2.9.5 Roll Axis Kinematics

In the same manner the pitch axis kinematics were derived, the roll axis kinematics are derived starting with the angular velocity, angular acceleration, and inertia tensor, given by $\vec{\omega}_R$, $\dot{\vec{\omega}}_R$, and I_R, respectively.

$$\vec{\omega}_R = \begin{bmatrix} \omega_{x_R} \\ \omega_{y_R} \\ \omega_{zR} \end{bmatrix}$$

Similarly,

$$\dot{\vec{\omega}}_R = \begin{bmatrix} \dot{\omega}_{x_R} \\ \dot{\omega}_{y_R} \\ \dot{\omega}_{zR} \end{bmatrix}$$

And the inertia tensor given by:

$$I_R = \begin{bmatrix} I_{xxR} & D_{xyR} & I_{xzR} \\ D_{xyR} & I_{yyR} & D_{yzR} \\ D_{xzR} & D_{yzR} & I_{zzR} \end{bmatrix}$$

Now, applying *Equation 2-6* above, the net external disturbance moment imposed on the roll gimbal can be found by:

$$M_R = I_R \cdot \dot{\vec{\omega}}_R \ + \vec{\omega}_R \mathrm{x}\, \vec{L}_R \tag{2-8}$$

And,

$$\vec{L}_R = I_R \cdot \vec{\omega}_R$$

$$\vec{L}_R = \begin{bmatrix} L_{x_R} \\ L_{y_R} \\ L_{zR} \end{bmatrix} = \begin{bmatrix} I_{xxR} & D_{xyR} & I_{xzR} \\ D_{xyR} & I_{yyR} & D_{yzR} \\ D_{xzR} & D_{yzR} & I_{zzR} \end{bmatrix} \cdot \begin{bmatrix} \omega_{x_R} \\ \omega_{y_R} \\ \omega_{zR} \end{bmatrix}$$

$$\vec{L}_R = \begin{bmatrix} L_{x_R} \\ L_{y_R} \\ L_{zR} \end{bmatrix} = \begin{bmatrix} I_{xxR}\omega_{x_R} + D_{xyR}\omega_{y_R} + I_{xzR}\omega_{zR} \\ D_{xyR}\omega_{x_R} + I_{yyR}\omega_{y_R} + D_{yzR}\omega_{zR} \\ D_{xzR}\omega_{x_R} + D_{yzR}\omega_{y_R} + I_{zzR}\omega_{zR} \end{bmatrix}$$

Finally,

$$M_R = \begin{bmatrix} M_{x_R} \\ M_{y_R} \\ M_{zR} \end{bmatrix} = \begin{bmatrix} I_{xxR} & D_{xyR} & I_{xzR} \\ D_{xyR} & I_{yyR} & D_{yzR} \\ D_{xzR} & D_{yzR} & I_{zzR} \end{bmatrix} \cdot \begin{bmatrix} \dot{\omega}_{x_R} \\ \dot{\omega}_{y_R} \\ \dot{\omega}_{zR} \end{bmatrix} + \begin{bmatrix} \omega_{x_R} \\ \omega_{y_R} \\ \omega_{zR} \end{bmatrix} \mathrm{x} \begin{bmatrix} I_{xxR}\omega_{x_R} + D_{xyR}\omega_{y_R} + I_{xzR}\omega_{zR} \\ D_{xyR}\omega_{x_R} + I_{yyR}\omega_{y_R} + D_{yzR}\omega_{zR} \\ D_{xzR}\omega_{x_R} + D_{yzR}\omega_{y_R} + I_{zzR}\omega_{zR} \end{bmatrix}$$

Yielding:

$$M_R = \begin{bmatrix} I_{xxR}\dot{\omega}_{x_R} + D_{xyR}\dot{\omega}_{y_R} + I_{xzR}\dot{\omega}_{zR} \\ D_{xyR}\dot{\omega}_{x_R} + I_{yyR}\dot{\omega}_{y_R} + D_{yzR}\dot{\omega}_{zR} \\ D_{xzR}\dot{\omega}_{x_R} + D_{yzR}\dot{\omega}_{y_R} + I_{zzR}\dot{\omega}_{zR} \end{bmatrix}$$
$$+ \begin{bmatrix} \omega_{y_R}(D_{xzR}\omega_{x_R} + D_{yzR}\omega_{y_R} + I_{zzR}\omega_{zR}) - \omega_{zR}(D_{xyR}\omega_{x_R} + I_{yyR}\omega_{y_R} + D_{yzR}\omega_{zR}) \\ \omega_{zR}(I_{xxR}\omega_{x_R} + D_{xyR}\omega_{y_R} + I_{xzR}\omega_{zR}) - \omega_{x_R}(D_{xzR}\omega_{x_R} + D_{yzR}\omega_{y_R} + I_{zzR}\omega_{zR}) \\ \omega_{x_R}(D_{xyR}\omega_{x_R} + I_{yyR}\omega_{y_R} + D_{yzR}\omega_{zR}) - \omega_{y_R}(D_{xzR}\omega_{x_R} + D_{yzR}\omega_{y_R} + I_{zzR}\omega_{zR}) \end{bmatrix}$$

Again, suspending the gimbal from its principal axis, by design, the inertia tensor reduces to:

$$I_R = \begin{bmatrix} I_{xxR} & 0 & 0 \\ 0 & I_{yyR} & 0 \\ 0 & 0 & I_{zzR} \end{bmatrix}$$

As such, the roll axis torque matrices above reduce to:

$$M_R = \begin{bmatrix} I_{xxR}\dot{\omega}_{x_R} \\ I_{yyR}\dot{\omega}_{y_R} \\ I_{zzR}\dot{\omega}_{zR} \end{bmatrix} + \begin{bmatrix} \omega_{y_R}(I_{zzR}\omega_{zR}) - \omega_{zR}(I_{yyR}\omega_{y_R}) \\ \omega_{zR}(I_{xxR}\omega_{x_R}) - \omega_{x_R}(+I_{zzR}\omega_{zR}) \\ \omega_{x_R}(I_{yyR}\omega_{y_R}) - \omega_{y_R}(I_{zzR}\omega_{zR}) \end{bmatrix}$$

$$M_R = \begin{bmatrix} I_{xxR}\dot{\omega}_{x_R} + (I_{zzR} - I_{yyR})\omega_{y_R}\omega_{zR} \\ I_{yyR}\dot{\omega}_{y_R} + (I_{xxR} - I_{zzR})\omega_{zR}\omega_{x_R} \\ I_{zzR}\dot{\omega}_{zR} + (I_{yyR} - I_{zzR})\omega_{x_R}\omega_{y_R} \end{bmatrix}$$

2.9.6 ISP Inverse Kinematics

In the scenario specific to the ISP being developed, the desired attitude of the platform is known. Through the addition of an IMU sensor, mounted on the payload platform, the platform angular position will be measured in real time. These values are measured in three dimensions relative to the inertial frame. Hence, inverse kinematic modelling is required as the desired platform angle relative to the inertial frame is known (0°) for both the roll and the pitch axes. The use of inverse kinematic modelling, therefore, allows the final desired orientation of the platform to be the main control input, which will produce the most robust, accurate controller reference signals for the gimbal control architecture. The following variable designations are therefore made:

- α_P is the pitching angle of the platform measured by the IMU.
- α_R is the roll angle of the platform measured by the IMU.
- $\alpha_{P,D}$ is the desired pitching angle of the platform.
- $\alpha_{R,D}$ is the desired roll angle of the platform.

Now, the pitch axis attitude control error, e_P, can be defined as follows in *Equation 2-11*.

$$e_P = \alpha_{P,D} - \alpha_P \tag{2-9}$$

And vice versa for the roll axis attitude control error. Using *Equation 2-2* above, the total rotation matrix of the system is modified to include the attitude control errors as follows:

$$R_e^R = \begin{bmatrix} cose_R & 0 & -sine_R \\ sine_P sine_R & cose_P & sine_P cose_R \\ cose_P sine_R & -sine_P & cose_P cose_R \end{bmatrix}$$

The input to the ISP in the context of this research project is the desired angular position of the payload platform relative to the ground. The attitude of the payload platform is read by an IMU and is recorded in terms of roll and pitch angles. Thereafter, the attitude control error is computed, and signals are sent to actuators to minimise the error based on the computed attitude control errors, via the control system architecture of the ISP. Hence, the ultimate goal of the control system is to minimise the attitude control error such that the attitude control error rotation matrix above where reduces to the matrix below, where $e_{P,R} = 0$.

$$R_e^R = \begin{bmatrix} 1 & 0 & 0 \\ 0 & 1 & 0 \\ 0 & 0 & 1 \end{bmatrix}$$

2.10 Chapter Summary

Chapter 2 contains the literature review of the research project dissertation. The chapter explored the factors of significance surrounding the research project. The chapter first provided a UAV overview before reviewing the DM300, which was the UAV being utilised by the project. The DM300 was deemed suitable as transportation device in disaster management and humanitarian aid scenario. Therefore, the potential integration of UAVs into the public health sector as was analysed. Existing UAV humanitarian aid delivery methods were identified, which complimented the intended use of the DM3300. Legislature governing the use of UAVs for the intended purpose ensued to identify any prohibiting regulations. Next, an overview of Inertial Stabilisation Platforms (ISPs) was given, consisting of ISP composition theory, commercially available units, and control system theory. The chapter then explored Advanced Manufacturing (AM) technologies and identified Fused Deposition Modelling (FDM) as a suitable manufacturing method for the ISP prototype. Finally, the mathematical modelling of the ISP system was presented.

3 DESIGN SPECIFICATIONS

3.1 Introduction

The following chapter presents the system specifications which were drawn upon for the development of the ISP. The insight gained from the conclusion of the literature review in Chapter 2 aided in developing the numerical specifications to constrain the design and development process. These numerical specifications provided quantifiable metrics which, if achieved, would ensure that the project aims were being met. The chapter first presents specifications derived from literature pertaining to the DM300 UAV, followed by the ISP target specifications. Thereafter, the operational specifications are detailed before the chapter is concluded.

3.2 UAV Specifications

The information portrayed below in Table 3-1 details the operational capabilities of the DJI Matrice 300 RTK UAV, which formed the basis upon which the research project was built. With reference to the discussion in chapter 2.3 above, the effectiveness of the UAV within the disaster management and humanitarian aid scenarios was dependent on the UAVs capabilities, functions, and characteristics. Whilst the various functions and characteristics of the UAV were discussed in chapter 2.3 above, this chapter evaluates the operational capabilities of the UAV by means of numerical specifications.

Table 3-1: UAV Specifications

Specification	Value	Reference/Reason
Weight	6.3kg (incl. Batteries)	[17]
Max Height	5000m	[17]
Max Transmission Range	15km	[17]
Max Payload	2.7kg	[17]
Max Flight Time (Unloaded)	55 minutes	[17]
Max Speed	23m/s (in S Mode)	[17]
Max Wind Resistance	15m/s	[17]
Operating Temperature	-20°C to 40°C	[17]

3.3 ISP Specifications

The purpose of the system was to achieve autonomous stabilisation of payload contents, thus mitigating dynamic disturbance forces on the UAV during use, through the development of an optimised mechatronic ISP system. Drawing on literature presented in Chapters 2.3-2.6 above, the ISP target specifications shown in Table 3-2 below were derived.

Table 3-2: ISP Target Specifications

Specification	Value	Reference/Reason
Mechanical Range: Roll/Pitch Axis	57.5° to 122.5°	Design Constraint
Controllable Range: Roll/Pitch Axis	60° to +120°	Design Constraint
Max Angular Velocity: Roll/Pitch Axis	300°/s	Design Constraint
Max Rotation Angle	30°	Design Constraint
Electronic System Voltage Range	5v<V<12v	Hardware Constraint
Power Source Voltage	2-4 x 3.7V Li-ion Cells	Hardware Constraint
Total Mass	<1kg	Design Constraint
Minimum Platform Dimensions [1]	200mm x 130mm	Design Constraint
Battery Run Time	>1 hr	Design Constraint
Gyro Detectable Rate	>300°/s	Hardware Constraint
Gyro Sample Rate	≥100 Hz	Hardware Constraint
Minimum Detectable Rotation	1°	Hardware Constraint
Stabilisation Error	1°	Hardware Constraint

[1] Required for the transportation of blood transfusion supplies. ISO 3826-1 specified size for a 500ml blood transfusion bag is 190mmx125mm [72]. This specification made provisions for the transportation of essential medical supplies. Approximate mass of full 500ml blood transfusion bag is 530g.

3.4 Operational Specifications

The specifications presented in Table 3-3 below provide insight into the constraints imposed on the design when in operation. These specifications apply strictly only when the UAV is being used in conjunction with the ISP. As per the discussion of Chapter 2.5 above, the addition of the ISP to the UAV imposes additional legislation on the operation and alters the UAV classification category.

Table 3-3: Operational Specifications

Specification	Value	Reference/Reason
Max Effective Velocity [2]	38m/s	Calculated Value
Max Flight Time (Loaded)	31 minutes	[17] [8]
Max Service Radius [3]	19251m	Calculated Value
Total Operational Weight [4]	<9kg	Calculated Value
Energy At Impact	>34kJ	SACAA Regulation, [37] [39]
Max Height	121.92m (400ft)	SACAA Regulation, [37] [39]
Max Take-Off Weight (MTOW)	<150kg	SACAA Regulation, [37] [39]
Battery Reserve	10%	SACAA Regulation, [37] [39]

[2] Calculated assuming the UAV is flying at maximum speed, with a headwind equal to the maximum allowable wind resistance. This metric allowed for aerodynamic design at worst-case scenario conditions.

[3] Calculated using half of the maximum loaded flight time after subtracting the 10% battery reserve, and the maximum speed. Halving the flight time ensure that there is enough battery power for the return trip with an additional 10% battery power remaining.
[4] Maximum allowable payload added to the weight of the UAV.

3.5 Chapter Summary

The specifications presented above served as design goals for the duration of the research project. Chapters 4 to 6 present the design procedure which was undertaken to produce a system which targeted these specifications. Thereafter, Chapters 7 and 8 present the results of the testing which was undertaken on the final system. Findings thereof are indicative of whether the ISP met the above target specifications.

4 MECHATRONIC DESIGN AND OPTIMISATION

4.1 Introduction

The following chapter presents the design and optimization of the ISP. The design process of an ISP is a complex endeavour, owing largely to the multidisciplinary nature which is typical of a mechatronic device. Although highly dependent on the specific application and operating environment, ISP design can be somewhat generalised, and some typical guidelines defined. The common function across ISPs of all kinds, is the ability to either hold or control an objects LOS relative to inertial space, or an object therein. The design presented by this research addresses the absence of suitable transportation of resources to disaster regions, by means of a mass stabilised ISP system. Recent developments in UAV technology, such as optimised flightpath planning and flight time, presents an opportunity for UAV technology to be integrated in disaster management. In this regard, a multifunctional ISP is required to attach the payload to the UAV since, according to this research, these devices have not yet been utilised by UAV technology for this purpose.

4.2 Mechatronic Design Approach

The necessity for the inclusion of mechanical, electrical, electronic components, and computer systems in the ISP development, in order to produce a system capable of meeting target specifications, indicates the inherent mechatronic nature of the project. The typical mechatronic system framework, depicted in Figure 4-1 below, outlines the interaction of these engineering technologies with one another, whilst further defining the role of each interaction. The typical mechatronic design of the ISP follows the diagram closely.

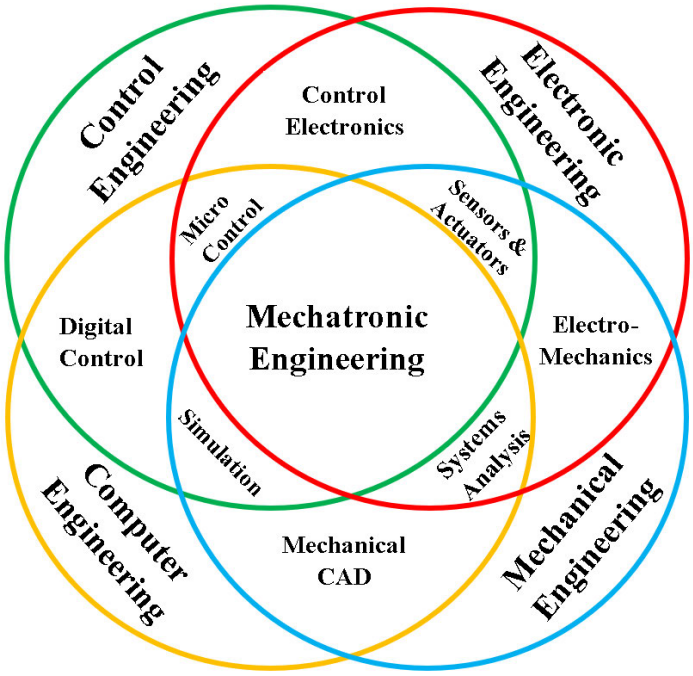

Figure 4-1: Mechatronic Engineering Framework

4.2.1 Mechatronic Framework of the ISP

Figure 4-2 below shows the simplified mechatronic system schematic of the ISP. From the figure, the inherent mechatronic nature of the ISP is portrayed visually. The ISP is comprised of five subsystems; a mechanical framework and cradle, an IMU, a microcontroller, actuators, and two batteries.

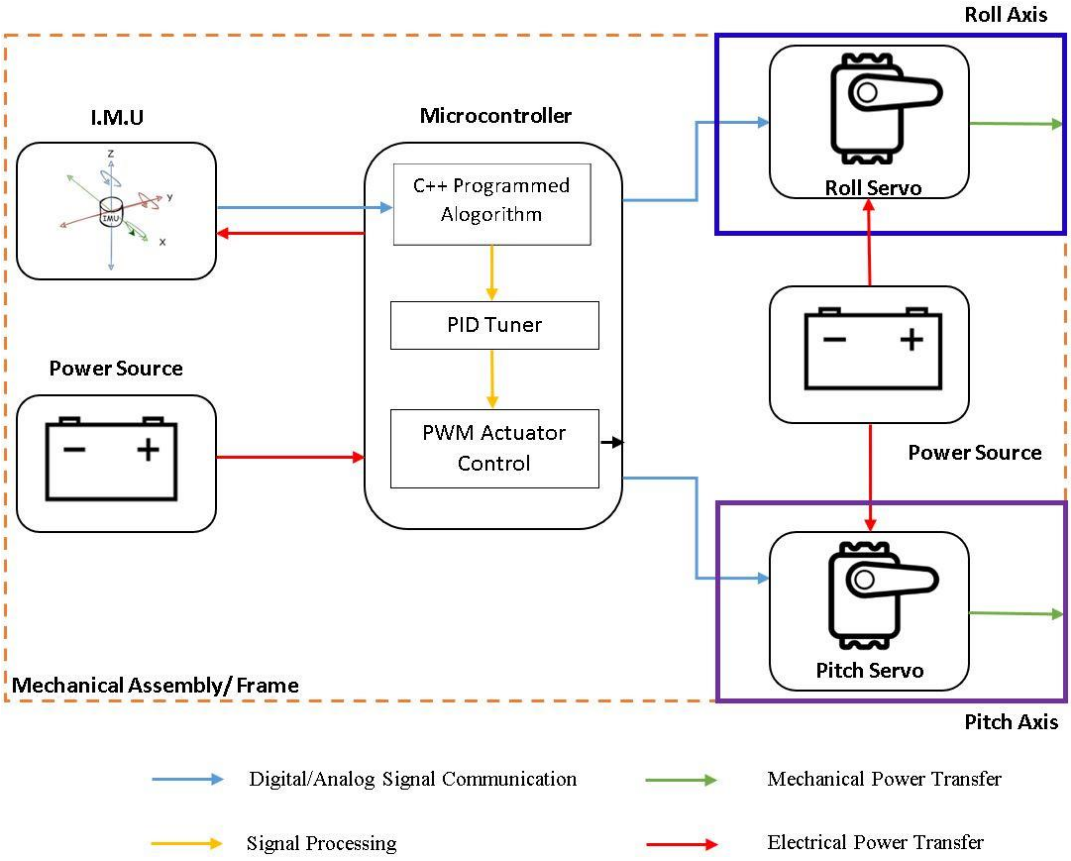

Figure 4-2: Simplified Mechatronic Schematic of the ISP

The schematic portrays the integration of components into the ISP system and describes, modestly, how stabilisation of the cradle is achieved. Electrical power distribution throughout the system is portrayed using red arrows. Signal communication within the system, shown using blue arrows, allows for the transfer of analogue and digital signals to and from the microcontroller to facilitate feedback control of the cradle. In the case of the servo motors, the communication arrows represent the PWM control of the servos. The IMU communication arrows are descriptive of the I^2C communication protocol. Signal processing (yellow) arrows indicate the data processing taking place within the microcontroller to convert the raw IMU sensor data into an error-mitigating PWM signal to the actuators via PID tuning. The geometrical distribution and proximity of subsystems within the ISP is contingent on the mechanical assembly, as illustrated. The mechanical assembly also forms the connection between the ISP and the UAV. However, within the mechanical assembly, both the roll and the pitch axes act as separate entities and can rotate independently to the remainder of the assembly and UAV, to facilitate cradle stabilisation. The successful culmination of these subsystems would enable the ISP to operate as a separate, autonomous, mechatronic system independently of the UAV. Mechanical power transfer between the servo motors and the ISP frame, which induces stability of the platform, is indicated by green arrows.

4.3 Conceptualisation of ISP Components

The identification of potential components, and the final selection of components suitable for the ISP, was a complex endeavour which was highly dependent on the final system requirements. The mechatronic nature of the ISP for disaster management and humanitarian aid scenarios added complexity to the component identification and selection process. This additional complexity hinged on the facts that all of the prospective components needed to be compatible with one another, in terms of communication capabilities, to be eligible for final selection and integration into the system. As is typical of any mechatronic design, this component identification process was also an iterative one, as each component was dependent on the previously selected component. Within this research project, the final ISP assembly mass dictated the final allowable payload mass for transportation, which needed to be maximised. As such, component identification and selection were also highly dependent on part mass. Hence, the accomplishment of an initial conceptual ISP design required the identification of individual components which satisfied system requirements. Table 4-1 presents the decomposition of the ISP into subsystems to aid in component identification.

Table 4-1: ISP Conceptualisation Subsystem Decomposition

Subsystem No.	Description	Function
1	Actuators	Provide mechanical energy to the system to respond to rotations
2	Battery Selection	Provide electrical energy to controller and actuators
3	I.M.U Selection	Measure platform angles and output them to the controller
4	Microcontroller	Receive IMU inputs, process, and output PWM signals to actuators
5	Mechanical Design	House components and provide framework for UAV integration

To aid in the conceptualisation phase of the mechatronic design, the official DJI Matrice 300 RTK 3D model was downloaded from the DJI website. The model is open source and can be downloaded in Standard for the Exchange of Product Data (STEP) format from [73], and is compatible with a plethora of 3D modelling software. The model was opened in the Dassault Systèmes SolidWorks software and was used explicitly for the purpose of deliberating different configurations and mounting concepts for the ISP. Figure 4-3 below shows the complete 3D model of the UAV, as downloaded from DJI, opened in the SolidWorks user interface.

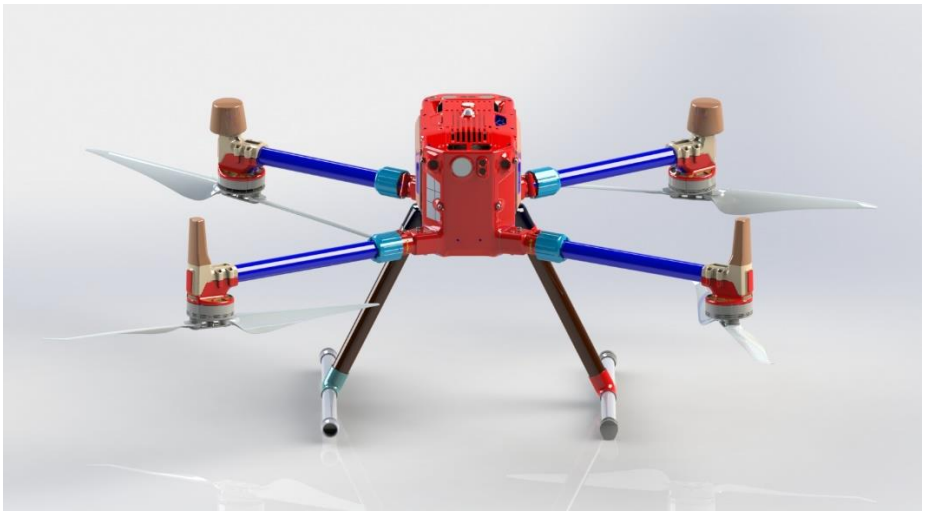

Figure 4-3: DJI Matrice 300 RTK CAD Model, Available at [74]

4.3.1 Actuators

Upon analysis of the research provided in the ISP overview in chapter 2.4 above, it was decided that a DC motor would be the ideal actuator for the project. This decision was made due to these motors being readily available, cost effective, and simple to integrate and control in comparison to the alternative AC motors, hydraulic, piezoelectric, or pneumatic actuation systems – which are less common for this reason.

The actuators of the ISP are critical components which directly affect the performance characteristics of the system. The ISP in this research project required two motors; one to facilitate actuation in the roll axis (gimbal), and one for the pitch axis (gimbal). Subsequently, it was imperative to ensure that prospective actuators were able to provide (in excess) the required torque to overcome disturbances whilst still facilitating stabilisation of the payload, at a rate which equalled that of the UAV, whilst being lightweight and of a small form factor. Where possible, motors should also show miniscule levels of hysteresis, viscous, and coulomb friction for optimal system performance.

The category of DC motors limited the motor selection criteria to Brushless Direct Current (BLDC) motors, simple direct drive DC motors, Geared DC motors, DC stepper motors, and DC servo motors. UAV and aerial robotic technologies readily use BLDC motors for propulsion as they are able to achieve substantial, controlled, rotor angular velocities and torque. These angular velocities, however, far exceeds the maximum rotational velocity of the DJI Matrice. Additionally, these motors require Electronic Speed Controllers (ESCs) to control rotational speeds and directions, which would increase the effective weight of the motor. As such, BLDC motors were, too, ruled out as prospective candidates for the actuator subsystem of the ISP.

In order to further define the requirements of the ISP actuators, such that potential candidates could be identified, it was necessary to determine the maximum allowable torque which the ISP payload would impose on the motor. Through inspection of the DJI Matrice 300 3D model, a set of dimensions for the

payload platform were hypothesized. These dimensions facilitated the most ergonomic fitting of the platform within the model. The specified payload platform dimensions were 300mm in length and 150mm in width. As noted in Chapter 3, these dimensions met the targeted platform dimensions in excess, thus allowing essential humanitarian aid supplies to be transported by the proposed method.

A total mass of 600grams was allocated to the assembly, and a designated payload of $F_{payload,allowed}$=2.1kg implemented during calculations. Hence, *Equations 4-1 and 4-2* below were used, in conjunction with the above information, to determine the required motor torque, T, for the roll and pitch axes, respectively.

$$T_{roll} = F_{payload,allowed} \times \frac{width\ platform}{2} = (2.1)(\frac{15}{2}) = 15.75\ kg.cm \quad (4\text{-}1)$$

$$T_{pitch} = F_{payload,allowed} \times \frac{Length\ platform}{2} = (2.1)(\frac{30}{2}) = 31.5\ kg.cm \quad (4\text{-}2)$$

The resulting torques identified the DSSERVO 35kg servo motor as a suitable actuator for the design. The DSSERVO 35kg is a coreless DC servo motor, which was found to be easily attainable from a variety of suppliers at a reasonable price. The specifications for the servo motor can be seen below in Table 4-2.

Table 4-2: DSSERVO 35kg Specifications [75]

Specification	Value
Supply Voltage	5 – 8.4V
Ideal Operating Voltage	7.4V
Torque at 7.4V	35.2kg.cm
Speed at 7.4V	0.12sec/60 degree
PWM Voltage[1]	3.3 – 5V
Idle Current	50mA
Stall Current	2.6A
Spline Type	25T
Weight	60g

[1] PWM: Pulse Width Modulation

The motor met the maximum required torque requirements of the ISP payload with a rated torque of 35.2kg.cm at maximum supply voltage (saturation), according to [75], with a reserve factor as calculated in *Equations 4-3 and 4-4* below.

$$RF_{torque,\ roll} = \frac{T_{available}}{T_{roll}} = \frac{35.2}{15.75} = 2.235 \quad (4\text{-}3)$$

$$RF_{torque,\ pitch} = \frac{T_{available}}{T_{pitch}} = \frac{35.2}{31.5} = 1.117 \quad (4\text{-}4)$$

Using the motor specification of $T_{available}$=35.2 kg.cm, the maximum available payload per axis, $F_{available,roll}$ and $F_{available,pitch}$,could be calculated using *Equations 4-5 and 4-6* respectively.

$$T_{available,} = F_{available,roll} \times \frac{width\ platform}{2} \Rightarrow F_{available,roll} = \frac{2\ x\ \text{Tavailable}}{width\ platform} = \frac{2\ (35.2)}{15} = 4.694\text{kg} \quad (4\text{-}5)$$

$$T_{available} = F_{available,pitch} \times \frac{Length\ Platform}{2} \Rightarrow F_{available,pitch} = \frac{2\ x\ \text{Tavailable}}{length\ platform} = \frac{2\ (35.2)}{30} = 2.347\text{kg} \quad (4\text{-}6)$$

As can be seen from the results of *Equations 4-5 and 4-6* above, the available payload in each axis, as supplied by the DSSERVO 35kg servo motor, was greater than the assumed payload mass of 2.1kg. Additionally, the above available payloads were calculated as point loads at the extremities of the payload cradle, to represent the worst-case scenario. Subsequently, the DSSERVO 35kg met the maximum torque requirements of the ISP.

With reference to Table 3-2 above, the UAVs maximum angular velocity is 300°/s. It was necessary for the selected actuator to match this specification for optimal performance of the ISP. The DSSERVO 35kg servo has a rated rotational speed of 0.12sec/60° at 7.4 V (saturation) [75]. Making use of ratios, the rotational speed of the DSSERVO was determined using *Equation 4-7* below.

$$\frac{0.12\ sec}{60\ deg} = \frac{1\ sec}{x\ deg} \quad \Rightarrow \quad x = \frac{60}{0.12} = 500°/\text{sec} \quad (4\text{-}7)$$

Since the available 500°/second exceeded the 300°/second, the criterion for the motor selection had been met by the DSSERVO 35kg. The above calculations showed that the DSSERVO 35kg servo motor comfortably met the performance criteria governing the selection of conceptual ISP components. Therefore, the specifications of the motor were used as variables within the battery pack calculations which follow. A previous project in the Department of Mechanical Engineering at the University of Kwa-Zulu Natal (UKZN) had utilised two of these servos, and completion of the project meant that these servos were made available to future projects. As such, these servos could be obtained from the Mechatronics and Robotics Research Group (MR^2G) in the department. Therefore, these servos were chosen to be used in the research project. In addition to meeting the torque requirements, speed requirements, and operational voltage requirements of the design, these servo motors are also waterproof, which made them ideal for their intended purpose within the design, as the assembly would inevitably be exposed to the elements. While not pertinent to the actuator specifications, the motor operating frequency was determined by *Equation 4-8* below, to be a comparable metric for the final system analysis.

$$f_{servo} = \frac{1}{Tservo} = \frac{1}{(0.12)(6)} = 1.389\ Hz \quad (4\text{-}8)$$

4.3.2 Battery Pack

Drawing on existing research surrounding the favoured power sources utilised in UAVs and commercially available camera stabilising ISPs, it became evident that Lithium-Ion (Li-Ion) batteries and Lithium Polymer (LiPo) batteries were the most prevalent. The DM300 utilises TB60 batteries, which are LiPo batteries, with a capacity of 5935mAh. Conversely, the remote controller for the DM300 houses a Li-Ion battery pack, composed of 18650 Li-Ion cells with a capacity of 5000mAh [8]. The integration of both of these lithium-based batteries into the UAV system is a testament to the versatility of these battery technologies. Comparatively, though, the gravimetric, volumetric, and energy densities of lithium-based batteries exceed those of all other alternative rechargeable batteries, making them the favourable choice for these systems [76]. Additionally, the heightened power efficiencies of these batteries and the ability to endure high current draws for prolonged periods of time makes both technologies optimum solutions to UAV electrical power demands.

Both Li-Ion and LiPo batteries possess the necessary characteristics to adequately power the ISP in this research project. To further discern which battery would be preferred, it was necessary to compare the metrics of charge capabilities, battery mass, and battery form factor. In general, Li-Ion batteries are more commonly available, owing to their higher energy densities and capacities than LiPo batteries. As such, Li-Ion batteries also last longer on average. LiPo batteries, however, are lighter and more flexible than the Li-Ion alternative, which is highly desirable in aerial applications. This is largely due to the soft polymer shell of these batteries. However, the use of these soft polymer shells gives LiPo batteries a rectangular-prism-like shape which is generally quite large in comparison to the battery's capacity. As a result, LiPo batteries are often disregarded due to their inherent hinderance of the design process of compact, aerodynamic components and assemblies. The alternative Li-Ion battery cell (most commonly the 18650 cell) have a set shape and dimensions, being a cylinder with a length of 65mm and a diameter of 18mm.Auspiciously, these batteries can be fabricated using several individual cells with customizable geometric proximities, thus minimizing the volume occupied by the battery if necessary. This versatility of Li-Ion battery packs means that a battery can be optimally developed to meet system power requirements without surplus capacity.

To ascertain the battery requirements of the system, the numerical values of the total loaded flight time, $T_{flight,\ total}$ = 31 minutes and the maximum current drawn by the DSSERVO motor, $I_{motor,stall}$ = 2.6A, were drawn upon from Table 3-3 and Table 4-2 respectively. The required battery capacity of the servo motors, $B_{capacity,\ servo}$, was then determined using *Equation 4-9*.

$$B_{capacity,\ servo} = (T_{flight,\ total})(I_{motor,stall}x2) = (\frac{31}{60})(2.6)(2) = 2.687\ Ah = 2687\ mAh \quad (4\text{-}9)$$

Where $B_{capacity,\ servo}$ is the ideal required battery capacity. However, assuming an electrical efficiency,$\eta_{electrical}$, of 95%, the actual capacity, $B_{capacity,actual}$, was found using *Equation 4-10*.

$$B_{capacity,actual} = \frac{Bcapacity,servo}{\eta\,electrical} = \frac{2687}{0.95} = 2828.42\ mAh \quad (4\text{-}10)$$

This required battery capacity would be due to the platform being loaded with payloads of either $F_{available,roll}$=4.693kg or $F_{available,pitch}$=2.35kg. These payloads would cause the motor to stall, which would cause the stall current, $I_{motor,stall}$, to be drawn. However, the maximum available payload mass in each axis could only be $F_{payload,allowed}$ =2.1kg due to the 600-gram allowance for the assembly mass. Therefore, the capacity requirement, $B_{capacity,required}$, of the servo motors could be scaled down according to *Equation 4-11* below. In this calculation, the available force in the pitch axis was used, as this represented the worst-case scenario battery capacity requirement.

$$B_{capacity,required} = \frac{Fpayload,allowed}{Favailable,pitch} \times B_{capacity,actual} = \frac{2.1}{2.35}(2828.42) = 2527.52\ mAh \quad (4\text{-}11)$$

The final required battery capacity for the servo motors was found to be $B_{capacity,required}$= 2527.52 mAh. Hence, a 7.4V 2600mAh Li-Ion battery pack was selected to power the servo motors. Due to availability, the same battery pack was chosen to power the microcontroller. The specifications of the chosen battery packs can be found below in Table 4-3.

Table 4-3: Battery Pack Specifications [77]

Cell type	Lithium Ion
Cell configuration	2S1P
Total capacity	2600mAh
Total voltage	7.4V
Discharge depth	80%
Cut-Off Voltage	5.44V

4.3.3 Inertial Measurement Unit

The selection of a suitable IMU to be integrated into the ISP was a crucial step in the conceptual design process. In ISP design – most notably in small-scale ISPs – the IMU is known to be the component responsible for restricting the operational performance. More specifically, the gyroscopic sensor portion of the IMU introduces noise into the system, which proves to be a major source of error, causing performance degradation, courtesy of the IMU sensor. Subsequently, it was imperative to identify and select an IMU which possessed a gyro with both minimal noise properties, and a bandwidth large enough to not hinder the performance of the control system.

The aerial nature of the ISP within this research project limited the search for available IMUs to Micro Electro-Mechanical System (MEMS) components due to their small form factors, miniscule weights, and their low power consumptions. These factors would allow for easier integration into the mechanical assembly of the ISP, as well as increasing battery run time, and increasing the final operational payload. All of these factors proved to be advantageous to the project and would aid in achieving the specifications laid out in Table 3-2 above. Moreover, these MEMS sensors readily detect orientation over multiple DOF, eliminating the need for multiple sensors to achieve two-axis stabilisation.

Following an extensive review of existing commercially available MEMS IMUs, an initial group of four IMUs were identified for the integration into the system. These were InvenSense's MPU-6050, MPU-6500, MPU-9250, and Bosch Sensortech's BNO055 IMUs. Table 4-4 below shows the initial search criteria comparison of these four sensors.

Table 4-4: IMU Initial Specifications Comparison [78] [79]

Sensor	MPU-6050	MPU-6500	MPU-9250	BNO055
DOF	6	6	9	9
Manufacturer	Invensense	Invensense	Invensense	Bosch Sensortec
Target Market	General Consumer	General Consumer	Drones, Wearables, IoT	Consumer Electronics
Sensors [1]	Acc + Gyro	Acc + Gyro	Acc + Gyro + Mag	Acc + Gyro + Mag
Sensor Fusion	No	DMP	DMP	FusionLib
Input Voltage	2.4 – 3.6 V	2.4 – 3.6 V	2.4 – 3.6 V	3.3 - 5 V
Size (mm)	4 x 4 x 0.9	3 x 3 x 0.9	3 x 3 x 1	3 x 4.5 x 0.95
Weight (grams)	1	2	5	3
Availability [2]	1	3	4	5

[1] Acc: Accelerometer Sensor, Gyro: Gyroscopic Sensor, Mag: Magnetometer Sensor

[2] A score of 1 means the component is readily available at local suppliers, a score of 5 means the component is not available at local suppliers or will need to be sourced/imported.

Table 4-4 above compares the general specifications of each IMU and gives an indication of how easily each IMU could be sourced, if selected to be integrated into the final design. However, research also indicated that the MPU-9250 IMU was developed based on the preceding MPU-6050 and MPU-6500, according to the schematic in Figure 4-4 below.

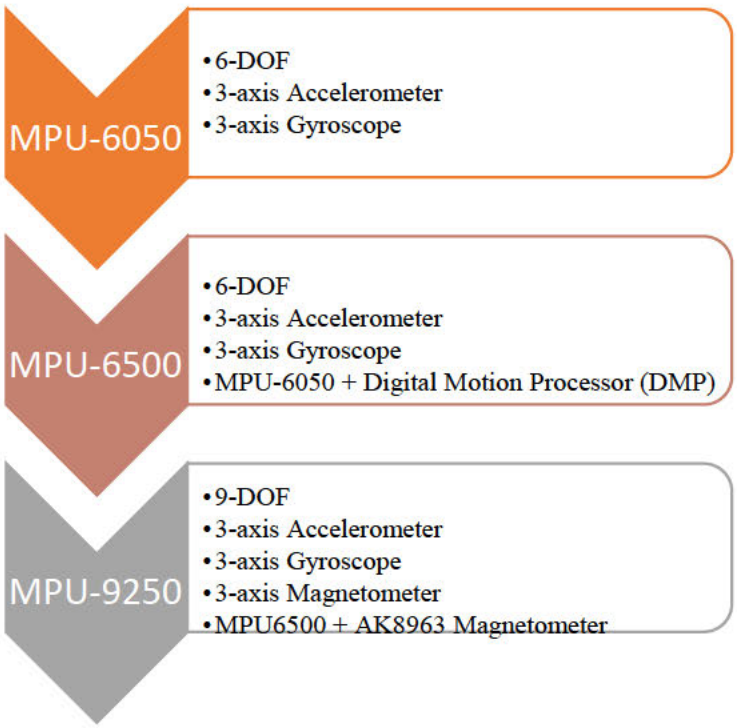

Figure 4-4: MPU-Series IMU Progression

Figure 4-4 above describes the InvenSense MPU-series IMU progression, outlining the constituents of each of the series' IMUs. The most basic of the IMU series, the MPU-6050, is highly prone to accelerometer noise due to gravitational and vibrational effects. Additionally, this sensor is also known to lose accuracy due to the effects of gyroscopic drift, caused by thermal affects, as well as integration of time measurements [80]. In response to this, InvenSense developed the MPU-6500, which consists of an MPU-6050 and a Digital Motion Processor (DMP). This iteration of the IMU uses the DMP to synchronize sensor timing, in an attempt to reduce the settling time and sensor drift by eliminating cross-axis alignment errors between the gyroscopes and the accelerometers [81]. While a notable reduction of sensor drift was realised with the MPU-6500, it was necessary to develop the final iteration, the MPU-9250, to further reduce the effects of sensor drift. This iteration featured an MPU-6500 IMU coupled with a built-in AK8963 Magnetometer to further eliminate the effects of sensor drift.

Considering the above information, the final IMU selection was narrowed down to the MPU-9250 and the BNO055. Table 4-5 below provides the numerical specifications of these two IMUs for comparison purposes.

Table 4-5: Final IMU Specification Comparison [79] [81]

Specification	MPU-9250	BNO055
Output Type	I2C, SPI	I2C, SPI
Full-Scale Range	< ±2000 °/s	125°/s - 2000°/s
Temperature Range	-40°C - 85°C	-40°C - 85°C
Nonlinearity	0.2%	0.2%
Sensitivity Scale Factor	± 0.04	±0.001
Bandwidth	27kHz – 33kHz	1000Hz
Sample Rate	4.4Hz – 9kHz	100Hz
Rate Noise Density	0.005 °/s/√Hz	0.014°/s/√Hz)

It is evident that both IMU choices are capable of measuring angular rates well in excess of the 300°/s required by the specifications of the ISP, depicted in Table 3-2 above. Both IMUs also met the target specifications for sample rate in excess. However, a study performed by [82] which analysed the orientation accuracy of various IMUs, including that of the MPU-9250 and the BNO055, concluded that the BNO055 IMU was able to produce superior orientation accuracy than its counterpart in both static and dynamic environments. The results of the tests carried out by [82] are appended in Table 4-6 below.

Table 4-6: BNO055 vs. MPU-9250 Orientation Accuracy Comparison [82]

IMU Sensor	Measurement	Roll Error (°)	Pitch Error (°)
BNO055	Static Test	0.08	0.03
MPU-9250	Static Test	1.31	1.45
BNO055	Rotating 90°	1.07	0.53
MPU-9250	Rotating 90°	1.51	1.78
BNO055	Rotating 180°	0.74	0.73
MPU-9250	Rotating 180°	0.57	1.73
BNO055	Rotating 270°	1.41	0.66
MPU-9250	Rotating 270°	1.65	1.83
BNO055	Rotating 360°	0.44	0.86
MPU-9250	Rotating 360°	1.12	1.70

From the results in Table 4-6, it is evident that the BNO055 produced the best results in the static test, which was carried out over a period of twenty-four hours - which signifies the repeatability of this sensor. The test showed the BNO055 could produce static orientation accuracies well within the specified 1° of Table 3-2 above. In the dynamic testing phase, the BNO055 produced dynamic orientation accuracy errors with a mean value of 0.92°and 0.7° in roll and pitch respectively. In contrast, the MPU-9250 produced mean error values of 1.2° and 1.76° in roll and pith, respectively.

The discernible difference in error values between the two sensors came as a result of sensor drift in the MPU-9250. Whilst this IMU is equipped with a DMP to mitigate sensor drift, it is still necessary to filter the output data to further alleviate the sensor drift. Kalman filters are commonly used for this purpose, or a complimentary filter on the orientation value using 96% gyro data and 4% accelerometer data. Conversely, it was evident that the BNO055 produced stable results with minimal error. This was due to the built-in sensor fusion algorithms in the IMU which blends the data from all three onboard sensors into a stable, 3-DOF, orientation output.

The BNO055 was eventually chosen as the IMU for the ISP system. The decision was based on the literature laid out in Tables 4-4 to Table 4-6 above. The BNO055 has a full-scale range which meets the requirements for the application (>300°/s), as specified in Table 3-2 above. The IMU has a sampling frequency high enough to not limit the control system operating speed, which satisfied the target specification in Table 3-2. Additionally, the small form factor and miniscule weight of the sensor proved to be lucrative characteristics for the aerial application of the ISP. The specifications of the BNO055 IMU are provided below in Table 4-7.

Table 4-7: BNO055 IMU Specifications [79] [83]

Specification	Value
Degrees of Freedom	9
Input Voltage	3.3-5.0 V
Output Voltage	3.3 V
Output Current	50 mA
Communication	I2C
Weight	3g
Data Output	
Absolute Orientation	Euler Vector, 100Hz (360° Sphere)
Absolute Orientation	Quaternion, 100Hz (4 Point)

4.3.4 Microcontroller

The microcontroller of the ISP formed the backbone of the system. This crucial component was responsible for the analysis of sensor data, storage of the system firmware and control architecture, as well as signal processing. Within the mechatronic framework of the ISP, the microcontroller was required to receive IMU output data (as an input), process the orientation data and determine an error between the required orientation of the platform and the actual platform orientation (as measured by the IMU). Thereafter, the error signal was to be fed into the onboard control system, for the tuning algorithm and gains to be applied to drive the error signal to zero. Finally, the microcontroller was required to determine a signal (based on the control system signal output), which would actuate the servo motors accordingly to obtain the required platform orientation.

The performance of the ISP was ultimately dependent on the selected microcontrollers' processing speed and processing power. Other limiting factors of the microcontroller selection included the weight and the form factor of the microcontroller, as well as – and more importantly- compatibility with external components. The most commonly available and supported microcontrollers for prototyping are Arduino's and Raspberry Pi's. A brief analysis of the key parameters of these devices showed that the Raspberry Pi has significantly greater computing capabilities than Arduino. Where Arduino's generally have a clock speed around 16MHz, the equivalent Raspberry Pi has a clock speed of around 1GHz [84]. In many robotic applications these vast processing speeds are desirable, however, in the ISP application the system operating speed is predetermined by the sample rate of the chosen IMU. Hence, an Arduino microcontroller could provide sufficient processing speeds for the application. Arduino microcontrollers are also better suited to projects requiring motor control and sensor readings and receiving analog inputs. In these scenarios, Raspberry Pi's often require additional components such as Analog-to-Digital Converters (ADCs). Finally, in comparison to the Raspberry Pi range of microcontrollers, Arduino microcontrollers are much more cost-effective.

After due consideration was given to the selection of a suitable microcontroller based on the above reasoning, the research project resorted to the use of an Arduino microcontroller for the ISP application. This decision was made due to the Arduino's greater compatibility with a wider range of ancillary components, as well as their adequate clock speeds for the application. The Arduino model which was most applicable to the application was the Arduino Nano. The Nano is the lightest available Arduino, with the smallest form factor, making it suitable for the aerial application of the ISP. Table 4-8 below provides the relevant specifications of this microcontroller.

Table 4-8: Arduino Nano Specifications [85]

Specification	Value
Microcontroller Chip	ATmega328
Operating voltage	5V
Clock speed	16MHz
Analog input pins	8
Input voltage	7-12V
PWM outputs	6
Communication	UART, I2C, SPI
Power Consumption	19mA
Weight	5g

As can be seen in Table 4-8 above, the Arduino Nano accepts an input voltage of 7V to 12V, which is compatible with the selected battery pack as described in Chapter 4.3.2 above and satisfies the requirements of Table 3-2. Additionally, the microcontroller can support more than the two required PWM outputs to control the actuators and is Inter-Integrated Circuit (I^2C) communication compatible which allows the microcontroller to communicate with the IMU.

4.3.5 ISP Mechanical Design Conceptualisation

The mechanical design of the ISP formed the base onto which the components mount, and through which the electro-mechanical assembly mounted to the UAV. The mechanical design of the ISP was a multi-step, iterative process, which involved synthesizing possible geometric configurations through which the system could be attached to the DM300. This process was undertaken using the CAD model of the DM300. This process was aided by developing a set of design objectives which, when achieved, would ensure that projects aims and objectives were being met. These design objectives are as follows:

I The system must attach to a DJI Matrice 300 UAV, without altering the existing structure.
II The system must comprise of commercially available actuators, a microcontroller, and an IMU which are most suitable for the lightweight, aerial application.
III The design must be lightweight to maximize the operational payload.
IV The aerodynamic profile of the design must be optimised to minimize drag.
V The mechanical design should be suitable for rapid prototyping through FDM.

When synthesizing different layouts of the mechanical design, it became apparent that each component of the mechanical design would need to be designed with at least one flat surface, such that the components were fit for FDM manufacture. Hence, it was decided that the mounting of the ISP onto the UAV would be achieved using a two-part clamping system, which would utilise the legs of the UAV as a mounting point. At this point, it was hypothesized that the cross-sectional profile of the ISP mechanical design could be integrated into the mounting system. This would be a desirable outcome for the design, because this

dual-purpose nature of components would mean that less components would need to be manufactured, thus, reducing the weight of the assembly. In this regard, and in accordance with the objectives above, it became necessary to optimise the cross-sectional profile of the mechanical design to promote efficient aerodynamic interactions between the ISP and the operating environment.

4.3.5.1 Aerodynamic Optimization

In order to meet the design objectives, it was necessary to incorporate aerodynamics into the ISP design to minimize the drag force acting on the UAV. Due to the ISP receiving its lifting force from the UAV, it was not necessary to generate lift with the design. It was, however, necessary for the frame of the ISP to be a symmetrical profile as the UAV could traverse forwards and backwards. To meet these criteria, research was conducted into the aerodynamics of various geometric profiles. It was deduced that an ellipse would be the most aerodynamic, symmetrical, profile [86]. Numerically, an ellipse with an Aspect Ratio (AR) of 2, would produce the lowest drag coefficient in the laminar flow regime [87]. Here, the AR was defined as the ratio of the minor arc radius to the major arc radius of the ellipse. This technique was adopted when designing the ISP, to optimise its aerodynamic abilities. Figure 4-5 below depicts the elliptical profile of the mechanical design.

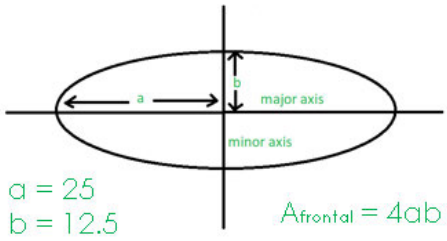

Figure 4-5: Elliptical Cross-Sectional Profile of Mechanical Design

As seen in Figure 4-5 above, the profile has a minor axis arc radius of a=25mm, and a major arc radius of b=12.5mm, thus giving it an AR of 2. These arc radii dimensions were assumed proportionately, using the DM300 CAD model. A Star CCM+ simulation was set up to determine the actual drag coefficient, C_D, of the profile. The simulation was subjected to the maximum effective speed of Table 3-3 above, of V_{eq}=38m/s. To accurately predict the atmospheric properties at this speed, a Reynold's number was required for the flow of fluid over the cross-sectional profile. To determine the prerequisite properties of the Reynold's number at this height, the data shown in Figure 4-6 was utilised.

Properties of the atmosphere at high altitude

Altitude, m	Temperature, °C	Pressure, kPa	Gravity g, m/s^2	Speed of Sound, m/s	Density, kg/m^3	Viscosity μ, kg/m·s	Thermal Conductivity, W/m·K
0	15.00	101.33	9.807	340.3	1.225	1.789×10^{-5}	0.0253
200	13.70	98.95	9.806	339.5	1.202	1.783×10^{-5}	0.0252
400	12.40	96.61	9.805	338.8	1.179	1.777×10^{-5}	0.0252
600	11.10	94.32	9.805	338.0	1.156	1.771×10^{-5}	0.0251
800	9.80	92.08	9.804	337.2	1.134	1.764×10^{-5}	0.0250
1000	8.50	89.88	9.804	336.4	1.112	1.758×10^{-5}	0.0249
1200	7.20	87.72	9.803	335.7	1.090	1.752×10^{-5}	0.0248
1400	5.90	85.60	9.802	334.9	1.069	1.745×10^{-5}	0.0247
1600	4.60	83.53	9.802	334.1	1.048	1.739×10^{-5}	0.0245
1800	3.30	81.49	9.801	333.3	1.027	1.732×10^{-5}	0.0244

Figure 4-6: Atmospheric Properties at High Altitude, Adapted from [88]

Interpolating at a height of 122.92m (400ft), the atmospheric density, ρ, was determined according to *Equation 4-12*.

$$\frac{200-121.92}{200-0} = \frac{1.202-\rho}{1.202-1.225} \Leftrightarrow \rho = 1.202 - \left(\frac{200-121.92}{200}\right)(1.202-1.225) = 1.211\,\frac{\text{kg}}{\text{m}^3} \quad (4\text{-}12)$$

Similarly, the atmospheric kinematic viscosity, μ , was determined as in *Equation 4-13* below.

$$\frac{200-121.92}{200-0} = \frac{1.783-\mu}{1.783-1.789} \Leftrightarrow \mu = 1.783 - \left(\frac{200-121.92}{200}\right)(1.783-1.789) = 1.785 \text{ x } 10^{-5}\ \frac{\text{kg}}{\text{m.s}} \quad (4\text{-}13)$$

The Reynold's number for the flow, Re, could then be calculated by *Equation 4-14* below, which gives the adjusted Reynold's number formula for boundary layer flow with an elliptical leading edge [89]. Here, the variable "b" refers to the major arc radius of the elliptical profile.

$$R_e = \frac{\rho v b}{\mu} = \frac{(1.221)(38)(0.0125)}{1.785\text{x } 10^{-5}} = 32491.60 \approx 3.25 \text{ x } 10^4 \quad (4\text{-}14)$$

It was then deduced, in accordance with [90] [87], that the flow under these conditions remained laminar, due to the laminar-turbulent transition point coinciding with a Reynold's number of Re≈2 x 10^5. Interpolating again using the data in Figure 4-6 above, the speed of sound, **c**, at the operational height was calculated as per *Equation 4-15*.

$$\frac{200-121.92}{200-0} = \frac{339.5-c}{339.5-340.3} \Leftrightarrow c = 339.5 - \left(\frac{200-121.92}{200}\right)(339.5-340.39) = 339.85\ m/s \quad (4\text{-}15)$$

Using the above calculated speed of sound, the Mach Number, M, can be determined to further define the flow characteristics using *Equation 4-16* as follows.

$$M = \frac{\text{Veq}}{c} = \frac{38}{339.85} = 0.112 \quad (4\text{-}16)$$

Since M<0.3, the flow was known to be subsonic. Furthermore, the flow was also classified as incompressible, and inviscid. To further enhance the CFD simulation accuracy, the atmospheric pressure, P, thermal conductivity, K, and temperature, T, were also calculated using Figure 4-6 data. The operational atmospheric pressure was determined by *Equation 4-17* below.

$$\frac{200-121.92}{200-0} = \frac{98.95-P}{98.95-101.33} \Leftrightarrow P = 98.95 - \left(\frac{200-121.92}{200}\right)(98.95 - 101.33) = 99.88\ \text{kPa} \quad (4\text{-}17)$$

Similarly, the atmospheric thermal conductivity was determined by *Equation 4-18* below.

$$\frac{200-121.92}{200-0} = \frac{0.0252-K}{0.0252-0.0253} \Leftrightarrow K = 0.0252 - \left(\frac{200-121.92}{200}\right)(0.0252 - 0.0253) = 0.02524\,\frac{\text{W}}{\text{m.K}} \quad (4\text{-}18)$$

Eventually, the atmospheric temperature could be calculated as per *Equation 4-19*.

$$\frac{200-121.92}{200-0} = \frac{13.70-T}{13.70-15} \Leftrightarrow T = 13.70 - \left(\frac{200-121.92}{200}\right)(13.70 - 15) = 14.21\ ^{\circ}\text{C} \quad (4\text{-}19)$$

The above-calculated physical properties were incorporated into the CFD analysis to produce the most accurate prediction of the C_D value. Figure 4-7 below shows the geometric model which was created and utilised within the CFD analysis. As can be seen in the figure, a 2D analysis was run to determine the ideal C_D value at any given point along the cross-sectional profile of the mechanical design. The geometry was meshed using a polyhedral mesh, with a base size of 15mm throughout the geometry, except for within the volumetric control block (shown in pink). Within the volumetric control block, mesh refinement was undertaken for further refinement of the flow characteristics and interactions within this area of interest. The mesh within the control block was reduced to 10% of the base mesh size, resulting in a 1.5mm mesh size around the boundary surface of the elliptical profile, and the number of prism layers increased to 6.

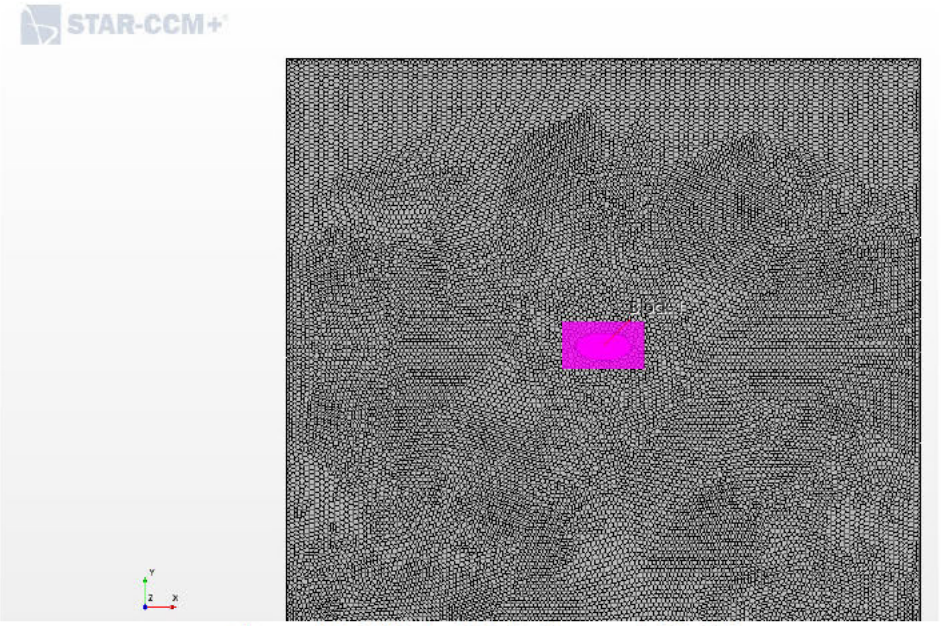

Figure 4-7: Elliptical CFD Geometric Model

The succeeding step in the CFD analysis was to define the physical models which would accurately mimic the elliptical profile in use. The physics models define the fluid state, reference values, initial conditions, boundary conditions, and the solver parameters to be used throughout the simulations. Figure 4-8 below provides the physics models applied to the simulation.

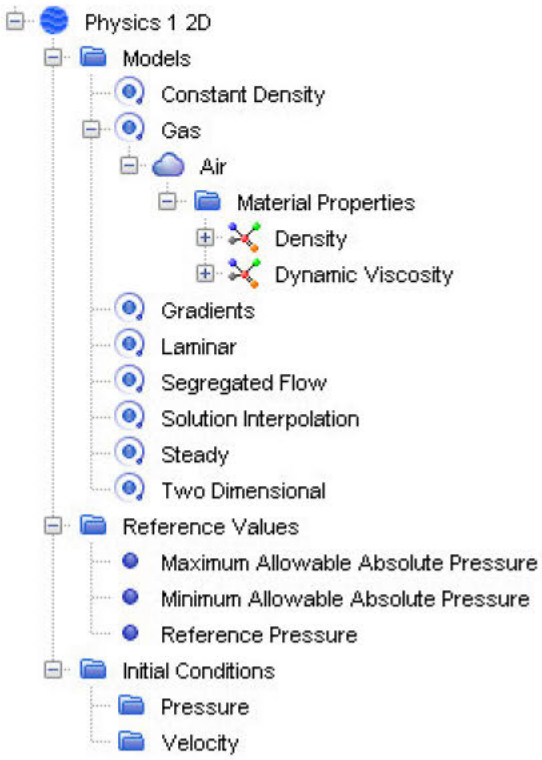

Figure 4-8: CFD Analysis Physics

Numerical values for the above material properties, reference values, and initial conditions are provided in Table 4-9 below.

Table 4-9: Physical Property Numerical Values

	Physical Property	Value
Material Properties		
	Density	1.221 kg/m^3
	Dynamic Viscosity	1.785 x 10^{-5} kg/m·s
Reference Values		
	Reference Pressure	101.325 kPa
Initial Conditions		
	Pressure	99.88 kPa
	Velocity	[38,0,0] m/s
	Static Temperature	14.21 °C

The above continua, geometry, model, and physical property values were used as inputs in the simulation and produced the scalar velocity profile shown in Figure 4-9 below. A resultant drag coefficient of C_D=0.0687 was realised, which agrees closely with the expected value alluded to by research in [86].

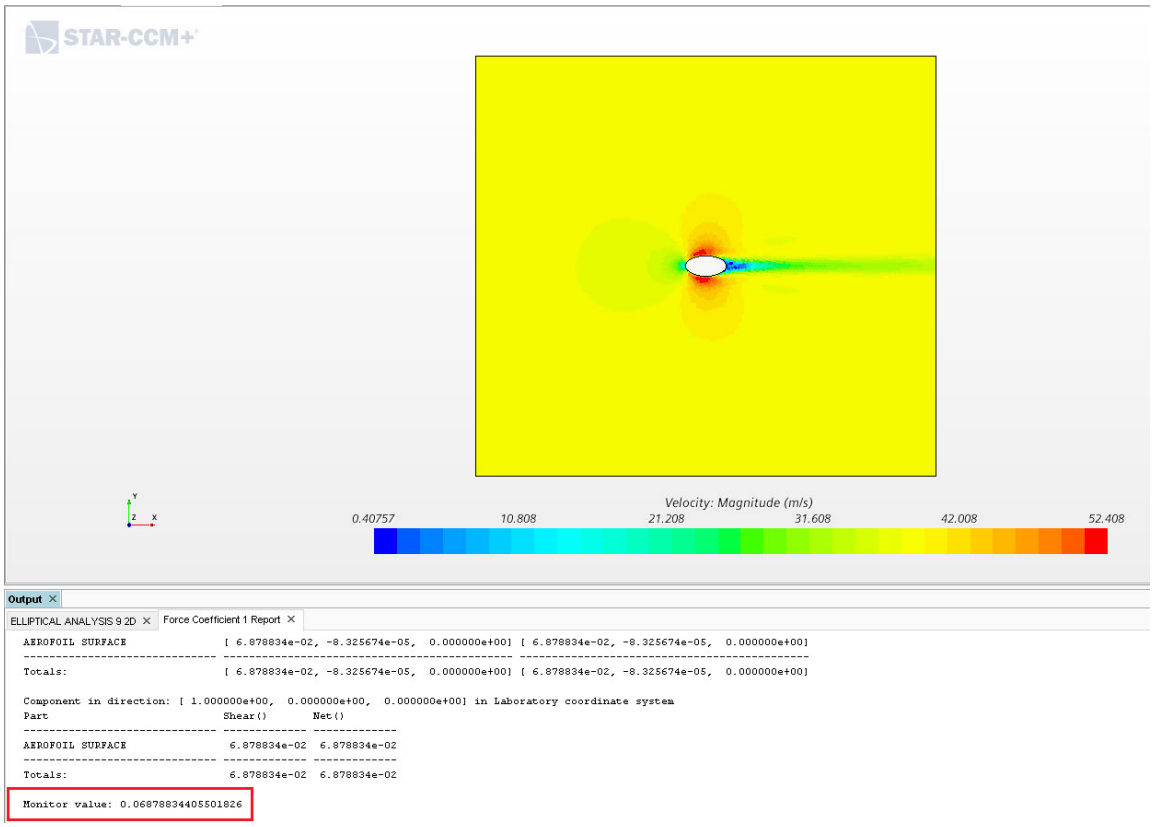

Figure 4-9: StarCCM+ Simulation Velocity Profile

Concluding the CFD analysis with a resulting C_D value closely agreeing with values shown by research meant that, under the calculated operational conditions, the simulation was successful in accurately predicting the fluid interactions with the elliptical profile. As can be seen by the velocity profile in Figure 4-9 above, the fluid interaction with the ellipse is completely symmetrical about the major axis of the profile. A region of reduced-speed fluid is seen to be present at the point of initial contact with the elliptical profile due to the rapid reduction in speed of the preceding fluid causing a backlog. A high-velocity stream of fluid can be seen along the leading edge of the profile. This stream dissipates outward into the freestream region at a point around the minor axis, with minimal bearing on the surrounding freestream and with separation from trailing edge conditions. The trailing edge of the profile shows a region of negative pressure flowing into a stream of reduced-speed fluid leaving the profile with no effect on the profile itself. Despite these flow conditions, as a result of the low C_D value, minimal resistive forces are expected to be transferred from the mechanical design of the ISP to the UAV. Subsequently, the aerodynamic optimization of the mechanical design cross-sectional profile meant that design objective IV was met.

4.4 Detailed Mechatronic Design

The final electro-mechanical design of the ISP was established based on insight and considerations gained from Chapter 2 and 3 above, and incorporated the analyses and components identified in the present chapter. The design can be seen to satisfy objective I as stated in Chapter 4.3.5 above, by successfully integrating the ISP onto the UAV without altering the existing structure of the UAV. Objective II of Chapter 4.3.5 was also met by the design as it integrated suitably sized commercially available components which are lightweight in nature (as identified in Chapter 4.3.1 to 4.3.4 above). The final electro-mechanical design of the ISP, assembled onto the DM300 is shown below in Figure 4-10. The modularity of the design is portrayed using colours to represent individual components.

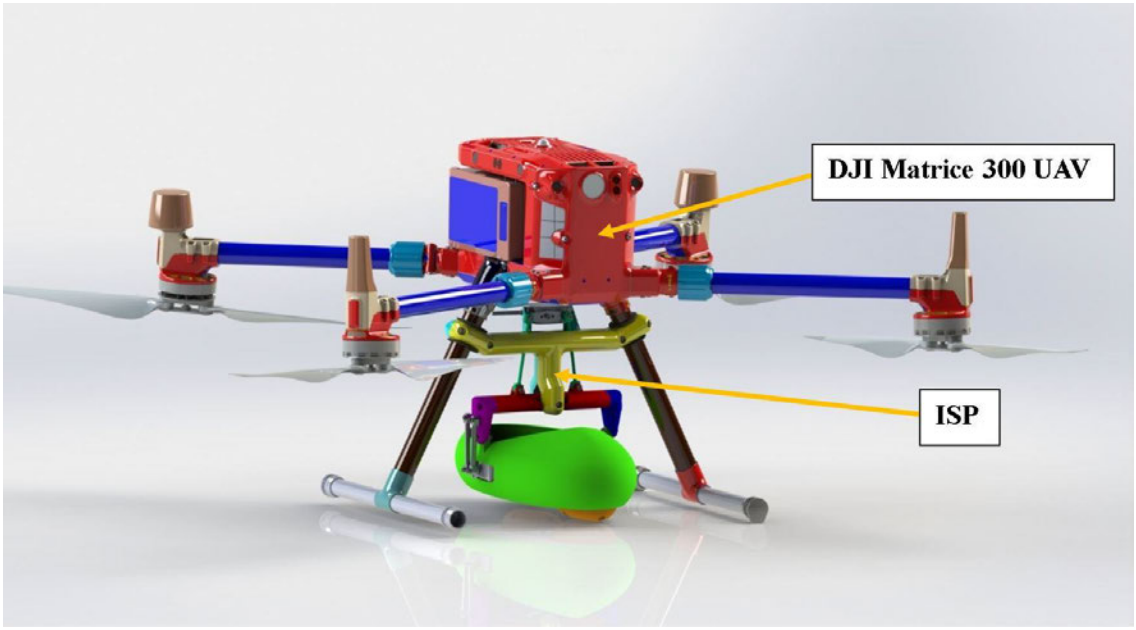

Figure 4-10: Final Electro-Mechanical Design. Adapted from [74]

The ISP was designed using the SolidWorks 3D modelling software package. The modularity of the design was driven by objective V in Chapter 4.3.5 above – which required the design to be fit for FDM manufacturing. In order to meet objective V, the design was segmented to allow DFM provisions to be included in the design of individual components, thus making components fit for FDM manufacture. These DFM provisions came as a result of the FDM manufacturing process requiring each component to be designed with at least on flat surface which could be placed down against the print bed during fabrication. Subsequent segmentation of the design allowed the necessary provisions to be made for FDM manufacture of the ISP mechanical design components. The following headings provide the final electrical design of the ISP, followed by detailed assembly renders of the ISP to further communicate the final design, as well as to preset the geometric proximities of subsystems within the assembly.

4.4.1 Final Electrical Design

The final electrical design formed the connection of the electrical and electronic components in a compatible fashion for the resulting electro-mechanical assembly to operate autonomously. As such, the resulting assembly met the prerequisites of a 4IR "intelligent Device". The final electrical design consisted of the Arduino Nano microcontroller, the BNO055 IMU, two DSSERVO 35kg servo motors, and two Li-ion battery packs. Ancillary components, which complete the charging circuit, include resistors, LEDs, and a charging power jack. Figure 4-11 below shows the detailed schematic of the final electrical system of the ISP.

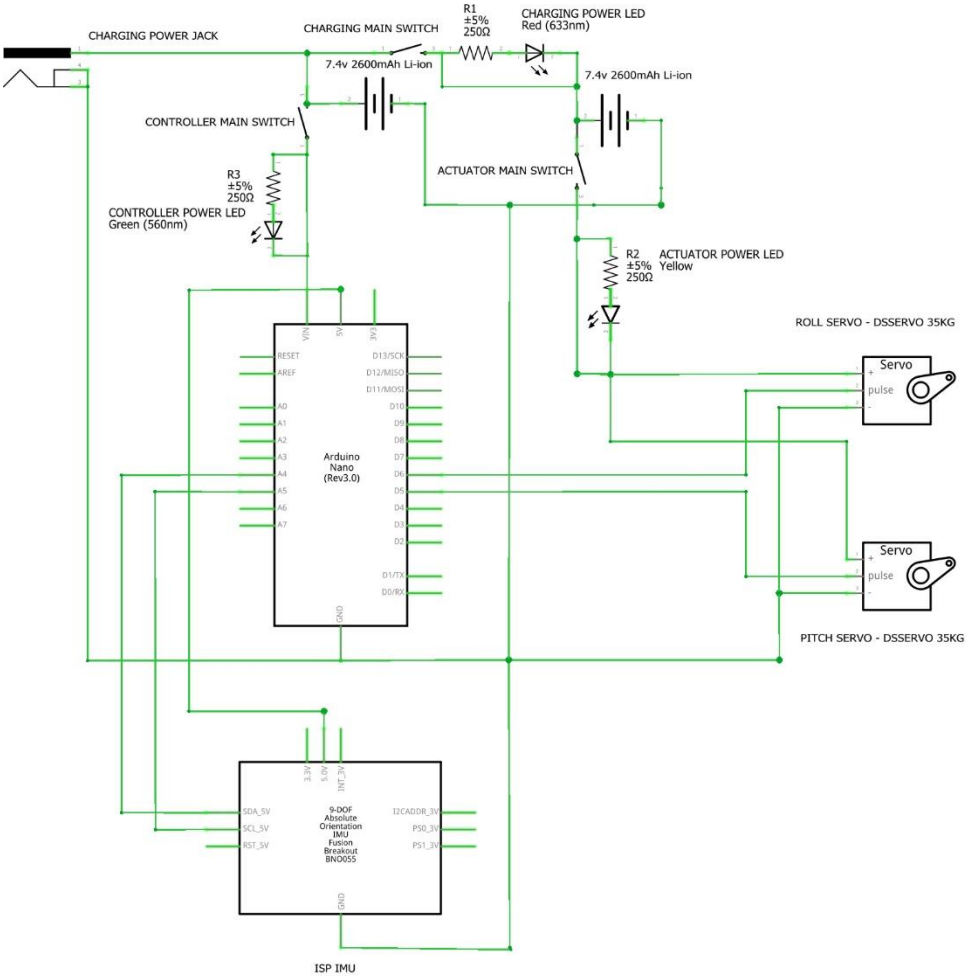

Figure 4-11: Detailed Electrical Design

In the electrical design, three manual switches are present, namely, "Controller Main Switch", "Actuator Main Switch", and "Charging Main Switch". These switches were present for control over the assembly during the parallel charging operation of the ISP. During charging, both the "Controller Main" and the "Battery Main" switches would be opened to isolate the microcontroller and actuators from the charging circuit. Simultaneously, the "Charging Main" switch would be closed (connected) so that both batteries would be connected in parallel for charging to occur. This charging system complimented section 4.4.3 below, for design optimization purposes.

4.4.2 Final Assembly

The following renderings show the final design and assembly of the ISP, including Commercial Off-The-Shelf (C.O.T.S) components. The C.O.T.S components shown in the renders include the various fasteners (listed in Table 4-12 and Table 4-13), bearings, and CAD models of the DSSERVO 35kg servo motor, Arduino Nano microcontroller, and the BNO055 IMU. The CAD models for these components can be found at [91], [92] ,and [93], respectively. Figure 4-12 below provides full assembly renderings of the final ISP design from two isometric views.

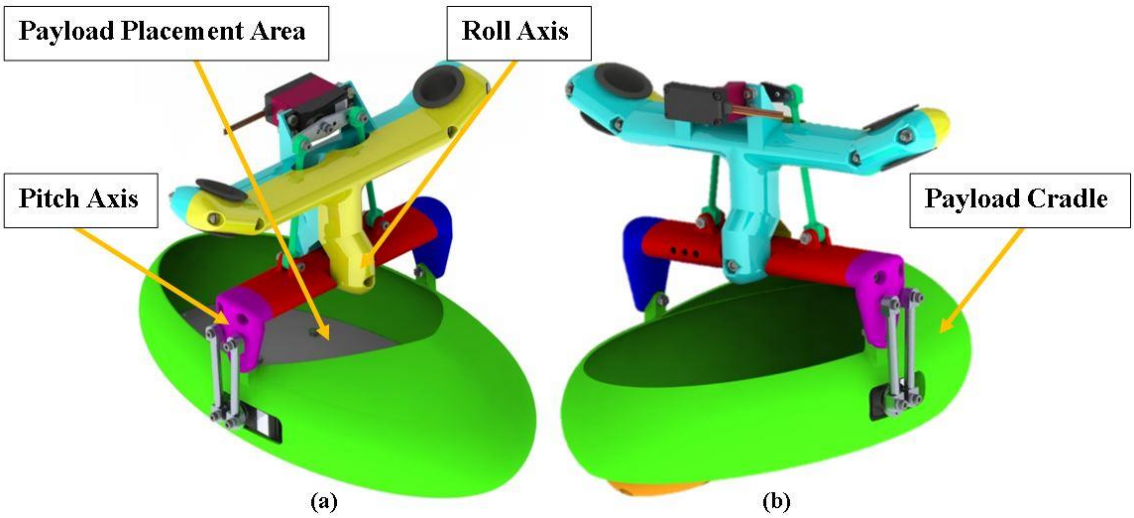

Figure 4-12: Final ISP Assembly Front (a) and Rear (b) Isometric Views

As can be seen in Figure 4-12, the mechanical framework of the ISP served as both the basis onto which the components mount, and through which the electro-mechanical assembly mounted to the UAV. The mounting points of the ISP were on the landing gear legs of the UAV. Thermoplastic Polyurethane (TPU) vibration-dampening bushes were clamped between the UAV landing gear legs and the mechanical design assembly mounting points, forming the attachment points. This is depicted below in Figure 4-13 below.

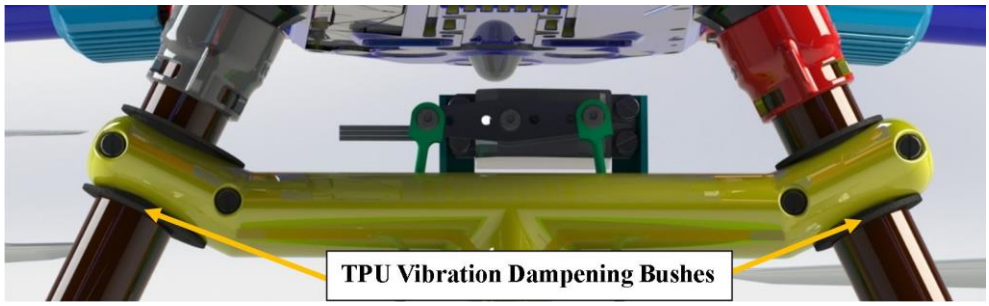

Figure 4-13: Mounting Location of the ISP, Complete with TPU Dampeners

The ISP assembly received electrical power from two Li-ion batteries as per the detailed electrical design schematic in Figure 4-11 above. The specifications of the selected battery packs can be found in subsection 4.3.2 above, and the location of the battery packs seen in Figure 4-14 below. In accordance with best practice, the design utilised two Li-ion batteries; one to power the microcontroller, and a second to power the servos. The individual battery pack isolated the microcontroller from servo noise and shielded it from sudden, high-power spikes in the battery which could damage or reset the microcontroller in use. The servo motors received power from their own battery pack and were controlled using PWM from the microcontroller, receiving signals from pins D6 and D5 on the microcontroller for the roll and pitch servo, respectively.

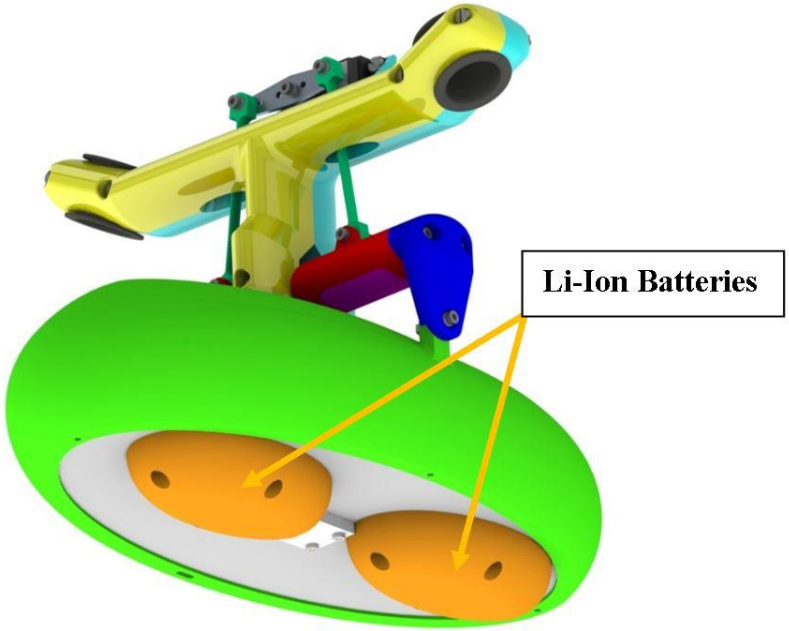

Figure 4-14: Battery Pack Position in Assembly

The selection of two Lithium-Ion batteries for the design also facilitated the permanent fixing of the batteries in the assembly and the use of parallel charging to charge the batteries in position. The batteries can be seen to mount beneath the payload platform. The position of the batteries was governed by mass centre optimization, which is explored in more detail in section 4.4.3 below. The relocation of the batteries to the bottom of the platform allowed the CoG of the assembly to be lowered, whilst also allowing for the batteries to be used as ballast weights to balance the ISP. With reference to Chapter 2.7.2.1 above, an ISP can be balanced by suspending the ISP by its principal axis, or by designing its CoG to coincide with one of the axes of rotation [49] [41]. The design in this research project attempted to coincide the ISP CoG with the pitch axis' axis of rotation. Notwithstanding the battery packs, further lowering of the CoG was required during the design process. This was achieved by the lowering of the pitch axis servo. The location of the servos can be seen in Figure 4-15 below. The necessity to lower the pitch servo to the position shown in the figure, naturally, caused an imbalance in the roll axis. This imbalance was counteracted by offsetting the positions of the battery packs, as can be seen in Figure 4-14 above, perpendicular to the roll axis' axis of rotation.

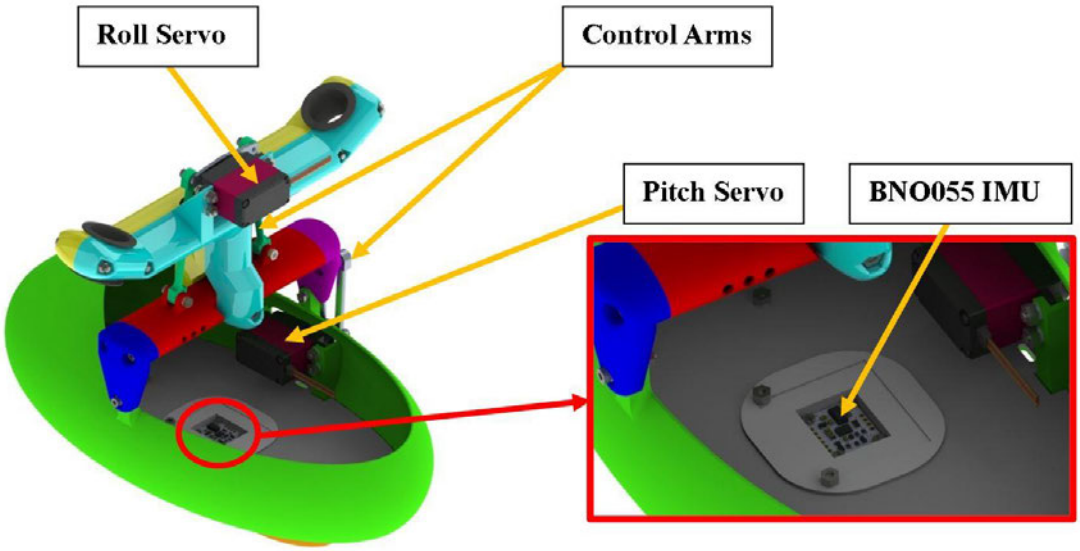

Figure 4-15: Servo Motors and IMU Location in Assembly

As shown by Figure 4-15, the pitch axis servo was located within the payload platform cradle of the assembly, which was notably offset from the pitch axis of rotation. Similarly, the roll axis servo, located at the top of the assembly, also displayed a large offset from its respective axis of rotation. As such, the design included a set of control arms in each axis of rotation which coupled the servo motor with its assigned axis of rotation. The control arms enabled the redistribution of motor torque to the axes, causing rotation and counteracting disturbances to the platform, whilst also being aerodynamic in shape to minimize their drag force on the assembly when in use. These control arms are labelled above in Figure 4-15.

Equivalently to the control arms, the counteraction of platform disturbances was expedited by the BNO055 IMU in the assembly. The final location of the IMU within the assembly is shown in Figure 4-15 above, where it can be seen mounted to the base of the payload platform, at the centre of rotation of the platform. It should be noted that the IMU was to be sealed within its housing, and that the lid has been left off in the renderings for visualisation purposes. The IMU housing and its corresponding lid can be seen in the drawing file, in Appendix D. The BNO055 was connected to the Arduino Nano using the I^2C communication protocol; the Serial Data Line (SDA) pin was connected to pin A4 (SDA) of the microcontroller, the Serial Communication Line (SCL) pin was connected to pin A5(SCL) of the microcontroller. A visual impression of these connections can be found in Figure 4-11 above. Once programmed and calibrated, the IMU, microcontroller, and servo motors operated autonomously, incorporating an element of AI into the ISP system.

The Arduino Nano, being the final assembly component to discuss, was mounted within the confines of the aero frame for protection against ingression of water and other airborne particles during use. Figure 4-16 displays the microcontroller position within the mechatronic design assembly.

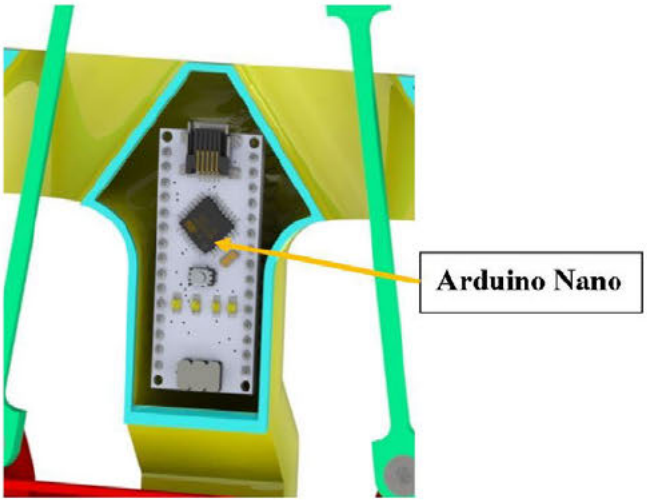

Figure 4-16: Microcontroller Position in Assembly

4.4.3 Mass Centre Optimization

To promote the efficiency of energy draw on the battery system, it was necessary to balance the ISP in the design phase of the project. This entailed manipulating the assembly CoM to correspond with the point of intersection of the axes of rotation. This point, being the designated reference point, was identified as the point of intersection of the planes produced perpendicular to the X, Y, and Z-axes, and passing through each axis of rotation. In doing so, when the platform was in the level position, it would be balanced independent of the motors, thus prolonging the battery life. This process was carried out iteratively in SolidWorks, and by the rearrangement of components within the assembly. The placement of the batteries below the platform, as well as the lowering of the pitch axis actuator allowed the assembly to be balanced to the extent presented below in Table 4-10. It should be noted that the Z-axis offset from the CoM had a negligible effect on the balancing of the ISP, provided that the X-axis and Y-axis were considered balanced.

Table 4-10: CoM Offsets from Reference Point

CoM Component	Offset from Reference Point
X	5.95mm
Y	0.14mm
Z	23.93mm

4.5 Design Analysis

Having completed the ISP mechatronic design, the design post-processing analysis sought to identify maximum tensile and compressive stress regions within the design. The SolidWorks mass approximation of the assembly was seen to be 1041.06 grams, which allowed for a final payload capacity of 1658.94 grams. However, the assembly mass was representative of FDM aero frame components manufactured with 100% infill, which would not be the case at the time of manufacture. This meant that the 1658.94-gram payload would not be an accurate representation of the final operational payload. Therefore, to analyse the strength of the ISP aero frame components, FEA analyses were run on components loaded with the maximum assumed payload mass of 2.2kg to identify worst-case loading stresses and deflections. The analysed components were the landing gear mounting assembly components and the pitch axis drop arm. These components were expected to be subjected to the greatest bending loads due to their geometries and positioning within the assembly. Figure 4-17 and Figure 4-18 below show the FEA simulation results for the landing gear mounting assembly components. The FEAs were conducted using the Ansys software package, with each simulation achieving mesh-independent stress values within 5% of each other across three iterations.

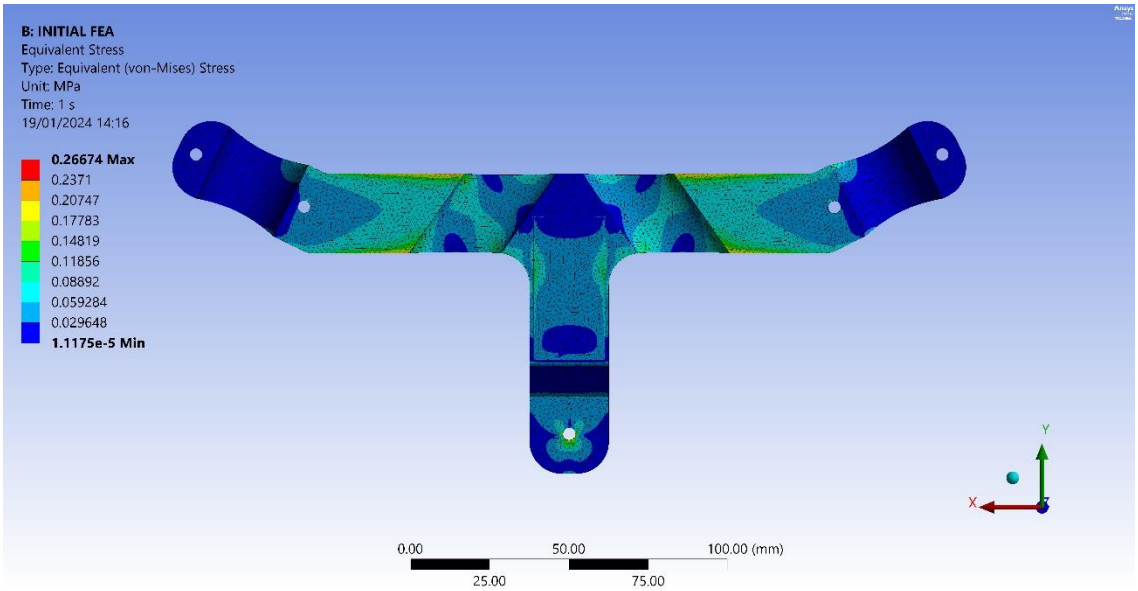

Figure 4-17: Front Landing Gear Mount FEA Analysis Equivalent Stress

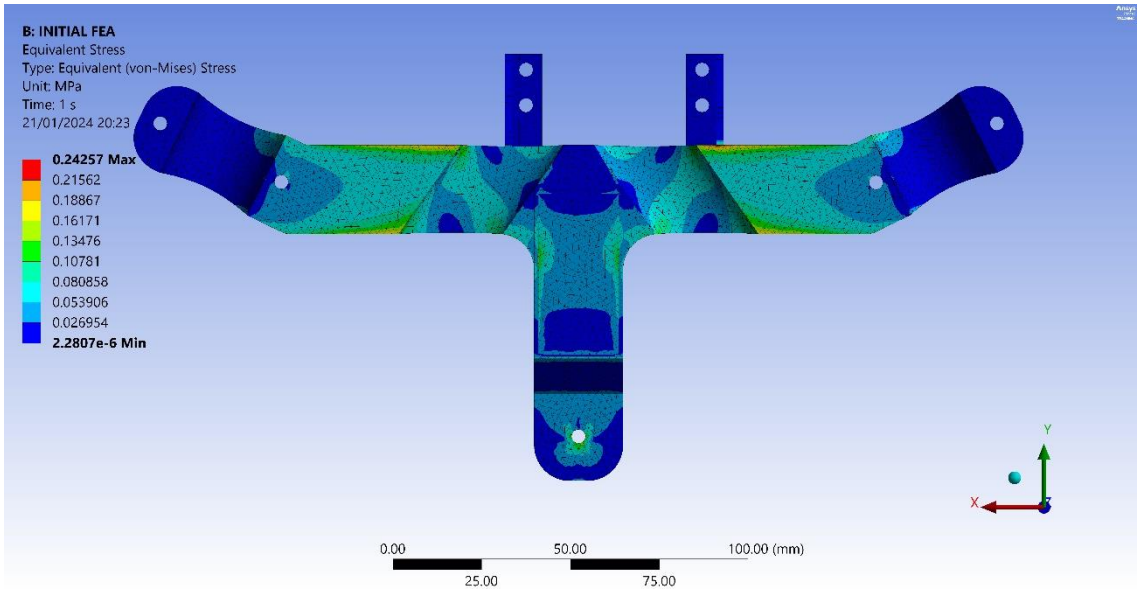

Figure 4-18: Rear Landing Gear Mount FEA Analysis Equivalent Stress

Figure 4-17 and Figure 4-18 are graphical illustrators of the areas of interest of the components. These areas are represented by the high stress regions corresponding to the colours of the simulation keys. As can be seen by the figures, the front and rear landing gear mountings indicated maximum equivalent stresses of 0.267MPa and 0.243MPa respectively. These values were well below the 65MPa Ultimate Tensile Strength (UTS) of the PLA material, indicating sufficient strength of the designed components. Figure 4-19 which follows illustrates the results of the pitch axis drop arm FEA results.

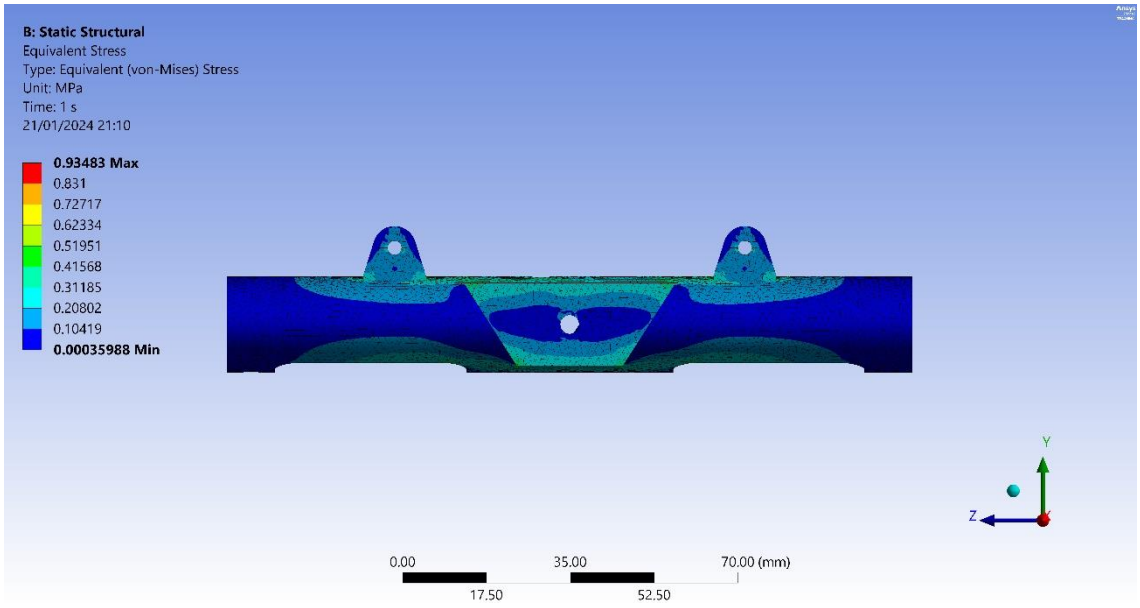

Figure 4-19: Pitch Axis Drop Arm FEA Analysis Equivalent Stress

The pitch axis drop arm FEA results displayed in Figure 4-19 above show the maximum equivalent stress seen by the component to be 0.935MPa, which falls well below the PLA material UTS of 65MPa. Again, this finding was indicative of a component designed with sufficient strength.

Analysis of the FEA results of the components showed that, under maximum loading conditions, the stresses imposed on the components all fell within 1.5% of the PLA material UTS. It should, however, be noted that, for simplicity, the components were analysed using anisotropic PLA material properties. Nevertheless, the findings identified the potential for the aero frame components to be lightened through the alteration of FDM parameters, whilst still maintaining the necessary structural integrity. Achieving this would satisfy the requirements of subsection 2.5.6 as well as those of design objective III. Subsection 2.5.6 called for the experimental determination of optimal FDM printing parameters to produce the most lightweight and durable prototype, with design objective III being satisfied through the lightweight criterion. The proposed method to meet these requirements was to empirically determine optimal process parameters for fabrication of the ISP through the destructive testing of FDM-made samples of varying layer heights, infill percentages, wall thicknesses, and infill patterns.

4.6 Commercial-Off-The-Shelf Components

The final design of the ISP presented above included several Commercial-Off-The-Shelf (C.O.T.S) components which needed to be procured for the final assembly of the prototype. Details of the components required for the final assembly are presented below in Table 4-11 and Table 4-12. These tables further categorise the required items as components and fasteners.

Table 4-11: ISP C.O.T.S Components

Component	Quantity	Specification	Source	Cost
IMU	2	BNO055	Amazon	R3273.41
Microcontroller	1	Arduino Nano	DIY Electronics	R219.95
Servo Motor	2	DSSERVO 35kg.cm	Micro Robotics	R355.35
Battery Pack	2	7.4V 2600mAh Li-Ion	DIY Electronics	R1179.90
Bearings	16	683-RS Ball Bearing	Bearing Man Group	R293.34
Total				**R5321.95**

Table 4-12: ISP C.O.T.S Fasteners

Fastener	Quantity	Specification/Material	Source	Cost
M2.5 Nut	8	Stainless Steel	EIS	R5.76
M2.5 Screw	4	2.5x6 Stainless Steel	EIS	R7.56
M3 Nut	14	Stainless Steel	EIS	R5.46
M3 Washer	31	3x7 Stainless Steel	EIS	R3.72
M3 Cap Screw	10	3x20 Stainless Steel	EIS	R8.20

Table 4-13: ISP C.O.T.S Fasteners Continued

M3 Cap Screw	3	3x10 Stainless Steel	EIS	R1.65
M3 Cap Screw	8	3x15 Stainless Steel	EIS	R5.52
M3 Screw	1	3x55 Stainless Steel	EIS	R2.05
M4 Screw	8	4x12 Galvanised Steel	EIS	R10.24
M4 Screw	4	4x40 Galvanised Steel	EIS	R9.32
M4 Nut	13	Galvanised Steel	EIS	R1.82
M4 Washer	8	Stainless Steel	EIS	R1.12
Total				**R62.42**

4.7 Assembly Precedence Diagram

Figure 4-20 below presents the assembly precedence diagram of the ISP. The components reference by the numbering system of the precedence diagram are elaborated upon in the succeeding Table 4-14. In addition to Figure 4-20, graphical illustrations of the ISP assembly can be found in the exploded subassembly diagrams in Appendix D, with drawing reference numbers SA1 and SA2. It should be noted that the assembly precedence diagram presented below does not include fasteners.

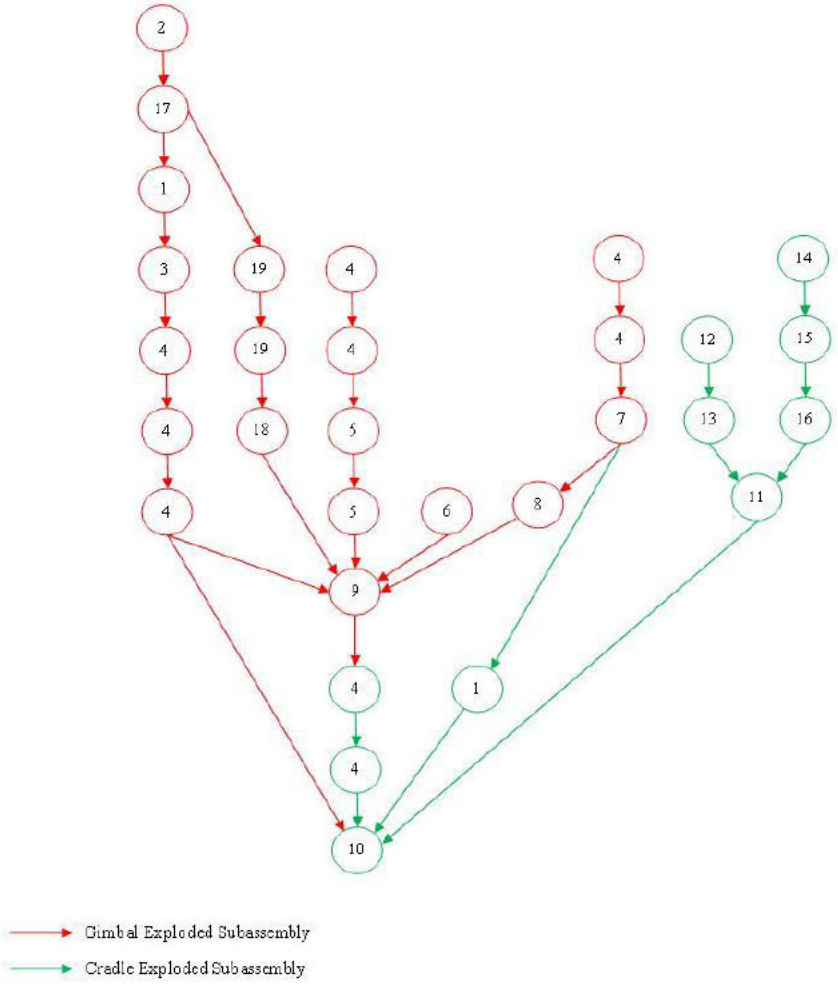

Figure 4-20: ISP Assembly Precedence Diagram

Table 4-14: Assembly Precedence Diagram Bill of Materials

No.	Description	Quantity	Drawing Reference
1	DSSERVO 35kg Servo Motor	1	-
2	Rear Landing Gear Mounting	1	P2
3	Pitch Axis Control Arm	2	P6
4	683-RS Ball Bearing	16	-
5	Drop Arm Lid	2	P7
6	Drop Arm End Cap	1	P3
7	Roll Axis Control Arm	2	P8
8	Drop Arm End Cap – Control Surface	1	P5
9	Drop Arm	1	P4
10	Payload Cradle	1	P9
11	Cradle Base	1	P12
12	7.4V 2600mAh Li-Ion Battery	2	-
13	Battery Housing	2	P13
14	BNO055 Housing Lid	1	P11
15	BNO055 IMU	1	-
16	BNO055 Housing	1	P10
17	Arduino Nano Microcontroller	1	-
18	Front Landing Gear Mounting	1	P1
19	TPU Vibration Dampener	2	P14

4.8 Chapter Summary

Chapter 4 presented the process adhered to when conceptualising, designing, and optimising the ISP prototype. The produced design met initial aims and objectives of the research by being capable of simple integration into the UAV structure, consisting of commercially available components, being aerodynamic, and fit for FDM manufacturing. The ISP electro-mechanical assembly was conceptualised concurrently to allow for electrical component target specifications to be calculated. The final electrical subsystem consisted of two DSSERVO 35kg.cm servo motors, two 7.4V 2600mAh li-ion battery packs, a BNO055 IMU, and an Arduino Nano microcontroller. The mechanical design subsections detailed the cross-sectional aerodynamic optimisation of the aero frame components before presenting the final assembly of the ISP. Renderings of the final ISP assembly were provided to give insight into the geometric locations of components within the assembly, and the method of attachment of the prototype onto the DM300 UAV. The mass centre optimisation of the assembly was presented, detailing the extent to which the final assembly was balanced. A structural analysis of the final, most-loaded ISP components was then undertaken. Findings thereof indicated that further mass reduction of FDM-produced components would be possible without compromising the strength properties of the components. The recommended method

to achieve this would be to alter the FDM process parameters during fabrication. Lastly, the chapter provided details of the components required to produce the ISP prototype, with associated costs and quantities, before concluding with the assembly precedence diagram.

Chapter 5 presents the empirical mass optimisation experimentation carried out to determine optimal FDM process parameters for fabrication of the ISP components. The process was determined to be necessary to fully satisfy subsection 2.5.6 and design objective III, by producing the most lightweight, durable ISP assembly possible.

5 FDM OPTIMISATION

5.1 Introduction

The following chapter presents the experimentation carried out, during the fabrication phase of the research project, to determine the optimal FDM parameters to produce the lightest possible parts whilst maintaining the necessary structural integrity for the application. The necessity to optimise the FDM parameters was in accordance with Chapter 2 above, where the literature suggested that varying FDM printing parameters could greatly alter part strength, mass, and overall resistance to deformation [94]. The parameters which have the most influence on the above part characteristics are the layer height, infill density, infill pattern, wall thickness, and print speed [66] [64] . These parameters were identified as areas of interest within the research project which required further investigation into their impact in the FDM process.

The FDM industry has been subjected to rapid advancements, such as new parameters, materials, complex geometry printing methods, and infills [95]. However, currently, there exists no FDM-specific Finite Element Analysis (FEA) software package to carry out FEA analyses on FDM-produced parts. Therefore, at present, the only way to predict the resilience of an FDM part against loading is through experimentation. The American Society for Testing and Materials (ASTM) International committee produce various documents annually, which present testing standards for a variety of materials. By adhering to these standards during testing, results are declared valid under the jurisdiction of the ASTM committee [96].

5.2 Methodology

The two main attributes of the FDM-fabricated part which were of interest to the research project were part mass and part strength. It is well document that these attributes are directly proportional in nature: as part mass increases, so too does part strength, and vice versa. This relationship emphasised the need for parameter optimisation for FDM to be a viable fabrication method for the ISP. Figure 5-1 below outlines the experimental methodology followed to optimise the FDM parameters specific to the research project. The figure describes the four-pronged approach to parameter optimisation experimentation before statistical analysis could be carried out.

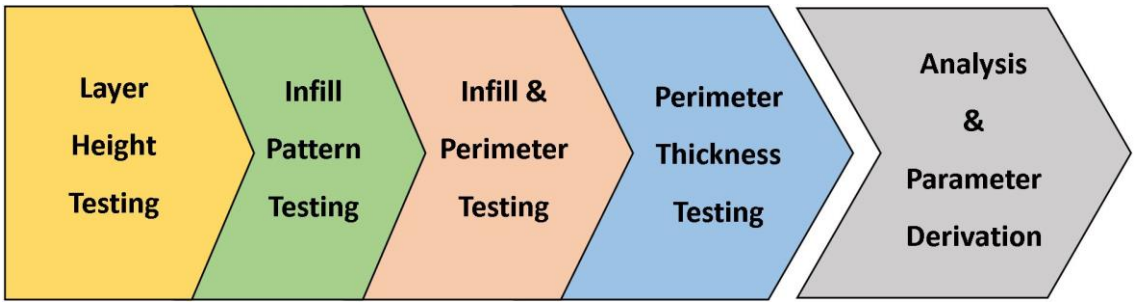

Figure 5-1: Parameter Optimisation Experimental Methodology

5.3 Material Properties

With reference to Chapter 2.8.4, it was ascertained that both the ABS and the PLA FDM materials are produced using the renewable substituents of sugarcane and maize [57]. As such, these materials are considered to be sustainable, whilst being both abundant and cost-effective to use [59]. PLA does, however, boast a higher strength threshold and lower ductility than ABS, which is of great significance to this research project [97]. Therefore, the accompanying material strength testing was carried out using the PLA FDM material rather than the ABS alternative. Table 5-1 below presents the mechanical properties of the PLA material used for testing.

Table 5-1: PLA Material Properties [95]

Property	Value	Unit
Elongation at Break	8	%
Melting Temperature	130-230	°C
Shear Modulus	1287	MPa
Elastic Modulus	3500	MPa
Rockwell Hardness	88	Hr
Yield Strength	70	MPa
Poisson's Ratio	0.360	-
Ultimate Tensile Strength	65	MPa
Tensile Modulus	2.7-16	GPA
Flexural Strength	97	MPa
Flexural Modulus	3600	MPa
Density	1.24	g/cm^3
Heat Distortion Temperature	56	°C
Melt Flow Index	5	g/10min
Izod Impact Strength	4	MPa
Print Temperature	190-210	°C
Print Bed Temperature	0-50	°C
Filament Diameter	1.75	mm
Dimensional Accuracy	$\pm$0.03	mm

5.4 Experimental Standardization

In order to ensure consistent results across all FDM parameter optimization experiments, ASTM standards were utilised. The standards relevant to the testing being conducted were standards *D638-14: Standard Test Method for Tensile Properties of Plastics*, and standard *D790-17: Standard Test Methods for Flexural Properties of Unreinforced and Reinforced Plastics and Electrical Insulating Materials*. These standards are available in [98] and [99], respectively. By ensuring that experimentation was carried out in accordance with these international standards, the results produced were declared valid under ASTM jurisdiction. Whilst these standards called for a minimum of five samples to be tested to account for anisotropy, only three samples were tested. Instead, anisotropy was accounted for through manufacturing the test samples at a variety of raster angles, as seen in Figure 5-2 below. Raster angles define the angle of the layer deposition path relative to the x-y print bed coordinates.

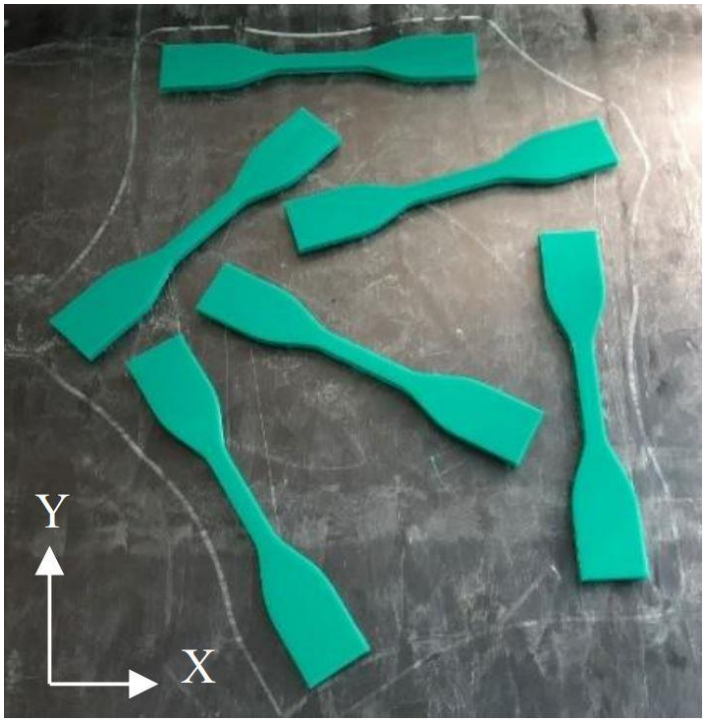

Figure 5-2: Test Sample Build Orientations

5.4.1 Test Specimen

ASTM D638-14 and ASTM D790-17 call for a common test specimen to be used during testing. While there are several variations of the specimen under the guidelines, they change only in scale, and dimensions are prescribed. Therefore, all specimens will produce repeatable results regardless of the specimen type used. Figure 5-3. below presents the geometry of the ASTM test specimen utilised during testing. The accompanying Table 5-2 provides the specimen dimensions.

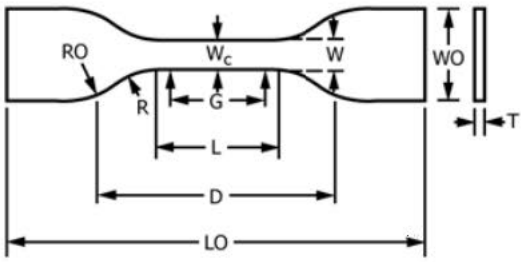

Figure 5-3: ASTM Test Sample Geometry, Adapted from [96]

Table 5-2: ASTM Test Sample Dimensions [98]

Dimension	Numerical Value (mm)	Tolerances
W – Width of narrow section	6	±0.5
L – Length of narrow section	33	±0.5
WO – Overall width (min)	19	+6.4
LO – Overall length (min)	115	No max
G - Gage length	25	±0.13
D – Distance between grips	65	±5
R – Radius of fillet	14	±1
RO – Outer radius	25	±1
T – Specimen thickness	3.2	+0.8

Using the data provided by Figure 5-3 and Table 5-2 above, a SolidWorks 3D CAD model was generated for the test specimen. The model was then exported as a Standard Tessellation Language (STL) file, and saved in .stl format, after which the specimen model was imported into the FDM software for fabrication preparation. Samples were prepared using a Creality CR10-S5 FDM printer using the print settings provided in Table 5-3. A 0,4mm nozzle was attached to the CR10-S5 with a feed of 1,75mm diameter CCTREE brand PLA filament.

Table 5-3: Sample Preparation Settings

Property	Value	Unit
Extruder temperature	200	°C
Build plate temperature	55	°C
Flow/ Extrusion multiplier	100	%
Print speed	50	mm/s
Outer wall speed	25	mm/s
Travel speed	120	mm/s
Perimeter layers (unless specified otherwise)	1	-
Top layers	2	-
Bottom layers	2	-

5.4.2 Testing Theory

The testing theory provided by this sub-heading was applicable to all tests carried out on the FDM specimens. ASTM standard D790-17 provide a basis for which the flexural properties of unreinforced and reinforced plastic specimens may be determined. The standards provide methods for the determination of the flexural modulus, flexural strength, flexural stress, and flexural strain at the samples breaking point. Of interest to the research project, was the flexural stress experienced by the sample as this data could be directly compared to FEA results for the sample. The flexural stress of the test specimen at failure was determined by *Equation 5-1* as follows:

$$\sigma_F = \frac{3Fl}{2TW^2} \tag{5-1}$$

where:

σ_F = Flexural stress at failure (MPa)

F = Flexural failure load (N)

l = Support span (mm)

T = Width of beam tested (mm), which corresponds to the specimen thickness given in Table 5-2 Above

W = Depth of beam tested (mm), which corresponds to the width of the narrow section of the sample, given in Table 5-2 Above

ASTM standard D638-14 describes the acceptable testing methods for FDM samples in tension. The tensile measurements of the samples are used to determine the Young's modulus, Poisson's ratio, Yield stress, Tensile Strength, and elongation of the sample at fracture. For the purpose of this research project, however, the tensile stress was the required outcome of the testing. The tensile stress of the specimen at failure was calculated according to *Equation 5-2.*

$$\sigma_T = \frac{P}{A_{cs}} \tag{5-2}$$

where:

σ_T = Tensile stress at failure (MPa)

P = Tensile Failure load (N)

A_{cs} = Cross- sectional area in gage length of specimen (mm^2), approximated using *Equation 5-3 below*:

$$A_{cs} = (T\ x\ W) - \big((T - 2nN)\ (W - 2nN)\big)(1 - \%_i) \tag{5-3}$$

Where:

T = Specimen thickness (mm)

W = Width of the narrow section of the sample (mm)

n = Number of Perimeter Layers

N = Nozzle diameter (mm)

$\%_i$ = Infill percentage, expressed as a decimal number

5.5 Apparatus

- Creality CR10-S5 FDM printer
- ASTM testing samples (3 per testing condition, per parameter increment)
- Instron 5500R load testing machine
- Digital scale

5.6 Procedure

The following procedure was common to all the testing which was carried out. Testing of the specimens was carried out using an Instron 5500R load testing machine at a ramp rate of 0.7mm/min.

- Prepare testing samples as per ASTM requirements, via FDM
- Weigh each sample and calculate the average mass of a sample for each test parameter increment.
- Place a sample in the testing apparatus and attach the sample to the universal connections using the screw connections, on both the crosshead and the load transducer.
- Zero the gauge length of the machine and the load transducer reading of the machine.
- Run the test.
- Once failure of the sample has occurred, record the failure load.
- Repeat the process for the remaining samples, in both tension and flexure.
- Determine the average failure loads for the flexure and tension conditions and record the values.
- Determine the average flexure and tensile stress for the samples at failure.
- Derive relationships as specified by the objectives of each test.

5.7 FDM Parameter Testing

5.7.1 Layer Height Testing

5.7.1.1 Aim

To determine the layer height which provides the best resistance to plastic deformation and delamination in both tension and flexure.

5.7.1.2 Objective

To determine the relationships between the layer height, part mass, print time, and failure load of FDM samples.

5.7.1.3 Variables

- Layer height (Independent variable)
- Print time (Dependent variable)
- Failure load (Dependent variable)
- Part mass (Dependent variable)

5.7.1.4 Theory

The purpose of the test was to derive quantifiable data regarding the part strength associated with layer heights. It is well documented that the layer height of the part is inversely proportional to the print time of the part. However, due to the aerial nature of the project, the layer height needed to be reduced as far as possible to reduce the stair-stepping effect on the aerodynamic surfaces of the prototype [64]. While this would ultimately result in longer print time for the parts, it would also result in a stronger part due to better layer adhesion [54].

5.7.1.5 Results Analysis

Figure 5-4 and Figure 5-5 below present the relationships between FDM parameters, and trendline equations. These trendline equations can be used to predict the print time and the specific strength of a part produced by FDM, which will be subjected to flexural or tensile forces in its application, at any given layer height ranging from 0.15mm to 0.35mm.

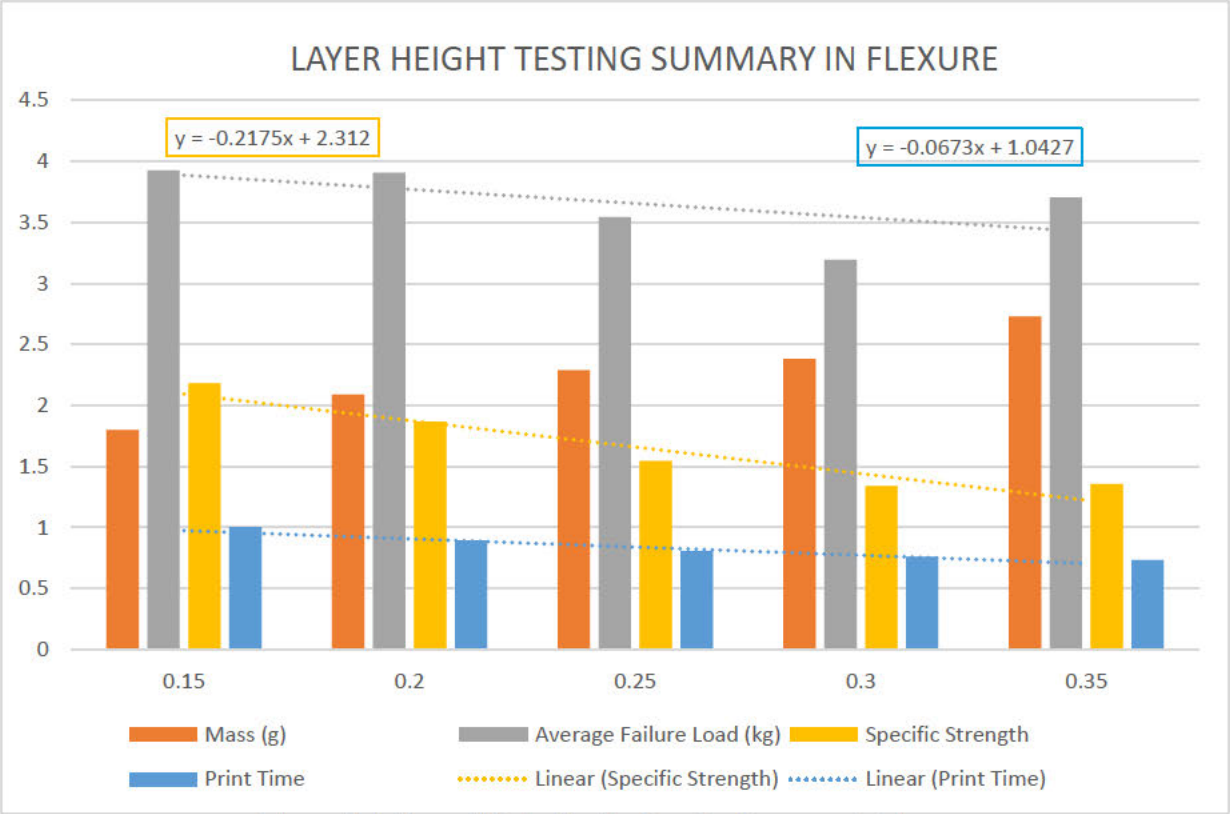

Figure 5-4: Layer Height Testing Results Summary in Flexure

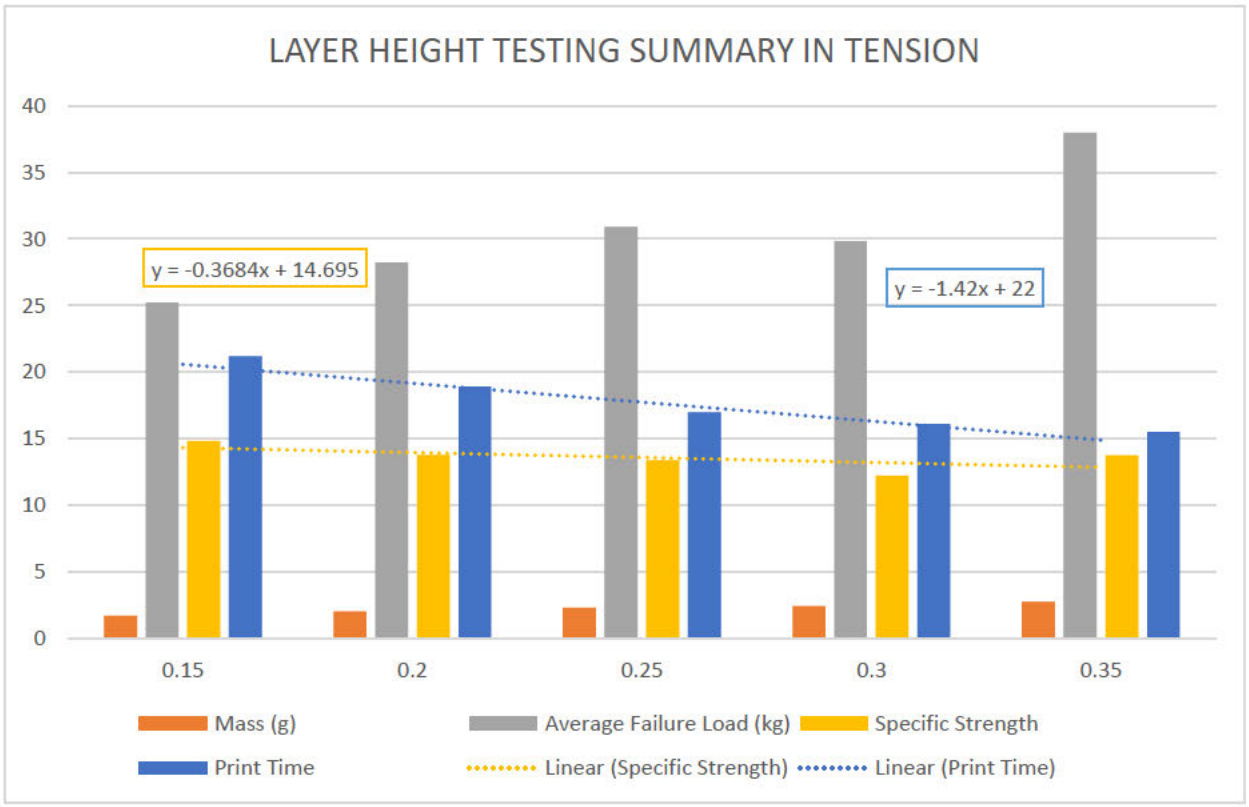

Figure 5-5: Layer Height Testing Results Summary in Tension

In the layer height test, the flexural test identified a declining specific strength as the layer height of the sample was increased. A maximum specific strength of 2.18kg/g was realised at 0.15mm layer height. This decreased to 1.36kg/g at 0.35mm layer height according to the linear equation provided by Figure 5-4. The same trend was seen in the tensile test portion of the layer height test, from a specific strength of 14.82kg/g at 0.15mm layer height to 13.76kg/g at 0.35mm layer height. The linear equation describing the tensile specific strength decrease can be found in Figure 5-5. This amounts to a total decrease of 37.61% in flexure, and 7.15% in tension. This trend suggested that, as the layer height was increased, more mass was being added to the part in comparison to the strength being added. The 0.3mm layer height was identified to be the weakest in both tension and flexure. In flexure, the experimental specific strength of the 0.3mm layer height was found to be 1.34kg/g. This proved to be 1.47% lower than the expected lowest specific strength of the 0.35mm layer height, in accordance with literature. In order to produce conservative results in the remainder of the tests, the 0.3mm layer height was used to produce testing samples.

5.7.2 Infill Pattern Testing

5.7.2.1 Aim

To determine which infill pattern provides the best resistance to plastic deformation in both tension and flexure.

5.7.2.2 Objective

To determine the relationships between the infill pattern, infill percentage, print time, failure load, and part mass of FDM samples.

5.7.2.3 Variables

- Infill Pattern (Independent variable)
- Infill percentage (Independent variable)
- Print time (Dependent variable)
- Failure load (Dependent variable)
- Part mass (Dependent variable)

5.7.2.4 Theory

The infill pattern test sought to determine whether the Gyroid or the Cubic infill pattern offered by the Cura slicing software was superior. Literature presented in chapter 2.8.6 above suggests that both the Gyroid and the Cubic infill patterns are the most stable infill patterns, boasting the best resistance to plastic deformation along all axes. The purpose of the infill pattern in the research project scenario was to ensure that the parts would retain their strength whilst material was removed from the internal volume of the parts during production to lighten the part as far as possible. Therefore, the specific strength of the infill pattern was to be determined for both patterns. Thereafter, the infill pattern which provided more strength to the part, per unit mass, could be identified.

5.7.2.5 Results Analysis

Figure 5-6 and Figure 5-7 provide the test results in summarised form complete with trendline equations, for flexure and tension, respectively. With regards to the reported trendline equations, the y-value gives the specific strength of the part, and the x-value gives the parameter being altered in each test.

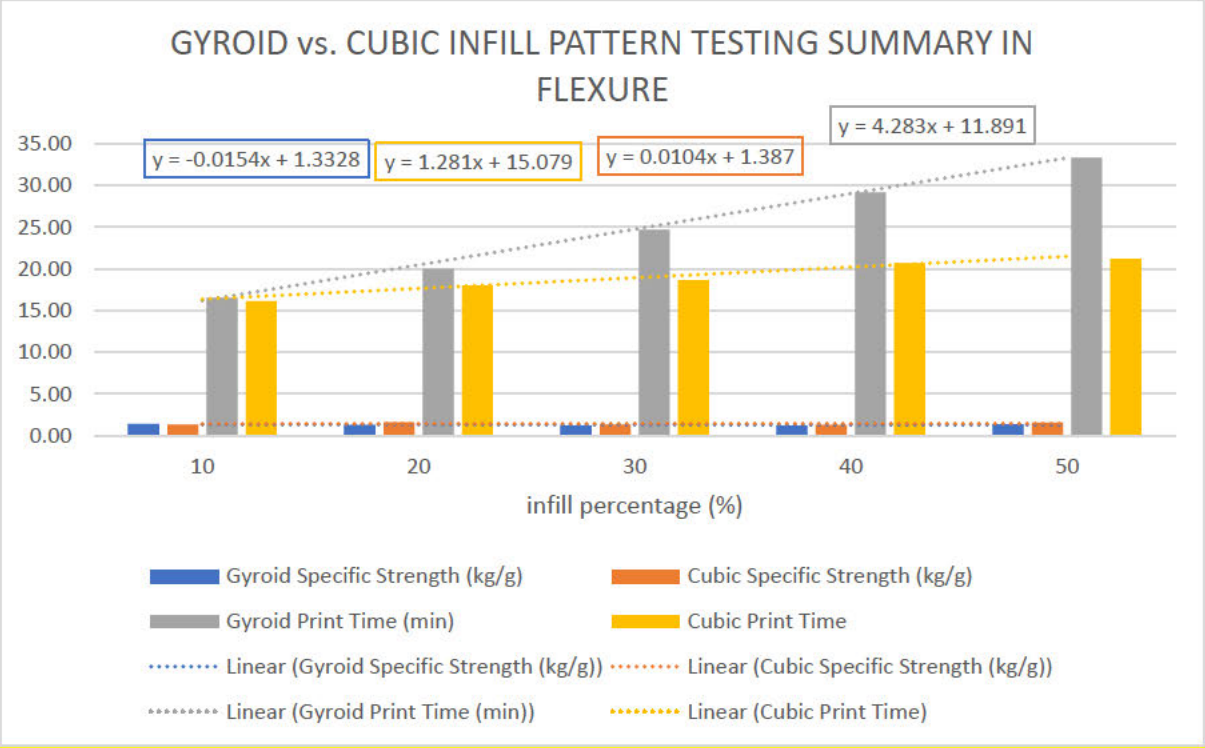

Figure 5-6: Infill Pattern Testing Results Summary in Flexure

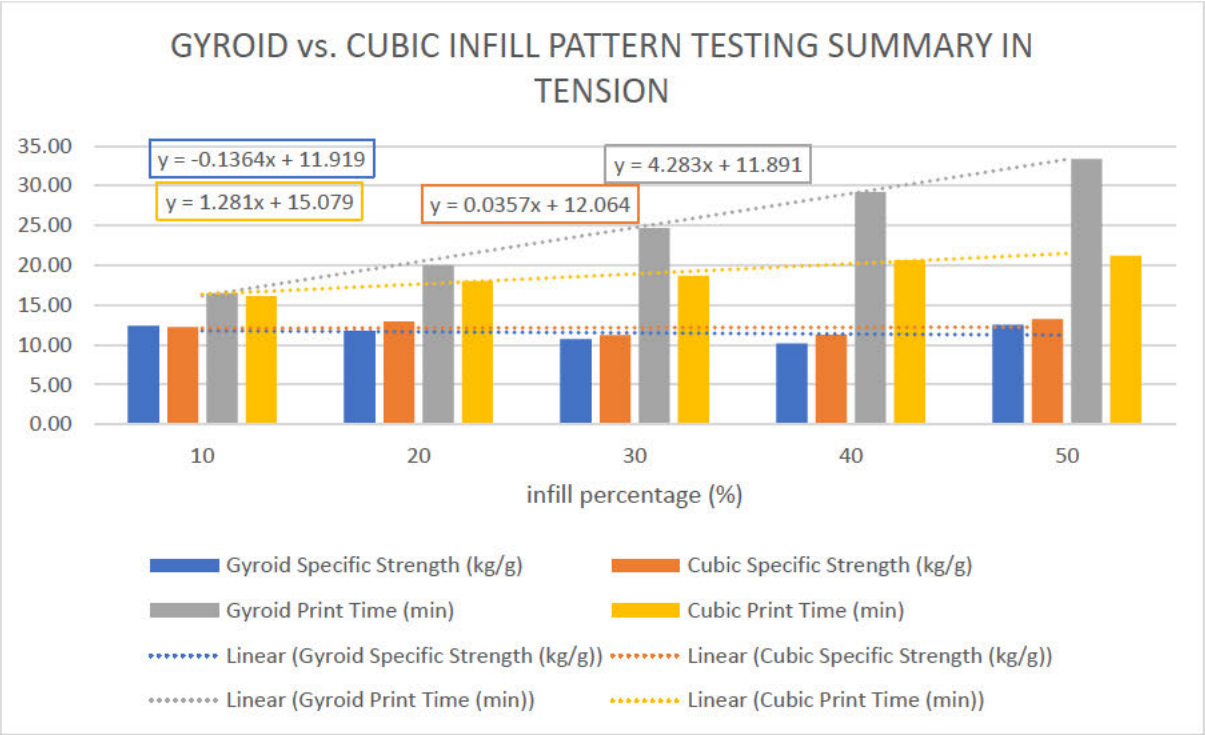

Figure 5-7: Infill Pattern Testing Results Summary in Tension

In the infill pattern test it was evident that, in flexure, the Gyroid infill pattern specific strength decreased as the infill percentage of the part is increased, whereas the Cubic infill pattern specific strength increased. Additionally, the Gyroid infill pattern print time increased at a noticeably greater rate than that of the Cubic infill pattern. The same trends of both the Gyroid and Cubic infill patterns were evident in tension. These trends can be seen in Figures 5-6 and 5-7 respectively. These trends alluded to the fact that the Cubic infill pattern is superior to the Gyroid infill pattern in terms of specific strength and print time. In flexure, the Gyroid infill pattern suffered a 1.43% loss in specific strength, from 1.40kg/g at 10% infill, to 1.38kg/g at 50% infill, with large fluctuations in specific strength being observed throughout the infill percentage range, with a standard deviation of 0.10kg/g. Conversely, the Cubic infill pattern showed a 12.99% increase in specific strength, from 1.34kg/g to 1.54kg/g at 10% and 50% infill, respectively, with a standard deviation of 0.13kg/g. The same trends held true in tension for both infill patterns. The Gyroid infill pattern displayed a slight increase in specific strength of 0.69%, from 12.41kg/g at 10% infill, to 12.53kg/g at 50% with a 1.05 kg/g standard deviation in specific strength values. However, when the fluctuation in specific strength values and outliers across the infill range were considered by the linear trendline, a trend of decrease was realised. This can be seen in Figure 5-6. The Cubic infill pattern in tension displayed a 7.49% increase in specific strength, from 12.22kg/g at 10% infill, to 13.21kg/g at 50% with a standard deviation of 0.91kg/g. Whilst the specific strength values across the infill percentage range fluctuated, the Cubic infill pattern linear trendline still showed a positive correlation when fluctuations and outliers were considered. As such, the Cubic infill pattern proved superior to the Gyroid infill pattern in both tension and flexure.

5.7.3 Infill and Perimeter Testing

5.7.3.1 Aim

To determine which infill pattern and perimeter shell thickness combination provides the best resistance to plastic deformation in both tension and flexure.

5.7.3.2 Objective

To derive relationships between the infill percentage, number of perimeter walls, print time, failure load, and part mass of FDM samples.

5.7.3.3 Variables

- Number of perimeter walls (Independent variable)
- Infill percentage (Independent variable)
- Print time (Dependent variable)
- Failure load (Dependent variable)
- Part mass (Dependent variable)

5.7.3.4 Theory

The purpose of the infill and perimeter test was to produce data which could be analysed to identify trends with regards to the strength each combination adds to the parts. To do this, the specific strength of each combination was analysed with the intention of identifying the strongest, most lightweight parameter combination.

5.7.3.5 Results Analysis

Figure 5-8 and Figure 5-9 below show summarised versions of the data produced by the infill and perimeter test. With reference to these graphs, the x-axis combination labels, such as “40%1P”, describe a sample manufactured with 40% infill and one perimeter layer.

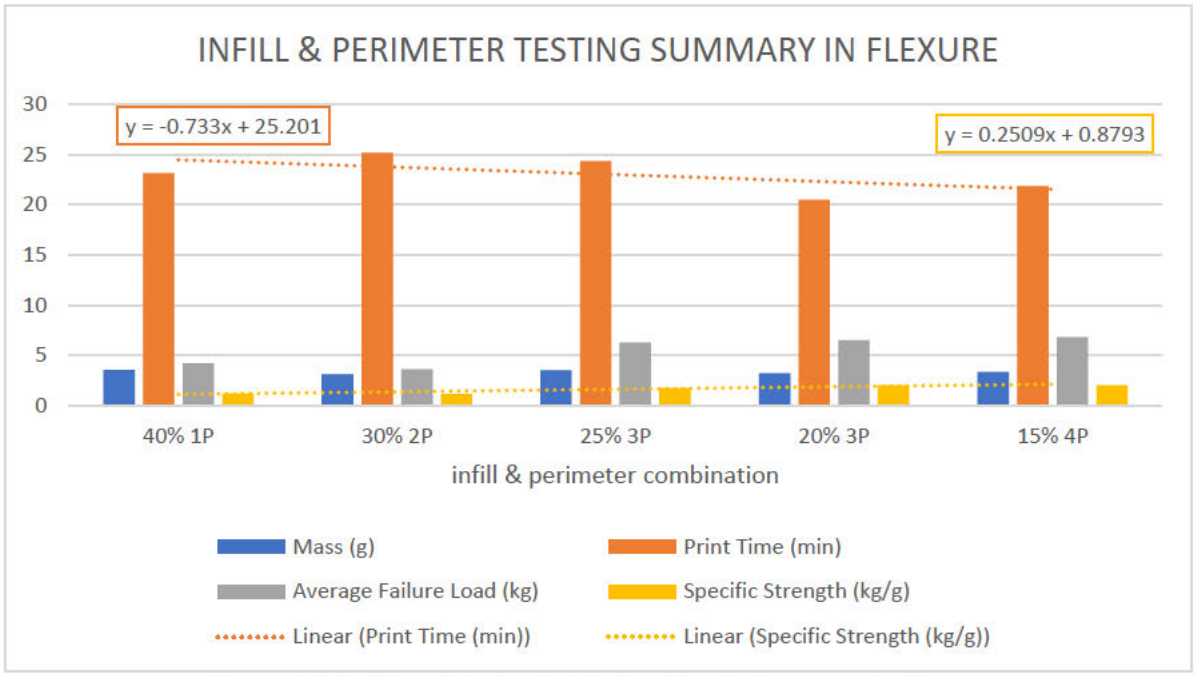

Figure 5-8: Infill and Perimeter Testing Results Summary in Flexure

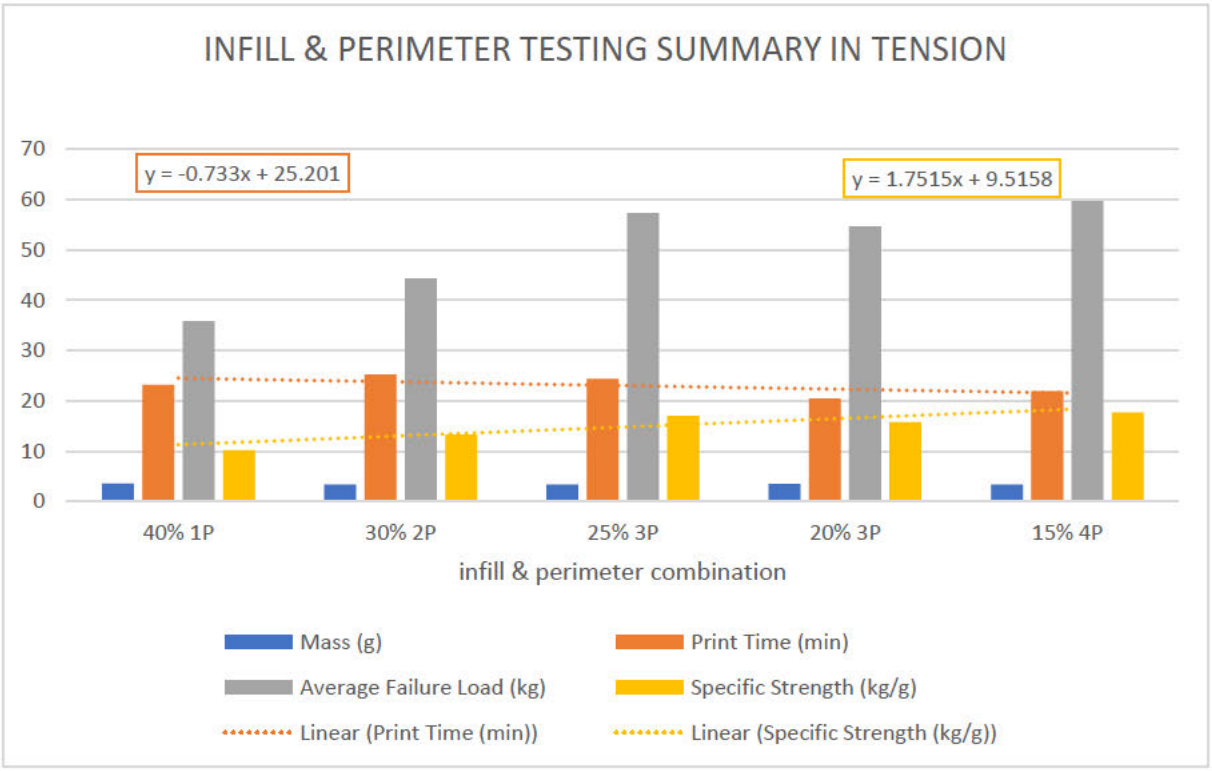

Figure 5-9: Infill and Perimeter Testing Results Summary in Tension

The infill and perimeter tests were conducted using the superior Cubic infill pattern and increasing the number of perimeter layers and decreasing the infill percentage. A positive correlation was realised between the specific strength of the sample and the increased perimeters with decreased infill percentage. Numerically, the specific strength increased by 41.09% in flexure, from 1.19kg/g to 2.02kg/g, and by 42.58% in tension, from 10.14kg/g to 17.66kg/g at 40% infill and 1 perimeter layer, and 15% infill with 4 perimeter layers, respectively. The equations governing these trends, with equations, can be seen in Figure 5-8 and Figure 5-9 above, along with a standard deviation of 0.42 kg/g in flexure, and 3.07 kg/g in tension, with regards to specific strength. Hence, it was evident that the number of perimeter layers of a part was more influential on part strength than the infill pattern or the infill percentage.

5.7.4 Perimeter Variation Testing

5.7.4.1 Aim

- To determine the strength of a hollow part prints with varying wall thickness.
- To compare the strength of varying infill percentage and perimeter wall combinations against the strength of a hollow part print with varying wall thickness.

5.7.4.2 Objective

To compare the specific strength of the samples produced through perimeter variation to the specific strength of the infill and perimeter testing samples.

5.7.4.3 Variables

- Number of perimeter walls (Independent variable)
- Print time (Dependent variable)
- Failure load (Dependent variable)
- Part mass (Dependent variable)

5.7.4.4 Theory

In this test, the testing data from the previous test was utilised. The testing data from the infill and perimeter testing was to be compared against specimens manufactured with 0% infill, but increased numbers of perimeter shells. The test endeavoured to directly compare the data produced by each of the tests to determine whether the orthodox method of infill and perimeter variation, or the unorthodox method of hollow shell printing, with more perimeter shells, provided more resistance to deformation per unit mass. To do this, the specific strength of the samples produced by each test method was to be compared to determine the superior parameter combination.

5.7.4.5 Results Analysis

Figures 5-10 and 5-11 below provide the summarised data of the complete perimeter variation test.

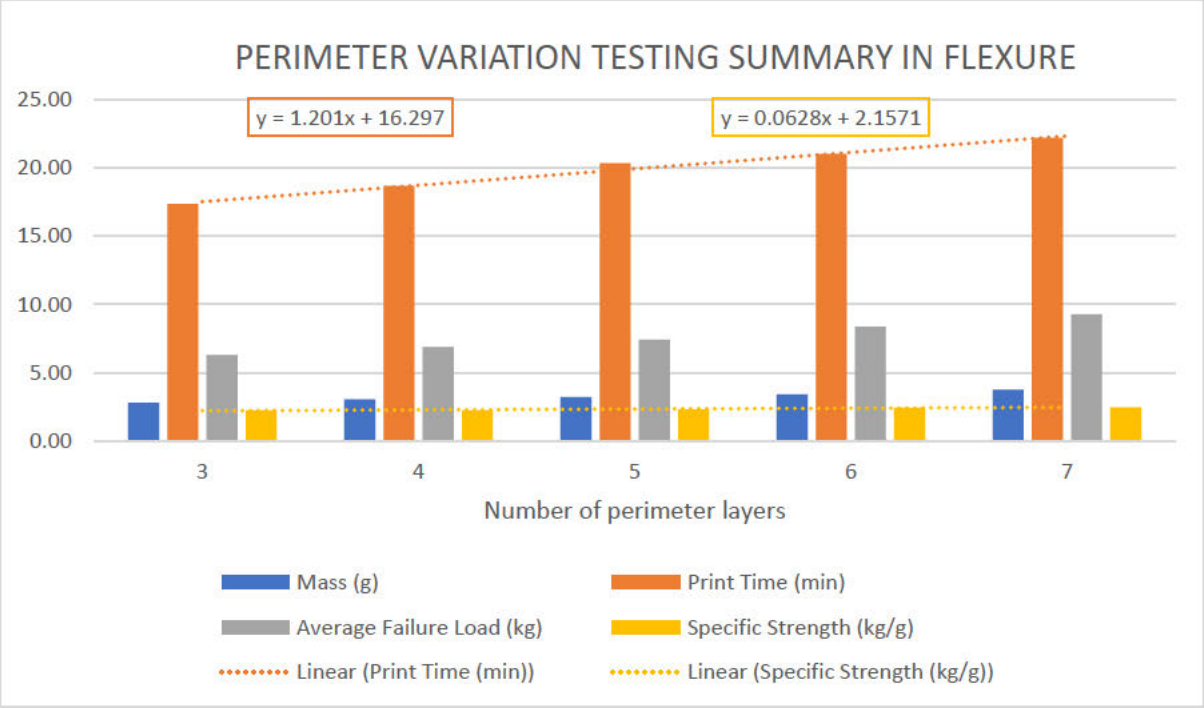

Figure 5-10: Perimeter Layer Variation Testing Results Summary in Flexure

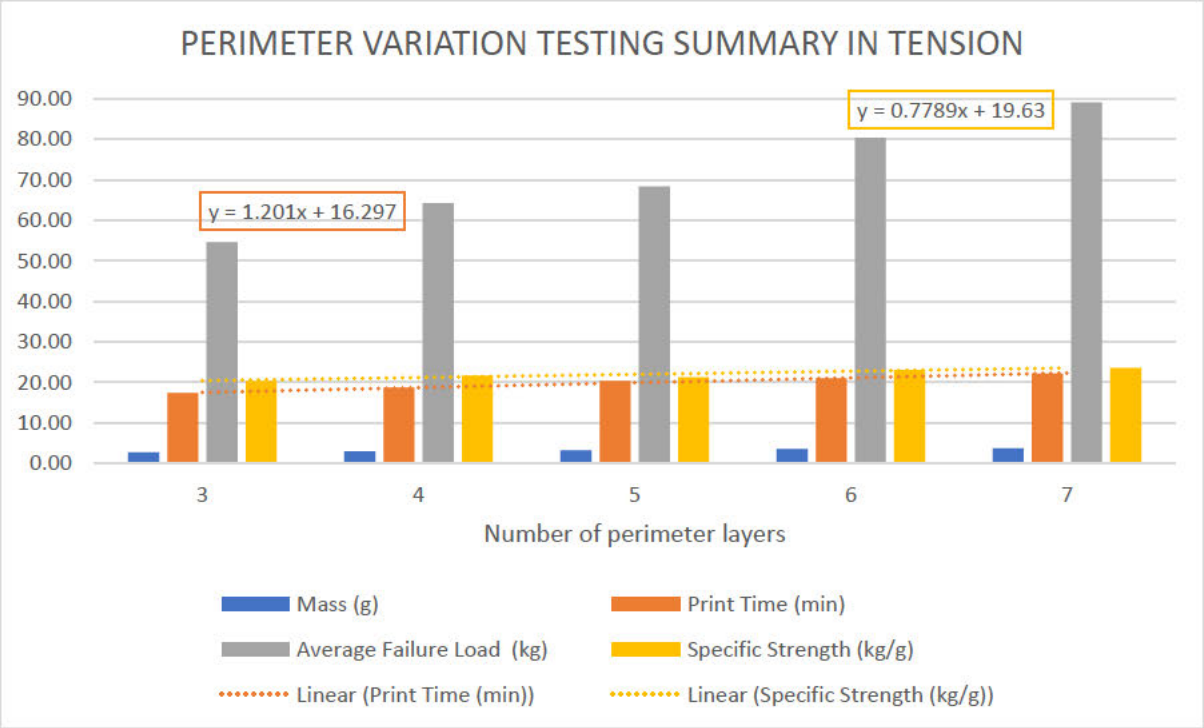

Figure 5-11: Perimeter Layer Variation Testing Results Summary in Tension

The perimeter variation test was conducted by varying the number of perimeter layers of the test sample with 0% infill. This was done in accordance with the findings of the infill and perimeter test. In flexure, a specific strength increase of 9.31% was observed, from 2.24kg/g with three perimeter layers, to 2.47kg/g with seven perimeter layers. In tension, the specific strength increased by 13.70% from 20.35kg/g to 23.58kg/g at three and seven perimeter layers respectively. Another noteworthy observation was that the minimum specific strength the perimeter variation test, observed at three perimeter shells of 2.24kg/g, was 9.82% greater than the maximum specific strength observed by the infill and perimeter testing, at 15% infill and four perimeter layers (in flexure). The same was true in tension, where the minimum observed specific strength of 20.35kg/g at 0% infill and three perimeter shells, was 13.22% greater than the maximum observed specific strength of 17.66kg/g in the infill and perimeter test, at 15% infill and four perimeter shells. This method also showed shorter print times than the infill and perimeter test.

5.8 Result Validation

The completion of the FDM optimization testing provided invaluable insight into the effects of various slicing parameters on the flexural and tensile capacities of the testing samples. The results identified the sample prepared using a 0.3mm layer height to be the least resistive to both flexural and tensile loads, when compared to the remaining samples produced with layer heights in the range of 0.15mm to 0.35mm. Additionally, the results proved the technique of perimeter layer variation to be superior to the commonly implemented infill and perimeter combination printing. This was assessed on the premises of print time, part mass, specific strength, and result stability (standard deviation) where it proved superior in all aspects.

To validate the results generated during testing, the average failure loads provided by the perimeter layer variation test were imposed on the samples in an FEA simulation with equivalent boundary conditions to those that were used during testing. The results of these FEA analyses can be found in Figures B-1 to B-18 of Appendix B. Table 5-4 below shows the comparison between the simulated stress and mass of the specimens during simulation, and the stress and mass of the specimens calculated using data from the tests. The comparisons were then used to calculate scaling factors which can be used to convert simulation data into a realistic prediction of the stress and mass of the ISP prototype components going forward. The relative wall thickness was calculated using the nozzle diameter of the CR10-S5, which was used to fabricate the test samples, and the number of perimeter walls. This metric made it possible to correlate the strength of parts manufactured with different wall thicknesses, to the data presented in Table 5-4 below.

Table 5-4: FDM Experimental and Simulation Result Correlations

Perimeter Layers	Relative Wall Thickness (mm)	Calculated Stress (MPa)	Simulated Stress (MPa)	Stress Scale Factor	Actual Mass (g)	Simulated Mass (g)	Mass Scale Factor
			Flexure				
3	1.2	72.46	58.17	1.25	2.81	2.90	0.97
4	1.6	79.09	61.23	1.29	3.04	3.09	0.98
5	2.0	85.34	66.64	1.28	3.21	3.29	0.98
6	2.4	96.18	74.46	1.29	3.43	3.48	0.99
7	2.8	106.72	83.73	1.27	3.76	3.67	1.02
			Tension				
3	1.2	32.78	55.42	0.59	2.68	2.90	0.92
4	1.6	32.79	59.17	0.55	2.96	3.09	0.96
5	2.0	32.21	57.73	0.56	3.22	3.29	0.98
6	2.4	37.31	62.92	0.59	3.49	3.48	1.00
7	2.8	43.37	65.25	0.66	3.78	3.67	1.03

The contents of Table 5-4 above describe a close correlation between the simulated and experimental testing results. From the tabulated results in flexure, the stress scale factors can be seen to vary by only 3.1%, and the mass scale factors by only 4.90%. Similarly, in tension, the stress and mass scale factors are shown to vary by 15.06% and 10.68% respectively. However, these indicators validate the experimental data only for the geometry of the ASTM testing standards. Therefore, to assess the experimental findings for a more complex geometry, a final set of destructive testing was undertaken on an ISP component.

The chosen ISP component for destructive testing was the pitch axis drop arm end cap. This component is represented graphically by drawing P3 of Appendix D. The drop arm end cap was chosen due to the predominant force acting on the component under operational conditions being tension. Whilst elements of combined loading would be present during operation due to the offsets of the mating surfaces, these effects proved minimal in comparison to the remaining ISP components. Hence, to identify mass-equivalent FDM parameter combinations with which to fabricate the test samples, Table B-8 and Table B-10 were utilised. These tables identified an infill and perimeter combination test sample with an acceptable mass-equivalence to a perimeter variation sample. These samples were the 0.3mm layer height, 20% cubic infill, and 3 perimeter sample, and the 0.3mm layer height, 0% infill, and 6 perimeter sample. Referring to Table B-8 and Table B-10, these samples are shown to weigh 3.46g and 3.49g, respectively. Following the fabrication and destructive testing of these samples, Table 5-5 below presents the experimental results.

Table 5-5: Final Destructive Testing Results

Sample	Layer Height (mm)	Infill (%)	Perimeters	Mass (g)	Failure Load (kg)	Specific Strength (kg/g)
1	0.3	20	3	8.17	59.75	7.32
2	0.3	0	6	7.27	62.59	8.61

The findings of the final destructive testing of the ISP drop arm end cap validated the findings of the FDM optimisation experimentation. As shown in Table 5-5 above, the perimeter variation method produced a greater specific strength than the infill and perimeter parameter method, even in the presence of combined loading. However, the combined loading was proven to significantly reduce the specific strength of the sample from the values obtained in pure flexure and tension.

5.9 Final Parameter Selection and Fabrication

The correlation between the results of the FDM parameter optimisation testing, FEA results, and destructive testing of ISP components provided the basis for the selection of optimal parameters for the fabrication of the ISP prototype. The testing processes found the optimal FDM part strength to be found by varying the perimeter wall thickness, with ideal specific strengths being shown in Table B-9 and Table B-10. However, an increase in specific strength, and therefore part strength, was possible by reducing the layer height of the parts.

As previously mentioned, due to the aerial nature of the research project, the surface finish and the part masses were the driving factors behind the FDM optimisation. For the surface finish of the components to be optimised, the final layer heights were restricted to a maximum value of 0.2mm. This maximum layer height was only applied to the components which had no bearing on the aerodynamic performance of the prototype. However, with reference to Figure 5-4 and Figure 5-5 above, the reduced layer heights also produced the most lightweight parts. Drawing on this knowledge, Table 5-6 below reveals the final FDM parameters used during the fabrication of the ISP, combined with individual component metrics of final part mass and print time. The sample preparation settings provided in Table 5-3 above were applied to the final fabrication procedure of the ISP to ensure consistent, repeatable mechanical properties of the final prototype components.

Table 5-6: Final ISP Component Fabrication Particulars

Part Drawing No.	Part Name	Qty.	Layer Height (mm)	Wall Thickness (mm)	Part Mass (g)	Unit Print Time (min)
P14	TPU Vibration Dampener	2	0.2	1.20	4.40	97
P1	Front Landing Gear Mount	1	0.15	1.40	41.81	373
P2	Rear Landing Gear Mount	1	0.15	1.40	44.92	497
P4	Pitch Axis Drop Arm	1	0.15	1.40	24.51	327
P7	Drop Arm Lid	2	0.15	1.40	1.63	24
P3	Drop Arm End Cap	1	0.15	0.90	6.22	103
P5	Control Surface End Cap	1	0.15	0.90	5.73	145
P10	Payload Cradle	1	0.15	0.45	102.26	1340
P12	Cradle Base	1	0.15	0.45 (50% Infill)	51.8	465
P10	BNO055 Housing	1	0.2	0.8	7.62	68
P11	BNO055 Housing Lid	1	0.2	0.5	1.49	18
P13	Battery Housing	2	0.15	0.6	9.77	114
P8	Roll Axis Control Arm	2	0.1	0.3 (50% Infill)	3.47	72
P6	Pitch Axis Control Arm	2	0.1	0.3 (50% Infill)	2.44	46.5
Total		**19**			**329.7**	**4013**

Concurrently to the final FDM parameter selection, FEA analyses were performed on the components which were expected to be subjected to high stress concentrations, bending stresses, tensile loads, and aerodynamic forces. The results of these FEAs are presented in Table 5-7 below.

Table 5-7: ISP Component FEA Results

FEA Reference	Part Name	Max. Von Mises Stress (MPa)	Max. Deflection (mm)
Figures B-1 and B-2	Front Landing Gear Mount	4.87	0.77
Figures B-3 t oB-5	Rear Landing Gear Mount	4.13	0.67
Figures B-6 to B-9	Pitch Axis Drop Arm	1.64	0.01
Figures B-10 to B-12	Drop Arm End Cap	0.93	0.00042
Figures B-13 and B-14	Control Surface End Cap	3.19	0.02
Figures B-15 to B-18	Payload Cradle	1.69	0.22

The results displayed above in Table 5-7 indicate that the final FDM parameter selections for the ISP components yielded sufficient results under loading, with the maximum stresses falling well within the maximum allowable stress threshold of the PLA material. The final FEA results can be found in Appendix B for the above-mentioned components. These analyses were conducted to account for the maximum loading conditions of the components, with an assumed total payload mass of 2.2kg, as discussed in Chapter

4 above. The final, assembled ISP mass was found to be 709.86g. Having ensured that the final parameter selections would produce structurally sound ISP components, the final components were fabricated. Figure 5-12 and Figure 5-13 below show the fabricated ISP components.

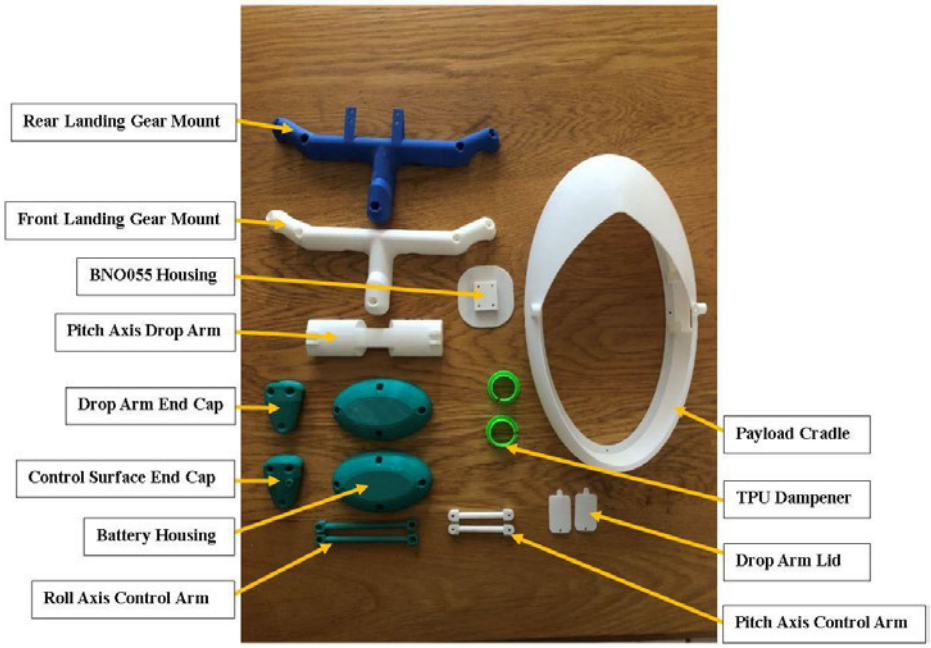

Figure 5-12: FDM Fabricated ISP Components

Figure 5-13: FDM Fabricated ISP Cradle Base

5.10 Chapter Summary

Chapter 5 discussed the experimental methodology followed for the empirical optimisation of FDM process parameters. Optimisation of the FDM process parameters was made necessary by Chapter 2.8.6, as well as design objective III of chapter 4, which required the ISP FDM components to be as light as possible whilst maintaining structural resilience.

The results indicated that optimal FDM part strength, mass, and print time was achieved by varying the perimeter wall thickness, at 0% infill. This method was validated through FEA analyses on the testing sample with equivalent boundary conditions. Results of the FEAs indicated that the FDM optimisation experimentation produced results with uniform correlation ratios to simulated results. In flexure, a 3.1% discrepancy was obtained across the stress correlation ratios, and a 15.06% discrepancy in tension, for the range of testing samples. Following this, a final destructive test was run on an ISP component. The chosen component was the pitch axis drop arm end cap. Two of these components were prepared; one with 20% cubic infill and 3 perimeter layers, and one with no infill and 6 perimeter layers. The test confirmed the findings of the FDM parameter optimisation, with the sample prepared using the perimeter variation method withstanding a greater failure load. Finally, the final ISP component FDM parameters were derived concurrently to final component FEA analyses to confirm structural resilience before the components were manufactured. The final FEA results showed maximum part stresses well below the stress threshold of the PLA material and were ensued by the FDM-fabrication of the final ISP prototype components. The assembled mass of the ISP prototype was determined to be 709.86g.

6 CONTROL SYSTEM IMPLEMENTATION

6.1 Introduction

Chapter 6 details the development and implementation of the ISPs control system. Control of the ISP was achieved using classical PID controllers. Whilst enhanced stabilisation performance was possible through the implementation of modern non-linear control techniques, classical controllers have been shown to produce adequate stabilisation performance with significantly reduced computational complexity [51]. This chapter first presents the control system simulation model development within the MATLAB Simulink environment. Thereafter, the practical implementation of the ISP control system is explained through a detailed description of the final programmed code.

6.2 Simulink Model Development

This section describes the simulation model development of the ISP within MATLAB Simulink, and the results of simulations run to confirm system performance throughout the process. The initial step of the process was to further divide the ISP into smaller individual subsystems which could be represented by block diagrams detailing the dynamic equations of the subsystems. Figure 6-1 below details the ISP decomposition to facilitate the development of the control system.

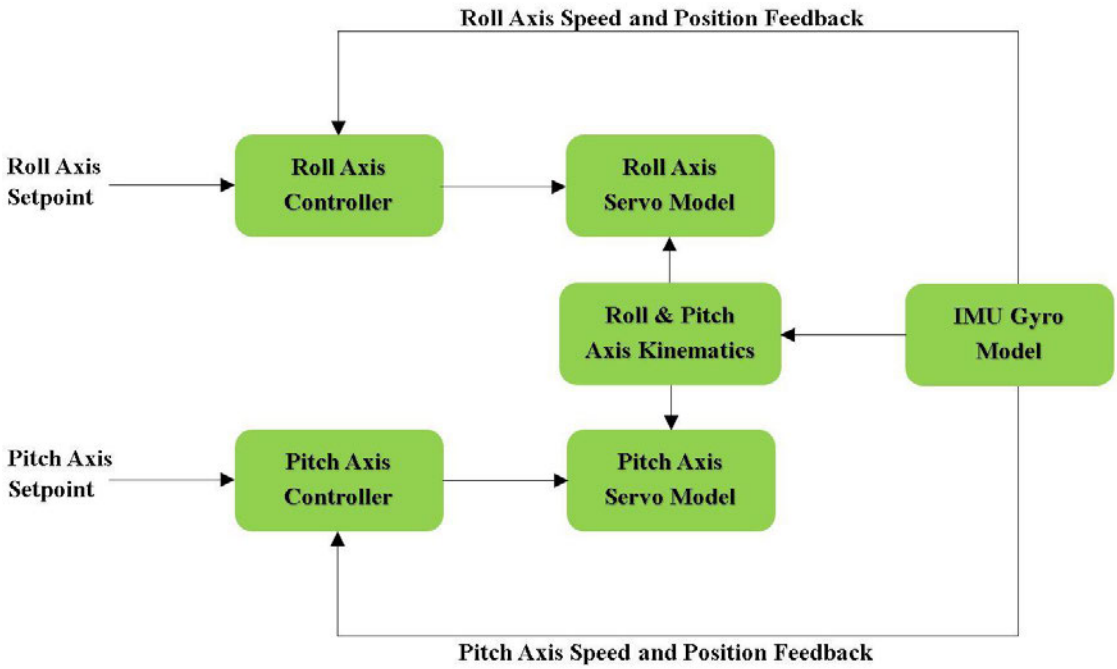

Figure 6-1: ISP Control Decomposition Diagram

As shown in Figure 6-1 above, the ISP was reduced to four main blocks for each axis; one to encapsulate the controller to be designed, one to represent the servo motor model, and one to represent the axis' kinematics, as derived in Chapter 2.9. The final block, representative of the IMU gyro, is seen to provide the speed and position feedback for each axis, whilst also being a contributor to the kinematics of each axis.

6.2.1 Servo Motor Model

The DC servo motor model used within the ISP Simulink model was based on existing research in [100], [101],and [102]. These publications derive the servo motor differential and steady state equations from first principles and convert the equations into a transfer function to be represented in block diagram format. Owing to this, the DC servo motor block diagram shown in Figure 6-2 below was developed and used within the ISP Simulink model.

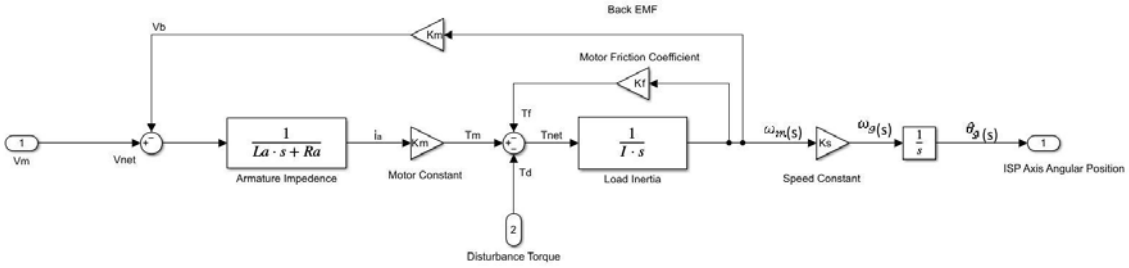

Figure 6-2: DC Servo Motor Simulink Block Diagram

Where:

V_m = Motor Voltage (V)

V_b = Back EMF Voltage (V)

V_{net} = Net Motor Voltage (V)

L_a = Armature Inductance (H)

R_a = Armature Resistance (Ω)

i_a = Armature Current (A)

K_m = Motor Torque to Current Constant (mKg.cm/A)

T_m = Motor Torque (Kg.cm)

T_f = Friction Torque (Kg.cm)

T_d = Disturbance Torque (Kg.cm)

T_{net} = Net Motor Torque (Kg.cm)

I = Motor Load Inertia (Kg. m^2)

K_f = Motor Friction Coefficient (mKg.cm/(°/s))

ω_m = Motor Speed (°/s)

K_s = Motor Speed to Gimbal Axis Speed Constant

ω_g = Gimbal Axis Speed (°/s)

θ_g = Gimbal Axis Angular Position (°)

The above block diagram was utilised within the ISP Simulink model to represents the roll and the pitch servo motors. While the layout of the block diagram remained the same for each axis' servo motor, the inertia term seen by each motor was dependent on the final design of the ISP, as well as the motor speed constant. The ideal inertia term seen by the roll axis servo would be that of the roll gimbal about x_R axis, such that $I_R = I_{xxR}$. Similarly, the ideal inertia term seen by the pitch axis servo motor would be that of the pitch gimbal about the y_P axis, with $I_P = I_{yyp}$. This would, however, require each ISP axis of rotation to pass through its CoM. Subsections 6.2.2 and 6.2.3 which follow explore the ISP inertia terms in greater detail.

The chosen servo motor for the ISP was the DSSERVO 35kg servo motor. This servo motor was previously determined to meet the design requirements and specifications of the ISP. Chapter 4.3.1 provides the full specifications of these servo motors (which were used within the simulation model), as well as a complete set of motor sizing calculations. As can be seen by the above block diagram, motor friction was assumed to be linearly proportional to the motor shaft speed, whilst subject to a coefficient of friction factor. Table 6-1 below details the servo motor block diagram values utilised within the simulation.

Table 6-1: Simulink Model Motor Parameter Values [75]

Parameter	Description	Value
V_M	Motor Voltage	7.4V
R_A	Armature Resistance	1.3Ω
L_A	Armature Inductance	0.23 H
K_M	Motor Constant	1.27
K_F	Friction Constant	0.8

6.2.2 Roll Axis Kinematics

The derivation of the ISP kinematics for the Simulink model was an extension of the mathematical modelling portrayed in Chapter 2.6. With reference to Chapter 2.6.5 specifically, the roll axis' inertia tensor was given as:

$$I_R = \begin{bmatrix} I_{xxR} & D_{xyR} & I_{xzR} \\ D_{xyR} & I_{yyR} & D_{yzR} \\ D_{xzR} & D_{yzR} & I_{zzR} \end{bmatrix}$$

In order to accurately quantify the inertia tensor, it was necessary to evaluate the final mass of the roll axis of the ISP. Following the fabrication of the ISP components, the components were weighed, and the mass of each component overridden within the ISP SolidWorks model. Following the mass override, the SolidWorks inertia tensor approximation for the roll axis was found to be:

$$I_R = \begin{bmatrix} 0.002933 & 0.00008458 & -0.00001601 \\ 0.00008458 & 0.003053 & -0.00003089 \\ -0.00001601 & -0.00003089 & 0.002769 \end{bmatrix} kg \cdot m^2 \quad (6\text{-}1)$$

Which was further reduced, due to the difference in the order of magnitudes of the terms, to:

$$I_R \approx \begin{bmatrix} 0.002933 & 0 & 0 \\ 0 & 0.003053 & 0 \\ 0 & 0 & 0.002769 \end{bmatrix} kg \cdot m^2 \quad (6\text{-}2)$$

The roll axis was defined to include all components which would contribute to the load experienced by the roll axis servo motor. Figure 6-3 below shows the roll axis form and the location of its CoM. The final estimated weight of the roll axis was m_{Roll} = 562.05g.

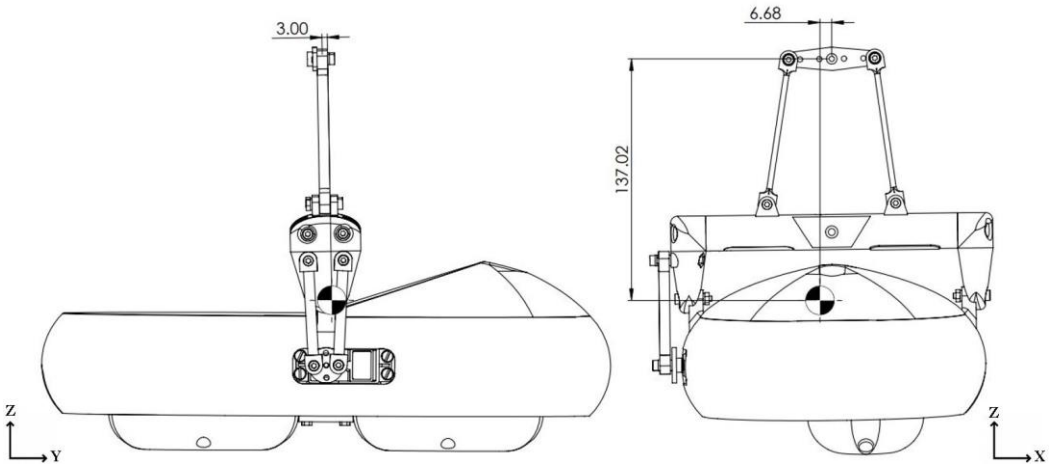

Figure 6-3: Roll Axis Configuration and CoM Location

Figure 6-3 above also elucidates the offset of the CoM of the roll axis relative to the location of the roll axis servo shaft. The offset CoM made it necessary to evaluate the MOI seen by the servo shaft for increased simulation accuracy. This evaluation was made using the parallel axis theorem to redefine the load seen by the roll servo, $I_{Servo,Roll}$, due to the CoM offset, $d_{xxr,}$ as per *Equation 6-3*, where:

$$I_{Servo,Roll} = I_{xxR} + m_{Roll} dxxr^2 \quad (6\text{-}3)$$

Which yielded:

$$I_{Servo,Roll} = 0.002958\, kg \cdot m^2$$

This value represented the inertia experienced by the roll servo shaft as a result of the ISP roll axis configuration. Interestingly, though, the magnitude of the tensor terms depicted in *Equation 6-1* allowed for the simplification of the roll axis inertia tensor to that shown in *Equation 6-2*. Therefore, despite the CoM offset, the kinematics of the roll axis could be modelled as an ideal gimbal suspended from its principal axis without loss of element definition. Referring to Figure 2-7, the roll axis of the ISP was shown to act in the X_I-Z_I plane. Therefore, the total external torque experienced by the roll axis was that of M_{xxR} in *Equation 2-10*, as shown by *Equation 6-4* below.

$$M_{xR} = I_{xxR}\dot{\omega}_{x_R} + (I_{zzR} - I_{yyR})\omega_{y_R}\omega_{zR} \quad (6\text{-}4)$$

Which could be represented in the model using standard Simulink blocks.

6.2.3 Pitch Axis Kinematics

The ISP pitch axis kinematics were derived synonymously to those of the roll axis. Referring to Chapter 2.6.4, the inertia tensor of the pitch axis was given as:

$$I_P = \begin{bmatrix} I_{xxp} & D_{xyp} & I_{xzp} \\ D_{xyp} & I_{yyp} & D_{yzp} \\ D_{xzp} & D_{yzp} & I_{zzp} \end{bmatrix}$$

The SolidWorks inertia tensor approximation, following the component masses being overridden, was found as shown in *Equation 6-5*.

$$I_P = \begin{bmatrix} 0.001671 & -0.00001429 & -0.000002693 \\ -0.00001429 & 0.002060 & 0.00003312 \\ -0.000002693 & 0.00003312 & 0.006201 \end{bmatrix} kg \cdot m^2 \quad (6\text{-}5)$$

Which simplified to *Equation 6-6* as follows:

$$I_P = \begin{bmatrix} 0.001671 & 0 & 0 \\ 0 & 0.002060 & 0 \\ 0 & 0 & 0.006201 \end{bmatrix} kg \cdot m^2 \quad (6\text{-}6)$$

The kinematics of the pitch axis was noted to also mimic that of an ideal gimbal, despites not being suspended by its principal axis. Figure 6-4 below shows the overall configuration of the ISP pitch axis and the location of the CoM relative to the principal axis. The final estimated mass of the pitch axis was found to be m_{Pitch}= 215.63g.

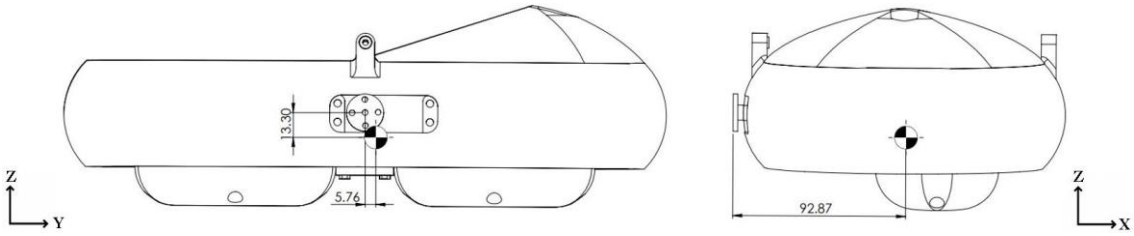

Figure 6-4:Pitch Axis Configuration and CoM Location

Again, the parallel axis theorem was utilised to determine the load inertia seen by the pitch servo, $I_{Servo,Pitch}$, due to the CoM offset, $d_{yyp,}$ as per *Equation 6-7*, where:

$$I_{Servo,Pitch} = I_{yyP} + m_{Pitch} dyyp^2 \quad (6\text{-}7)$$

Giving:

$$I_{Servo,Pitch} = 0.002067\ kg \cdot m^2$$

Referring again to Figure 2-7, the ISP pitch axis was constrained to the Y_I-Z_I plane. Hence, the total external torque experienced by the pitch axis, M_{yyP}, was as shown by *Equation 6-8* as follows:

$$M_{yP} = I_{yyp}\dot{\omega}_{y_P} + (I_{xxp} - I_{zzp})\omega_{zp}\omega_{x_P} \quad (6\text{-}8)$$

Which, too, could be represented using standard Simulink blocks.

6.2.4 IMU Gyro Model

The final component of the Simulink model to be developed was the IMU gyro. The gyro model was needed to measure the inertial rates of rotation of the axes. *Equation 6-4* and *Equation 6-8* above show the inherent dependence of the ISP roll and pitch axes on the IMU gyro for angular velocity measurements. These measurements, in turn, determine the disturbance torques on the control system due to the kinematics of each axis. The gyro modelling process was based on the linearised gyro model in [103]and [104]. Because the BNO055 IMU possesses a MEMS gyro, the vibrating mass within the gyro which governs the output reading can be represented by a second-order dynamic transfer function. Figure 6-5 below shows the linear model of the MEMS gyro, as proposed by the research.

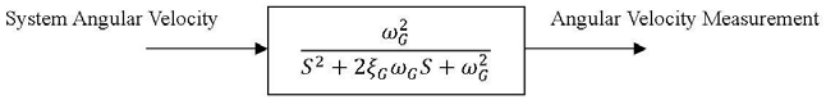

Figure 6-5: Linearised MEMS Gyro Model

Where the gyro sample rate, $\omega_G = 100Hz = 628.32\ rad/s$, and the gyro damping factor, ζ_G, was assigned a value of 0.7. The research published in [103] found that by using the gyro model within a feedback control loop, static errors within the nonlinear model, such as bias and scale factors, were compensated for by the feedback signal. Gaussian noise was also removed within the study, due to it having a mean value of zero, and was found to have negligible effect on the results of the simulation. The resulting recommendation, then, was to place the gyro model within a simple feedback loop between the system output and the reference input.

6.2.5 ISP Simulation Model

The complete ISP Simulink model was constructed by combining the above subsystem models in the manner described by Figure 6-1. The main objective of the Simulink model was to simulate the response of the ISP configuration to varying tuning parameters. The intention behind this was to accurately determine the optimal PID gains which would produce the most robust stabilisation capabilities in the roll and pitch axes. Figure 6-6 below details the complete ISP Simulink model.

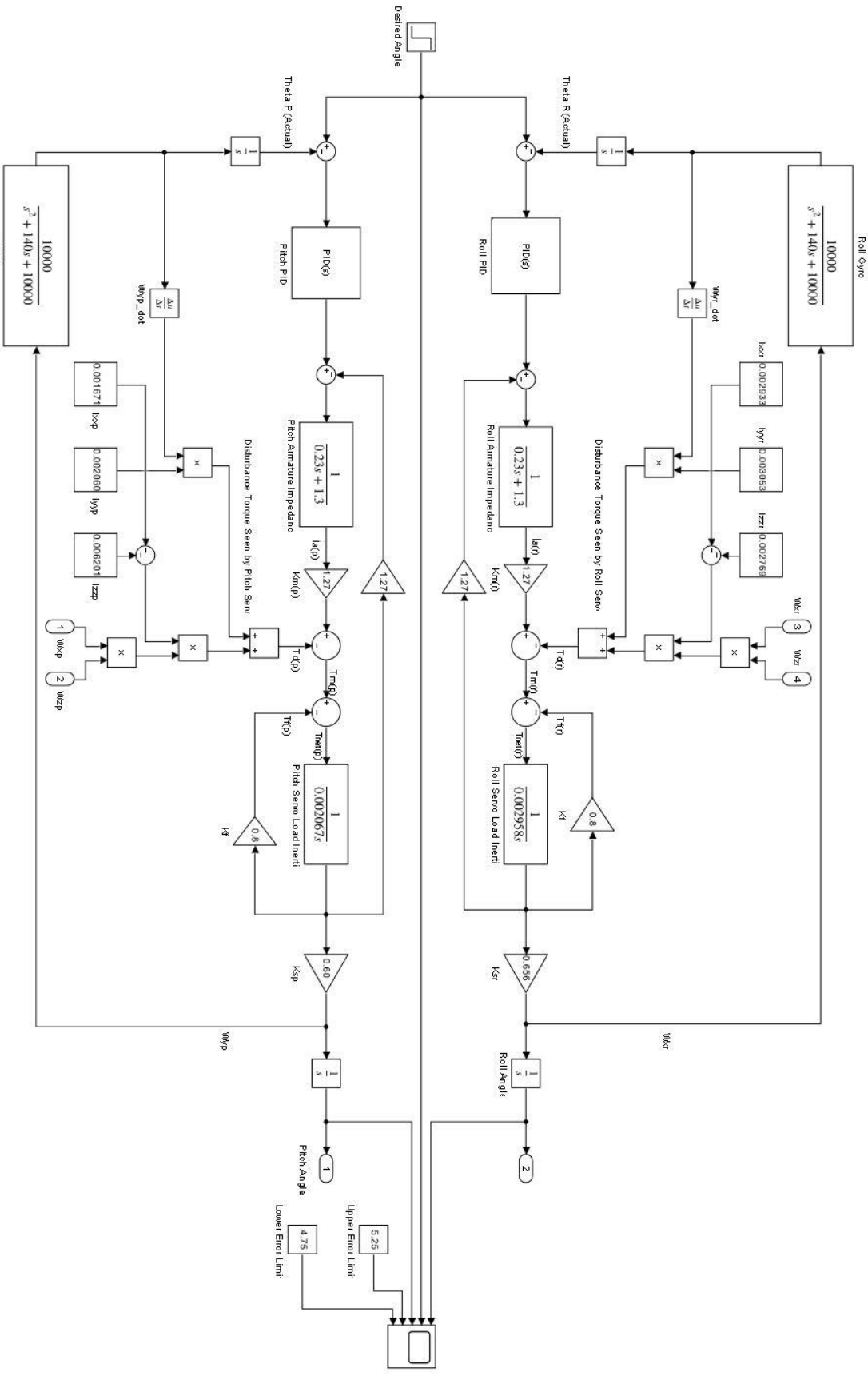

Figure 6-6: ISP Simulink Model

Once the Simulink model had been created, the input tracking characteristics of the system needed to be analysed. To do this, a step input with a magnitude of 5° and a step time of 5s was used. Figure 6-7 below shows the untuned system response to the step input.

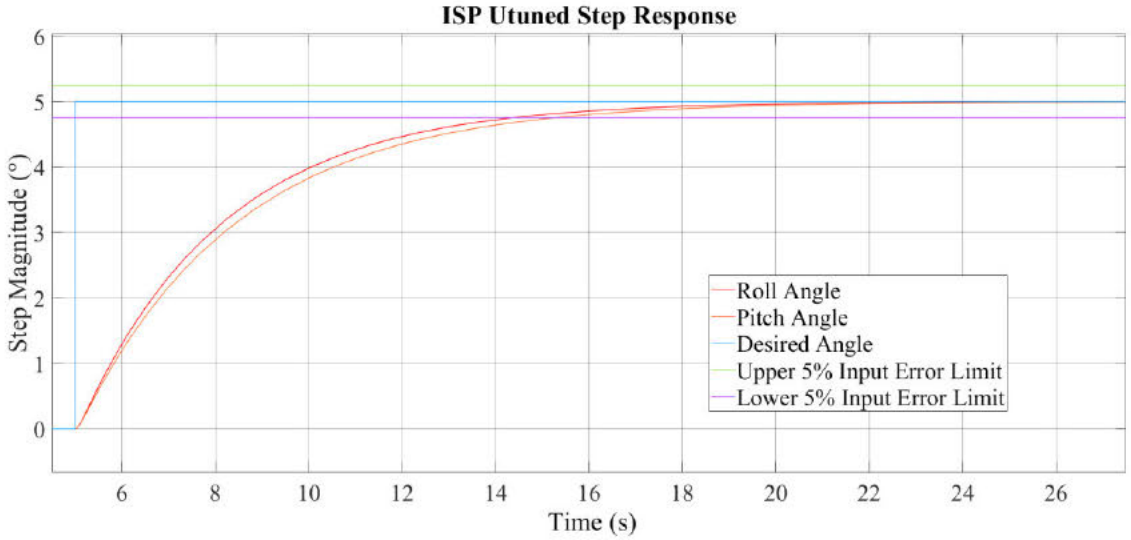

Figure 6-7: ISP Simulink Model Untuned Response

As shown in in Figure 6-7 above, the untuned ISP system was successful in following the input step command, as it converged within the allowed 5% error limit. However, the response time of the system was deemed to be too slow with settling times of 6.877s and 7.751s being observed in the roll and pitch axes, respectively. Here, the settling time was defined as the time at which the response signal entered the allowable error region without exiting the region again. Therefore, the Simulink "PID Autotune" function was used to determine optimal PID gains for the ISP roll and Pitch axes. The gains produced by Simulink were then varied slightly to decrease the response time of the system. Table 6-2 below gives the final PID gains utilised within the simulation model.

Table 6-2: ISP Simulink Model Final PID Gains

Metric	Roll Axis	Pitch Axis
K_P	16.809	19.4609
K_I	0.001513	0.00440197
K_D	2.186	8.850

Figure 6-8 below shows the PID-tuned system response to the step input as described above. The final system response metrics are provided after the figure in Table 6-3.

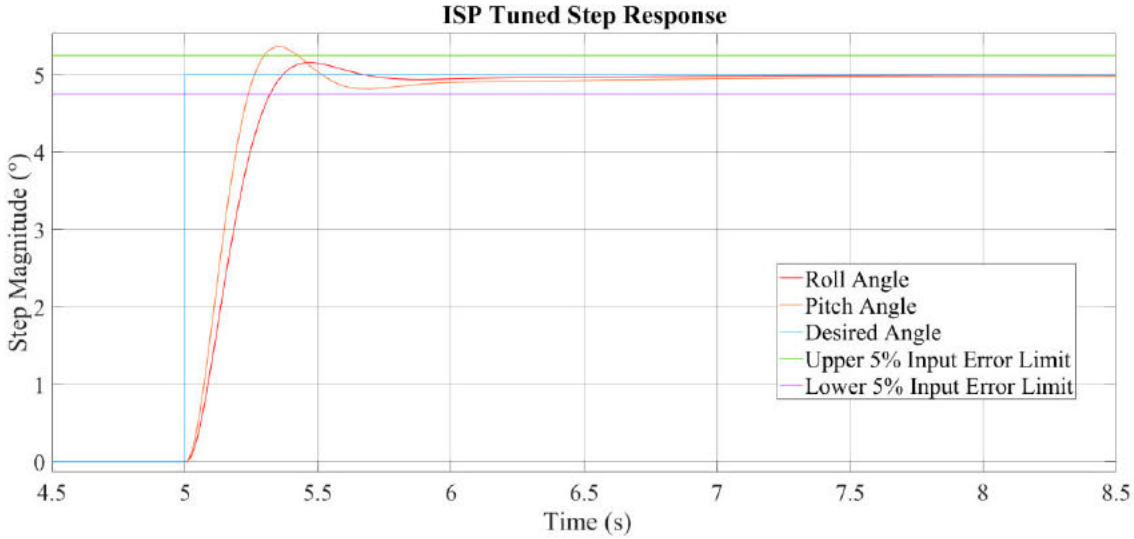

Figure 6-8: ISP Simulink Model Tuned Response

Table 6-3: ISP Simulink Model Tuned System Response Metrics

Metric	Roll Axis	Pitch Axis
Overshoot (%)	3.464	6.989
Rise Time (ms)	226.990	171.181
Settling Time (ms)	320.772	427.942

Comparing the settling time metrics of the tuned and untuned system simulations, the roll axis settling time can be seen to have been reduced by 95.35%, and that of the pitch axis by 94.48%. These substantial settling time improvements alluded to the simulated PID controllers being successful in mitigating system errors, while also being successful in tracking the input signals. It should be noted that these metrics were in response to the unloaded ISP system kinematics only, meaning that they represent the ideal case, with a negligible disturbance torque load being realised.

Having successfully developed an operational Simulink model for the ISP, the next task was to implement the simulated PID gains into the physical system via the ISP program firmware to be stored on the Arduino Nano microcontroller.

6.3 ISP Software and Firmware Implementation

The following subsections describe the development of the ISP program software to be contained by the Arduino Nano microcontroller, referred to as the firmware, or code. The function of the firmware was to bring the simulated ISP system to fruition by integrating the previously determined PID gains into the physical system. As such, the code was tasked with reading and processing raw sensor data from the BNO055 IMU and generating a PID-tuned response signal for the servo motors to counteract platform disturbances detected by the IMU. Figure 6-9 below shows the control algorithm used within the ISP firmware.

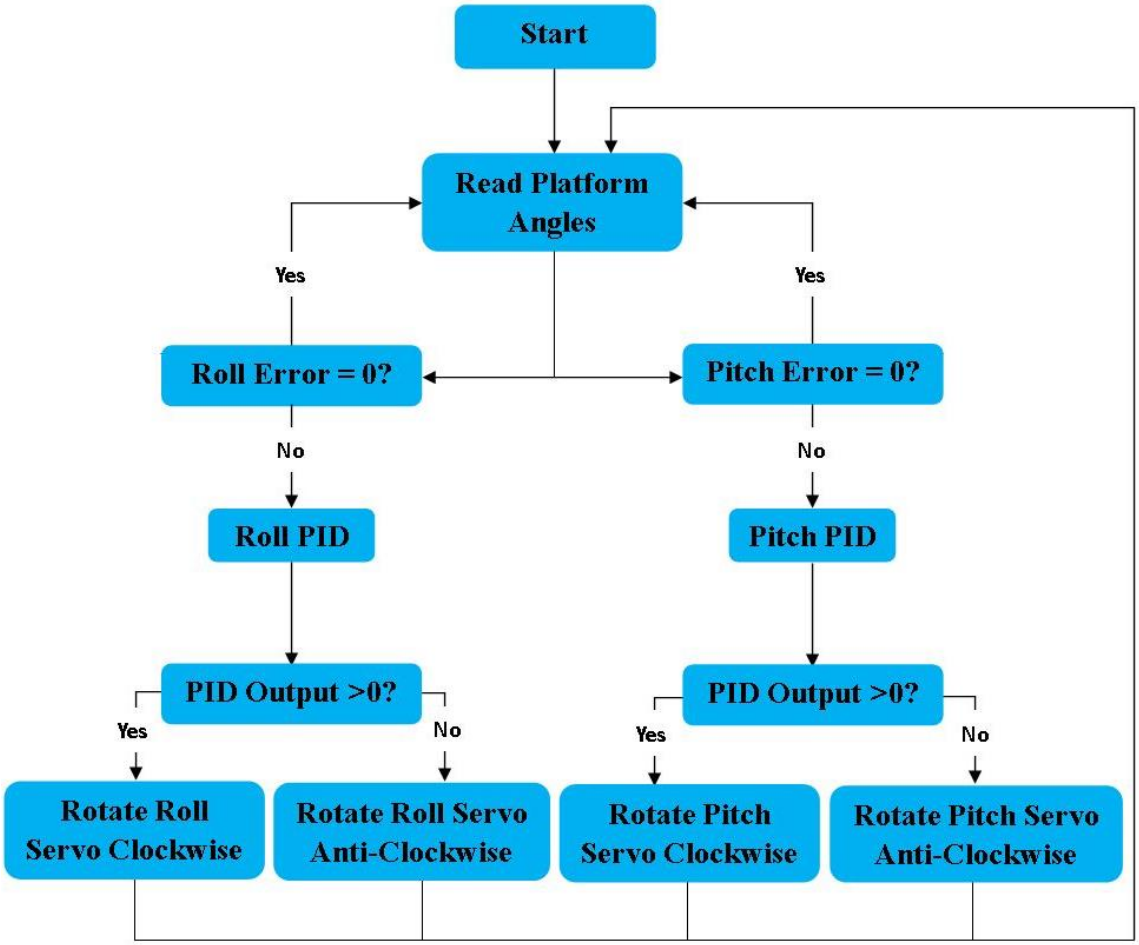

Figure 6-9: ISP Program Code Control Algorithm

The firmware was written using the opensource Arduino Integrated Development Environment (IDE) software, which uses a variant of the C++ programming language [105]. The subsections to follow provide a detailed breakdown of the complete ISP code. When analysing the contents, reference must be made back to the detailed electrical design schematic in Figure 4-11. This figure provides a graphical illustration of the pin allocations which are made within the firmware, for increased reading coherence.

6.3.1 Requisite Libraries

The preliminary step in the development of the firmware was to determine the libraries required by the Arduino IDE software to facilitate the unhindered communication between the ISP components. Figure 6-10 below shows a snippet of the code which contains these libraries.

```
 6   #include <Adafruit_BNO055.h>
 7   #include <Adafruit_Sensor.h>
 8   #include <Servo.h>
 9   #include <Wire.h>
10   #include <Math.h>
11   #include <utility/imumaths.h>
```

Figure 6-10: ISP Code Libraries

As can be seen in the above figure, the code required six libraries in total. These libraries contained the various functions required for the code to control the system data and hardware as necessary. Lines 6 and 7 indicate the libraries which act as drivers for the IMU. Namely, the Adafruit BNO055 (Adafruit_BNO055.h) library and the Adafruit sensor library (Adafruit_Sensor.h). However, these libraries only facilitated the communication with, and retrieval of data from the IMU. Therefore, an additional library (refer to line 11), namely the IMU maths library (imumaths.h) was required. Subsequently the math library (Math.h), seen in line 12, was also required as it contained the necessary mathematical operator's folder. The final libraries required were the servo library (Servo.h) to control the servo motors, and the wire library (Wire.h) to enable device communication over I^2C.

6.3.2 Declarations and Variables

Following the addition of the required libraries, system components were declared, and variables created. The code shown in Figure 6-11 below illustrates the components and variables which were required.

Firstly, analysing the object declarations made, lines 15 and 16 declared two servo objects, named "RollServo" and "PitchServo", within the code to which the roll and pitch servo names are attached for future reference. This command also linked the two servo objects to the abovementioned servo library and gave access to the associated functions within the library. Similarly, line 72 declared the presence of a BNO055 IMU in the system, named "ISP_IMU", and gave the object access to the functions included in the IMU libraries. Prior to declaring the IMU object, however, line 70 declared the speed at which any and all BNO055 IMUs would run within the ISP firmware. Analysis and explanation of the coded variables ensues Figure 6-11.

```
15  Servo RollServo;
16  Servo PitchServo;
17
18  double Q0;
19  double Q1;
20  double Q2;
21  double Q3;
22
23  double RollInput = 0;
24  double RollOutput;
25  double RollError;
26  double RollSignalCommand = 135;
27
28  double RollErrorOverwrite;
29  double DeltaRollError;
30  double GradRollError;
31  double RollErrorArea = 0;
32
33  double PitchInput = 0;            //Angle Setpoint
34  double PitchOutput;               //Angle Reading From IMU
35  double PitchError = 0;            //Setpoint to Input Difference
36  double PitchSignalCommand = 135;  //Initial Servo Orientation
37
38  double PitchErrorOverwrite;
39  double DeltaPitchError;
40  double GradPitchError;
41  double PitchErrorArea = 0;
42
43  //Timer Varibles
44  double PitchStartTime;
45  double PitchEndTime;
46  double PitchDeltaTime;
47
48  double RollStartTime;
49  double RollEndTime;
50  double RollDeltaTime;
51
52  double LoopStartTime;
53  double LoopEndTime;
54  double LoopDeltaTime;
55
56  double SettleErrorPos = 1;
57  double SettleErrorNeg = -1;
58
59  //Roll Axis Tuning Gains
60  double Kp_Roll = 1.6809;
61  double Ki_Roll = 0.000001513;
62  double Kd_Roll = 2.186;
63
64  //Pitch Axis Tuning Gains
65  double Kp_Pitch = 1.94609;
66  double Ki_Pitch = 0.00000440197;
67  double Kd_Pitch = 8.850;
68
69  //Setting IMU Sample Rate
70  #define BNO055_SAMPLERATE_DELAY_MS (100)
71
72  Adafruit_BNO055 ISP_IMU = Adafruit_BNO055();
```

Figure 6-11: ISP Code Variables and Declarations

Lines 18-21 in Figure 6-11 above created a series of variables against which raw Quaternion data from the IMU could be allocated for storage. Section 6.3.5 provides more information on the allocation of the Quaternion components to the variables.

Next, lines 23-25 and 33-35 show the variables created to track the cradle platform orientation in the roll and pitch axes, respectively. In both cases, the "Input" variable referred to the sought-after 0° orientation of the axis. The "Output" variables referred to the actual platform orientation in each axis, as measured by the IMU. The final "Error" variables represented the difference between the input and output variables.

The "roll and pitch "SignalCommand" variables referred to in Lines 26 and 36 were created to aid in setting the platform to the 0° orientation in both axes during the ISP initialisation sequence. Section 6.3.3 elaborates further on the initialisation sequence. The signal command variable was also used within the stabilisation loop of the code to apply the PID tuned servo signals to the servo motors. Refer to section 6.3.5 for more on this.

The variables created in lines 44-46, lines 48-50, and lines52-54 served as the loop timer variables. In all cases, the "StartTime" variables referred to the start time of a single iteration of a roll or pitch stabilisation loop, or the loop timer. "EndTime" variables captured the end time of the loops, and "DeltaTime" referred to the difference between the end time and the start time. After each successive loop iteration, the start time variable was overwritten by the end time variable for the timer to progress with the loop iteration in progress. Section 6.3.5 provides further explanation on this topic.

Lines 56 and 57 show two optional variables which were created to plot the allowed stabilisation error limits in the serial monitor in real time for a graphical analysis of system data.

The remaining variables were created for the purpose of PID tuning the error signals produced by the variables of lines 25 and 35. However, because the PID tuning algorithm was manually coded instead of using an existing PID library, these variables are explained fully in section 6.3. 5. The final variables captured by lines 60-62 and 65-67 can be seen to contain the PID gains determined by the Simulink ISP model presented previously.

6.3.3 System Initialisation

The third step in the development of the ISP firmware was to develop a start-up sequence for the ISP, which would be run when the system was powered on. This portion of the code was contained in the setup, as it was only required to run once after the system received electrical power. The purpose of the start-up sequence was to combine the servo motos with their relevant PWM pins on the microcontroller and to initialise communication protocols between components. This also allowed sufficient time to pass for the IMU to activate fully. The final function of this portion of the code was to set the ISP cradle platform to the absolute zero position in both axes. Figure 6-12 provides a code snippet showing these processes being performed by the code.

```
74  void setup() {
75    Serial.begin(115200);
76    ISP_IMU.begin();
77    delay(1000);
78    Wire.begin();
79    ISP_IMU.setExtCrystalUse(true);
80    RollServo.attach(6);
81    PitchServo.attach(5);
82
83    RollServo.write(RollSignalCommand);
84    delay(20);
85    PitchServo.write(PitchSignalCommand);
86    delay(20);
87
88
89    PitchStartTime = millis();
90    RollStartTime = millis();
91    LoopStartTime = millis();
92  }
```

Figure 6-12: ISP Code Initialisation Sequence

Line 75 of Figure 6-12 above initialised serial data communication within the code. Communication was set to 115200 baud (bits of data transferred per second). Thereafter, line 76 activated the IMU. A 1000ms delay ensued activation to allow completion of the activation process. I^2C communication was initialised in line 78 which facilitated the transfer of orientation data to and from the microcontroller. Thereafter, line 79 set the IMU to make use of its external crystal to increase the accuracy of readings.

The roll and pitch servo motors were affixed to their designated PWM pins of the microcontroller in lines 80 and 81. These connections corresponded to those shown in Figure 4-11. Thereafter, in lines 83 and 85 the servo motor output shafts were instructed to be oriented at 135°, which is in the middle of their 270° total rotation range. The assembly of the servo motor drive horns was such that in the 135° position of each servo motor the platform would be oriented in the 0° position in both the roll and pitch axes. A 20ms delay can be seen to ensue each servo orientation command, which allowed the servos to settle in their instructed positions before the code continued.

To conclude the system initialisation, lines 89 to 91started the roll, pitch, and loop timers.

6.3.4 Orientation Data Conversion

The following segment of the ISP code constituted the void loop to be run continuously while the ISP was switched on. The code configured and calibrated the IMU before retrieving orientation data. The code then organised and converted the orientation data into the format required by the PID tuning segment to follow in section 6.3.5. Figure 6-13 below shows the orientation data conversion code segment.

```
 94  void loop() {
 95    uint8_t system, Gyro, Accel, Mag = 0;
 96    //Calibrating IMU
 97    ISP_IMU.getCalibration(&system, &Gyro, &Accel, &Mag);
 98    // Pulling raw Quaternion data from IMU
 99    imu::Quaternion Quat = ISP_IMU.getQuat();
100
101    //Capturing & Organising Quaternion Data
102    Q0 = Quat.w();
103    Q1 = Quat.x();
104    Q2 = Quat.y();
105    Q3 = Quat.z();
106
107    //Computing Euler Angles from Quaternion Data
108    //Roll Euler Angle (Answer in Radians)
109    RollOutput = atan2(2 * (Q0 * Q1 + Q2 * Q3), 1 - 2 * ((pow(Q1, 2)) + (pow(Q2, 2))));
110    //Converting the Roll Output Euler Angle from Radians to Degrees
111    RollOutput = RollOutput * (180 / PI);
112
113    //Pitch Euler Angle (Answer in Radians)
114    PitchOutput = asin(2 * (Q0 * Q2 - Q1 * Q3));
115    //Converting the Pitch Output Euler from Radians to Degrees
116    PitchOutput = PitchOutput * (180 / PI);
```

Figure 6-13: ISP Code Data Conversions

As shown in Figure 6-13 above, the code first declared "uint8_t" variables in line 95. These variables were of 8-bit unsigned integer form and functioned as the calibration registers for the IMU. Line 97 then calibrated the IMU using the registers created above.

Line 99 then retrieved the cradle platform orientation data in Quaternion format before capturing the data in lines 102-105. TheBNO055 IMU produces Quaternion data in the standard, component-wise, format shown by *Equation 6-9*.

$$q = w + (xi + yj + zk) \tag{6-9}$$

As can be seen in lines 102-105, these components were arranged sequentially and stored in the "Q" variables created in the beginning of the code. Since the Simulink model PID gains were determined in response to a system using angular inputs in terms of degrees, the quaternion readings needed to be converted as such. *Equation 6-10* and *Equation 6-11* below describe the angular conversion equations used within the code, which were adapted from [106] [107] . These equations convert the Quaternions into Euler angles. It should be noted that while Euler angles could have been directly obtained from the IMU, quaternions are known to be more computationally efficient and produce more stable data than Euler angles [108] [109].

$$\theta_R = tan^{-1}\, 2\left(\frac{2(Q_0Q, + Q_2Q_3)}{1-2(Q_1^2+Q_2^2)}\right) \tag{6-10}$$

$$\theta_P = \sin^{-1}(2(Q_0Q_2 - Q_1Q_3) \tag{6-11}$$

These equations do, however, produce angles measured in radians. Therefore, lines 111 and 116 converted the roll and pitch angles unit of measurement to degrees.

6.3.5 P.I.D Tuning

The final requirement of the code to invoke stabilisation into the ISP system was PID tuning. As previously alluded to, the PID tuning algorithm was manually coded rather than utilising an existing Arduino PID library. This was done to further enhance the learning experience of the research project. The PID tuning of the ISP system within the code followed the generic PID controller expression given by *Equation 6-12*.

$$u(t) = K_P e(t) + K_I \int_0^t e(t) + K_D \frac{de}{dt}(t) \qquad (6-12)$$

Where u(t) is the servo control signal, the PID gains, "K_P", "K_I", and "K_D", were previously declared in section 6.3.2, and the error terms "e(t)" were computed in lines 118 and 119 of Figure 6-14 below.

```
118    RollError = RollInput - RollOutput;
119    PitchError = PitchInput - PitchOutput;
120
121    //Pitch PID Timer Setup
122    PitchEndTime = PitchStartTime;
123    PitchStartTime = millis();
124    PitchDeltaTime = PitchStartTime - PitchEndTime;
125
126    PitchErrorOverwrite = PitchError;
127
128    DeltaPitchError = PitchError - PitchErrorOverwrite;
129
130    GradPitchError = DeltaPitchError / PitchDeltaTime;
131
132    PitchErrorArea = PitchErrorArea + PitchError * PitchDeltaTime;
133
134    PitchSignalCommand = PitchSignalCommand - (Kp_Pitch * PitchError + Ki_Pitch * PitchErrorArea + Kd_Pitch * GradPitchError);
135
136    if (abs(PitchOutput) < 30) {
137      PitchServo.write(PitchSignalCommand);
138    }
139
140    //Roll PID Timer Setup
141    RollEndTime = RollStartTime;
142    RollStartTime = millis();
143    RollDeltaTime = RollStartTime - RollEndTime;
144
145    RollErrorOverwrite = RollError;
146
147    DeltaRollError = RollError - RollErrorOverwrite;
148
149    GradRollError = DeltaRollError / RollDeltaTime;
150
151    RollErrorArea = RollErrorArea + RollError * RollDeltaTime;
152
153    RollSignalCommand = RollSignalCommand - (Kp_Roll * RollError + Ki_Roll * RollErrorArea + Kd_Roll * GradRollError);
154
155    if (abs(RollOutput) < 30) {
156      RollServo.write(RollSignalCommand);
157    }
158    //Loop Timer
159    LoopEndTime = LoopStartTime;
160    LoopStartTime = millis();
161    LoopDeltaTime = LoopStartTime - LoopEndTime;
```

Figure 6-14: ISP Code PID Tuning

As can be seen by *Equation 6-12* above, the PID tuning computation was composed of time-dependent error terms, which generated the need for the roll and pitch timers created in the previous code segments. In order to compute the integral and derivative terms of the PID controller, these timers were used in conjunction with the computed error terms. Figure 6-15 below provides a graphical illustration to convey the integral and derivative term approximation method.

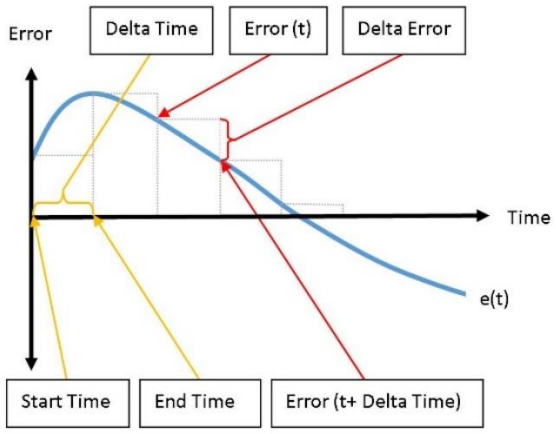

Figure 6-15: ISP Code PID Integral and Derivative Term Approximation

Figure 6-15 above depicts a generic system error signal. Analysing the contents of the figure, the error signal, e(t), is seen to be a time-dependent function of the system error. To approximate the derivative term of the PID controller, firstly, *Equation 6-13* below was derived from the contents of the above figure.

$$Grad\ Error = \frac{de}{dt}(t) = \frac{Delta\ Error(°)}{Delta\ Time\ (ms)} = \frac{Error(t + Delta\ Time) - Error(t)}{End\ Time - Start\ Time}\ (°/ms) \quad (6-13)$$

Referring back to Figure 6-14 now, lines 128 and 147 calculated the "DeltaError" terms of the above equation. The roll and pitch axis timers, and associated variable terms were constructed and cumulated in lines 122-124 and 141-143, respectively. Next, the error signal derivative term approximation, "GradError", was computed by lines 139 and 149.

Looking now at the integral term approximation, the error trace, e(t), was split up into imperceptible rectangular segments with height equal to the error, and a width equal to the timer variable "DeltaTime" of each axis. An exaggerated illustration of these rectangles can be seen in Figure 6-15 above. Using these variables, the area of each rectangle was calculated and cumulated to form the integral term. Lines 132 and 151 show the cumulative area computations of the roll and pitch axes, respectively, which formed the PID controller integral term.

It should be noted that the proportional and integral gain variables were scaled within the code to account for the difference in timing units between the Simulink simulation and the code. Because the code timers operated in units of milliseconds, the integral term gain was reduced by a factor of 10^{-3} to convert the integral (area) term to a unit of measurement of $°/s$, which was the same as that used within the Simulink model. In practice, reducing the integral terms resulted in increased system oscillations, which required the proportional gains to be reduced by a factor of 10 to account for the oscillations.

Eventually, the PID tuned servo control signals were developed in lines 134 and 153 of the code in Figure 6-14, by combining the above error terms and the relevant PID gain variables. The PID tuning process was

completed by lines 136-137 and 155-156, which applied the adjusted servo control signals to the respective servo motor by overwriting the previous loop iteration signal.

Finally, the code segment was concluded by processing the loop timer data in lines 159-161 to create a cumulative stabilisation loop timeline.

6.3.6 Data Outputs

The following code segment was not required for the ISP to function, but rather wrote the ISP cradle platform orientation data to the Arduino serial monitor and plotter for analysis of numerical data, and visualisation thereof, respectively. Figure 6-16 shows the final ISP code snippet which gives the commands necessary to write the ISP cradle platform orientation data to the serial monitor and plotter.

```
164     Serial.print("Roll Input");
165     Serial.print(",");
166     Serial.print(RollInput);
167     Serial.print(",");
168     Serial.print("Roll Error");
169     Serial.print(",");
170     Serial.print(RollError);
171     Serial.print(",");
172     Serial.print("Pitch Input");
173     Serial.print(",");
174     Serial.print(PitchInput);
175     Serial.print(",");
176     Serial.print("Pitch Error");
177     Serial.print(",");
178     Serial.print(PitchError);
179     Serial.print(",");
180     Serial.print("LoopTime");
181     Serial.print(",");
182     Serial.print(LoopDeltaTime);
183     Serial.print(",");
184     Serial.print(SettleErrorPos);
185     Serial.print(",");
186     Serial.print(SettleErrorNeg);
187     Serial.println(system);
```

Figure 6-16: ISP Code Serial Data Outputs

6.4 Chapter Summary

Chapter 6 discussed the development and implementation of the ISP control system using the MATLAB Simulink and Arduino IDE software packages. A virtual Simulink model of the ISP system was created using the mathematical modelling results of Chapter 2.9, and the ISP SolidWorks model. Additional first-principal transfer function equations were included to represent the servo motors and the IMU in the model. Following the PID tuning of the individual roll and pitch axes, settling time reductions of 95.35% in the roll axis and 94.48% in the pitch axis were realised in comparison to the untuned ISP model.

The virtual simulation model was then incorporated into the physical system through the ISP firmware which was developed in the Arduino IDE software. The firmware integrated the scaled PID gains computed in the Simulink environment into the physical system to facilitate real-time PID tuning of the ISP, with a stabilisation loop time of 105ms being realised, corresponding to a frequency of 9.524Hz. Refer to Appendix C to view the complete, compiled, ISP firmware. Chapter 7, which follows, evaluates the effectiveness of the developed control system through ISP performance testing.

7 SYSTEM PERFORMANCE VERIFICATION

7.1 Introduction

The previous three chapters outlined the design, optimisation, and development of a two-axis, roll-pitch ISP for disaster management and humanitarian aid purposes. The following chapter details the experimental performance verification of the complete ISP prototype. Quantitative data was recorded to verify the accuracy of the simulated ISP model when compared to the true model.

The first step in the verification process was the determination of baseline stabilisation characteristics of the ISP in the individual axes. These results allowed the author to determine the system response capabilities and stabilisation times. An operational performance evaluation of the ISP was then conducted and reported upon.

7.2 Baseline Stabilisation Response Evaluation

In order to produce measurable data against which the final operational characteristics could be compared, the baseline responses of the ISP roll and pitch axes were required. Subsection 7.2 provides the experimental procedure followed to produce the baseline characteristics of the ISP.

7.2.1 Aim

To determine stabilisation responses to disturbances of varying magnitudes in both the roll and the pitch axis of the ISP, individually.

7.2.2 Objectives

- To derive a relationship between the magnitude of the imposed disturbance and the settling time of the ISP, for each axis, in the unloaded condition.
- To compare the ISP baseline stabilisation response characteristics to simulated results.

7.2.3 Variables

- Disturbance Magnitude (Independent Variable)
- Settling Time (Dependent Variable)

7.2.4 Apparatus

- ISP prototype
- Micro SD Card Data Logging Module

7.2.5 Methodology

The baseline characteristics of the ISP are crucial metrics which are required to justify previous design decisions and specifications. The baseline responses of the ISP axes were evaluated by setting the system up such that motion in only a single plane would be imposed on the system. Thereafter, within the software code, the final servo positioning command following the PID tuning algorithm was commented out. This was done by commenting out the *PitchServo.Write* command (refer to Figure 6-14, line 137) when testing the roll axis, and vice versa. By switching off one axis, the remaining axis could be tested individually, as required. Once the above processes had been completed, the ISP was switched on and given short, rapid pulses of rotation and allowed to settle. Simultaneously, the readings from the ISP IMU were logged on an external Secure Digital (SD) card (see subsection 8.6.2 for more information on how data logging was implemented).

The data logging apparatus recorded (for each separate axis' DOF) the desired setpoint, the platform orientation, and the timestamp during testing and recorded the data to a text (.txt) file. The recorded data was then opened with Microsoft Excel, analysed, and graphed to produce graphical representations of the baseline response during testing. Figure 7-1 below shows an example of a graphical representation of the baseline response of the ISP pitch axis.

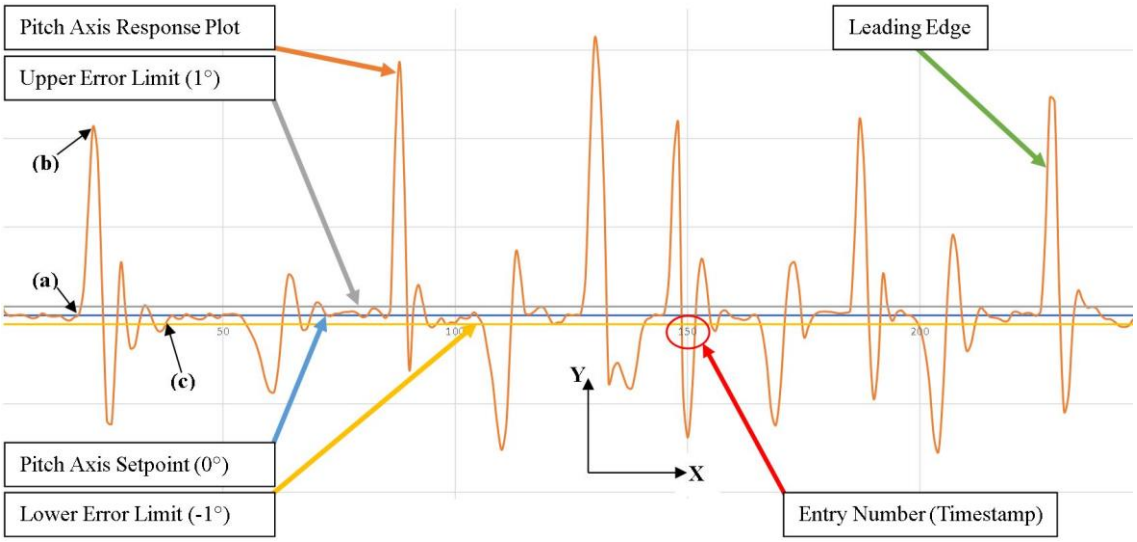

Figure 7-1: Pitch Axis Baseline Response Graphical Representation Example

Figure 7-1 above illustrates the baseline response characteristic graph visually and indicates the features of importance which were used when analysing the recorded data. With reference to Chapter 3, it was noted that the desired stabilisation error of the ISP was 1° or less. This specification was integrated into the evaluation and analysis process (as can be seen above) as an error limit of magnitude 1° from the desired setpoint. As such, the desired settlement error was utilised when analysing testing data as a settling time reference, which ensured that this specification was met by the design. In accordance with control theory, the settling time of the ISP axis was defined as the point at which the axis response (the pitch axis response

plot in the case of Figure 7-1) entered the settlement region for the final time during the axis settlement response. This point is indicated by (c) in Figure 7-1. Similarly, (a) and (b) define the point of initial disturbance, and the point of maximum disturbance, respectively. The point of initial disturbance was defined as the point at which the axis response plot crossed the setpoint line for the final time at the base of the leading edge. The point of maximum disturbance was defined as the point along the leading edge with the largest magnitude of error relative to the setpoint. In a similar fashion, the leading edge of the response plot was defined as the approximately linear region of the response plot which ensued the point of initial disturbance.

To approximate the baseline characteristic on the basis of the magnitude of the imposed disturbance versus the settling time, as outlined by the objectives above, the previously mentioned indicators were drawn upon. With reference to Figure 7-1, the indicators (a), (b), and (c) have respective (logged) coordinates of (1.195;0.15), (2.281;21.360), and (4.156; -1). Using these known coordinates, the disturbance magnitude, $|T_D|$, was approximated according to *Equation 7-1* as follows:

$$|T_D| = \left|\frac{\text{Change in Magnitude}}{\text{Change in Time}}\right| = \left|\frac{b_y - a_y}{b_x - a_x}\right| = \left|\frac{21.36 - 0.15}{2.281 - 1.195}\right| = 19.53\ °/s \quad (7\text{-}1)$$

The second metric of interest, the settling time of the disturbance, T_S, was calculated as per *Equation 7-2* below. This constituted the time taken to settle within the allowed error region.

$$T_S = c_x - a_x = 4.156 - 1.195 = 2.96s \quad (7\text{-}2)$$

Equations 7-1 and 7-2 above serve merely as sample calculations to illustrate the conversion process between the data logged during testing and the baseline values generated during testing, with the roll and the pitch axis being evaluated in an identical manner. Recalling, from Chapter 2, that the DM300 has a maximum angular velocity of 300°/s, the testing process aspired to achieve various baseline response characteristics ranging 0°/s to 300°/s, such that the aim and objective of the experiment were achieved.

7.2.6 Results and Analysis

The graphs following in Figures 7-2 and 7-3 below provide the results of the baseline response characteristics testing procedure. The figures were generated using data produced over a minimum of six tests of equal duration to that in Figure 7-1, in each axis to ensure that repeatable results were being obtained. Additionally, the pulses eligible for analysis during these tests were constrained to those which showed a settled response for a minimum of two seconds prior to the point of initial disturbance. This constraint was implemented to ensure error-free, repeatable results were being drawn. Such a pulse was used in Figure 7-1, to introduce the coordinate indicators. The graphs also show baseline response characteristics obtained through simulation using the ISP Simulink model.

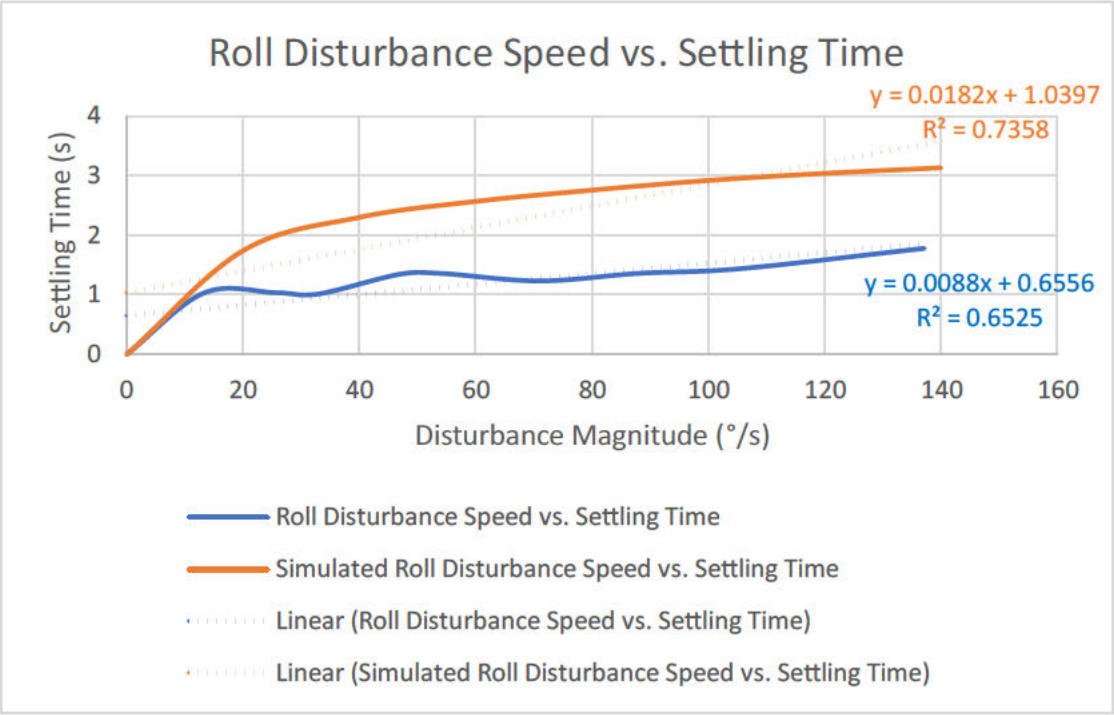

Figure 7-2: Roll Axis Baseline Response Characteristics

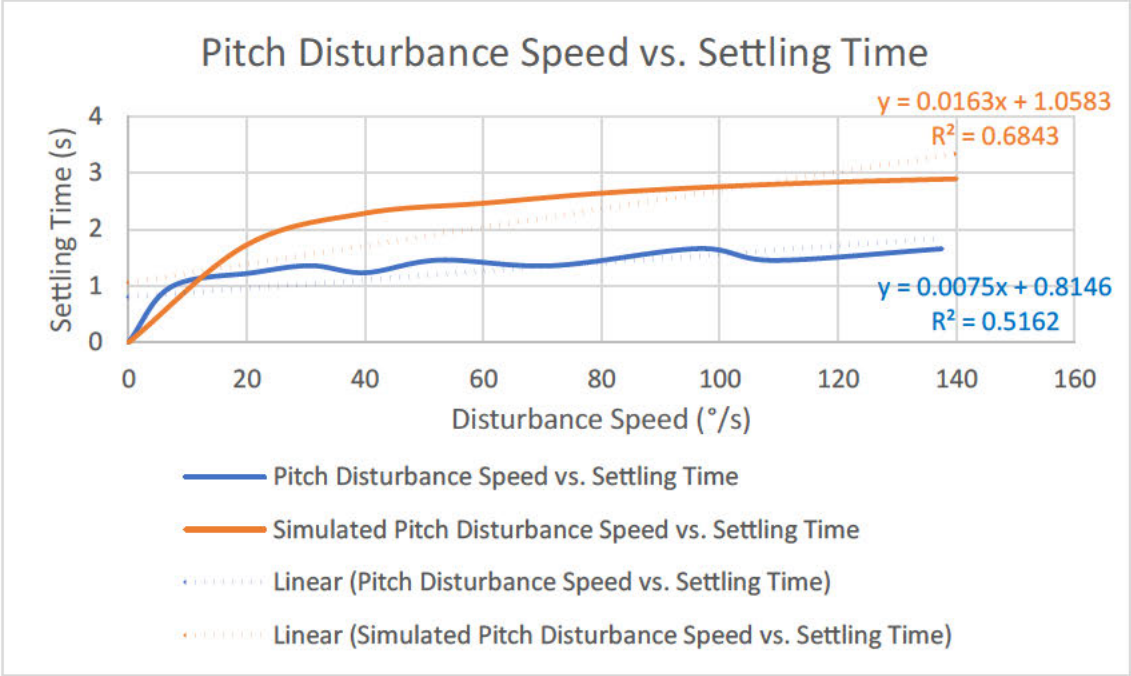

Figure 7-3 Pitch Axis Baseline Response Characteristics

As can be seen by Figures 7-2 and 7-3 above, the dynamic stabilisation responses of the ISP axes were determined for a range of varying disturbance torques, thus satisfying the aim of the experiment. Upon plotting the generated data from the experiment, a positive correlation between the disturbance magnitude and the settling time became evident. By plotting the simulated baseline stabilisation data obtained in Chapter 6, comparisons could be made between the testing results and the simulated results.

From Figure 7-2 and Figure 7-3 above, it is evident that, in both cases, the maximum disturbance magnitude obtained through experimentation was ≈137°/s. Albeit contradictory to the initial hypothesis prior to testing, this was a well-received observation which alluded to the fact that the system response time did not allow for a greater magnitude disturbance to be obtained. At the maximum obtained disturbance magnitude, however, the roll axis settled in 1.78 seconds and the pitch axis in 1.66 seconds. The corresponding disturbances were 137.08 °/s and 137.64 °/s respectively. These figures represented the unloaded, best-case-scenario ISP settling times in response to the maximum obtainable disturbances.

Referring to Figure 7-2 above, it was noted that the experimental stabilization capabilities of the roll axis displayed a positive correlation between the disturbance magnitude and the settling time of the axis. Whilst this outcome was expected, the data displayed fluctuations between consecutive data points, which resulted in an undulating baseline. This contradicted the expected linear baseline. Nevertheless, a linear trendline was plotted on the graph, which considered statistical variations between data points. A trendline equation with a slope of $0.0088s^2/°$ was realised. The obtained slope magnitude indicated that the disturbance speed was increasing at a rate significantly greater than that of the settling time. This showed that the axis was stable against the varied disturbance magnitudes.

The experimental pitch axis stabilisation capabilities shown in Figure 7-3 produced a baseline graph with similar characteristics to that of the roll axis. A positive correlation between the disturbance magnitude and the settling time of the axis was noted to confirm the expected correlation. However, the baseline of the pitch axis can be seen to feature larger fluctuations between consecutive data points than the roll axis. In a similar manner to the roll axis experimental baselines, a linear trendline was plotted on the pitch axis graph, producing a slope of $0.0075s^2/°$. As was the case with the roll axis, the magnitude of the obtained trendline slope was indicative of the pitch axis stability in response to the disturbance magnitudes imposed during testing.

Comparatively, the roll axis baseline response trendline showed the settling time to increase at a rate which was 14.77% faster than that of the pitch axis, indicating the potential for disturbances with a larger magnitude to induces a greater level of instability in the roll axis. Conversely, this observation also indicated a superior stability of the pitch axis to large-magnitude disturbances. While, ideally, both axes should show equivalent stabilisation capabilities and sensitivities, superior stability of the pitch axis was the preferred outcome due to this axis being subjected to greater torques and bending stresses due to its geometric layout.

The above-mentioned conclusions were drawn from the linear trendlines plotted on the graphs in Figures 7-2 and 7-3 above. However, the roll and pitch axis baseline graphs show a R-Squared (R^2) regression coefficient of 0.6525 and 0.5162, respectively. These indicators imply that the plotted trendlines agree with the produced baselines with 65.25% accuracy for the roll axis, and 51.62% accuracy for the pitch axis.

When comparing the obtained experimental data to the simulation data in the above figures, large discrepancies were observed. Numerically, in the roll axis, the simulated data at the experimentally determined maximum disturbance magnitude of 137.08°/s, the interpolated settling time was found to be 3.123 seconds. The percentage error between the settling times of the experimental and simulated values at this point was then determined to be 43%. Statistical analysis of the simulated roll values produced a trendline, as shown above, with a slope of $0.0182s^2/°$and a reliability of 73.58%. The slope value showed a 51.65% increase compared to the experimental values, indicating a more rapid increase in settling time of the axis.

Repeating the above analysis for the pitch axis data, at the maximum experimentally obtained disturbance magnitude of 137.64°/s, an interpolated, simulated, settling time of 2.866 seconds was observed. In comparison to the experimentally obtained settling time of 1.66 seconds, the simulated value exceeded the experimental by 42.5%. As was noted with the roll axis, the simulated pitch axis trendline slope showed a 54% greater rate than that of the experimental trendline. The observed trendline slope of the simulated pitch axis was found to be $0.0163s^2/°$, with a 68.43% reliability of the trendline.

The above comparisons between the experimentally obtained data and simulated data identified an error of approximately 43%, in the simulated values of the ISP. However, because the physical ISP system was settling at a rate which was 43% faster than the anticipated, simulated system, the accuracy of the simulation model was considered to be acceptable.

Upon consideration of the above findings and test data, the baseline testing procedure was considered to be successful, with the generated results agreeing with the hypothesis that that the settling time would increase with increasing disturbance magnitudes. Statistical analysis of the presented data identified an area for potential improvement in the performance of the ISP axes. The recommended method of improvement would be to generate a larger database of baseline datapoints, such that the interval between plotted points is reduced. This recommendation is anticipated to produce a linear trendline with a higher R^2 value which would better represent the data for predictions to be made, and conclusions to be drawn with increased accuracy. However, since R^2 values greater than 0.5 are still considered statistically significant, the experimental data was still described adequately by the trendlines, thus verifying the system performance which incorporated the Simulink model.

7.3 Chapter Summary

Chapter 7 discussed the experimental performance verification of the ISP following the control system implementation. The ISP was used to develop baseline stabilisation response data for each axis. The developed data was compared against simulated response data from the ISP Simulink model to equivalent disturbance magnitudes. The baseline stabilisation response analyses of the ISP axes showed a positive correlation between the disturbance magnitude and the settling time of each axis, as hypothesized. The roll axis was determined to be more prone to instability, with a trendline slope 14.77% greater than that of the pitch axis. The baseline experimental data comparison to the simulated baseline data showed a 43% discrepancy. However, the validity of the ISP Simulink model was confirmed due to the physical system performance surpassing that of the simulation model, the performance of which was previously deemed acceptable in Chapter 6.

8 OPERATIONAL PERFORMANCE EVALUATION OF THE ISP

8.1 Introduction

Ultimately, the final testing of the ISP was necessary to evaluate the usefulness of the system for disaster management and humanitarian aid purposes, as described throughout this research project. However, intrinsic to the final evaluation, it was necessary to evaluate the extent to which the final ISP met the required operational specifications as stated in Chapter 3. The following subsection describes the experimental procedure adhered to during the final testing phase of the ISP.

8.2 Aim

To determine stabilisation capabilities of the ISP in response to UAV kinematics under operational conditions.

8.3 Objectives

- To determine the effect (if any) of noise transferral from the UAV to the ISP
- To determine the final stabilisation capabilities of the system
- To identify sources of error within the system
- To analyse the performance and identify possible areas of improvement.

8.4 Variables

- UAV Orientation (Independent Variable)
- Disturbance Magnitude (Independent Variable)
- Payload Mass (Independent Variable)
- Settling Time (Dependent Variable)

8.5 Apparatus

- DM300 UAV
- ISP prototype
- Micro SD Card Data Logging Module
- 1x Additional BNO055 IMU
- 1x 8GB SD Card

8.6 Experimental Setup

Subsection 8.6 describes the hardware and software integration and the experimental procedure which were utilised during the final performance evaluation of the ISP. The hardware and software integration elaborates on the ancillary modules required for testing and the integration thereof. The experimental procedure details the events of the testing process which were adhered to produce the data required to analyse the performance of the ISP with respect to the variables of interest.

8.6.1 Hardware Integration

The final operational performance of the ISP was evaluated through flight tests on the DM300 to assess the capabilities of the system within the operating realm described by the research project. As alluded to by the aim and objectives of the current experimental investigation, the orientation of both the ISP and the UAV were needed to be able to determine the ISP response to the UAVs kinematics in real time. To meet this requirement, a second BNO055 IMU was needed. The second IMU was attached to the UAV through a bracket produced by FDM. The bracket can be seen in Appendix D, drawing T1. The IMU shared the bracket with a micro-SD card module which facilitated flight data logging during testing. For additional information on the selected micro-SD module, see [110]. The assembly of these additional modules onto the UAV is shown by Figure 8-1 below. The sensor mounting bracket attached to the UAV through four M3 machine thread screws. As can be seen in the figure, the IMU mounts on the underside of the bracket. In order to produce positive orientation angles when the UAV rotated in the global positive x, y, and z-axes, it was imperative that the IMU be accurately aligned with global coordinates.

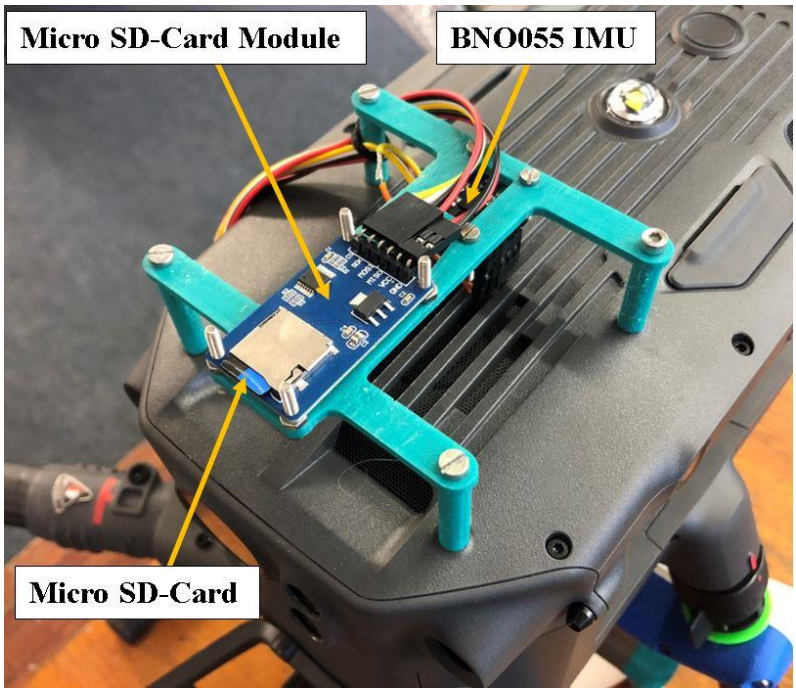

Figure 8-1: Testing Modules Mounted on UAV

To integrate the additional modules into the ISP prototype, the electrical design schematic in Chapter 4 was modified to suit the requirements of the modules. The micro-SD card module interfaces with the microcontroller via the SPI communication protocol. This protocol requires the module to be connected using four wires (excluding the power and ground wires). These wires are for the Master Output/Slave Input (MOSI), Master Input/Slave Output (MISO), Serial Clock (SCLK), and the Chip Select (CS) pins. The connection of these pins to the microcontroller was done as per the detailed testing electrical schematic portrayed in Figure 8-2 below, to the corresponding pin on the Arduino Nano with the exception of the CS

pin. The CS pin was connected to pin D10 of the microcontroller, and the code modified to reflect the connection location.

Adding a second IMU to the system proved to be a challenge as the BNO055 has a standard I^2C communication address of 0x28. Moreover, under the I^2C communication protocol, a microcontroller is unable to communicate with more than one component with the same address on the same I^2C bus. This challenge was overcome by changing the address of the second BNO055 to 0x29. Acting in accordance with the IMUs datasheet in [79], the address was changed by setting the Address (ADR) pin to low by connecting it to the 3.3V pin. These changes can be seen reflected in Figure 8-2 below.

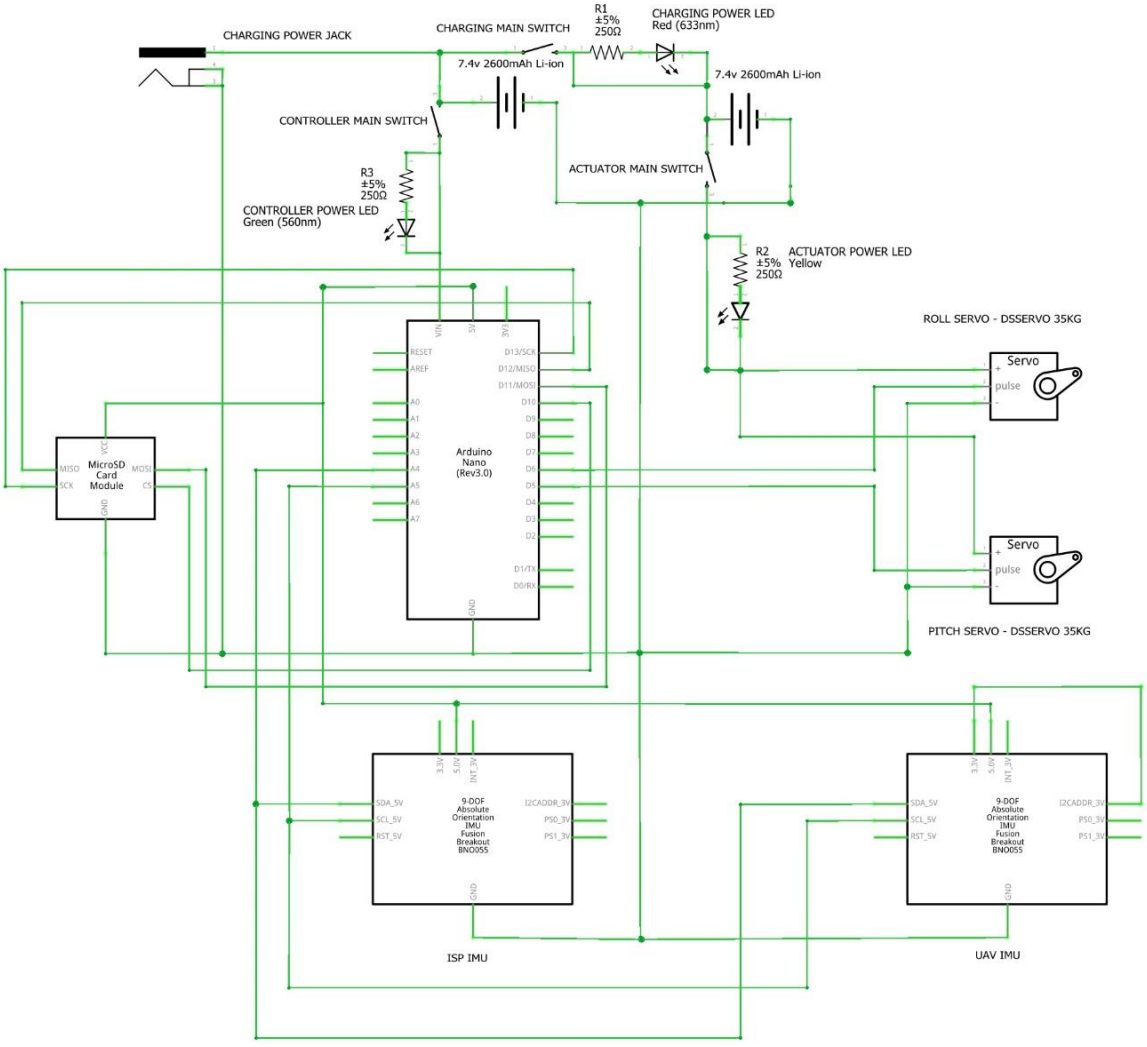

Figure 8-2:Detailed Electrical Schematic for Testing

8.6.2 Firmware Alteration

In a similar manner to the modified detailed electrical schematic shown above reflecting the hardware changes for testing, modification of the firmware presented in Chapter 6 was required to reflect the hardware changes and ensure functionality of the system. The complete, modified, code can be found in Appendix C. Due to the requirements of the ISP performance evaluation testing, the code was modified to determine and record the following measurements in real time:

- The ISP Setpoint
- The ISP Roll Orientation
- The ISP Pitch Orientation
- The UAV Roll Orientation
- The UAV Pitch Orientation
- A Loop Time Indicator

The above-mentioned data was required to be able to plot the detailed, real-time testing data to produce visual representations of the test flights. The loop time indicator was incorporated into the experimental design to be able to identify the point in time at which each set of measurements was produced. The loop timer was then accumulated to produce the timestamp of the test.

The orientation measurements of both the ISP axes and the UAV were provided by the second BNO055 IMU in the system. The software integration of the second IMU was a simple process and followed the same processes and code described in Chapter 6. The only additional requirement to be met was the incorporation of the new I^2C address of the second IMU into the code. This can be seen in line 88 of the code snippet in Figure 8-3 below.

```
82   const int ChipSelectPin=10;
83   File TestDataFile;
84   //Setting IMU Sample Rate
85   #define BNO055_SAMPLERATE_DELAY_MS (100)
86
87   Adafruit_BNO055 ISP_IMU = Adafruit_BNO055();
88   Adafruit_BNO055 UAV_IMU = Adafruit_BNO055(55, 0x29);
89   void setup()
90   {
91
92    Serial.begin(115200);
93    ISP_IMU.begin();
94    delay(1000);
95    UAV_IMU.begin();
96    delay(1000);
97    Wire.begin();
98   //Initialise SPI Communication
99    SPI.begin();
100   SD.begin(ChipSelectPin);
```

Figure 8-3: Performance Analysis Testing Code Pre-Processing

The code snippet depicted in Figure 8-3 above also shows the software integration of the micro-SD card module. The module was responsible for writing the previously mentioned measurements onto a removeable SD card in text (.txt) format. Integration of the module required the CS pin location to be specified. As previously stated, the location of the CS pin was pin D10 of the microcontroller. Line 82 of the above figure shows the specification of the CS pin location within the code. Following this, a file was declared named "TESTDATAFILE" (see line 83 of Figure 8-3), to create a data file to which the SD card could write. Lines 99 and 100 then initialised SPI communication with the micro-SD card module and instruct data transfer to the SD card to be made only via the CS pin connection.

Whilst the data generation and processes of the testing code was equivalent to that of the ISP code detailed in Chapter 6, the conclusion of the testing code differed slightly. Figure 8-4 below shows the conclusion of the testing code (which is within of the infinity looping component of the code). As can be seen in the figure, the first order of operation was to open the SD card to allow for data to be transferred, as well as to specify the file name and format for the resulting data to be saved under. This command can be seen in line 217 in Figure 8-4.

```
216   //Writing Raw IMU Data to SD
217    TestDataFile=SD.open("TestData.txt", FILE_WRITE);
218
219   if(TestDataFile)
220     {
221   // Writing Outputs to SD Card
222
223   TestDataFile.print(RollInput);
224   TestDataFile.print(",");
225   TestDataFile.print(RollError);
226   TestDataFile.print(",");
227   TestDataFile.print(PitchError);
228   TestDataFile.print(",");
229   TestDataFile.print(TestRollOutput);
230   TestDataFile.print(",");
231   TestDataFile.print(TestPitchOutput);
232   TestDataFile.print(",");
233   TestDataFile.print(LoopDeltaTime);
234   TestDataFile.println();
235   TestDataFile.close();
236     }
```

Figure 8-4:Performance Analysis Testing Code Conclusion

Conclusively, lines 223-234 were used to write the required measurements (as specified above) to the SD card, in column format. Line 235 then closed the SD card to prevent further data transfer for that specific loop iteration. The complete testing code can be found in Appendix C.

8.7 Experimental Procedure

Following the experimental setup and pre-processing discussed in the previous subheadings, the final experimental proceedings commenced. The ISP and testing sensors were assembled onto the DM300 UAV as shown in Figure 8-5 and Figure 8-6 below.

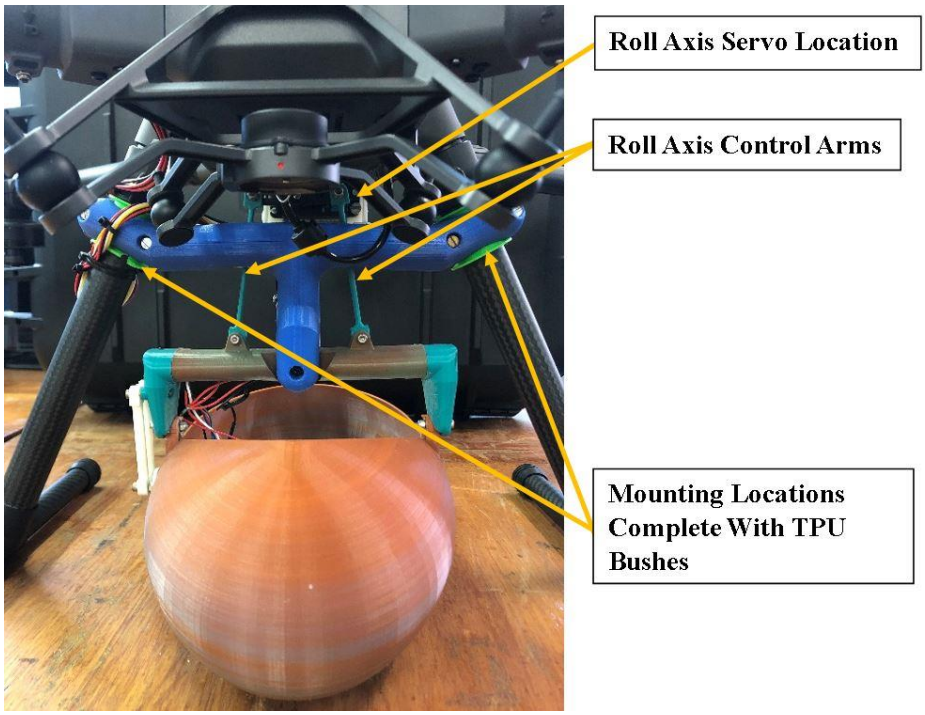

Figure 8-6: ISP Mounted on DM300 UAV Front View

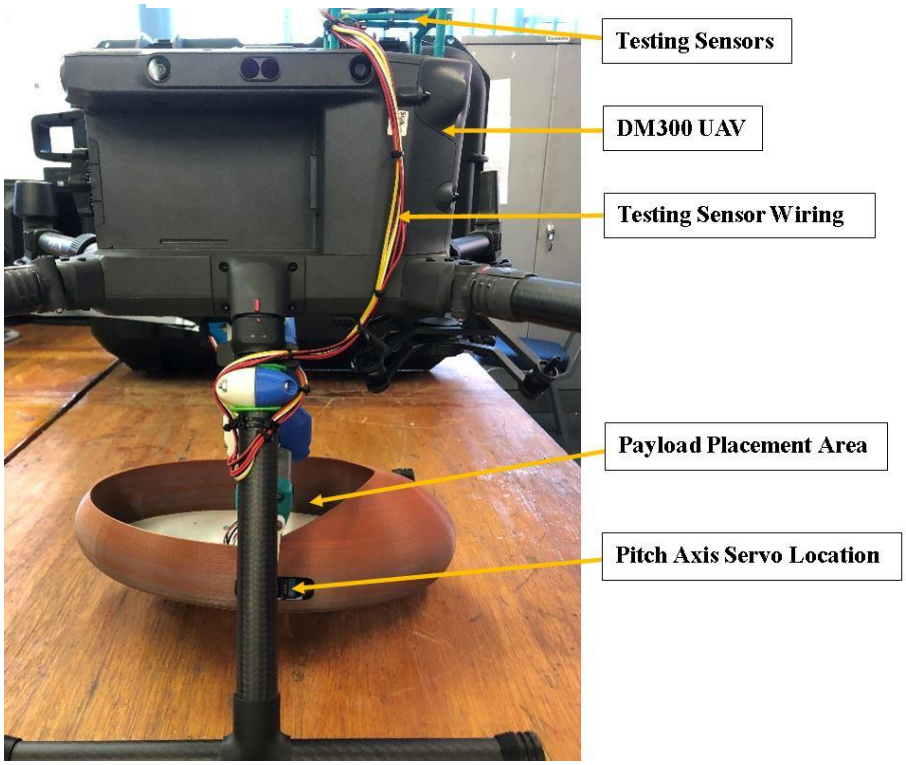

Figure 8-5: ISP and Testing Sensors Mounted on DM300 UAV Side View

Once the ISP and sensors had been mounted on the UAV, the DM300 was placed on a flat, level surface. A micro-SD card was then secured in the micro-SD card module. The ISP was switched on and sufficient time allowed for calibration of the IMUs to be achieved. Thereafter, the system data was logged for approximately 25 seconds. The reasoning behind the test was to confirm that the system was functioning completely, as well as to test the mounting compliance of the testing sensors. The logged data was analysed to produce the graph shown by Figure 8-7 below. It should be noted that, for better viewing quality, the graph only shows 5.25 seconds worth of data. Nevertheless, the IMUs can be seen to have calibrated successfully, and the ISP axes to have settled well within the 5.25 seconds.

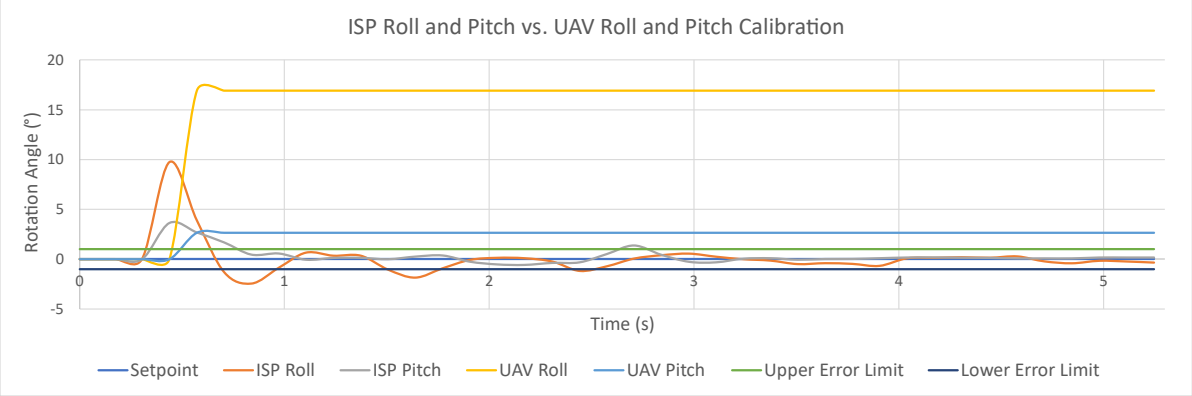

Figure 8-7: ISP and UAV IMU Calibration and Mounting Compliance Data

From Figure 8-7 above, a discrepancy in the mounting of the UAV testing IMU was noted. Analysing the data in the graph, the magnitude of the roll and pitch axis orientation offsets were found to be 16.9° and 2.69°, respectively. These identified offset values were to be deducted from the relevant UAV IMU readings moving forward.

Before any flights could take place using the DM300, a flight demonstration and flight tests were conducted, overseen by a qualified pilot holding a valid MR-RPL, to ensure the relevant legislature pertaining to the flight of the UAV for the operation was met. It was noted at this stage that, at full tilt, the UAV did not roll or pitch to an angle of 30° as expected in accordance with the data sheet in [8]. Further to this, it was challenging to achieve any tilt angle other than the maximum and minimum tilt angles in both roll and pitch directions. Therefore, preventing the logging of stabilisation data at any rotational velocity points other than the upper and lower limits. The final observation generated from the flight demonstration was that returning the UAV to a level (hovering) position following a pitching or rolling sequence caused a rapid, counteracting rotation (opposite to the direction of travel) to maintain maximum horizontal position accuracy. This function could not be turned off or overridden, as it is a pre-programmed function of the UAV.

An initial unloaded and unlogged flight test was conducted with the UAV hovering approximately 600 mm above the ground to test that the UAV was functioning properly with the newly added payload. It was noted that one of the UAVs downward-facing obstacle avoidance sensors had been triggered by the ISP, and the

obstacle avoidance system attempted to cease the UAV from landing. This issue did not affect any of the other features of the UAV and movement in all other directions was unaffected (roll, pitch, yaw, and vertical). The issue was overcome by holding the vertical flight direction joystick down for a period of 5 seconds. This allowed the obstacle avoidance system (in the downward direction) to be overridden and for the UAV to be landed manually and visually by the pilot.

The unloaded, logged, flight test was then conducted. The planned duration of flight tests was 1 minute due to the number of data points being logged for each second. However, the unloaded flight test lasted ~162 seconds. The majority of the extra flight time was allocated to hovering to generate data which could be used for a noise transferral analysis. The generated hovering data was omitted from the kinematic analysis and graphing of the unloaded flight test.

The final ISP performance evaluation flight test was then conducted. The ISP was loaded with the maximum allowable payload of 1.9kg, as determined by Chapter 5. The payload consisted of a plastic bag loaded with beach sand with a total mass of 1904g. The loaded ISP-UAV assembly is depicted in Figure 8-8 which follows.

Figure 8-8: Loaded ISP-UAV Assembly

As can be seen in the above figure, the loading of the ISP cradle represented a worst-case loading scenario, with the payload being offset both rearwards and to the left. The final loaded flight test lasted ~ 134 seconds. During both flight tests, multiple kinematic responses were logged for both the rolling and pitching motions of the UAV. Images of the final flight test of the loaded ISP-UAV assembly are shown below in Figure 8-9 and Figure 8-10. The figures depict the ISP-UAV assembly during the final flight test whilst hovering and rolling respectively.

Figure 8-9: ISP-UAV Assembly Hovering During Final Flight Test

Figure 8-10: ISP-UAV Assembly Rolling During Final Flight Test

8.8 Noise Transferral Analysis

A noise transferral analysis was conducted on the ISP to evaluate the extent to which the TPU vibration dampening bushes mitigated vibration, as well as to compare the in-operation stabilisation capabilities to the baseline stabilisation capabilities. As such, the amount of noise in the system due to aerodynamic forces, UAV kinematic, and propeller vibrations could be quantified.

The technique which was adhered to when analysing the effect of external noise on the ISP stabilisation capabilities can be seen below in Figure 8-11 and Figure 8-12. The graphs depicted by these figures showcases superimposed stabilisation data of the ISP in the static unloaded case, the dynamic unloaded case, and the loaded dynamic case. For experimental standardization purposes, the data was collected with a stationary (hovering) UAV in the dynamic cases, and the static data drawn from the calibration test discussed previously.

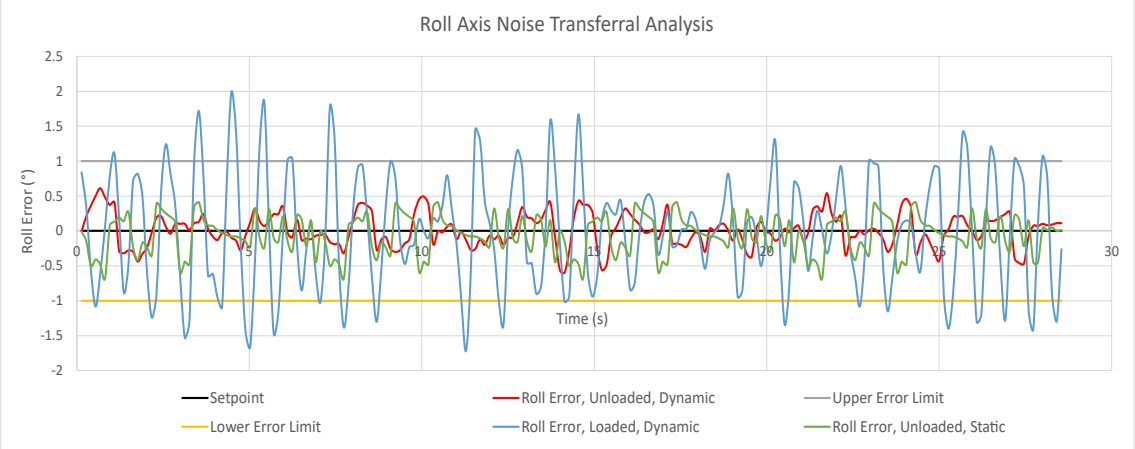

Figure 8-11: Roll Axis Noise Transferral Results

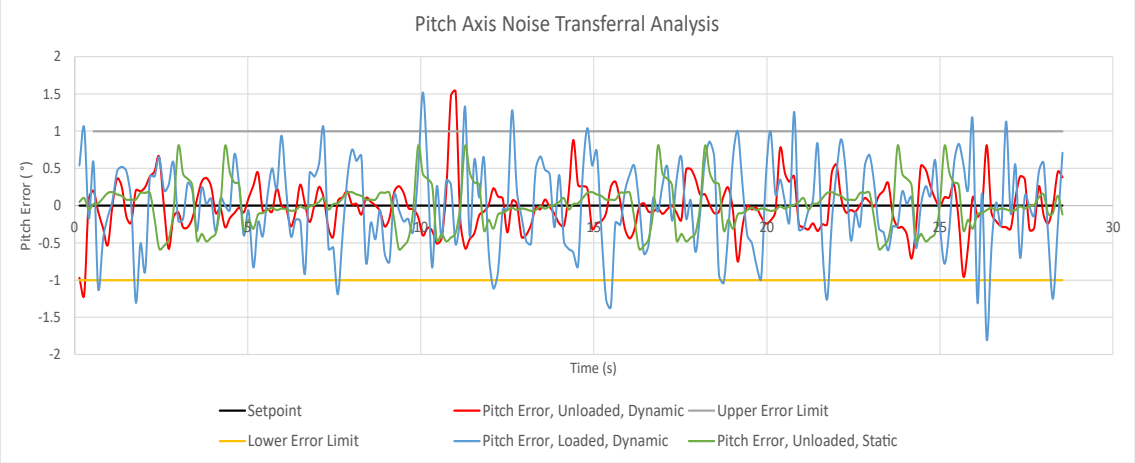

Figure 8-12: Pitch Axis Noise Transferral Results

The graphical representations of the noise transferral analysis experiment are depicted above in Figure 8-11 for the roll axis, and Figure 8-12 for the pitch axis. For uniformity across the analyses of all testing data, the stability criterion was considered met when the standard deviation of a particular response trace had a magnitude less than 1. Any trace to have met this requirement would be suggestive of at least 68% of the logged data points falling within the allowable error range.

Referring back to Figure 8-11 first, the static, unloaded roll error was expected to serve as a stable, symmetrical baseline trace with small oscillations about the setpoint. However, the figure shows the trace to have taken on a non-uniform, rippled waveform. The same can be seen to be true for the static unloaded pitch error in Figure 8-12 above. Nevertheless, statistical analysis of the data showed the roll axis trace to have a mean value of -0.060° and a standard deviation of 0.275°. In the pitch axis, a mean value of -0.0016° was realised with a standard deviation of 0.289°. These values, in both cases, are indicative of a stable system, because 68% of the obtained data points lay within 30% of the allowable error range of 2°.

Analysing the unloaded, dynamic response traces (orange) of the roll and pitch axes in Figures 8-11 and 8-12 in the same manner, it was evident that external noise transferral from the UAV into the ISP was present. These waveforms, too, took on a rippled waveform with minimal uniformity. The resulting mean values for these waveforms were determined to be 0.0010° in the roll axis and -0.0166° in the pitch axis. The respective standard deviations were determined to be 0.234° and 0.335°. Again, the obtained data values were indicative of a stable system as 68% of the data fell within 34% of the allocated error limit range.

The loaded, dynamic noise transferral analysis data can be seen represented by the blue traces in Figure 8-11 and Figure 8-12 above. These traces show an unexpected less rippled waveform, with significantly more uniformity than the unloaded error waveforms. This finding was hypothesized to be as a result of the payload damping the motion of the system by increasing the cradle inertia term. The roll axis produced a mean value of -0.00395° and a standard deviation of 0.808°. The corresponding values of the pitch axis were calculated to be 0.00457° and 0.591°. Under these conditions, the system was determined to be stable as 68% of the data values fell within 80% of the allowable error range.

Following the analyses of the individual testing environments and their contribution to the system noise, several noteworthy observations were made. Firstly, when comparing the roll axis mean values across the first two tests, the unloaded dynamic test mean can be seen to have reduced by a factor of -60 in comparison to the static unloaded test. This observation contradicted the hypothesized effect of vibrational resonances from the UAV propellers in flight, which was the increase of oscillations about the setpoint. Instead, the observation suggested the presence of destructive interference between the roll error trace and the propeller noise. This interference actually aided in suppressing the oscillations of the roll axis error about the setpoint. Visually, the finding translates to a more uniform roll error trace, with reduced rippling. The same finding did not hold true for the dynamic unloaded pitch axis error mean, which can be seen to have increased by a factor of 10.38 in comparison to the mean of the static unloaded pitch axis error. This finding was consistent with the hypothesised effect of vibration resonances from the UAV propellers on the ISP.

Additionally, this finding was expected due to the greater moment of inertia of the cradle in the pitch axis in comparison to the roll axis.

The standard deviation of the traces, whilst dependent on the mean value, provided valuable information regarding the distribution of the data within the experimentation. This information could be further used to analyse the performance of the axes individually and make cross axis performance comparisons. Comparing the standard distributions of the unloaded tests, a 4.84% difference between the standard deviations of the roll and pitch axes was observed. The miniscule difference between these values shows that, regardless of the uniformity of the waveform of the axes, the overall performance of the axes was equally matched This observation was construed as an indication of an efficient, robust control system.

Comparing the standard deviations of the static unloaded test to those of the dynamic unloaded test, the effect of vibrational resonances from the UAV propellers was noted. In the roll axis, the standard deviation from the static unloaded test, as with the mean value, showed a 14.91% reduction from 0.275° to a value of 0.234° in the dynamic unloaded test. Again, this finding was indicative of the propeller vibrations aiding in oscillation suppression. The same trend did not hold true in the pitch axis, with a decline in standard deviation between the static and dynamic test of 13.73% being realised. Subsequently, these two contrasting trends induced a 30.15% difference between the standard deviations of the roll and the pitch axis. This substantial difference in the standard deviation values concluded that the UAV propeller noise caused an overall degradation in the system performance. This conclusion was drawn due to the pitch axis stabilization capabilities diminishing in the presence of external noise.

Ultimately, the dynamic loaded test which was included in the noise analysis was not necessary for a complete analysis to be carried out. However, the inclusion thereof aided greatly in the deciphering of the testing results prior to the analyses. The dynamic loaded test showed a decline in the standard deviations of both axes. Interestingly, the roll axis was shown to be more prone to destabilization due to loading, despite the smaller loading fulcrum. The roll axis standard deviation declined by 71.04% to a final, worst-case scenario value of 0.808°, which still fell well within the allowable error margin. The pitch axis declined only by 43.31% to a final value of 0.591°. Again, this standard deviation fell well within the allowable error range. However, the 26.86% difference between the values of these standard deviations showed a negligible (10.91%) difference in the system performance between the unloaded and the loaded dynamic tests, owing mainly to the reduced stabilisation capabilities of the roll axis.

A final, pertinent observation was made, justified by the loaded dynamic test. The uniformity of the waveform was shown to have a significant effect on the mean value of each specific data set. This can be seen when comparing the waveforms of the loaded test against those of the unloaded static test in Figure 8-11and Figure 8-12 above. The traces of the loaded test waveforms both show significantly reduced rippling and more uniform oscillations about the setpoint in comparison to the unloaded tests. This can be seen to translate to a final roll axis mean value of -0.00395°, which shows a 106.58% improvement from the static unloaded test mean value of -0.060°. While such a substantial mean value improvement was not

observed in the pitch axis, the loaded dynamic test proved to be the only test in which the mean value of the roll and pitch axis did not differ by at least one order of magnitude. Subsequently, the tie between the uniformity of the trace signal and the mean value was determined to be true.

Upon completion of the noise transferral evaluation, it was evident that the UAV propeller noise resulted in a minimal overall system degradation. This finding was consistent with the hypothesized effect of noise in the ISP. The observed system degradation was due to unmatched axis performance resulting from the noise. However, it was noted that this degradation was due to a decline in the stabilisation capabilities of the pitch axis in the dynamic unloaded case. In the loaded dynamic case, this finding did not hold true, with the pitch axis displaying superior stabilisation capabilities over the roll axis, despite the longer loading fulcrum in this axis. Following this, it was observed that the loading of the ISP resulted in more uniform signal traces in both axes due to damping effects. Conclusively, it was determined that the ISP produced acceptable stabilisation capabilities in the presence of external noise from the UAV propellers.

8.9 ISP Kinematics Analysis

The final ISP kinematic analysis results can be seen below in Figure 8-14 through to Figure 8-17. In the same manner as the noise analysis preceding the tests, the final kinematic tests were carried out individually as an unloaded test flight and then a loaded test flight. The results of these tests in the hovering state of flight can be seen analysed above in subsection 8.8.

A noteworthy point to reiterate is that the loaded dynamic test of the ISP, which produced the data displayed in the above graphs, represented a worst-case loading scenario with the intention of producing data representative of the maximum operational capabilities. Whilst an element of load distribution was realised due to the size of the payload used during the experimental flight process, it was assumed that such a load distribution would be true of any payload of maximum allowable mass placed within the cradle.

The method of analysis of the ISP kinematic test data was two-fold: the stability of the ISP was analysed at the transition point from the hovering state to a rolling or pitching motion, as well as during the rolling or pitching motion. The composition of the result traces, including the previously mentioned data segments are explained by Figure 8-13 below.

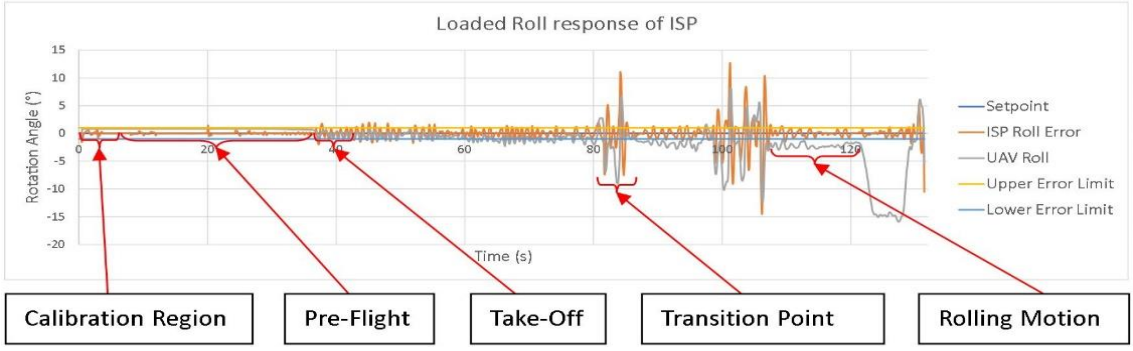

Figure 8-13: Kinematic Analysis Results Composition

As shown in Figure 8-13, the resulting data trace of each flight test was comprised of a short calibration region in which the ISP was powered up and the IMUs are calibrated. Thereafter, the trace shows a pre-flight segment with a length determined by the pilot. The trace then shows a take-off region, which was signified by excitation of the ISP roll and pitch signals due to the additional system noise as previously discussed. In the above example, the take off point was followed by a hovering period. The hovering period was signified by concurrent oscillations of both the ISP and the UAV (roll or pitch) axis signal about the setpoint. As previously mentioned, the transition point was an area of interest for the kinematic analysis. The transition point was signified by a change from a hovering state to a rolling or pitching state, or vice versa. This region can be seen to cause a rapid disturbance to the stability of the ISP and, thus, required additional analysis. The final region of the trace, which was also a region of interest to the analysis, is denoted the rolling motion within the above example. For the analysis of a pitch axis trace, this region would be denoted the pitching motion. This region was signified by a UAV rolling or pitching state with a magnitude which fell outside of the indicated allowable error range. The ISP response in these regions required analysis to deduce whether the ISP was able to adequately stabilise the cradle in flight. The results of the kinematic analysis flight test of the ISP can be seen in Figures 8-14 through 8-17 below.

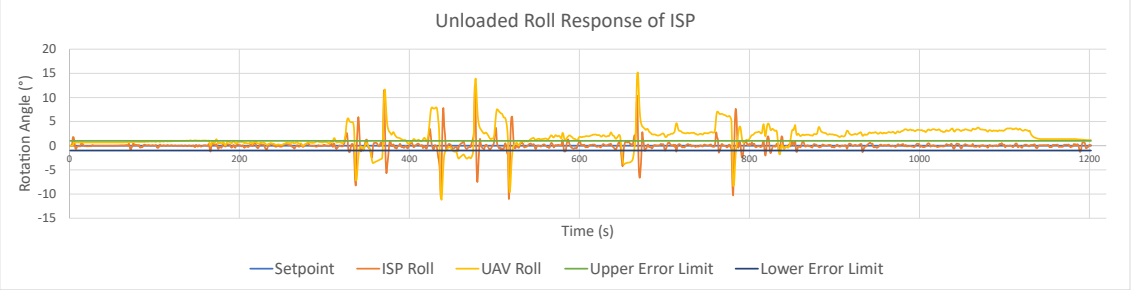

Figure 8-14: Unloaded Roll Response of the ISP

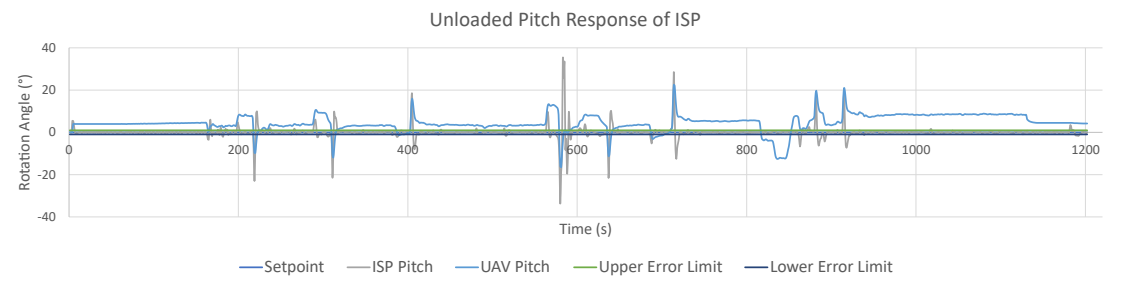

Figure 8-15: Unloaded Pitch Response of the ISP

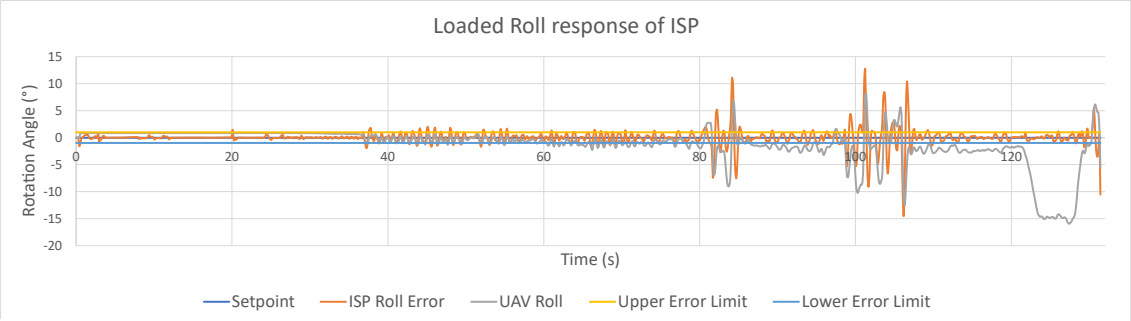

Figure 8-16: Loaded Roll Response of the ISP

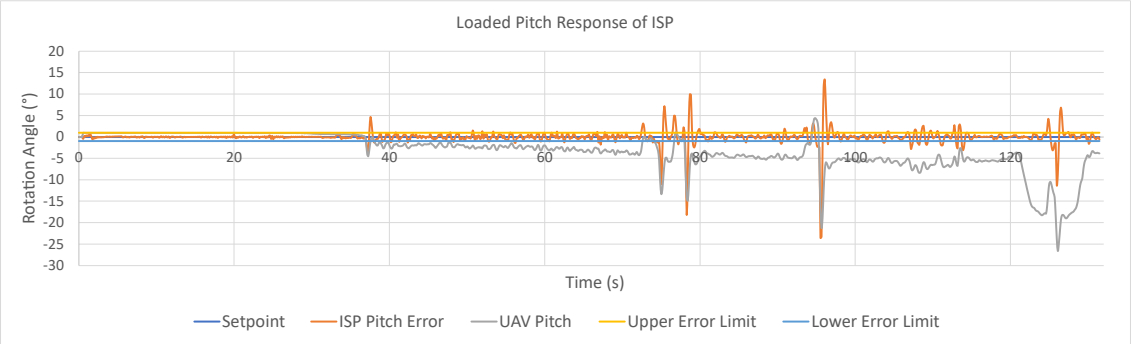

Figure 8-17: Loaded Pitch Response of the ISP

The primary purpose of the analysis of the ISP kinematics was the evaluation of the ISP performance characteristics at the transition points of the testing traces. This proved to be a challenge due to the UAVs horizontal position accuracy system causing large, involuntary rotations at the transition points, as discussed prior in subheading 8.6. The resulting traces generated at these points were, in some cases, not of an acceptable form for analysis. Nevertheless, all of the eligible waveforms at the transition points were analysed in the same manner explained in subheading 7.2.5 above. The results of these analyses were plotted in the same manner as the baseline response characteristics in Figure 7-2 and Figure 7-3 above. Subsequently, the graphs shown in Figure 8-18 and Figure 8-19 below were generated, for further statistical analysis to be performed.

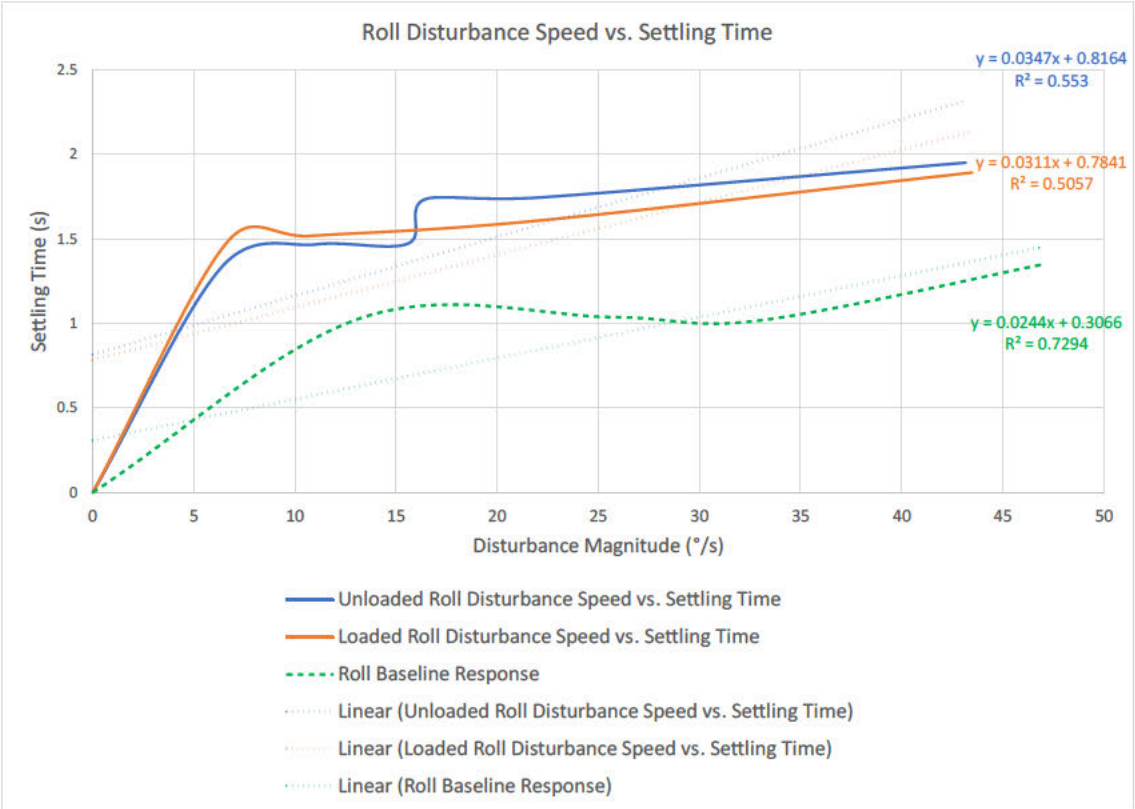

Figure 8-18: Roll Axis Kinematic Response Characteristics

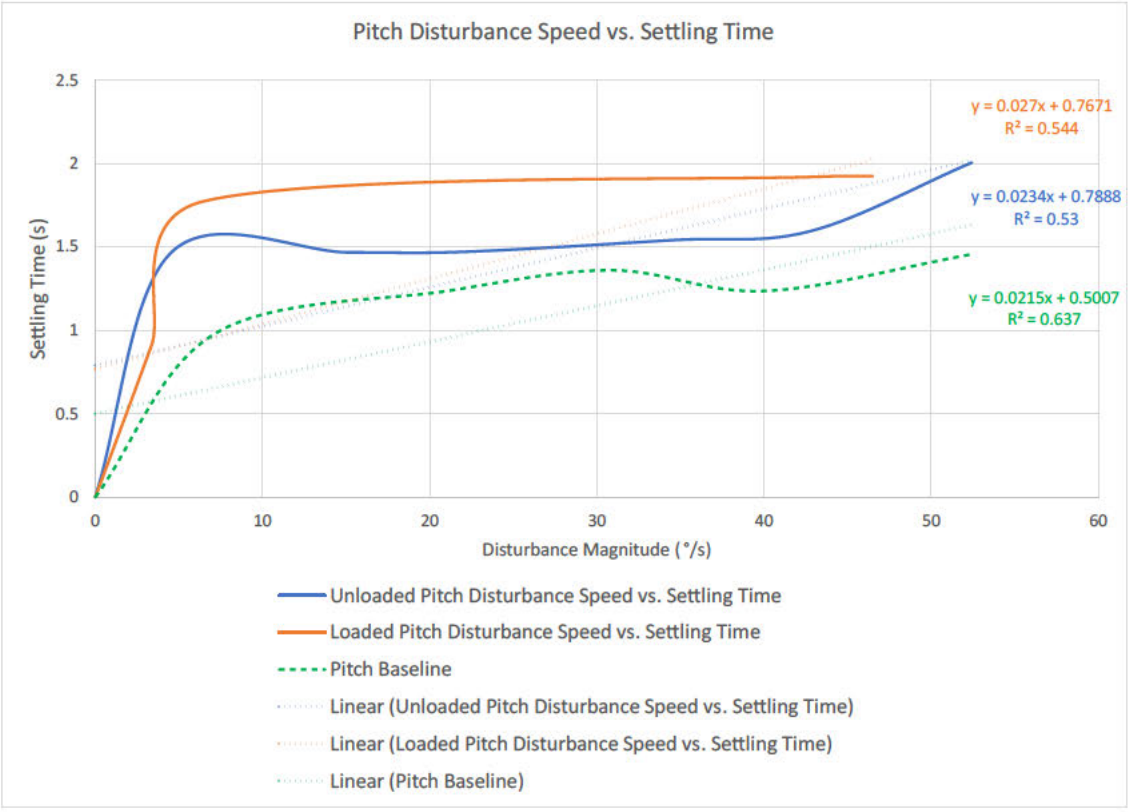

Figure 8-19: Pitch Axis Kinematic Response Characteristics

Referring to Figure 8-18 and Figure 8-19 above, it is evident that the discrepancy between the unloaded ISP axis performance and the loaded axis performance was minimal when analysing the data trendlines. In the roll axis case, a 10.37% difference in the rate at which the settling time increases across both tests was determined. Similarly, in the pitch axis a 13.33% rate increase was realised between the loaded and the unloaded kinematic tests. Intriguingly, it was observed that the settling times of the roll axis in the loaded test were faster than those of the unloaded roll axis. This trend can also be seen reflected in the trendline gradients. The same trend did not hold true for the loaded pitch axis, which settled 13.33% slower, as previously indicated. However, the pitch axis was anticipated to settle slower in the loaded state than in the unloaded state due to the increased inertia seen by the pitch servo as a result of loading.

The same damping effect due to loading, which was noted in the noise analysis, can be seen present within the kinematic test results above. In both the roll and the pitch axes, the loaded kinematic response graphs can be seen to be more uniform than the unloaded equivalent graph, with minimal fluctuations. Moreover, the uniformity of these graphs also supersedes that of the baseline response characteristics which were superimposed onto the above graphs within the region of interest. The fluctuations in the baseline response graphs are noticeably larger than those obtained during the kinematic analyses.

As previously mentioned, it proved difficult to achieve any rotational velocities apart from the maximum and minimum values. Subsequently, the amount of data points generated to produce the above graphs were minimal – this was identified as a source of error within the experiment. Despite this, however, the graphs produced data with R^2 values greater than 50%. This finding meant that the data was adequately represented by the trendlines, despite the reduced number of data points. As with the baseline response characteristics analysis, the recommended method to achieve a trendline with a greater R^2 value to represent the ISP kinematic responses would be to generate more data points through testing with a more proficient pilot for the UAV.

It can be observed from the graphs that the UAV dynamics had a definite effect on the settling times of the ISP. In the roll axis, the loaded kinematic test shows a maximum settling time of 1.89 seconds corresponding to the maximum observed disturbance magnitude of 43.48°/s. In comparison to the baseline roll response data, this equates to an increase in settling time of approximately 33.33%, with the interpolated baseline settling time at 43.48°/s being 1.26 seconds. In the pitch axis, the maximum loaded settling time of 1.92 seconds at 46.51°/s corresponds to an interpolated baseline settling time of 1.35 seconds at the same disturbance magnitude. These data points reveal a 29.69% increase in settling time between the baseline and the loaded kinematic test in the pitch axis. Due to the variances between the baseline and the loaded test in the roll and pitch axes, it is evident that the stabilising capabilities of the ISP are reduced by maximum one third when UAV noise, dynamics, and loading of the ISP are considered, representing the absolute worst-case scenario.

The final operational stabilisation of the ISP was evaluated over a duration of ~10 seconds in the unloaded and loaded states during rolling and pitching travel segments. The results of these evaluations are displayed in Figure 8-20 and Figure 8-21 below.

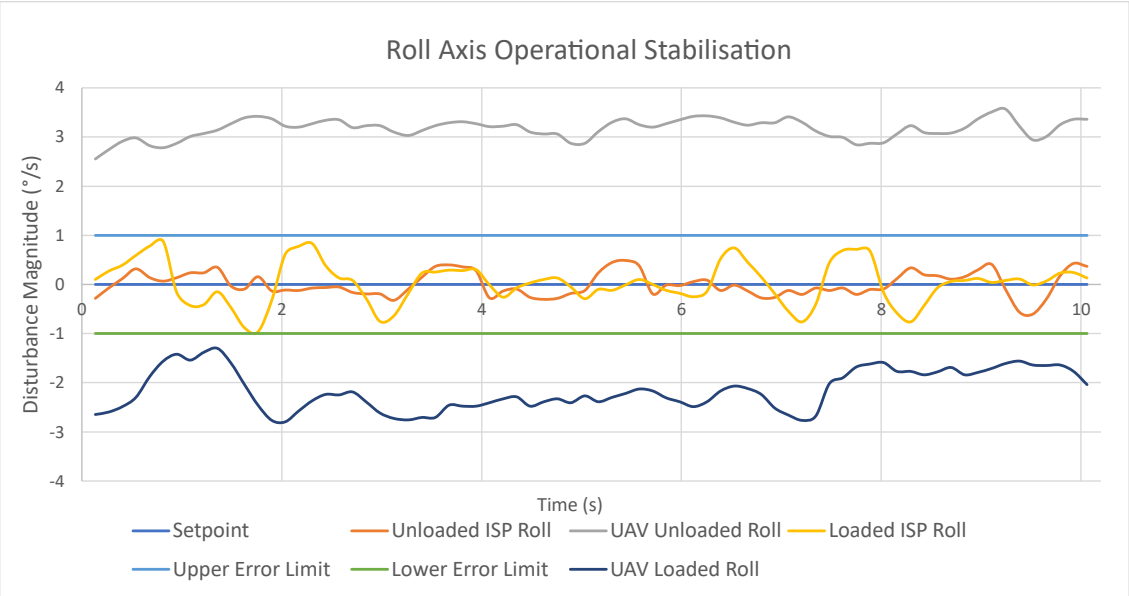

Figure 8-20: Roll Axis Operational Stabilisation Results

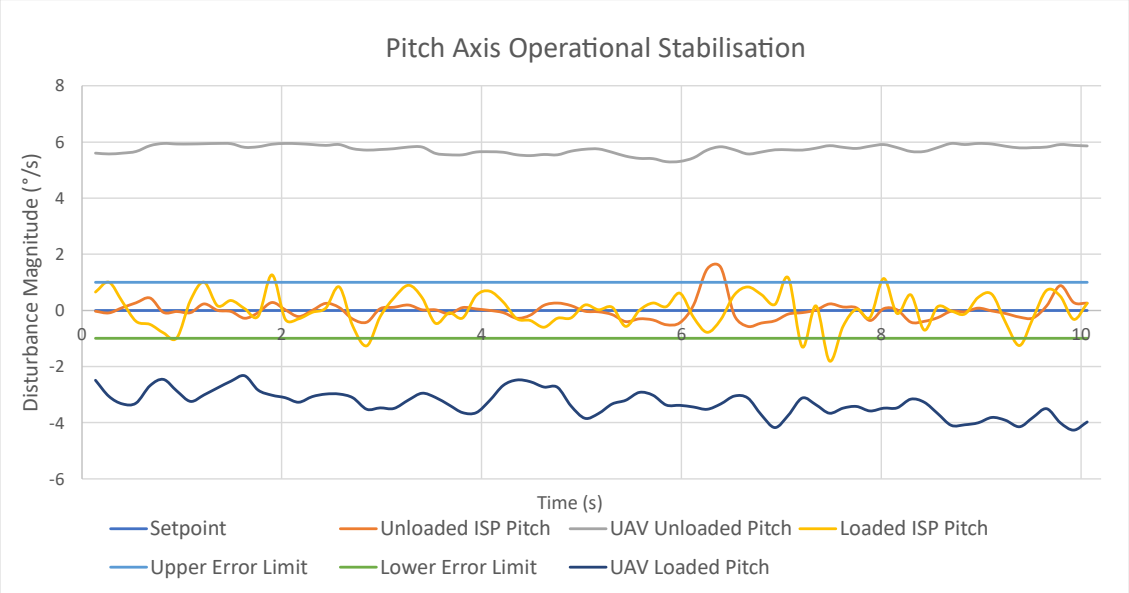

Figure 8-21: Pitch Axis Operational Stabilisation Results

As can be seen in the above figures the roll and pitch traces were plotted in the loaded and unloaded states, against the associated UAV roll and pitch traces in the loaded and unloaded states. The above data was graphed to produce data eligible for analysis in the same manner as the noise transferral analysis was performed.

With reference to Figure 8-20 firstly, in the unloaded roll axis kinematic case, the UAV trace was determined to have a mean value of 3.166°. Under these conditions, the ISP roll axis produced a mean value of 0.01°, and a standard deviation of 0.243°. Comparing the obtained values back to the hovering data analysed in the noise analysis, the mean value was identical, while the standard deviation showed a 3.70% increase. Considering the above comparisons, it was determined that the unloaded roll axis suffered no degradation in stabilisation capabilities during a rolling motion sequence of the ISP.

In the case of the loaded roll axis kinematic analysis, the UAV trace was ascertained to have a mean magnitude of 2.157°. Analysis of the ISP loaded roll trace produced a mean value and a standard deviation of 0.0257° and 0.422°, respectively. The noise analysis comparison of these values identified an 84.63% increase in the roll mean value, while the standard deviation decreased by 47.76%. These statistics represent substantial changes in the operational stabilisation capabilities in the loaded roll axis kinematic test. However, the overall proximity of the produced metrics to the setpoint show that the axis remained stable under loading and throughout a prolonged period of rolling motion.

Referring now to Figure 8-21, the unloaded kinematic test in the pitch axis produced a mean UAV orientation of 5.74°. The ISP pitch axis responded to the disturbance by stabilising the axis with a trace mean value of -0.003° and a standard deviation of 0.352°. Comparatively, from the dynamic baseline data in the noise transferral analysis, the mean value showed an 82.35% reduction. Conversely, the standard deviation increased by 4.83%. Concluding remarks regarding the unloaded pitch axis stabilisation during the pitching sequence were that the pitch axis suffered negligible degradation in stabilisation capabilities.

Analysis of the loaded pitch axis during a pitching motion revealed the UAV to have a mean pitching angle of magnitude 3.306°. The ISP response to this motion was a trace comprised of a 0.015° mean value, and standard deviation of magnitude 0.6177°. Hence, from the dynamic baseline values, the axis suffered a 69.53% increase in mean value, as well as a 4.26% increase in standard deviation. Notwithstanding the decrease in proximity of both the mean and standard deviation values, the loaded ISP pitch axis still produced acceptable stabilisation characteristics.

8.10 Chapter Summary

This chapter presented the reasoning behind, and the results of, the various tests performed to evaluate the operational capabilities of the ISP. The experimental performance evaluation of the ISP consisted of the. The culmination of the experimental procedure produced results which satisfied aims and objectives.

The noise transferral analysis between the UAV and the ISP system showed the resulting noise transferral to produce a minute degradation in the performance of the system. Statistical analysis in the worst-case-scenario loaded test determined the extent of the system noise degradation to be a maximum of 26.86%. This value represented the percentage error between the standard deviations of the roll and pitch axes under

maximum loading. Whilst both standard deviations still fell well within the allowable error range, the high error between the values showed the roll axis, again, to be more unstable than the pitch axis. However, despite the identified degradation of the system due to UAV noise, the ISP maintained acceptable stabilisation capabilities.

Analysis of the ISP under kinematic conditions showed loading to induce more uniformity into the response data. Under maximum loading, the maximum settling times obtained were 1.89 seconds in the roll axis and 1.92 seconds in the pitch axis. Close agreement of these maximum values was noted to imply equivalent axis performance, which was a desirable outcome. Due to the ISP performance relying solely on the PID gains produced by the system simulation, the equivalent axis performance coupled with the acceptable stabilisation capabilities of the system under loading validated the simulation model. It was concluded that, while discrepancies were present between the final performance capabilities and the simulation, the simulation represented the final ISP system with acceptable accuracy.

To conclude, it was found that the combined effects of UAV noise, loading of the ISP, and UAV motion resulted in a maximum increase in settling time of 33.33%. However, the system remained stable under these conditions.

9 DISCUSSION

9.1 Introduction

The rationale of this dissertation was to research and design a mechatronic device for the existing DM300 UAV which improved the UAVs pertinence in disaster management and humanitarian aid situations. The research was concerned with integrating technologies encapsulated by 4IR to create a device suitable for transporting fragile cargo, unbalanced loads, and emergency resources into affected areas via the DM300. Chapter 9 confers an overview of the work conducted throughout the project in the research and design fields and analyses the viability of the resulting device, based on the research questions and project objectives. In addition to the research overview, chapter 9 provides areas for future work in the mechatronic device.

9.2 Overview of Research

9.2.1 Background and Literature Review

When reviewing the rationale behind the development of the ISP for disaster management and humanitarian aid purposes, the research questions in Chapter 1.4 arose. A set of objectives contingent on the questions was developed to seek answers. The first objective was to assess the potential for a UAV such as the DM300 to be used for the intended purpose of the research project, with focus on relevant legislature. Analysing the DM300 capabilities, the UAV was shown to comprise of many desirable features such as real-time FPV camera imaging, thermal imaging and object tracking transmission. However, the most pertinent capabilities to the research project were the UAVs 23m/s maximum speed, 2.7kg payload, 31-minute loaded flight time, and 15km transmission range. With the anticipated delivery destinations being distant from available healthcare and resources such as public hospitals and metropolitan regions, the above UAV specifications yield a theoretical, maximum distance, minimum response time of 11 minutes. In comparison to existing methods, the UAV-ISP operation was shown to possess the potential to become an essential response tool with a significantly faster response time than conventional emergency services and the ability to access areas in which existing roads and infrastructure may have been damaged, hindering land vehicles from entering [23] [21]. With 84% of South African citizens being dependent on the public health system for medical assistance outside of disaster events, the inherent need for additional resource delivery methods during these events can be seen for the purpose of aiding existing methods [111].

Research indicated that the use of a UAV for disaster management and humanitarian aid was not only possible, but a regular occurrence of Zipline [34]. Nevertheless, the SACAA requires the operator of the UAV to be in possession of a valid RPAS licence, as well as a MR-RPL complete with a BVLOS endorsement for the operation to be legal within Southern Africa. Assuming the operation became commercialised (within Southern Africa), it would be necessary to register the operation and have the UAV inspected and tested by a SACAA official. Combining the ISP and UAV classified the operation as a Class

3A category, which further restricted the UAV to a maximum permissible flight altitude of 121.92m and a MTOM of less than 150kg.

The next research objective was to identify commercially available ISPs and the components responsible for the control thereof. The research conducted in section 2.6 identified several commercially available ISPs, which were limited to those produced by DJI enterprises. The ISPs were divided between handheld devices and UAV-compatible devices, which were further refined to DM300-compatible devices. The review of existing, commercially available devices identified numerical specifications pertaining to the design of a DM-300-compatible ISP. The relevant specifications were the mechanical and controllable ranges of these devices, and the angular vibration range of magnitude 0.01°, which aided in the development of the ISP target specifications detailed in Chapter 3. Furthering the research into ISPs, it was found that the ideal ISP is composed of a payload, and electro-mechanical assembly, and a control system. While the payload of the ISP was already known, the intricacies of the electro-mechanical assembly were found to be dependent on the type of stabilisation required for the payload. The stabilisation category was refined into three distinct classifications, namely mass stabilisation, mirror stabilisation, and alternative stabilisation techniques. Here, it was concluded that mass stabilisation would be utilised within the ISP assembly. In addition to mass stabilisation being the most common, it was found to require fewer components than both mirror stabilisation and alternative stabilisation techniques, whilst also being known to provide superior results over mirror stabilisation, with a less complex overall system. The electro-mechanical components required to control a mass stabilised system were, then, identified to be actuators, bearings, gyros, conductors, power supply, and a suspension system for the ISP (a mechanical mounting system). The final aspect of the ISP composition, responsible for combining the previous systems, was the control system. The primary aims of the control system were described fully before identifying and scrutinizing the commonly utilised control systems. Ultimately, a PID control system was decided upon due to the abundance of information available to aid in developing these control systems in comparison to the more complex control methods. However, information regarding the PID control implementation within a roll-pitch ISP specifically was found to be ill-defined.

The third objective was to review manufacturing methods used in aerial robotic prototypes, and to identify relevant methods of fabrication for the ISP. It was found that, conventionally, foam cutting technologies and manual hand fabrication using balsa wood or composite materials were used to manufacture UAVs and associated aerial prototypes. However, AM technologies were shown to produce more complex parts in a desirable manner with respect to process complexity, method restrictiveness, and part tolerance [54]. Upon analysis of the commonly utilised AM technologies for the aerial robotic prototype scenario, FDM was chosen to produce the ISP due to the method's, affordability, applicability, and sustainability. Further refinement of research into FDM found that current configurations are known to produce parts with high accuracy, surface finish, and better structural integrity than ever before, thus, making FDM more applicable to engineering design and associated components, such as those within the research project. From a sustainability point of view, AM technologies produce significantly less waste than alternative manufacturing techniques. This is due to each individual process only adding the required material for the

part being manufactured, with the exception of support material required for overhanging part regions. However, under the FDM envelope, further design sustainability can be induced through the use of sustainable materials. The most common materials used in FDM fabrication were found to be ABS and PLA – both of which have a main constituents of sugarcane and maize, rendering the materials to be biodegradable and sustainable [57]. Whilst both PETG and Nylon materials are also common to FDM fabrication, the research considered only ABS and PLA for the manufacture of the ISP prototype. This decision was made due to the ease of use and superior strength of these materials in comparison to the PETG and Nylon alternatives. Subsequently, PLA was chosen as the material for ISP manufacturing, hinging on the material sustainability and ease of use in comparison to ABS. The controllability of the FDM fabrication method was found to be extensive, with many process parameters available for alteration to produce part geometries with complexities which cannot be matched by any other manufacturing method. However, the method does possess shortfalls associated with these process parameters. Notable process parameters were found to be the layer height, infill density, infill pattern, wall thickness, and print speed. The layer height was identified to be directly proportional to the drag coefficient, with a greater layer height increasing the C_D value, while the infill pattern and density were shown to account for the structural integrity of the part. Analysing the various infill patterns offered by the Cura slicing software, the most-structurally-sound patterns were found to be the Gyroid and Cubic infill pattern. These respective patterns showed uniaxial compressive forces of 246kg and 250kg. Conclusively, it was decided that further, empirical, parameter optimisation was required using PLA to deduce unique parameter combinations for the ISP components to achieve the required engineering stress and deflection values.

9.2.2 Electrical System Design

The fourth research objective was to develop an optimised design of the ISP which incorporated the necessary components to produce the required stabilisation capabilities. This objective, therefore, included the electrical design, mechanical design, control system implementation, and software development which attempted to satisfy the design specifications detailed in Chapter 3. The electrical system was the first system to be addressed. The derivation of system requirements and specifications for the electrical system posed a challenge due to the dependence of most components on the final operational payload mass, and the resulting torques. To overcome this issue, a final payload mass of 2.2kg, and maximum payload platform dimensions of 300mm in length and 150mm in width were assigned. The 2.2kg payload allowed a final (and realistically unattainable) ISP assembly mass of 500 grams. The implication of the higher payload being that, while components were specified for this maximum mass, should the ISP assembly mass exceed 500 grams the components would not need to be respecified, but an effective reserve factor would develop with increasing assembly mass. The electrical design progressed with calculations being performed to identify potential components to satisfy system requirements. The specifications of the identified components were then analysed to confirm suitability within the system before final component selections were made. The final electrical design system featured two servo motors with a maximum torque specification of 35.2kg.cm at 2.6A, powered by a li-ion battery pack with fully charged 7.4V, 2600mAh specifications. The calculations of Chapter 4 proved the capacity of the battery pack to be sufficient to

power the servo motors for the entire duration of the UAVs maximum loaded flight time, whilst under maximum loading. Additional components of the electrical design were an Arduino Nano microcontroller and a BNO055 IMU. A second battery pack, with the formerly mentioned specifications, was used to power the microcontroller. A list of all the components required for the ISP prototype can be found in Table A-1.

9.2.3 Mechanical System Design and Optimisation

The mechanical design of the ISP was required to house the electrical design (thus forming the electro-mechanical assembly) and form the connection between the ISP and the UAV. In the initial design phase, the mechanical and electrical design were developed concurrently. The DM300 CAD model was utilised to hypothesize and assign the maximum cradle dimensions which provided the starting point of the mechanical design and allowed for the electrical component specifications to be calculated. Following the resultant selection of electrical components, CAD models of the components were obtained and used to proportionately conceptualise geometric configurations for the ISP within the existing DM300 structure. Having identified the necessary mounting points for the ISP, the design process commenced.

Firstly, it was concluded that the cross-sectional profile of the mechanical design frame needed to be optimised, as per the mechanical design objectives. The optimised cross-sectional profile was determined to be an ellipse with an AR of 2. A CFD analysis of the profile under the operational conditions of the ISP found the C_D value to be 0.068, which agreed closely with the research in [86]. The final elliptical dimensions were fixed at 25mm for the major arc radius and 12.5mm for the minor arc radius. Proceeding with the design, both battery packs were lowered to beneath the cradle platform, and the pitch servo motor lowered to within the cradle area to lower the CoG of the assembly. This allowed the ISP to be balanced by manipulating the position of the batteries under the platform to shift the ISP CoG. The final desired CoG position was the intersection between the roll axis' line of rotation projection onto the pitch axis' line of rotation. The final offsets magnitudes of the ISP CoG from the desired position were determined to be 5.95mm in the roll axis and 0.14mm in the pitch axis. These values deemed the assembly to be acceptably balanced, with the resulting torques being negligible.

The mechanical design of the optimized ISP presented in Chapter 4 met the initial aims and objectives of the design. The design was capable of simple integration into the UAV structure, whilst consisting of commercially available components, being lightweight, aerodynamic, and fit for FDM manufacturing. However, in the initial configuration, the SolidWorks mass approximation of the assembly was 1041.06 grams, modelled with 100% density for all components. FEAs conducted on components showed that at 100% infill, the deformation and deflection of components were well below the allowable threshold for the PLA material. Therefore, weight reduction was deemed possible via the alteration of printing parameters of parts during FDM manufacturing, with the weight reduction further optimising the design. The hypothesized method of optimization was to empirically determine the optimal process parameters to be used when manufacturing the ISP components. It was proposed that this be done through the destructive testing of FDM-made samples of varying layer heights, infill patterns, infill percentages, and wall thicknesses to determine the specific strength of each parameter combination.

9.2.4 FDM Optimisation

The fourth research objective, and the aerial application of the ISP necessitated the optimisation of FDM parameters before fabrication of the prototype could commence to minimise the mass of the final ISP assembly. The detailed FDM optimisation process can be found in Chapter 5. Due to the limited payload carrying capacity of the DM300, this meant that the payload capacity of the ISP was maximised, which was a desired outcome of the research project.

A total of 150 ASTM test samples were manufactured and underwent destructive testing to produce the final testing data. Various raster angles were used in each specimen batch to account for anisotropy in the material. However, even with the above measure in place, the impact of anisotropy was still observed in the form of large fluctuations in the failure loads of specimens. The aims and objectives of each test were met, with sufficient data being produced to predict the specific strength and print time of FDM parts fabricated under the conditions prescribed in Chapter 5. Using the data provided by the tests, relationships were derived between the FDM process parameters. The resultant trendline equations are located on the graphs of each test and can be used to accurately predict the specific strength of a part. The four-stage approach to parameter optimisation (refer to Figure 5-1) used a follow-on approach, where insight from each test was integrated into the succeeding test to streamline the optimisation process. The layer height test identified the 0.3mm layer height to produce the lowest specific strength in both flexure and tension of 1.34kg/g and 12.22kg/g respectively. This layer height was therefore used in the tests that followed to produce more conservative results. The infill pattern test identified the Cubic infill pattern to be superior to the Gyroid infill pattern in terms of stability (fluctuations in test values), specific strength and print time. For this reason, the Cubic infill pattern was used in the infill and perimeter test which followed. The results of the test indicated that the number of perimeter layers was more influential on the overall part strength than what the infill pattern or infill percentage was. This insight led to a perimeter variation test being conducted where infill was kept constant. Optimal FDM part strength, mass, and print time was realised by varying the perimeter wall thickness, at 0% infill.

The perimeter variation method was validated through FEA analyses on the test sample geometry, using equivalent boundary conditions, and the average failure loads found during testing. A final destructive test of an ISP component produced using the perimeter variation method ensued, which proved the method to be superior to the conventional infill and perimeter method of FDM manufacturing. The ISP component CAD models were then revised to take on a hollow-shell structure following the designation of the final fabrication parameters, and final FEA analyses run on the components. Results of these FEAs showed fully loaded part stresses to be well below the stress threshold of the PLA material, thus validating the perimeter variation FDM fabrication method. Table B-11 provides a full account of the FEA setup particulars, followed by the results of the final FEA analyses.

9.2.5 ISP Fabrication and Assembly

The fabrication and assembly of the ISP represented research objective five and ensued the FDM optimisation experimental procedure. To incorporate DFM best practices, the final ISP design was segmented to allow for each component to feature at least one flat surface which could be placed on the print bed during manufacturing. While this decision was marginally detrimental to the structural integrity of components and added weight to the assembly in the form of additional fasteners, the maintenance accessibility and replaceability of components was enhanced. Analysing the results of the FDM optimisation, the selection of final FDM process parameters opted for a maximum layer height of 0.2mm to be used, with a minimum of three perimeter walls. The fabrication of the ISP components was completed with a total of 19 separate components being produced, cumulating 67 hours of printing and 329.7 grams of PLA. Assembly of the completed ISP proved a simple task, with components mating using standard metric fasteners. Assembly was further aided through self-locking nut recesses being designed into components as far as possible to reduce the number of tool required for assembly down to four - a small Phillips head screwdriver, a 2.5mm Allen key, and a 7mm and 8mm spanner. The simple assembly using fasteners and diminished tooling requirements made for easy access to onboard electronics for maintenance and repair. The culmination of the assembly of the ISP allowed for the final system mass of 709.86 grams to be realised. Hence, the maximum final operational payload allocated to the ISP was specified to be 1900 grams, which allowed for a leeway of 90 grams to account for any calibration discrepancies between measuring equipment during the loading process. The final operational payload of the ISP met both the geometric and payload mass design requirements of chapter 3. The ISP payload cradle minimum dimensions of 150mm x 300mm exceeded the required 130mm x 200mm dimensions of the intended, most influential payload. Additionally, the final operational payload of the ISP was found to be in excess of triple the required payload requirement.

9.2.6 Control System and Software Implementation

Following completion of the fabrication and assembly of the final optimised ISP prototype, the control system design and software implementation were attended to. The details of these elements of the ISP are provided in Chapter 6. The control system was developed using MATLAB Simulink software. The Simulink model of the ISP formed a connection between the servo motors, the required 0° orientation of the cradle platform, the IMU orientation data, as well as the geometric and kinematic torque disturbances. The geometric and kinematic disturbance torques were determined from first principles in Chapter 2.9. The kinematic torque disturbances were dependent on the MOI values of the relevant roll and pitch axis components' final masses. Once the final component mass data was obtained in Chapter 5, the SolidWorks CAD model mass data was overridden to produce the final MOI values. Combining the final MOI terms for each axis, as well as the calculated motor parameter values, the autotune Simulink function was utilised to produce PID gains for the roll axis and the pitch axis. The resulting roll axis PID gains produced a step response settling time of 320.77ms, a rise time of 226.99, and an overshoot of 3.464%. In the pitch axis, the resulting settling time was 427.942ms, the rise time was 171.181, and the overshoot was deemed to be

6.989%. These values represented the ideal case, with a negligible torque disturbance being experienced by the system.

Having obtained the necessary PID gains which produced acceptable axis stabilisation characteristics, the ISP code was developed using the Arduino IDE interface. The code functioned as a virtual representation of the Simulink ISP model. Instead of analysing the system response characteristics, however, the code ensured the necessary compatibilities between components which allowed for optimal function of the electro-mechanical assembly. As such, the software code was successful in converting the IMU digital data outputs into physical actuator responses to counteract cradle platform disturbances. A final stabilisation loop time of ~105 milliseconds was determined, corresponding to a loop frequency of 9.524Hz. While this value was seen to limit the IMUs 100Hz sample rate, the components noted to restrict the overall system response speed were the servo motors. The servo motors were determined to have a maximum theoretical operating frequency of 1.389Hz, based on the calculations in *Equation 4-8*. As such, the 16MHz clock speed of the Arduino Nano was noted to be sufficient for the application.

9.2.7 Analysis of ISP Performance

The fourth research objective also required the operational performance characteristics of the ISP to be analysed and compared to the target specifications for the design, to ensure that target specifications had been met. Three sets of experiments were conducted to wholly test the ISP performance capabilities. Logged response traces were obtained in both the roll and pitch axis throughout testing. As such, whilst portrayed individually, the roll and pitch axes were tested together. This excludes the baseline response testing, during which axes were tested separately. Inherent geometric couplings associated with ISPs meant that the roll axis stabilisation characteristics included the effects of the roll axis, and vice versa. Subsequently, the individual portrayal of results was presumed valid. The first experiment tested the ISP axes individually in a static environment to ascertain the baseline response and stabilisation characteristics of the ISP axes. The second test analysed the stabilisation characteristics of the ISP axes on the UAV in an unloaded, static environment, followed by analyses in both the unloaded and loaded dynamic environment (flight test with the UAV hovering). The final performance analysis test of the ISP focused on the system response to dynamic UAV operations such as rolling and pitching motion sequences.

9.2.7.1 Baseline Response Analysis

The first experiment determined the baseline stabilisation settling time of the roll and pitch axes to be 1.78 seconds and 1.66 seconds respectively, obtained at a disturbance magnitude of approximately 137°/s. However, analysis of the trendlines pertaining to the obtained data it was noted that the roll axis response rate increased 14.77% faster than that of the pitch axis. This observation indicated that the pitch axis possessed superior stabilisation capabilities when facing larger disturbance magnitudes. Comparatively, when the ISP simulation model was subjected to the same conditions, it was found that the settling times of the real ISP system were 43% faster at the maximum disturbance magnitude. Further analysis of the simulation data trendlines identified a close correlation to the behaviour of the axes in the experimental

case. Moreover, a 10.44% increase in the roll axis response rate over that of the pitch axis was observed. Again, this finding indicated the pitch axis stabilisation capabilities to be more consistent under maximum disturbance magnitudes. While the trends within the experimental data held true for the simulation data, the 43% error between the obtained values disputed the accuracy of the simulation model. It was hypothesised that the magnitude of the error between the simulated results and the physical results could be due to inaccuracies in the estimation of the chosen motor parameter values. The simulation was considered valid owing to the physical system responding faster than the simulation model had predicted and producing acceptable stabilisation results. Therefore, whilst the error was large in magnitude, the settling time of the system was more intrinsic to driving the project forward than what the error was.

9.2.7.2 Noise Transferral Analysis

The second experiment performed on the ISP analysed the extent to which the UAV noise degraded the system performance. Statistical analysis of the unloaded static test data found the roll axis standard deviation to be 0.275°, and the pitch axis' to be 0.289°. The obtained standard deviations represented a stable system, as 68% of the obtained data points fell within 30% of the allowable $\pm 1°$ allowable error range. The 4.84% difference between the standard deviations of the obtained data indicated equivalent axis performance under the unloaded, static UAV conditions. The minuscule difference between the stabilisation characteristics of the axes was taken to indicate a robust, effective control system produced by the ISP simulation model.

The unloaded, dynamic test of the ISP took place with the UAV hovering in a stationary, level position. Under these conditions, the ISP roll axis recorded date with a standard deviation of 0.234° from the setpoint, whereas the pitch axis data produced a standard deviation of 0.335° from the setpoint. These indicators represented a stable system, with both axes stabilising the platform within 34% of the allowable error range 68% of the time. The findings of the first dynamic flight test of the ISP produced two noteworthy findings. Firstly, in the roll axis, it was evident that the introduction of external noise into the system reduced the standard deviation value by 14.91%. This observation was taken to indicate possible destructive interference between the UAV propeller vibrations and the roll axis setpoint oscillations, which aided in stabilisation. Secondly, the pitch axis' standard deviation was seen to increase by 13.73% indicating a degradation in axis stabilisation capabilities. However, the pitch axis was anticipated to display performance degradation resulting from noise due to the greater moment of inertia of the cradle in the pitch axis. Nevertheless, the standard deviations of both axes displayed an almost equivalent variation magnitude resulting from the introduction of UAV propeller vibrations, indicating a comparable tendency of the control system to restrain the effects of vibrations. A 30.15% difference between the roll and pitch axis standard deviations was noted. This showed an appreciable increase from the static unloaded test, indicating definitive effect of noise on the system.

The loaded, dynamic test of the ISP was conducted, again, with the UAV hovering. The resulting test data showed a standard deviation of 0.808° in the roll axis and 0.591° in the pitch axis. These metrics determined a 71.04% increase in standard deviation, equating to a 71.04% decline in stabilisation performance in

comparison to the unloaded dynamic test. Contrarily, even with a significant performance decline, the standard deviation represented a stable axis as 68% of the obtained data fell within 80.8% of the allowable error range. In the pitch axis a decline in stabilisation performance of only 43.31% was noted. Again, a stable system was realised with 68% of the obtained data points falling within 59.1% of the allowable error range. Comparing the obtained standard deviation values, a 26.86% discrepancy was calculated between the roll axis and pitch axis values. Comparably, the obtained discrepancy showed a 10.91% decrease in comparison to the dynamic unloaded test, indicating closer roll-pitch axis stabilisation capabilities under loading. Mean error values were noted to be 0.00457° in the roll axis, and 0.00395° in the pitch axis. These values were noted to satisfy the required 0.1° angular vibrational range target specification. Loading of the ISP was eventually determined to induce additional uniformity to the resulting stabilisation data in the form of less rippled waveforms.

Analysis and comparison of the data produced through the experimental procedure in the static, dynamic, unloaded, and loaded conditions showed the introduction of external noise (in the form of UAV propeller vibrations) to negatively affect the ISP axes. A 33.33% degradation in the stabilisation of the axes was noted in the form of increased discrepancies between the standard deviations between the roll and pitch axes indicating unequal stabilisation abilities. In accordance with the findings of the baseline response analysis findings, though, the noise transferral analysis data confirmed the roll axis to be more susceptible to performance alteration in response to different loading.

9.2.7.3 ISP Kinematic Analysis

The final series of testing conducted on the ISP analysed the system performance under kinematic conditions. The UAV was found to produce a rapid transition between kinematic (rolling or pitching) movements and hovering states, whilst also proving difficult to achieve a wide range of rotational velocity values. Subsequently, the test data analysis was separated to analyse the ISP performance at the transition points as well as during kinematic movements, individually.

The first phase of kinematic testing was concerned with the response of the ISP to high-velocity rotations when returning to a hovering state following a rolling or pitching movement. At the maximum transition point, the loaded roll axis suffered a 10.37% increase in settling time in from the unloaded test and produced a final settling time of 1.89 seconds in response to a 43.48°/s rotation. The pitch axis settling time increased by 13.33% from the unloaded test to the loaded test. The final, loaded pitch axis settling time was found to be 1.92 seconds for a 46.51°/s rotation. The resulting graphs plotted from the obtained data show a linear relationship between the loaded axis settling times and rotation magnitude variables at the maximum extremities. Therefore, a linear interpolation of results was deemed appropriate. As such, the loaded pitch was interpolated to produce a settling time of 1.89 seconds for a rotation of 43.48°/s. The loaded ISP response time interpolation to a rotation of 43.48°/s allowed for direct comparison of settling times between the unloaded and the loaded ISP. The resulting loaded settling time of 1.89s approximated equivalent axis performance under worst-case scenario conditions.

The second phase of kinematic analysis sought to analyse the ISP response to rolling and pitching movements of the UAV over a duration of 10 seconds. The anticipated, ideal, outcome from the test was identical results to the previous dynamic hovering test results. Analysis of the unloaded roll axis data found a standard deviation of 0.243° in response to a UAV roll movement with magnitude 3.166°. The obtained standard deviation showed a 3.70% increase from the hovering state. The loaded roll axis, in response to a 2.157° magnitude UAV roll movement, produced data with a standard deviation of 0.422°. The obtained data showed a standard deviation decrease of 47.76% from the loaded axis hover test. The pitch axis results were analysed in the same manner. In the unloaded axis, a standard deviation of 0.352° was obtained, showing an increase of 4.83% from the hovering data, responding to a 5.74° UAV pitching movement. The loaded pitch axis responded to a 3.306° UAV pitching movement with a standard deviation of 0.6171°. This showed a 4.26% increase in standard deviation from the loaded hover test. The results of the test showed the system to remain stable under kinematic conditions, with negligible change in the results from the hovering test. In fact, the loaded roll axis showed a significant improvement in stabilisation capabilities in response to the kinematic movement.

9.3 Future Work

9.3.1 Future Work in FDM Optimisation

The scope of the experimentation conducted in the FDM optimisation portion of the research project can be found in Chapter 5. A noteworthy finding across all four experiments was the significant fluctuations in failure loads of the testing samples. These findings were noted to be caused by the anisotropic nature of the FDM process. In a bid to minimise the effect of anisotropy on the results, the three test samples were printed at different raster angles. Further testing of the effects of raster angles on the part strength of the ASTM samples would be beneficial to the research. This would identify the superior raster angle, which is most capable of mitigating the effects of anisotropy. As such, the fluctuations in failure loads would be reduced during testing, to produce more repeatable and reliable data. While ASTM test standards call for a minimum of five samples to be tested to account for anisotropy. However, a multidisciplinary interaction with project supervisors and material strength staff alike recommended the number of samples be reduced to three. This route was taken to reduce both the time and the computational efforts required during post-testing. Instead, anisotropy was accounted for through the variation of raster angles of the printed test samples – a method which is not mentioned in the ASTM standards. Nevertheless, repeating the testing with at least five samples, all at different raster angles would produce the most reliable, repeatable results.

9.3.2 Future Work in Control System Design

The discrepancies between the simulated response times and the experimentally obtained response time are indicative of errors within the ISP simulation model values. Despite the apparent errors, the control system was proven to produce acceptable results by the ISP testing process, as detailed in Chapter 7 and Chapter

8. Whilst the research project aimed to create the simplest, most efficient, and robust control system for the ISP, the approximation of the motor model parameters identified room for improvement within the model and, thus, the control system.

Future revisions of the ISP prototypes could incorporate a better estimation of motor parameter values using an existing Simulink blockset. Within the Simulink environment, a motor parameter estimation tool is available, under the Motor Control Blockset. This tool requires the input of physical motor motion data such as a sinusoidal shaft output. Once received, the estimation tool varies the motor parameter gains iteratively to obtain the closest possible recreation of the motor input data. The determined motor parameter gain values (which produced the closest recreation of the physical system output) can then be utilised within the Simulink model. This method is anticipated to greatly enhance the accuracy of the simulation model and cease the need to approximate the parameter gains using first principles.

9.4 Chapter Summary

Chapter 9 provided a succinct, detailed discussion of the research conducted throughout the project, as presented by the research dissertation. Points of discussion were aligned with the objectives put forth in Chapter 1.5. Insight gained throughout the literature review chapter was compared against the first three objectives. The detailed mechatronic design of the ISP was then discussed, including the electrical and mechanical subsystems. FDM parameter optimization was then explored as an empirical mass reduction technique prior to prototype manufacture. The mechatronic design portion of the research was noted to satisfy the fourth research objective. Next, the control system and software implementation were discussed. The results of the final ISP performance evaluation tests were discussed and compared to the target specifications derived in Chapter 3. The remaining objectives in Chapter 1.5 were then analysed against the findings of the final chapters of the dissertation. Potential areas of future work in the mechatronic ISP were discussed.

10 CONCLUSION

10.1 Introduction

This dissertation aimed to utilise the prevailing characteristics of the DM300 UAV for disaster management and humanitarian aid abetment. The UAV was shown, through leading research, to be suitable for the intended purpose, however, no commercially available attachments exist to equip the DM300 for payload transportation. Therefore, the research project aimed to develop a mechatronic ISP to be combined with the UAV to facilitate the transportation of resources, whilst making provisions for fragile resources, blood samples and vaccines.

Chapter 10 concludes the research project dissertation and addresses the contributions to research, insights gained, and recommendations developed throughout the research project duration. Future work regarding FDM optimisation, and the ISP is proposed.

10.2 Research Contribution

The research provided a solution to the lack of available payload transportation devices fit for UAV integration, as well as a viability assessment on the transportation of goods using a DM300 UAV, with an integrated ISP for payload stabilisation. Whilst there are currently aerial vehicles which have the sole purpose of transportation of goods, the integration of an ISP into the structure of an existing commercially available UAV for the sole purpose of payload transportation has not been documented according to this research. Addressing these niche areas of research formed the first research contribution. However, further analysis of the developed ISP provided three additional research contributions.

The next two research contribution areas hinged on the novelty of payload transportation and stabilisation using the mechatronic ISP. The novelty of this method is two-fold. Firstly, the method made provisions for the transportation of blood samples and vaccines, which are considered dangerous goods, which may not be shaken during transportation. Achieving the safe transportation of these dangerous goods contributed a new and improved transportation method in addition to the existing methods of hard mounting the payload to the UAV or suspending it from the UAV using a string. Secondly, unlike commercially available ISPs such as camera gimbals, the only restriction using this method is the 1.9kg payload mass threshold, provided that the prospective cargo can fit within the dimensional confinements of the ISP payload cradle. While additional legal restrictions may deem certain payloads unfit for transportation, the achievement of a universal payload ISP formed a research contribution.

The next research contribution is a reconfigurable mechatronic system development method for an unrestricted self-stabilising payload transport attachment for UAVs. The research presents a novel ISP designed specifically for the integration into the structure of DM300 UAV. However, following the completion of the research project, the mechanical aero frame assembly could be modified to attach to any

commercially available UAV for the same purpose. The electrical and electronic subsystems would not need to be altered for similar payload mass requirements. However, one would be able to scale the ISP presented by this research to meet the specifications of another UAV for the same purpose.

The final research contribution made by the project was in the field of FDM manufacturing. The use of FDM technology allowed components with more complex geometries and topologies to be manufactured faster, whilst maintaining the mechanical properties desired by the application. FDM technology does, however, produce parts which are intrinsically affected by anisotropy. The research proposed the process of destructive testing of FDM samples to analyse the effects of printing parameters to identify the parameter combination which was most applicable to aerial robotic prototypes. This combination was identified based on specific strength – the combination which provided the greatest part strength per unit part mass. The method provided results which were inclusive of the effects of anisotropy which agreed with FEA predictions, thus, validating both the FDM optimisation process and the structural integrity of parts manufactured using this method. Acceptance of the FDM optimisation process, results, and strength prediction data by the International Conference on Informatics in Control, Automation, and Robotics (ICINCO) as well as the Rapid Product Development Association of South Africa (RAPDASA) international conference further accentuated its pertinence in aerial robotic applications. In this regard, the data produced using this method formed its own research contribution as it will be made available to fellow researchers who require a strength prediction method for FDM fabricated components.

10.3 Research Challenges

Several challenges were faced throughout the research project relating to the research, conceptualisation, and design of the ISP. In the research phase of the project, a lack of previous research was identified relating specifically to the roll-pitch ISP configuration, as utilised within the research project. This posed a challenge to the initial synthesis of a geometric layout for the design due to the lack of existing products from which inspiration could be drawn. Additionally, the development of the ISP control system and simulation model was impacted, with minimal existing information being available to guide the process (pertaining specifically to the roll-pitch configuration). The result of this challenge was an unsophisticated control system, which produced acceptable results, but left scope for further refinement and improvement.

The next challenge faced was the determination of component specifications during the design conceptualisation phase. The intrinsic reliance of the ISP component specifications on the final operational payload required the final payload to be known before the design could commence. An intuitive expected maximum payload was specified to overcome this challenge. However, the expected maximum payload was specified in excess of the anticipated final payload to ensure a reserve factor on selected component specifications when the final payload was determined.

10.4 Recommendations

The research project aimed to produce a lightweight ISP fit for integration into the DM300 UAV to aid disaster management and humanitarian aid strategies. The objectives assigned to the research project to achieve the aim were all met. Moreover, the third research objective was satisfied by identifying FDM as an applicable manufacturing technology for the design. Using FDM to fabricate the ISP components induced additional complexity and mass to the assembly as a modular design was required for the components to be fit for FDM manufacturing. Such a design required additional fasteners which added mass to the assembly, and additional components yielding a greater assembly complexity. However, the modular nature of the design proved to enhance the serviceability of the system and the replaceability of components. Nevertheless, the surface finish on the components showed the stair stepping effect known to be associated with the FDM process. Whilst steps were taken to mitigate the effect as far as possible, it proved impossible to avoid the phenomenon altogether. Therefore, it is recommended that the FDM components of the ISP be coated with epoxy resin and cured in a vacuum chamber to produce a smooth, glassy surface finish. This method was considered through the course of the manufacture and assembly process, but the resulting mass addition from the epoxy resin could not be justified without knowing the final assembly mass. However, knowing the final 1900-gram allowable payload mass has a 90-gram leeway, the epoxy resin coating is anticipated to have minimal effect on the final allowable payload mass post coating.

10.5 Future Work

Two areas of future work were identified following the completion of the research project. Firstly, in the area of FDM optimisation, future work is required to investigate the effect of raster angles on part strength. Identification of the most stable raster angle would allow the ASTM testing to be completed with reduced fluctuations in test sample breaking loads. The resulting implications of the future work would be more uniform results with closer correlations to the data trendlines. To further enhance the predictability of the test data in the presence of anisotropy, the number of testing samples per increment in each test segment should be increased to at least five in both tension and flexure.

Future work in the control system design of the ISP is suggested to improve the simulation model correlation to the real system. Utilising the Simulink motor parameter estimation tool will provide improved accuracy to the servo motor model within the simulation and negate the need for parameter estimation using first principal calculations. While the control system of the ISP proved to generate the PID gains with acceptable accuracy, further refinement of the simulation model would undoubtedly generate more precise gains, which could potentially produce improved performance capabilities.

10.6 Chapter Summary

Chapter 9 served to conclude the research dissertation and outline the main research components. The dissertation details the research, design, manufacture, and performance evaluation of a two-axis, roll-pitch, ISP as a solution to the lack of UAV-compatible payload transportation devices. The resulting mechatronic device was developed to aid in disaster management and humanitarian aid efforts. A comprehensive performance analysis, consisting of four phases of experimental testing, was carried out. The dissertation showed the aim of the project to have been achieved, and all research objectives met.

REFERENCES

[1] A. Ceruti, P. Marzocca, A. Liverani and C. Bil, "Maintenance in aeronautics in an Industry 4.0 context: The role of Augmented Reality and Additive Manufacturing," *Journal of Computational Design and Engineering,* vol. 6, pp. 516-526, 2019.

[2] National Research Council of the National Academics, Improving Disaster Management: The Role of IT in Mitigation, Preparedness, Response, and Recovery, National Research, 2007.

[3] Disaster Medicine, [Online]. Available: https://disastermedicine.wordpress.com/four-phases-of-disaster-management/. [Accessed 16 December 2021].

[4] International Federation of Red Cross and Red Crescent Societies, "IFRC," 2022. [Online]. Available: https://www.ifrc.org/what-disaster. [Accessed 4 January 2022].

[5] AkitaBox, "AkitaBox," 21 June 2023. [Online]. Available: https://home.akitabox.com/blog/4-phases-of-disaster-management/. [Accessed 26 August 2023].

[6] H. L. Tay, R. Banomyong, P. Varadejsatitwong and P. Julagasigorn, "Mitigating Risks in the Disaster Management Cycle," *Advances in Civil Engineering,* vol. 2022, pp. 1-14, 2022.

[7] DJI Enterprises, [Online]. Available: https://enterprise.dji.com/public-safety/rescue-services. [Accessed 14 May 2024].

[8] DJI Enterprise, "Data Sheet - Matrice 300 RTK," OPTRON (Pty) Ltd, Centurion.

[9] Engineering 360, "globalspec," American Institute of Aeronautics and Astronautics, Inc., 2004. [Online]. Available: https://www.globalspec.com/reference/40223/203279/appendix-a-significant-dates-in-unmanned-aviation. [Accessed 23 March 2022].

[10] M. Mozaffari, W. Saad, M. Bennis and Y.-H. a. D. M. Nam, "A Tutorial on UAVs for Wireless Networks: Applications, Challenges, and Open Problems," *IEEE Communications Surveys & Tutorials,* vol. 21, pp. 2334-2360, 2019.

[11] A. Fotouhi, H. Qiang, M. Ding and J. Yuan, "Survey on UAV Cellular Communications: Practical Aspects, Standardization Advancements, Regulation, and Security Challenges," *IEEE Communications Surveys & Tutorials,* vol. 21, pp. 3417-3442, 2019.

[12] C. Stöcker, R. Bennett, F. Nex, M. Gerke and J. Zevenbergen, "Review of the Current State of UAV Regulations," *Remote Sensing 9,* vol. 5, p. 459, 2017.

[13] D. Rahman, A. Sitorus and A. Condro, "From Coastal to Montane Forest Ecosystems, Using Drones for Multi-Species Research in the Tropics," *MDPI Journals: Drones 2022,* vol. 6, no. 1, 2021.

[14] P. Janik, M. Zawistowski, R. Fellner and G. Zawistowski, "Unmanned Aircraft Systems Risk Assessment Based on SORA for First Responders and Disaster Management," *Journal of Applied Sciences,* vol. 11, no. 12, pp. 1-12, 2021.

[15] DSLRPros, "DJI Matrice 300 RTK VS 210: What is the Difference? - DSLRPros Official Blog," DSLRPros, Chatsworth, California, 8 May 2020.

[16] Alternative Pest Control (ALPECO), “IP Rating Reference Chart,” ALPECO, Rotorua, New Zealand.

[17] DJI, “DJI Matrice 300 Specifications,” DJI, China, 2022.

[18] DJI Enterprises, “dji.com,” [Online]. Available: https://www.dji.com/matrice-300?site=brandsite&from=nav. [Accessed 22 August 2022].

[19] J. Sathish Kumar, S. Kumar, M. Choksi and M. Zaveri, “Collaborative data acquisition and processing for post disaster management and surveillance related tasks using UAV-based IoT cloud,” *International Journal of Ad Hoc and Ubiquitous Computing,* vol. 34, no. 4, pp. 216-232, 2020.

[20] A. Islam and S. Shin, “A blockchain-based secure healthcare scheme with the assistance of unmanned aerial vehicle in In-ternet of Things,” *Computers & Electrical Engineering,* vol. 84, 2020.

[21] K. Laksham, “Unmanned aerial vehicle (drones) in public health: A SWOT analysis,” *Journal of Family Medicine and Primary Care,* vol. 8, no. 2, pp. 342-346, 2019.

[22] M. Eichleay, E. Evens, K. Stankevitz and C. Parker, “Using the Unmanned Aerial Vehicle Delivery Decision Tool to,” *Global Health: Science and Practice,* vol. 7, no. 4, pp. 500-506, 2019.

[23] J. E. Scott and C. H. Scott, “Drone Delivery Models for Healthcare,” in *Proceedings of the 50th Hawaii International Conference on System Sciences*, Honolulu, 2017.

[24] Y. Karaca, M. Cicek, O. Tatli, A. Sahin, S. Pasli, M. F. Beser and S. Turedi, “The potential use of unmanned aircraft systems (drones) in mountain search and rescue operations,” *The American Journal of Emergency Medicine,* vol. 36, no. 4, pp. 583-588, 2018.

[25] M. Javaid, I. H. Khan, R. P. Singh, S. Rab and R. Suman, “Exploring contributions of drones towards Industry 4.0,” *Industrial Robot,* vol. 49, no. 3, pp. 476-490, 2022.

[26] B. Z. Boukoberine MN, “A critical review on unmanned aerial vehicles power supply and energy management: Solutions, strategies, and prospects,,” *Applied Energy,* vol. 255, 2019.

[27] C. Werber, “Huff Post,” Quartz Africa, 14 October 2014. [Online]. Available: https://www.huffpost.com/entry/drone-delivery-service-launched-in-rwanda_n_5800f353e4b0162c043b7739. [Accessed 21 February 2023].

[28] S. Perry, “Aljazeera,” 27 October 2016. [Online]. Available: https://www.aljazeera.com/news/2016/10/27/drones-launch-off-grid-healthcare-in-rural-madagascar/. [Accessed 21 February 2023].

[29] P. Van de Voorde, A. Momont, S. Guatama, C. M. Ionescu, P. De Paepe and N. Fraeyman, “The drone ambulance [A-UAS]: golden bullet or just a blank?,” *Resuscitation,* vol. 116, pp. 46-48, 2016.

[30] W. J, “Newsweek,” 5 February 2016. [Online]. Available: https://www.newsweek.com/2016/02/05/ndia-organ-transplant-drones-419013. [Accessed 21 February 2023].

[31] J. R. Scalea, S. Restaino, M. Scassero, S. T. Bartlett and N. Wereley, “The final frontier? Exploring organ transportation by drone,” *American Journal of Transportation,* vol. 19, no. 3, pp. 962-964, 2019.

[32] E. Chow, A. Cuadra and C. Whitlock, “The Washington Post,” The Washington Post, 19 January 2016. [Online]. Available: https://www.washingtonpost.com/graphics/national/drone-crashes/database/. [Accessed 21 February 2023].

[33] R. K. Saini, M. S. Raju and A. Chail, “Cry in the sky: Psychological impact on drone operators,” *Industrial Psychiatry Journal,* vol. 30, no. 1, pp. S15-S19, 2022.

[34] A. Gangwal, A. Jain and S. Mohanta, “Blood Delivery by Drones: A Case Study on Zipline,” *International Journal of Innovative Research in Science, Engineering and Technology,* vol. 8, no. 8, pp. 8760-8766, 2019.

[35] B. Y. Lee, “Drones to the Rescue,” Massachusetts Institute of Technology (MIT), Baltimore, Maryland, 2017.

[36] T. V. D. Schyff, “Drone Laws,” Drone Laws For a Safer Airspace, 20 October 2021. [Online]. Available: https://drone-laws.com/drone-laws-in-south-africa/#Agencies_Responsible_for_regulating_drones_in_the_Republic_of_South_Africa. [Accessed 23 March 2023].

[37] South African Civil Aviation Authority, “Civil Aviation Act, 2009 (Act No. 13 of 2009): SA-CATS 101,” SACAA, 2009.

[38] The South African Civil Aviation Authority, “CIVIL AVIATION ACT, 2009 (ACT NO. 13 OF 2009) EIGTH AMENDMENT OF THE CIVIL AVIATION REGULATIONS, 2015,” The South African Department of Transport, 27 May 2015.

[39] South African Civil Aviation Authority, “Remotely Piloted Aircraft Systems Regulations,” SACAA.

[40] South African Government, “Civil Aviation Act, 2009 (Act No. 13 Of 2009),” South African Government, Centurion, 2015.

[41] M. J. Hilkert, “Inertially Stabilised Platform Technology Concepts and Principles,” IEEE Control Systems Magazine, 2008.

[42] Z. Mahmoud, H. Ghanbarpourasi and M. R. Arvan, “Initial Alignment Error Analysis for Gimbaled Navigation System,” in *The 15th International Conference of Iranian Aerospace Society*, 2016.

[43] DJI Enterprises, [Online]. Available: https://www.dji.com/zenmuse-h20-series/specs. [Accessed 16 February 2023].

[44] Z. Ding, F. Zhao, Y. Lang, Z. Jiang and J. Zhu, “Anti-Disturbance Neural-Sliding Mode Control for Inertially Stabilized Platform With Actuator Saturation,” *IEEE Access,* vol. 7, pp. 92220-92231, 2019.

[45] N. Yu and J. Shang, “A Uniform Method of Mechanical Disturbance Torque Measurement and Reduction for the Seeker Gimbal in the Assembly Process,” *Mathematical Problems in Engineering,* vol. 2017, pp. 1-12, 2017.

[46] S. Frasnedo, G. Sandou, G. Duc, C. Chapuis and P. Feyel, “Line of sight controller tuning using Bayesian optimisation: application to adouble stage stabilisation platform,” *International Journal Of Systems Science,* vol. 50, no. 1, pp. 8-22, 2019.

[47] H. F. Mokbel, L. Q. Ying and C. G. Hua, “A NEW CONCEPT FOR THE LINE OF SIGHT STABILIZATION “BALL STABILIZATION”,” in *16th International Conference on Applied Mechanics and Mechanical Engineering,* Cairo, Egypt, 2014.

[48] W. J. Titterton D, Strapdown Inertial Navigation Technology 2nd Edition, London: The Institution of Engineering and Technology, 2004.

[49] M. M, “Inertially Stabilized Platforms for Optical Imaging Systems,” *IEEE Control Systems Magazine,* pp. 47-64, February 2008.

[50] J. H. Hepworth, “Systems Development of a Two-Axis,” The University of Cape Town, Cape Town, 2018.

[51] S. Li and M. Zhong, “High-Precision Disturbance Compensation for a Three-Axis Gyro-Stabilized Camera Mount,” *IEEE/ASME Transactions on Mechatronics,* vol. 20, no. 6, pp. 3135-3147, 2015.

[52] D. H. Lee, D. Q. Tran, Y. B. Kim and S. Chakir, “A Robust Double Active Control System Design for Disturbance Suppression of a Two-Axis Gimbal System,” *Electronics,* vol. 1638, no. 9, pp. 1-18, 4 October 2020.

[53] J. Osborne, G. Hicks and R. Fuentes, “Global Analysis of The Double-Gimbal Mechanism,” *IEEE Control Systems Magazine,* vol. 28, no. 4, pp. 44-64, 2008.

[54] G. D. Goh, G. L. Agarwala, G. L. Goh, V. Dikshit, S. L. Sing and W. Y. Yeong, “Additive manufacturing in unmanned aerial vehicles (UAVs): Challenges and potential,” *Aerospace Science and Technology,* vol. 63, pp. 140-151, 2017.

[55] D. Walker, D. Lui and A. Jennings, “Wing design utilizing topology optimization and additive manufacturing,” in *Additive Manufacturing Handbook,* Boca Raton, CRC Press, 2017, p. 4.

[56] U. Chandrasekhar, L. J. Yang, B. Esakki, S. Suryanarayanan and S. Salunkhe, “Rapid Prototyping Of Flapping Mechanisms For Monoplane And Biplane Ornithopter Configurations,” *International Journal of Modern Manufacturing Technologies,* vol. 9, no. 2, pp. 18-22, 2017.

[57] H. A. Wong KV, “A Review of Additive Manufacturing,” *International Scholarly Research Network,* pp. 1-5, 17 June 2012.

[58] eSUN, “3D Printing Filament Specifications,” eSUN, Shenzhen, China.

[59] A. Malik, M. L. Ul Haq, A. Raina and K. Gupta, “3D printing towards implementing Industry 4.0: sustainability aspects, barriers and challenges,” *Industrial Robot,* vol. 49, no. 3, pp. 491-511, 2021.

[60] M. Harcus, “Fused Deposition Modelling (FDM) To Fabricate A Transitional Vertical Take-Off And Landing(Vtol) Unmanned Aerial Vehicle (Uav) Fortransportation Of Medical Supplies Inunderdeveloped Areas,” The University of KwaZulu-Natal, Durban, 2020.

[61] J. Pakkanen, D. Manfredi, P. Minetola and L. Luliano, “About the Use of Recycled or Biodegradable Filaments for Sustainability of 3D Printing,” in *International Conference on Sustainable Design and Manufacturing*, 2017.

[62] R. Zagidullin, N. I. Zezin and N. V. Rodionov, “Improving the quality of FDM 3D printing of UAV and aircraft parts and assemblies by parametric software changes,” *IOP Conference Series: Materials Science and Engineering,* pp. 1-6, January 2021.

[63] A. Y. Dmitriev, R. S. Zagidulin and T. A. Mitroshkina, “Special Aspects of Quality Assurance in the Design, Manufacture, Testing of Aerospace Engineering Products,” in *IOP Conference Series: Materials Science and Engineering*, Moscow, Russian Federation, 2020.

[64] F. M. Mwema and E. T. Akinlabi, “Basics of Fused Deposition Modelling (FDM),” in *Fused Deposition Modeling Strategies for Quality Enhancement*, Springer International Publishing, 2020, pp. 1-15.

[65] P. J. Nuñez, A. Rivas, E. Garcia-Plaza, E. Beamud and A. Sanz-Lobera, “Dimensional and Surface Texture Characterization in Fused Deposition Modelling (FDM) with ABS plus,” *Procedia Engineering,* vol. 132, pp. 856-863, 2015.

[66] O. Lužanin, D. Movrin and M. Plancak, “Effect Of Layer Thickness, Deposition Angle, And Infill On Maximum Flexural Force In FDM-Built Specimens,” *Journal for Technology of Plasticity,* vol. 39, no. 1, pp. 50-58, 2014.

[67] B. Goldschmidt, “All3DP,” All3DP, 20 October 2022. [Online]. Available: https://all3dp.com/2/cura-infill-patterns-all-you-need-to-know/. [Accessed 7 March 2023].

[68] J. O'Connell, “All3DP,” All3DP, 18 November 2021. [Online]. Available: https://all3dp.com/2/strongest-infill-pattern/. [Accessed 7 March 2023].

[69] J. Johansson, “Modelling and control of an advanced camera gimbal,” Linköpings universitet, Linköping, Sweden, 2012.

[70] A. I. Tas, M. Iscan, A. B. Ozden, E. Cinar, B. Vural and C. Yilmaz, “Real Time Discrete Control Algorithm for Gimbal System Design in Mini Unmanned Aerial Vehicles,” in *International Congress on Human-Computer Interaction, Optimization and Robotic Applications (HORA)*, Istanbul, 2022.

[71] B. J. Kuipers, “Quaternions and Roatation Sequences,” *Geometry, Integrability and Quantization,* vol. 1, no. 10, pp. 127-143, 1999.

[72] International Organization for Standardization (ISO), “ISO 3826-1,” International Organization for Standardization (ISO), Geneva, Switzerland, 2019.

[73] D. Enterprises, “DJI Enterprises,” 21 April 2021. [Online]. Available: https://www.dji.com/global/downloads/products/matrice-300. [Accessed 18 December 2023].

[74] DJI, “dji.com,” [Online]. Available: https://www.dji.com/downloads/products/matrice-300. [Accessed 25 April 2022].

[75] Micro Robotics, “robotics.org,” Micro Robotics, [Online]. Available: https://www.robotics.org.za/DS3235-270. [Accessed 22 August 2022].

[76] D. Deng, “Li-ion batteries: basics, progress, and challenges,” *Energy Science & Engineering,* vol. 3, no. 5, pp. 385-418, 2015.

[77] DIY Electronics, “diyelectronics,” [Online]. Available: https://www.diyelectronics.co.za/store/li-ion-li-po/2753-li-ion-battery-pack-74v-2600mah-2c-2s1p.html. [Accessed 22 August 2022].

[78] TDK InvenSense, “InvenSense,” TDK InvenSense, [Online]. Available: https://invensense.tdk.com/smartmotion/. [Accessed 21 September 2022].

[79] Bosch Sensortec, “BNO055 Intelligent 9-axis absolute orientation sensor Data sheet,” Bosch, 2016.

[80] M. J. Hyder, N. N. Malik and A. Shah, “Experimental Investigation On Techniques To Improve The Accuracy Of MPU 6050 For Tilt Measurement,” *Journal Of Harbin Institute Of Technology,* vol. 54, no. 9, pp. 158-174, 2022.

[81] TDK InvenSense, “InvenSense,” TDK InvenSense, [Online]. Available: https://invensense.tdk.com/products/motion-tracking/6-axis/mpu-6500/. [Accessed 21 September 2022].

[82] Z. Lin, Y. Xiong, H. Dai and X. Xia, “An Experimental Performance Evaluation of the Orientation Accuracy of Four Nine-Axis MEMS Motion Sensors,” in *5th International Conference on Enterprise Systems*, Beijing, China, 2017.

[83] Adafruit, “Adafruit BNO055 Absolute Orientation,” Adafruit, 2022.

[84] K. Oliynyk, “WebbyLab,” 6 April 2023. [Online]. Available: https://webbylab.com/blog/arduino-vs-raspberry-pi-key-differences-comparison-table/#:~:text=Arduino%20is%20better%20suited%20for,cheaper%20than%20Raspberry%20Pi%20devices.. [Accessed 25 October 2023].

[85] Arduino, “Arduino Store,” [Online]. Available: https://store-usa.arduino.cc/products/arduino-nano?selectedStore=us. [Accessed 22 August 2022].

[86] B. Gumusel, Kavurmacloglu and C. Camci, “Aerodynamic drag characteristics and shape design of a radar antenna used for airport ground traffic control,” *Progress in Computational Fluid Dynamics An International Journal,* pp. 1-9, 2014.

[87] J. Carvill, Mechanical Engineer's Data Handbook, Butterworth-Heinemann, 1994.

[88] Y. A. Cengel and M. A. Boles, “Properties Of The Atmosphere At High Altitude,” in *Thermodynamics - An Enginerring Approach*, New York, McGraw-Hill Education, 2015, p. 923.

[89] L. U. Schrader, “Receptivity of Boundary-Layer Flows over Flat and Curved Walls,” KTH Royal Institute of Technology, Stockholm, Sweden, 2010.

[90] S. Behara and S. Mittal, “Transition of the boundary layer on a circular cylinder in the presence of a trip,” *Journal of Fluids and Structures,* vol. 27, pp. 702-715, 2011.

[91] G. Elliott, “GrabCad,” 11 December 2019. [Online]. Available: https://grabcad.com/library/dsservo-ds3225mg-metal-gear-25kg-4-8-6-5v-servo-1. [Accessed 1 August 2022].

[92] R. Mohamed, “GrabCad,” 28 February 2022. [Online]. Available: https://grabcad.com/library/arduino-nano-26/details?folder_id=11829621. [Accessed 1 August 2022].

[93] P. Pamir, “GrabCad,” 10 October 2017. [Online]. Available: https://grabcad.com/library/adafruit-bno055-1/details?folder_id=3590424. [Accessed 1 August 2022].

[94] M. Eryildiz, “The Effects Of Infill Patterns On The Mechanical Properties Of 3D Printed Pla Parts Fabricated By FDM,” *Ukrainian Journal Of Mechanical Engineering And Materials Science,* vol. 7, no. 1, pp. 1-8, 2021.

[95] S. Raja, A. P. Agrawal, P. P. Patil, P. Thimothy, R. Y. Capangpangan, P. Singhal and M. T. Wotango, “Optimization of 3D Printing Process Parameters of Polylactic Acid Filament Based on the Mechanical Test,” *International Journal of Chemical Engineering,* pp. 1-7, 2022.

[96] A. M. Forster, “Materials Testing Standards for Additive Manufacturing of Polymer Materials: State of the Art Standards Applicability,” National Institute of Standards and Technology, 2015.

[97] B. Jackson, K. Fouladi and B. Eslami, “Multi-Parameter Optimization of 3D Printing Condition for Enhanced Quality and Strength,” *Polymers,* pp. 1-13, 2022.

[98] American Society for Testing and Materials (ASTM) International, “D638-14: Standard Test Method for Tensile Properties of Plastics,” American Society for Testing and Materials (ASTM) International, West Conshohocken, 2015.

[99] American Society for Testing and Materials (ASTM) International, “D790-17: Standard Test Methods for Flexural Properties of Unreinforced and Reinforced Plastics and Electrical Insulating Materials,” American Society for Testing and Materials (ASTM) International, West Conshohocken, 2017.

[100] A. O. Elnady and A. Mohamed, “Implementation of Position Control Servo DC Motor with PID Controller to Humanoid Robot Arm,” in *The 5th International Under-Graduate Research Conference,* Cairo, 2021.

[101] L. S. Mezher, “Characteristics of Servo DC Motor with PID Controller,” *Journal of Mechanical Engineering Research and Developments* , vol. 44, no. 2, pp. 392-400, 2021.

[102] G. W. Youkin, “Electric Servo Motor Equations And Time Constants,” Bulls Eye Marketing, Inc, Fond du Lac.

[103] E. H. Kapeel, A. M. Kamel and A. O. El Farouk, “Modeling and Simulation of Low Cost MEMS Gyroscope Using MATLAB (SIMULINK) for UAV Autopilot Design,” in *IT Misr University for Science and Technology (MUST) CONFERENCE,* Giza, Egypt, 2019.

[104] S. Muthuviswadharani, G. Prabhakar and S. Selvaperumal, “Analysis on Soft Sensor Design in Simulink,” in *International Conference on Advanced Communication Control and Computing Technologies (ICACCCT),* Ramanathapuram, India, 2016.

[105] S. Chatterjee, “Emeritus,” 23 January 2023. [Online]. Available: https://emeritus.org/blog/coding-arduino-programming-language/. [Accessed 11 March 2024].

[106] E. Bernardes and S. Viollet, “Quaternion to Euler angles conversion: A direct, general and computationally efficient method,” *PLoS ONE,* vol. 17, no. 11, 2022.

[107] J. L. B. Claraco, “A tutorial on SE(3) transformation parameterizations and on-manifold optimization,” Cornell University, New York, 2022.

[108] M. Toso, E. Pennestri and V. Rossi, “SA multibody simulator for spacecrafts’ ascent and landing in a microgravity environment,” *CEAS Space Jounal,* vol. 7, no. 3, 2015.

[109] H. Parwana and M. Kothari, “Quaternions and Attitude Representation,” Cornell University, New York, 2017.

[110] DIYElectronics, “diyelectronics,” [Online]. Available: https://www.diyelectronics.co.za/store/memory/512-micro-sd-card-module.html?search_query=micro+sd&results=161. [Accessed 22 January 2024].

[111] W. T. Maphumulo and B. R. Bhengu, “Challenges of quality improvement in the healthcare of South Africa post-apartheid: A critical review,” *Curatioinis,* vol. 42, no. 1, 2019.

[112] South African Government, “Disaster Management Act,” South African Government, Cape Town, 2003.

[113] National Research Council, Improving disaster management, Washington, D.C: National Research Council, 2007.

[114] DJI Enterprises, “dji.com,” [Online]. Available: https://www.dji.com/matrice-300. [Accessed 16 February 2023].

[115] DJI Enterprises, “dji store.com,” [Online]. Available: https://store.dji.com/guides/camera-gimbal-stabilizer/. [Accessed 16 February 2023].

[116] Optron, [Online]. Available: https://optron.com/dji/wp-content/uploads/2020/05/ds_dji-matrice-300-rtk.pdf. [Accessed 6 January 2022].

[117] Physiopedia, [Online]. Available: https://www.physio-pedia.com/Disaster_Management#cite_note-p2-3. [Accessed 6 January 2022].

[118] D. Enterprise, “DJI Enterprise,” DJI Enterprise, [Online]. Available: https://enterprise.dji.com/public-safety/rescue-services. [Accessed 23 March 2023].

[119] Github, “DS3235-270 Datasheet,” [Online]. Available: https://github.com/microrobotics/DS3235-270/blob/master/DS3235-270_datasheet.pdf. [Accessed 21 August 2022].

[120] Y. S. Narayan and S. A. Kumar, “Tensile Testing and Evaluation of 3D-Printed PLA Specimens as per ASTM D638 Type IV Standard,” *Lecture Notes in Mechanical Engineering,* pp. 79-95, 2019.

[121] I. A. Meer, M. Ozger, M. Lundmark, K. W. Sung and C. Cavdar, “Ground Based Sense and Avoid System for Air Traffic Management,” IEEE Xplore, Istanbul, Turkey, 2019.

[122] R. Jones, P. Haufe, E. Sells, P. Iravani, V. Olliver, C. Palmer and A. Bowyer, "RepRap – the replicating rapid prototyper," *Robotica,* vol. 29, no. 1, pp. 177-191, 2011.

[123] M. Usman, "Quadcopter Modelling and Control With MATLAB/Simulink Implementation," LAB University of Applied Sciences, 2020.

[124] S. Li, M. Zhong and J. Qin, ""The Internal Model Control Design of Three-axis Inertially Stabilized Platform for Airborne Remote Sensing," *8th IEEE International Symposium on Instrumentation and Control Technology (ISICT),* pp. 5-10, 2012.

APPENDICES

APPENDIX A: PROJECT MANAGEMENT

Table A-1: Project Budget Overview

Component	Quantity	Specification	Source	Cost
IMU	2	BNO055	Amazon	R3273.41
Microcontroller	2	Arduino Nano	DIY Electronics	R347.74
Servo Motor	2	DSSERVO 35kg.cm	Micro Robotics	R355.35
Battery Pack	2	7.4V 2600mAh Li-Ion	DIY Electronics	R1179.90
Bearings	16	683-RS Ball Bearing	Bearing Man Group	R293.34
Battery Charger	1	XY-L30A	Amazon	R575.00
Filament	1	CCTREE 1kg 1.75mm PLA	DIY Electronics	R252.13
Filament	1	SunLu 0.5kg 1.75mm TPU	DIY Electronics	R226.04
Data Logger	1	Micro SD Card Module	DIY Electronics	R34.74
M2.5 Nut	8	Stainless Steel	EIS	R5.76
M2.5 Screw	4	2.5x6 Stainless Steel	EIS	R7.56
M3 Nut	14	Stainless Steel	EIS	R5.46
M3 Washer	31	3x7 Stainless Steel	EIS	R3.72
M3 Cap Screw	10	3x20 Stainless Steel	EIS	R8.20
M3 Cap Screw	3	3x10 Stainless Steel	EIS	R1.65
M3 Cap Screw	8	3x15 Stainless Steel	EIS	R5.52
M3 Screw	1	3x55 Stainless Steel	EIS	R2.05
M4 Screw	8	4x12 Galvanised Steel	EIS	R10.24
M4 Screw	4	4x40 Galvanised Steel	EIS	R9.32
M4 Nut	13	Galvanised Steel	EIS	R1.82
M4 Washer	8	Stainless Steel	EIS	R1.12
Sub-Total				R6472.28
Total				R7443.12

APPENDIX B: FDM OPTIMISATION

B.1 FDM Optimisation Testing Data

The following tables contain the testing data which was obtained throughout the FDM optimisation experimental procedure. The tabulated data was used to produce the summarised data graphs portrayed in Chapter 5.

Table B-1: Layer Height Testing Results in Flexure

Parameter	Unit	1	2	3	4	5
Layer Height	mm	0.15	0.2	0.25	0.3	0.35
Infill percentage	%	10	10	10	10	10
Mass (g)	g	1.80	2.09	2.29	2.38	2.73
Print time	min	21.20	18.90	17.00	16.10	15.50
Failure load 1	kg	3.74	3.94	3.16	3.12	3.94
Failure load 2	kg	3.85	4.12	3.44	3.23	3.56
Failure load 3	kg	4.19	3.66	4.03	3.23	3.62
Average failure load (F) in flexure	kg	3.93	3.91	3.54	3.19	3.70
Flexural stress	MPa	45.14	44.91	40.73	36.71	42.61
Specific Strength	kg/g	2.18	1.87	1.55	1.34	1.36

Table B-2: Layer Height Testing Results in Tension

Parameter	Unit	1	2	3	4	5
Layer Height	mm	0.15	0.2	0.25	0.3	0.35
Infill percentage	%	10	10	10	10	10
Mass (g)	g	1.70	2.05	2.31	2.44	2.76
Print time	min	21.20	18.90	17.00	16.10	15.50
Failure load 1	kg	26.68	28.78	30.56	28.78	35.09
Failure load 2	kg	24.70	27.73	31.95	31.76	40.38
Failure load 3	kg	24.21	28.19	30.19	28.93	38.42
Average failure load (T) in tension	kg	25.20	28.24	30.90	29.82	37.96
Tensile stress	MPa	31.02	34.76	38.04	36.72	46.74
Specific strength	kg/g	14.82	13.77	13.38	12.22	13.76

Table B-3: Gyroid Infill Pattern Testing Results in Flexure

Parameter	Unit	1	2	3	4	5
Layer Height	mm	0.3	0.3	0.3	0.3	0.3
Infill percentage	%	10	20	30	40	50
Mass	g	2.48	2.92	3.30	3.55	4.05
Print time	min	16.50	20.00	24.70	29.17	33.33
Failure load 1	kg	3.4	3.76	4.15	4.26	5.6
Failure load 2	kg	3.39	3.9	3.63	4.06	5.54
Failure load 3	kg	3.64	3.67	3.8	4.38	5.57
Average failure load (F) in flexure	kg	3.48	3.78	3.86	4.23	5.57
Flexural stress	MPa	39.97	43.42	44.37	48.67	64.03
Specific Strength	kg/g	1.40	1.29	1.17	1.19	1.38

Table B-4: Cubic Infill Pattern Testing Results in Flexure

Parameter	Unit	1	2	3	4	5
Layer Height	mm	0.3	0.3	0.3	0.3	0.3
Infill percentage	%	10	20	30	40	50
Mass	g	2.38	3.04	3.23	3.59	4.05
Print time	min	16.10	18.00	18.67	20.67	21.17
Failure load 1	kg	3.12	4.82	3.93	4.67	5.92
Failure load 2	kg	3.23	4.72	4.51	4.3	6.37
Failure load 3	kg	3.23	4.87	4.57	4.88	6.43
Average failure load (F) in flexure	kg	3.19	4.80	4.34	4.62	6.24
Flexural stress	MPa	36.71	55.22	49.85	53.07	71.74
Specific Strength	kg/g	1.34	1.58	1.34	1.29	1.54

Table B-5:Gyroid Infill Pattern Testing Results in Tension

Parameter	Unit	1	2	3	4	5
Layer Height	mm	0.3	0.3	0.3	0.3	0.3
Infill percentage	%	10	20	30	40	50
Mass	g	2.51	2.90	3.30	3.53	4.04
Print time	min	16.50	20.00	24.70	29.17	33.33
Failure load 1	kg	33.33	34.42	34.11	38.23	48.98
Failure load 2	kg	30.28	31.76	34.50	38.03	49.23
Failure load 3	kg	29.83	36.07	37.44	31.17	53.67
Average failure load (T) in tension	kg	31.15	34.08	35.35	35.81	50.62
Tensile stress	MPa	3.91	3.70	3.38	3.06	3.91
Specific Strength	kg/g	12.41	11.75	10.71	10.14	12.53

Table B-6:Cubic Infill Pattern Testing Results in Tension

Parameter	Unit	1	2	3	4	5
Layer Height	mm	0.3	0.3	0.3	0.3	0.3
Infill percentage	%	10	20	30	40	50
Mass	g	2.44	3.04	3.22	3.6	4.05
Print time	min	16.1	18	18.67	20.67	21.17
Failure load 1	kg	28.78	40.90	32.74	39.60	54.87
Failure load 2	kg	31.76	38.29	35.87	42.47	51.14
Failure load 3	kg	28.93	38.62	39.61	39.99	54.48
Average failure load (T) in tension	kg	29.82	39.27	36.07	40.69	53.50
Tensile stress	MPa	36.72	41.80	33.82	34.08	40.49
Specific Strength	kg/g	12.22	12.92	11.20	11.30	13.21

Table B-7:Infill and Perimeter Testing Results in Flexure

Parameter	Unit	1	2	3	4	5
Layer Height	mm	0.3	0.3	0.3	0.3	0.3
Infill percentage	%	40	30	25	20	15
Perimeter layers	-	1	2	3	3	4
Mass	g	3.55	3.11	3.54	3.23	3.37
Print time	min	23.17	25.17	24.33	20.5	21.84
Failure load 1	kg	4.26	3.62	6.26	6.47	6.72
Failure load 2	kg	4.06	3.45	6.13	6.53	6.89
Failure load 3	kg	4.38	3.76	6.38	6.6	6.77
Average failure load (F) in flexure	kg	4.23	3.61	6.26	6.53	6.79
Flexural stress	MPa	48.67	41.50	71.93	75.11	78.10
Specific Strength	kg/g	1.19	1.16	1.77	2.02	2.02

Table B-8:Infill and Perimeter Testing Results in Tension

Parameter	Unit	1	2	3	4	5
Layer Height	mm	0.3	0.3	0.3	0.3	0.3
Infill percentage	%	40	30	25	20	15
Perimeter layers	-	1	2	3	3	4
Mass	g	3.53	3.33	3.38	3.46	3.38
Print time	min	23.17	25.17	24.33	20.5	21.84
Failure load 1	kg	38.23	44.26	56.66	56.77	58.54
Failure load 2	kg	38.03	45.87	55.34	55.89	61.16
Failure load 3	kg	31.17	42.76	59.96	51.21	59.36
Average failure load (T) in tension	kg	35.81	44.30	57.32	54.62	59.69
Tensile stress	MPa	29.99	30.45	33.00	31.71	30.50
Specific Strength	kg/g	10.14	13.30	16.96	15.79	17.66

Table B-9:Perimeter Layer Variation Testing Results in Flexure

Parameter	Unit	1	2	3	4	5
Perimeter layers	-	3	4	5	6	7
Layer Height	mm	0.30	0.30	0.30	0.30	0.30
Infill percentage	%	0	0	0	0	0
Mass (g)	g	2.81	3.04	3.21	3.43	3.76
Print time	min	17.33	18.67	20.33	21.00	22.17
Failure load 1	kg	6.21	7.07	7.48	8.45	9.49
Failure load 2	kg	6.48	6.75	7.41	8.32	9.28
Failure load 3	kg	6.22	6.82	7.38	8.33	9.08
Average failure load (F) in flexure	kg	6.30	6.88	7.42	8.37	9.28
Flexural stress	MPa	72.46	79.09	85.34	96.18	106.72
Specific strength	kg/g	2.24	2.26	2.31	2.44	2.47

Table B-10:Perimeter Layer Variation Testing Results in Tension

Parameter	Unit	1	2	3	4	5
Perimeter layers	-	3	4	5	6	7
Layer Height	mm	0.30	0.30	0.30	0.30	0.30
Infill percentage	%	0	0	0	0	0
Mass (g)	g	2.68	2.96	3.22	3.49	3.78
Print time	min	17.33	18.67	20.33	21.00	22.17
Failure load 1	kg	54.27	63.88	67.14	82.03	88.50
Failure load 2	kg	54.87	62.92	69.95	78.29	91.73
Failure load 3	kg	54.48	65.73	67.83	80.62	87.16
Average failure load (T) in tension	kg	54.54	64.18	68.30	80.31	89.13
Tensile stress	MPa	32.78	32.79	32.21	37.31	43.37
Specific strength	kg/g	20.35	21.68	21.21	23.01	23.58

B.2 FEA Analysis Results

The following section contains the setup and results of the FEA analyses conducted on the final ISP components prior to FDM fabrication. The FEAs were conducted on the ISP components following the final FDM parameter selections. FEAs were conducted using Ansys engineering simulation software. Each FEA achieved stress convergence values within 5% across three consecutive simulation iterations. The initial assumed payload mass of 2.2kg was utilised within the FEAs and distributed amongst the mounting locations of the components. This was done to simulate the component structural resilience at worst case operating conditions, whilst maintaining a safety factor of 1.16 on the final allowable 1.9kg payload mass.

Table B-11: FEA Analysis Particulars

Component	Material	Load Magnitude and Type	Constraints	Mesh Type	Max. Deflection (mm)	Max. Stress (MPa)
Front Landing Gear Mount	Anisotropic PLA	Horizontal = 0N Vertical = 5.3955N (Linear Static)	- Fixed support at UAV attach point -Symmetry plane -Loading at roll axis pivot point location	Tetrahedrons	0.77	4.87
Rear Landing Gear Mount	Anisotropic PLA	Horizontal = 0N Vertical = 10.791N (Linear Static)	- Fixed supports at UAV attach points - Fixed supports at roll servo mounting hole locations -Loading at roll axis pivot point location	Tetrahedrons	0.67	4.13
Drop Arm	Anisotropic PLA	Horizontal = 0N Vertical = 5.3955N (Linear Static)	- Fixed support at roll axis pivot bearing location - Loading at end cap and control arm mounting locations	Tetrahedrons	0.00041	0.93
End Cap	Anisotropic PLA	Horizontal = 0N Vertical = 5.3955N (Linear Static)	- Fixed support at bolting location -Symmetry plane -Loading at pitch axis pivot point location	Tetrahedrons	0.06	8.35
End Cap Control Surface	Anisotropic PLA	Horizontal = 0N Vertical = 5.3955N (Linear Static)	- Fixed support at bolting location -Symmetry plane - Loading at pitch axis pivot and control arm mounting locations	Tetrahedrons	0.02	3.19
Payload Cradle	Anisotropic PLA	Horizontal = 0N Vertical = 21.59N (Linear Static)	- Fixed supports at pitch axis pivot bearing location - Fixed supports at pitch servo mounting hole locations -Loading at cradle base fixture location	Tetrahedrons	0.22	1.69

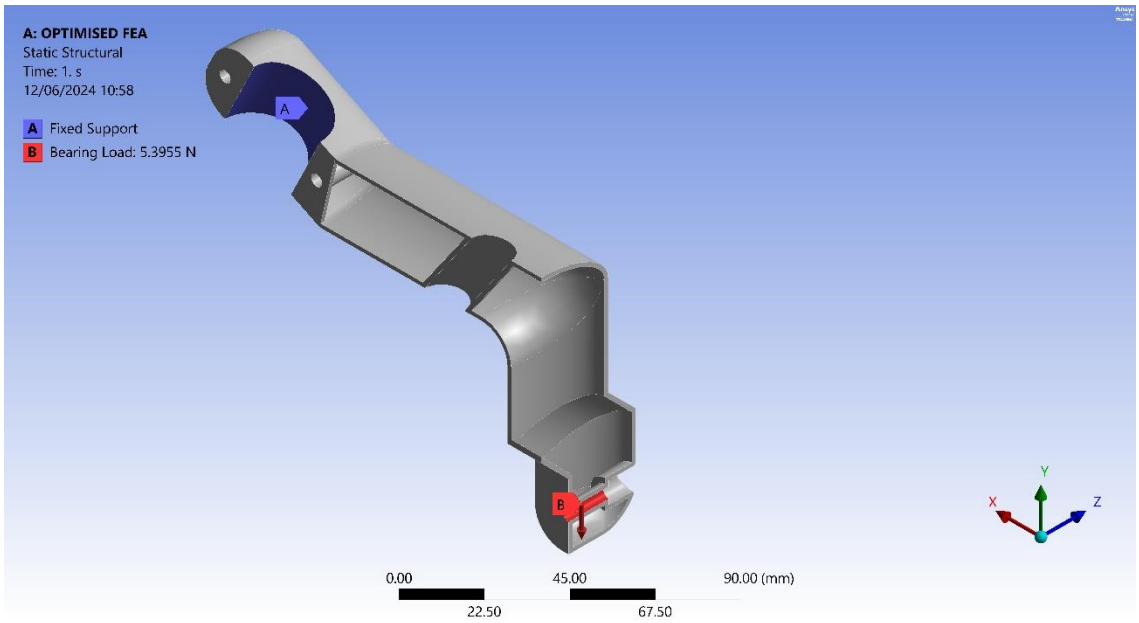

Figure B-1: Front Landing Gear Mount FEA Loads and Constraints

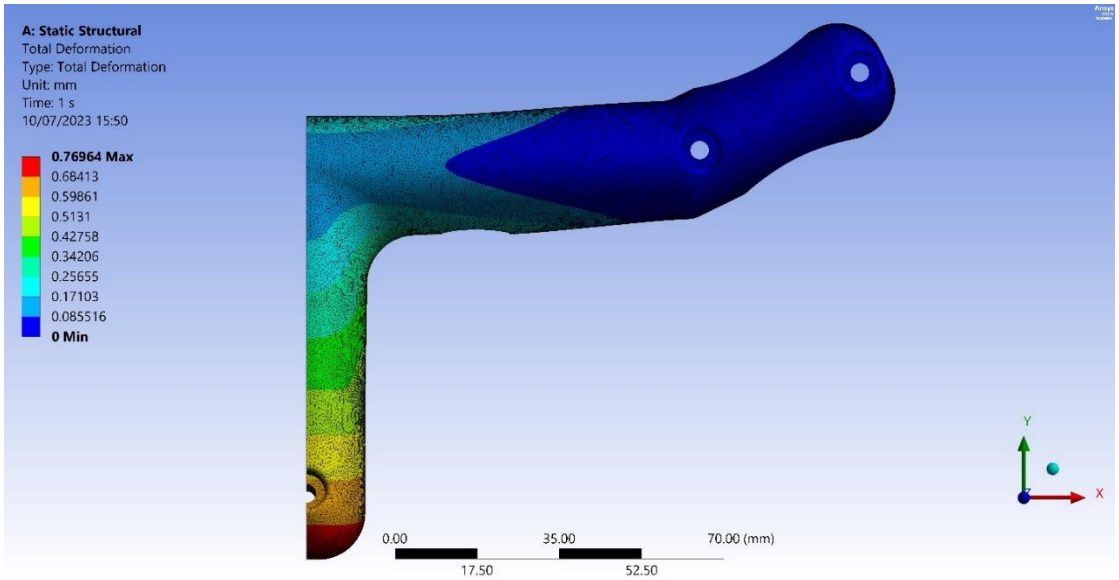

Figure B-2: Front Landing Gear Mount FEA Deflection

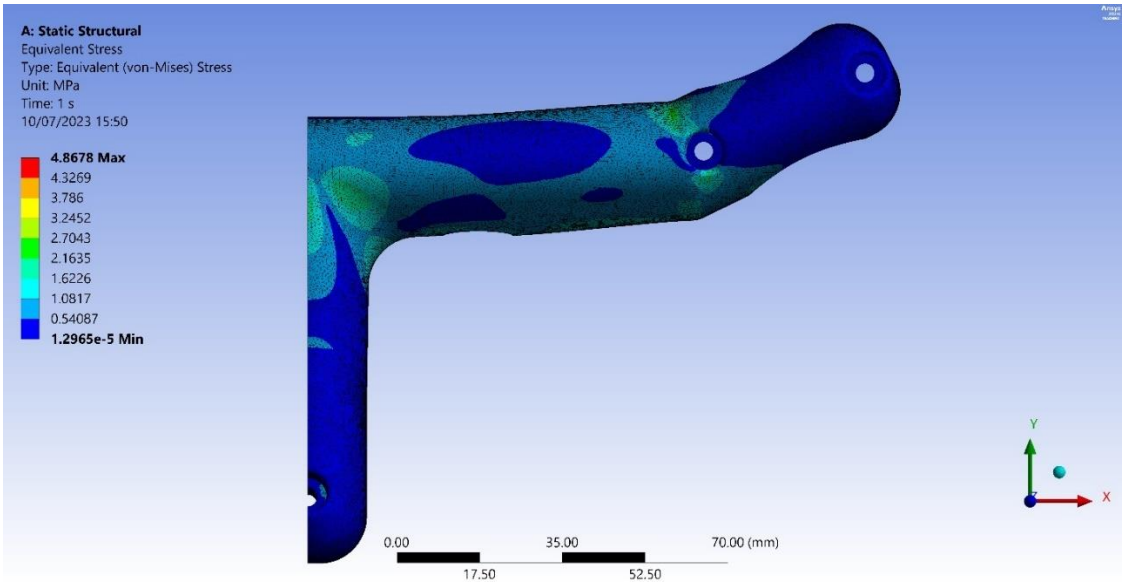

Figure B-3: Front Landing Gear Mount FEA Stress

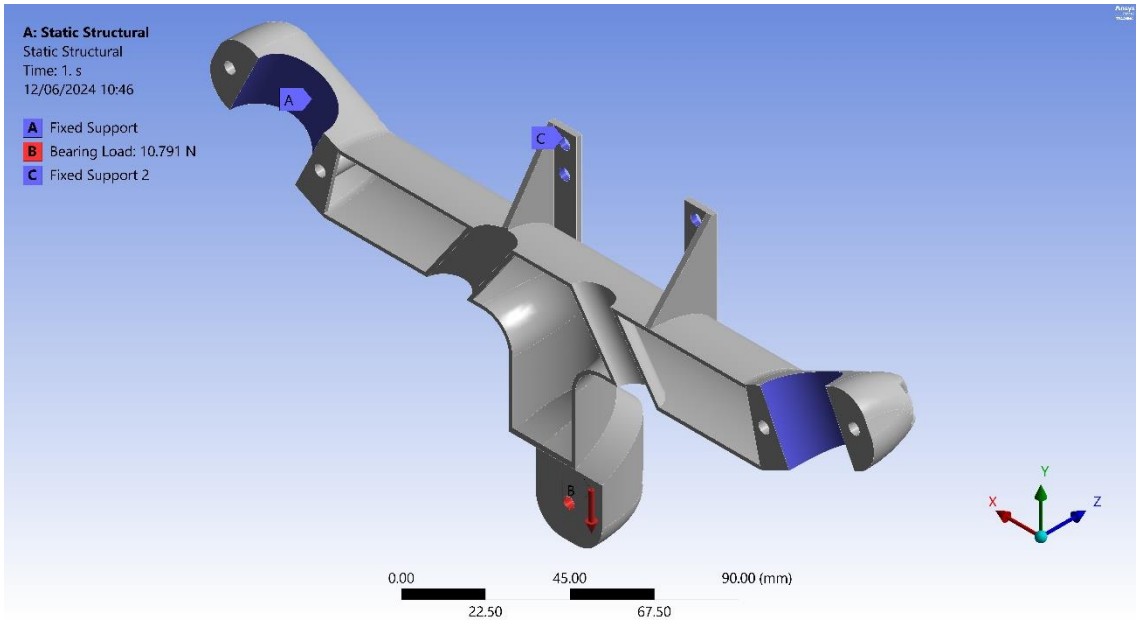

Figure B-4: Rear Landing Gear Mount FEA Loads and Constraints

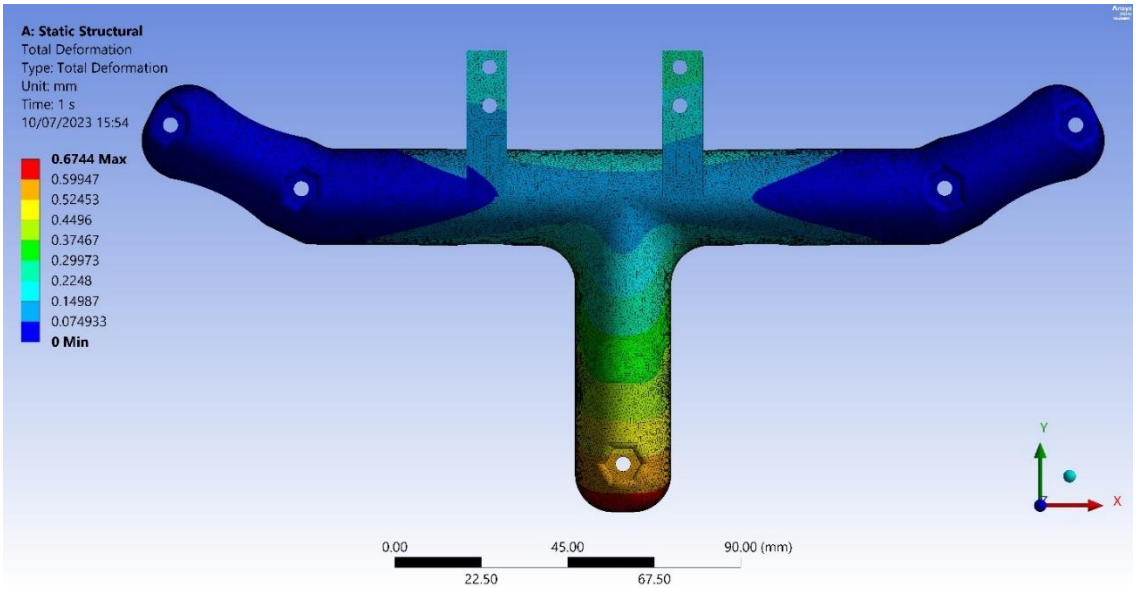

Figure B-5: Rear Landing Gear Mount FEA Deflection

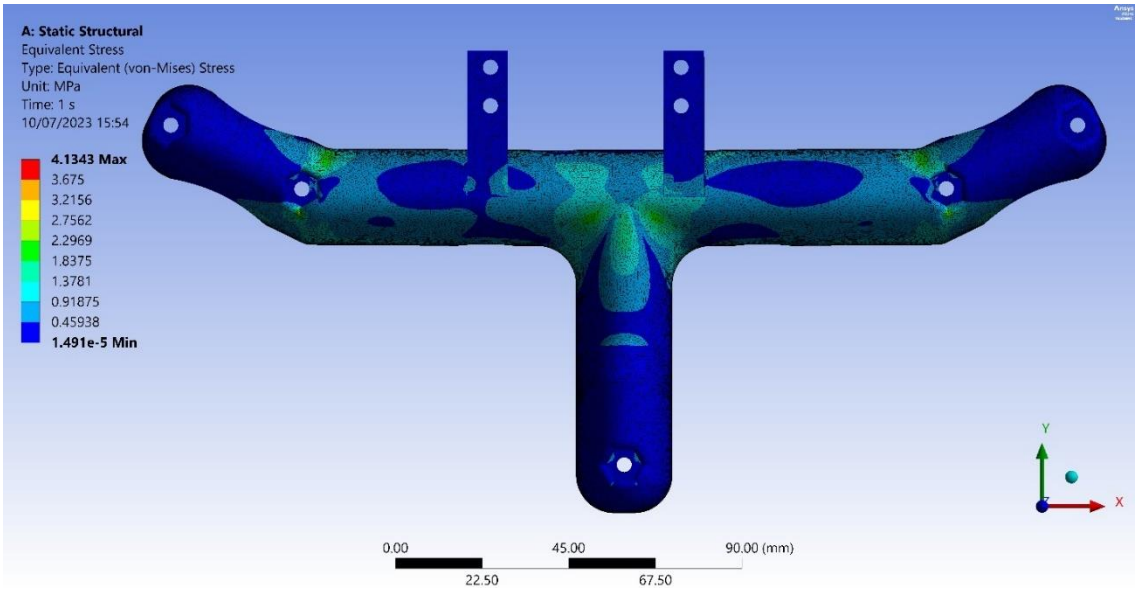

Figure B-6: Rear Landing Gear Mount FEA Stress 1

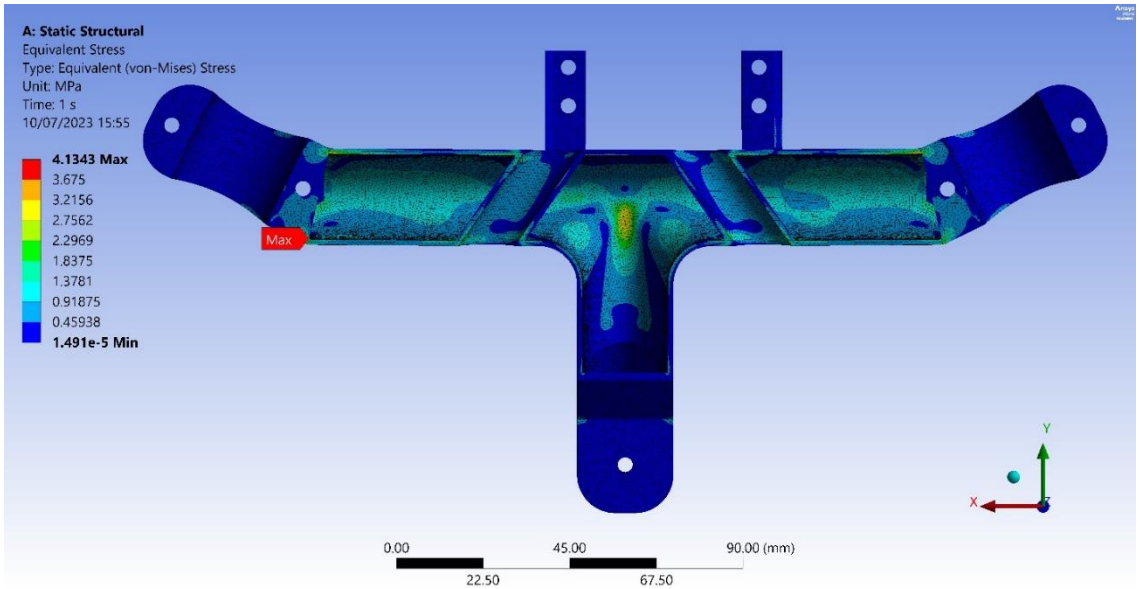

Figure B-7: Rear Landing Gear Mount FEA Stress 2

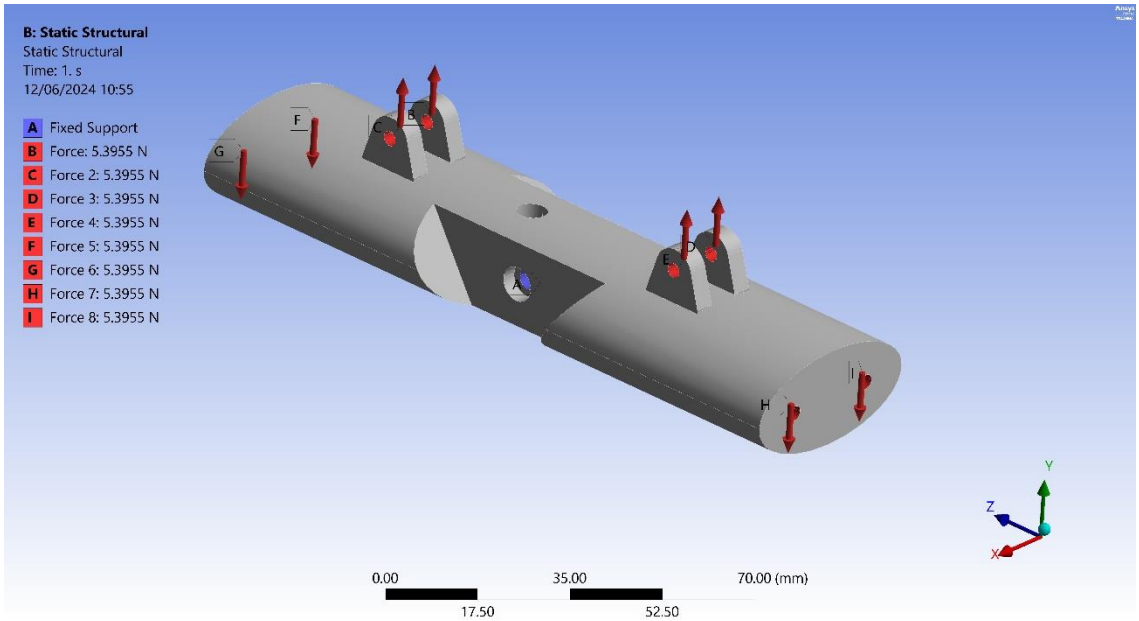

Figure B-8: Drop Arm FEA Loads and Constraints

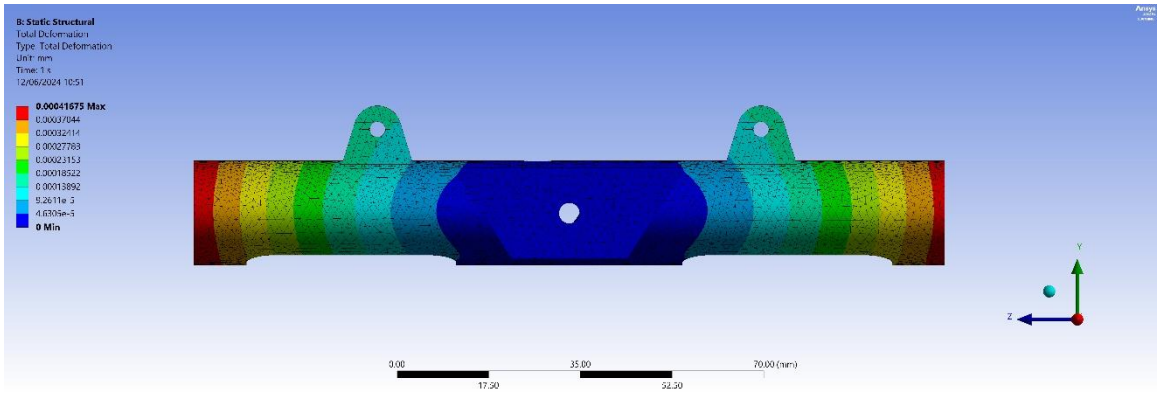

Figure B-9: Drop Arm FEA Deflection 1

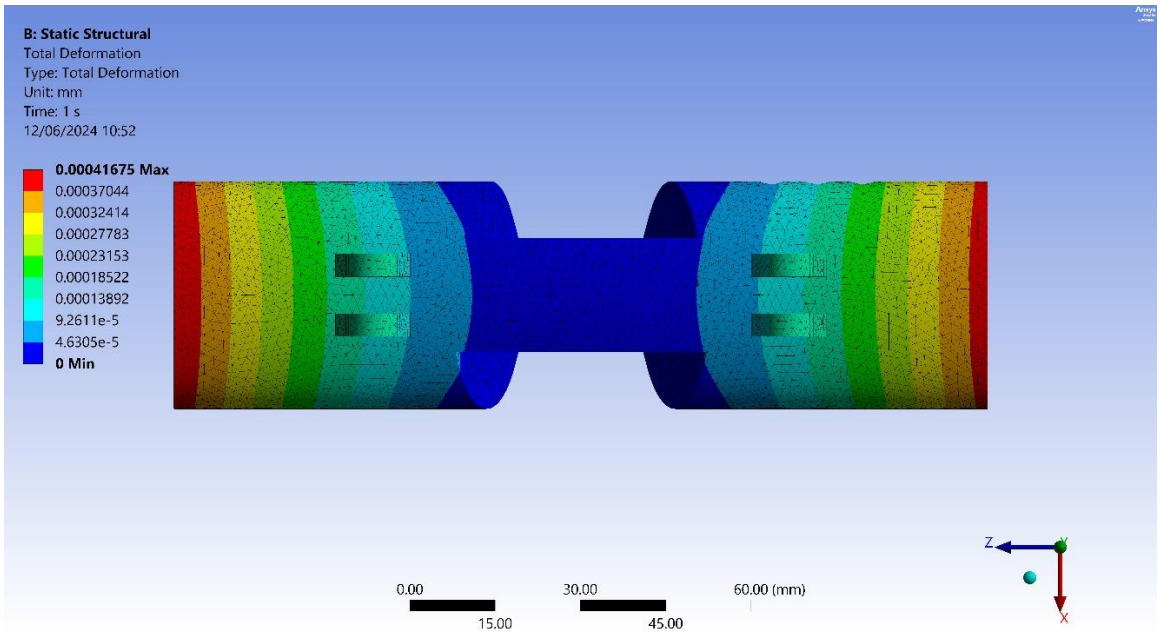

Figure B-10: Drop Arm FEA Deflection 2

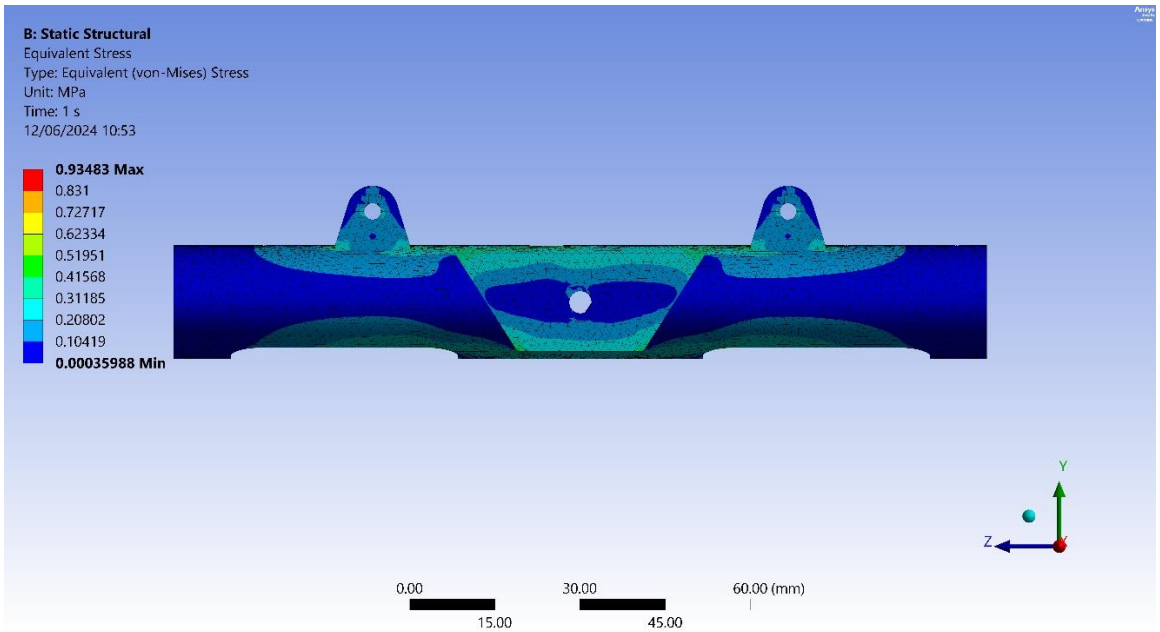

Figure B-11: Drop Arm FEA Stress 1

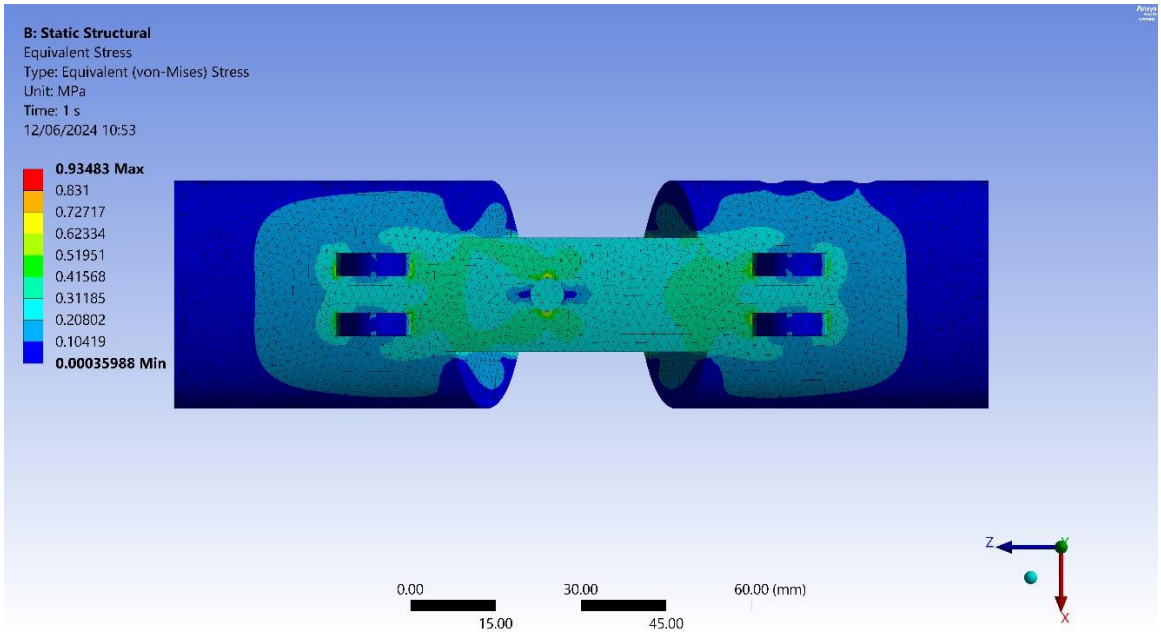

Figure B-12: Drop Arm FEA Stress 2

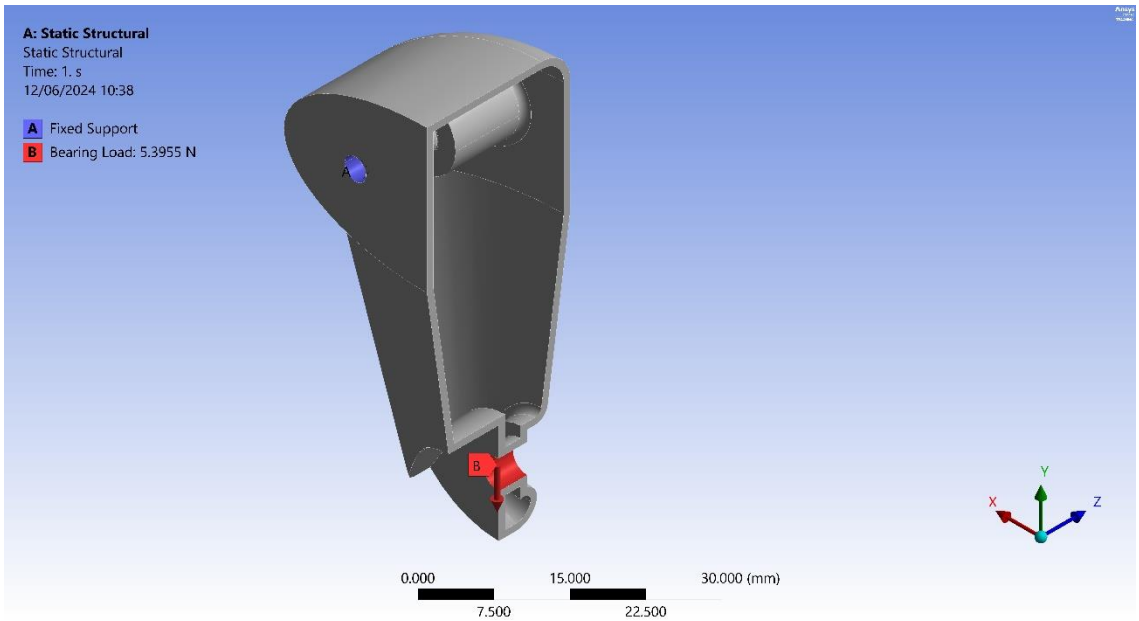

Figure B-13: Drop Arm End Cap FEA Loads and Constraints

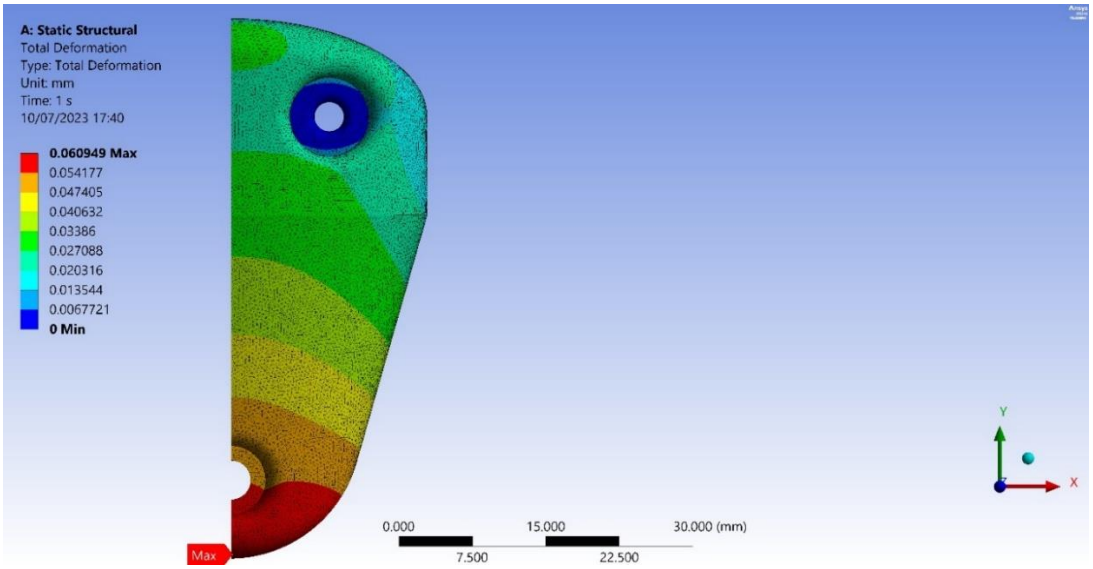

Figure B-14: Drop Arm End Cap FEA Deflection

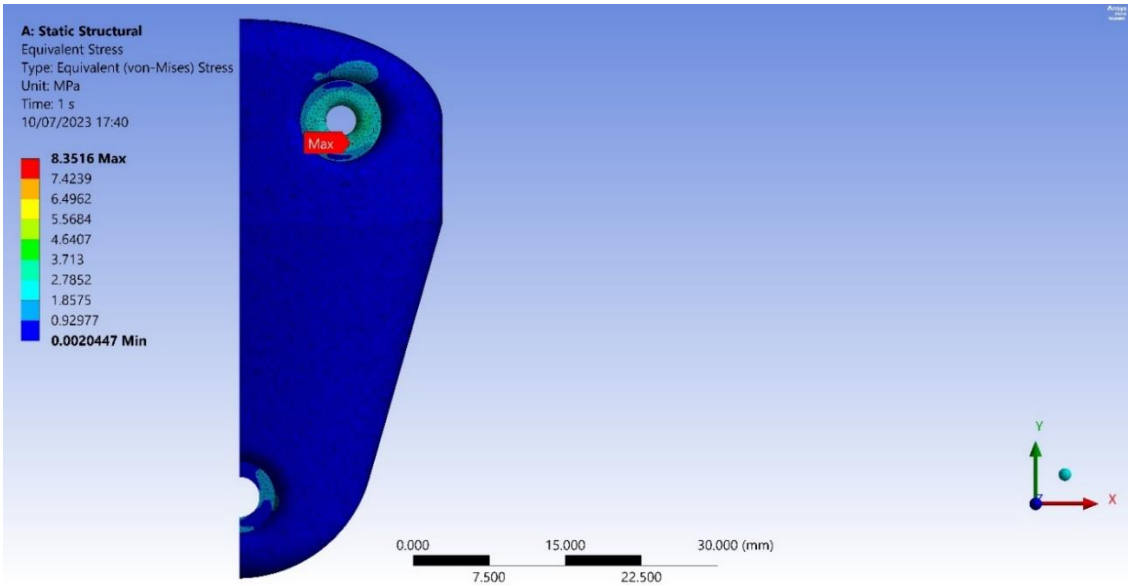

Figure B-15: Drop Arm End Cap FEA Stress 1

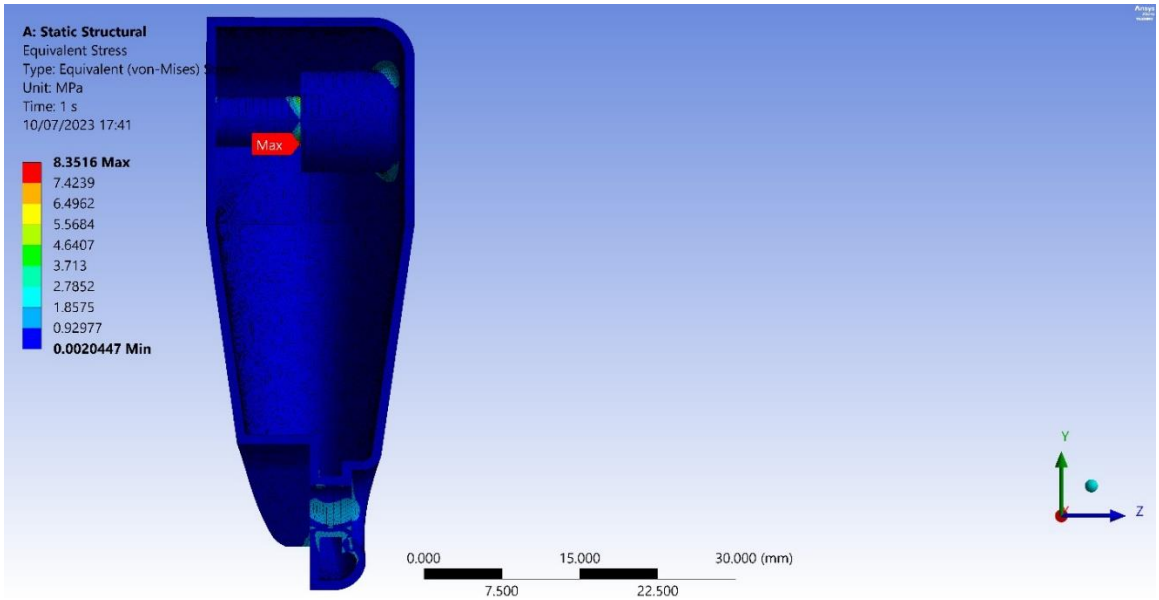

Figure B-16: Drop Arm End Cap FEA Stress 2

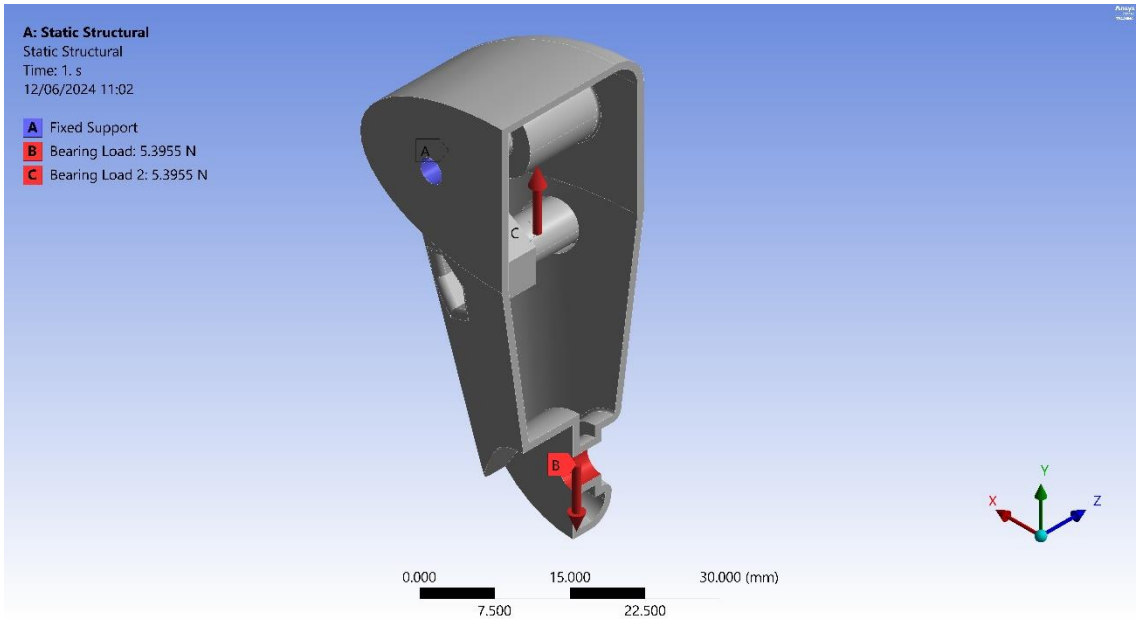

Figure B-17: Drop Arm End Cap Control Surface FEA Loads and Constraints

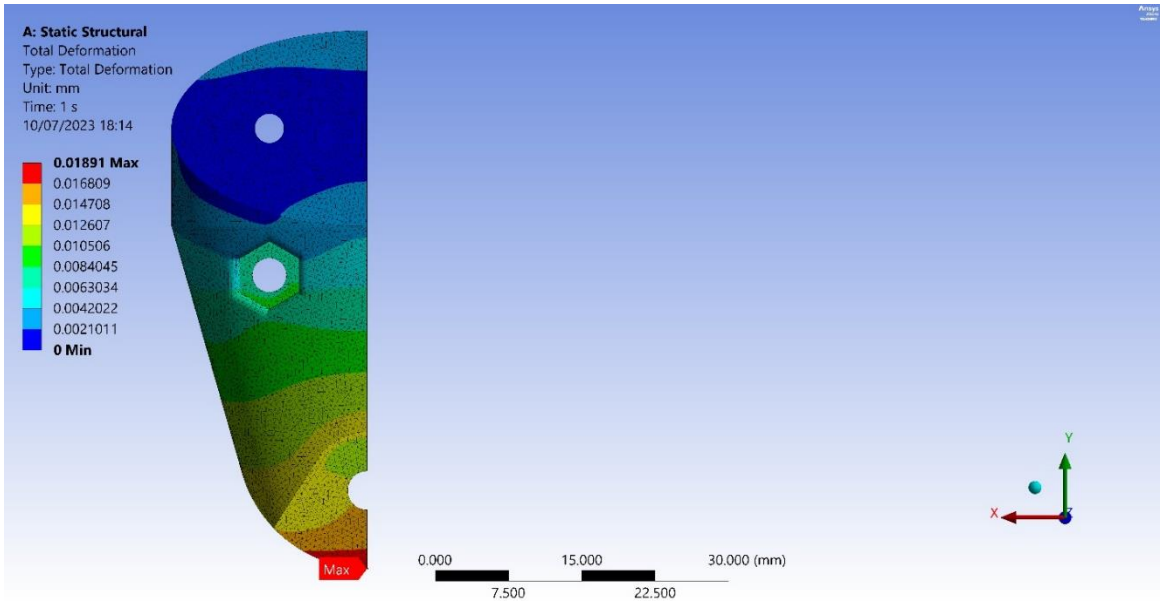

Figure B-18: Drop Arm End Cap Control Surface FEA Deflection

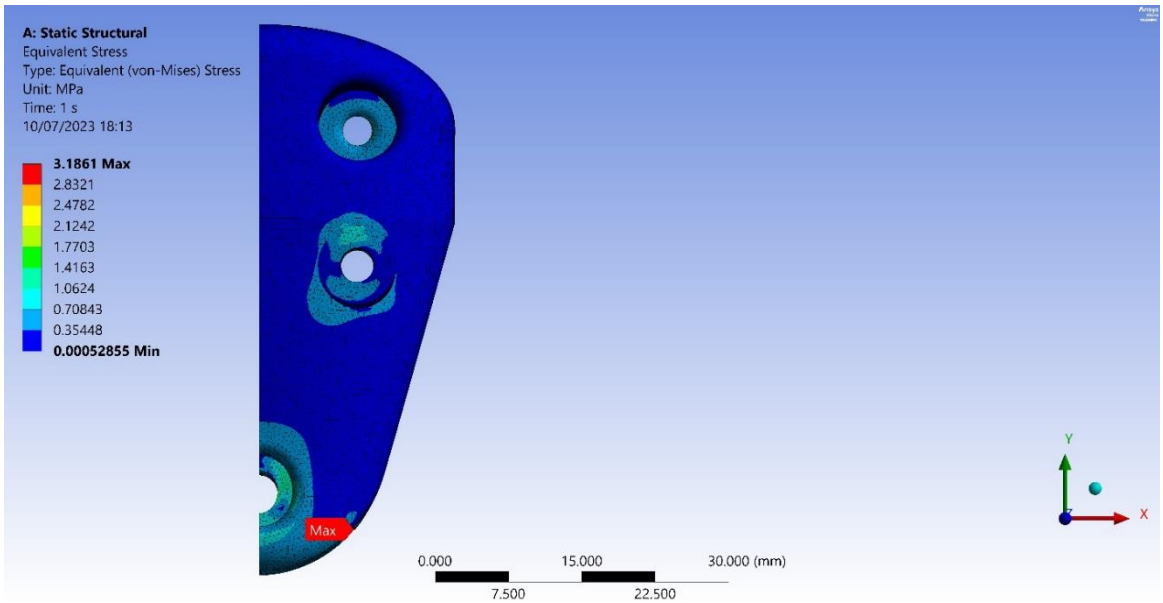

Figure B-19: Drop Arm End Cap Control Surface FEA Stress

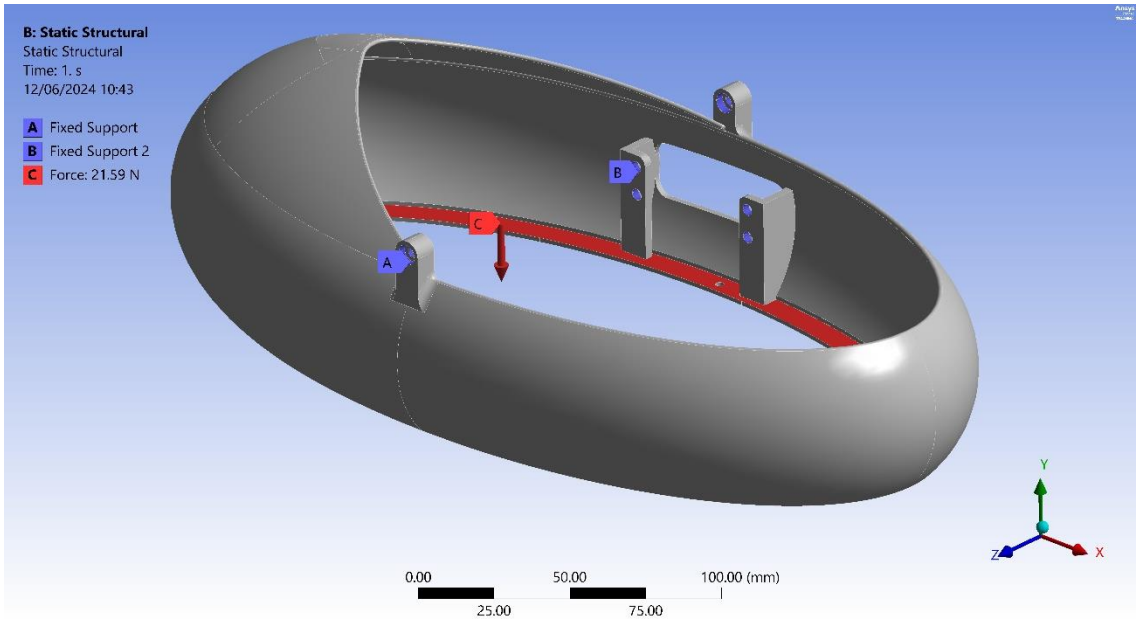

Figure B-20: Payload Cradle FEA Loads and Constraints

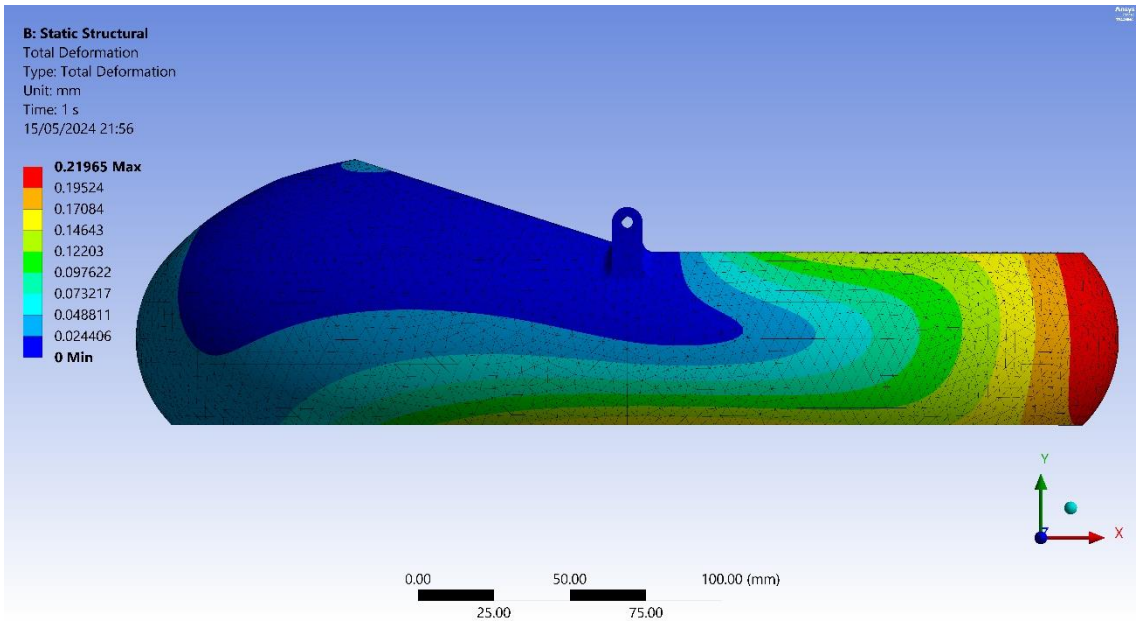

Figure B-21: Payload Cradle FEA Deflection 1

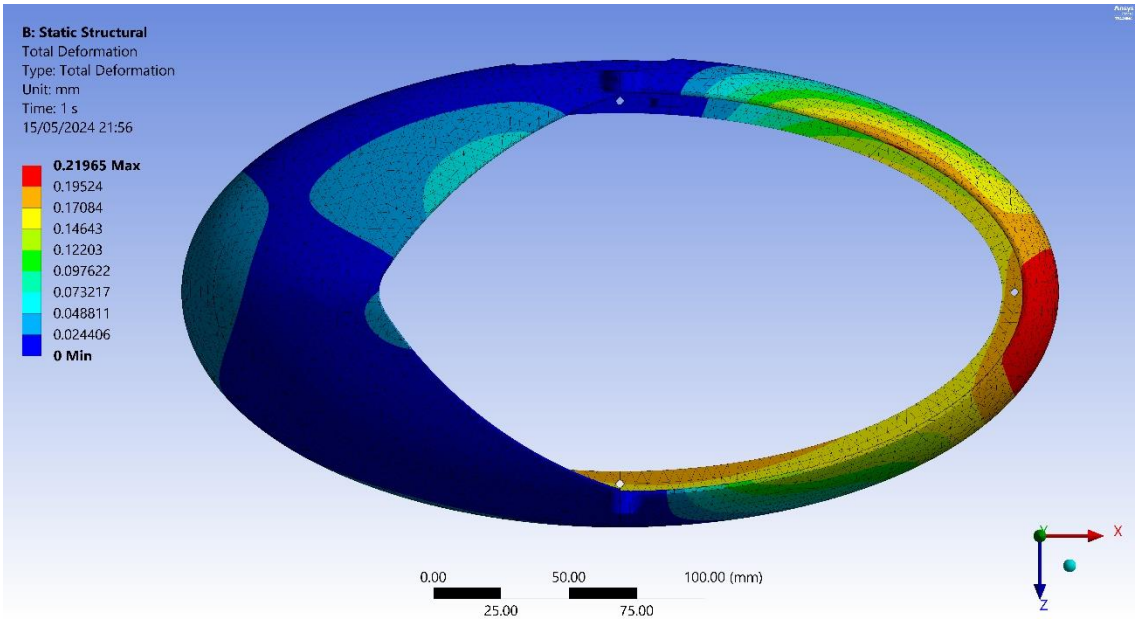

Figure B-22: Payload Cradle FEA Deflection 2

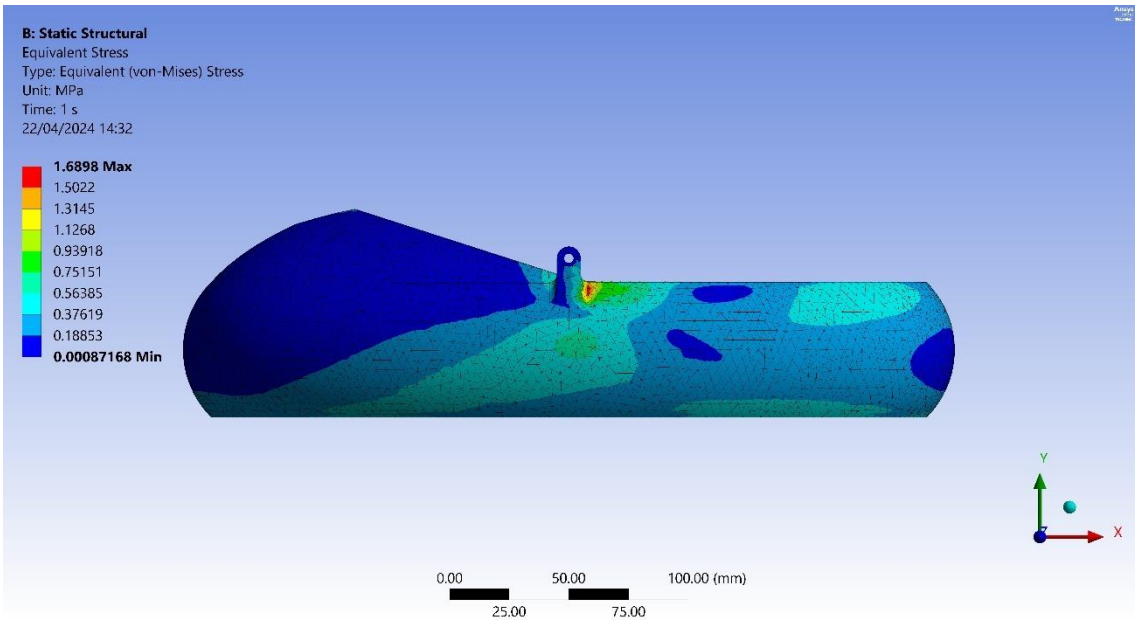

Figure B-23: Payload Cradle FEA Stress 1

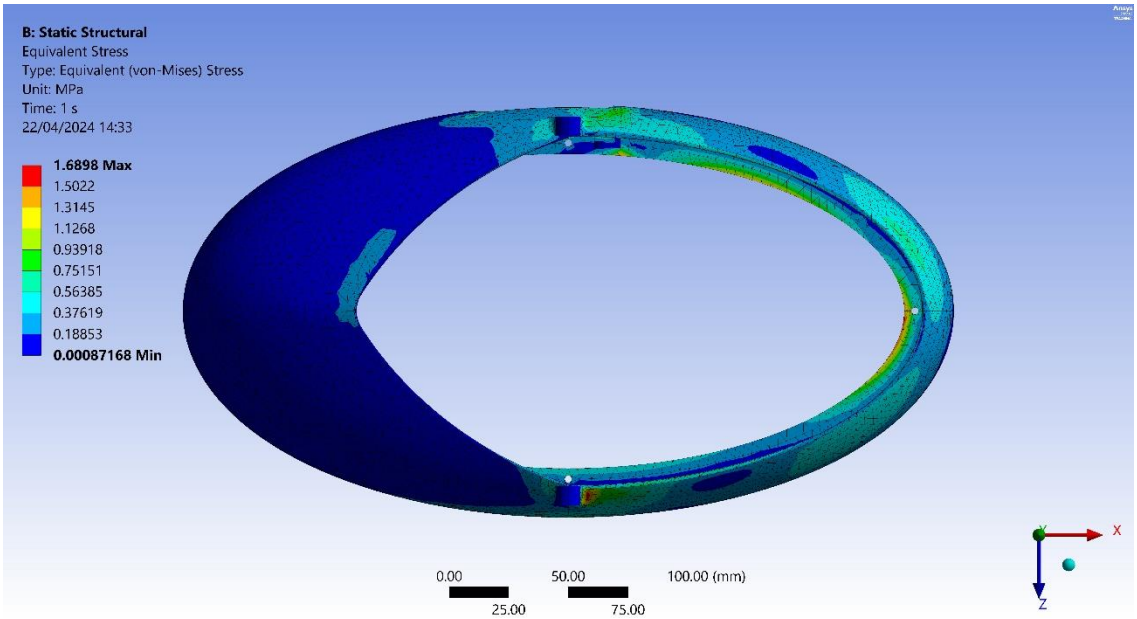

Figure B-24: Payload Cradle FEA Stress 2

APPENDIX C: PROJECT CODES

The code shown below was used to control the final ISP prototype, as described in Chapter 6 above.

```
//Matthew Swanepoel
//218039131@stu.ukzn.ac.za
//MSc Mechatronics Research Project
//Inertial Stabilisation Platform Code

#include <Adafruit_BNO055.h>
#include <Adafruit_Sensor.h>
#include <Servo.h>
#include <Wire.h>
#include <Math.h>
#include <utility/imumaths.h>

Servo RollServo;
Servo PitchServo;

double Q0;
double Q1;
double Q2;
double Q3;

double RollInput = 0;
double RollOutput;
double RollError;
double RollSignalCommand = 135;

double RollErrorOverwrite;
double DeltaRollError;
double GradRollError;
double RollErrorArea = 0;

double PitchInput = 0;          //Angle Setpoint
double PitchOutput;             //Angle Reading From IMU
double PitchError = 0;          //Setpoint to Input Difference
double PitchSignalCommand = 135;  //Initial Servo Orientation

double PitchErrorOverwrite;
```

```
double DeltaPitchError;
double GradPitchError;
double PitchErrorArea = 0;

//Timer Varibles
double PitchStartTime;
double PitchEndTime;
double PitchDeltaTime;

double RollStartTime;
double RollEndTime;
double RollDeltaTime;

double LoopStartTime;
double LoopEndTime;
double LoopDeltaTime;

double SettleErrorPos = 1;
double SettleErrorNeg = -1;

//Roll Axis Tuning Gains
double Kp_Roll = 1.6809;
double Ki_Roll = 0.000001513;
double Kd_Roll = 2.186;

//Pitch Axis Tuning Gains
double Kp_Pitch = 1.94609;
double Ki_Pitch = 0.00000440197;
double Kd_Pitch = 8.850;

//Setting IMU Sample Rate
#define BNO055_SAMPLERATE_DELAY_MS (100)
Adafruit_BNO055 ISP_IMU = Adafruit_BNO055();

void setup()
 {
  Serial.begin(115200);
  ISP_IMU.begin();
  delay(1000);
  Wire.begin();
```

```
 ISP_IMU.setExtCrystalUse(true);
 RollServo.attach(6);
 PitchServo.attach(5);

 RollServo.write(RollSignalCommand);
 delay(20);
 PitchServo.write(PitchSignalCommand);
 delay(20);

 PitchStartTime = millis();
 RollStartTime = millis();
 LoopStartTime = millis();
}

void loop()
 {
 uint8_t system, Gyro, Accel, Mag = 0;
 //Calibrating IMU
 ISP_IMU.getCalibration(&system, &Gyro, &Accel, &Mag);
 // Pulling raw Quaternion data from IMU
 imu::Quaternion Quat = ISP_IMU.getQuat();

 //Capturing & Organising Quaternion Data
 Q0 = Quat.w();
 Q1 = Quat.x();
 Q2 = Quat.y();
 Q3 = Quat.z();

 //Computing Euler Angles from Quaternion Data
 //Roll Euler Angle (Answer in Radians)
 RollOutput = atan2(2 * (Q0 * Q1 + Q2 * Q3), 1 - 2 * ((pow(Q1, 2)) + (pow(Q2, 2))));
 //Converting the Roll Output Euler Angle from Radians to Degrees
 RollOutput = RollOutput * (180 / PI);

 //Pitch Euler Angle (Answer in Radians)
 PitchOutput = asin(2 * (Q0 * Q2 - Q1 * Q3));
 //Converting the Pitch Output Euler from Radians to Degrees
 PitchOutput = PitchOutput * (180 / PI);

 RollError = RollInput - RollOutput;
```

```
  PitchError = PitchInput - PitchOutput;

  //Pitch PID Timer Setup
  PitchEndTime = PitchStartTime;
  PitchStartTime = millis();
  PitchDeltaTime = PitchStartTime - PitchEndTime;

  PitchErrorOverwrite = PitchError;

  DeltaPitchError = PitchError - PitchErrorOverwrite;

  GradPitchError = DeltaPitchError / PitchDeltaTime;

  PitchErrorArea = PitchErrorArea + PitchError * PitchDeltaTime;

  PitchSignalCommand = PitchSignalCommand - (Kp_Pitch * PitchError + Ki_Pitch * PitchErrorArea + Kd_Pitch * GradPitchError);

  if (abs(PitchOutput) < 30) {
    PitchServo.write(PitchSignalCommand);
  }

  //Roll PID Timer Setup
  RollEndTime = RollStartTime;
  RollStartTime = millis();
  RollDeltaTime = RollStartTime - RollEndTime;

  RollErrorOverwrite = RollError;

  DeltaRollError = RollError - RollErrorOverwrite;

  GradRollError = DeltaRollError / RollDeltaTime;

  RollErrorArea = RollErrorArea + RollError * RollDeltaTime;

  RollSignalCommand = RollSignalCommand - (Kp_Roll * RollError + Ki_Roll * RollErrorArea + Kd_Roll * GradRollError);

  if (abs(RollOutput) < 30) {
    RollServo.write(RollSignalCommand);
```

```
  }
  //Loop Timer
  LoopEndTime = LoopStartTime;
  LoopStartTime = millis();
  LoopDeltaTime = LoopStartTime - LoopEndTime;

  //Writing Outputs to Serial Monitor
  Serial.print("Roll Input");
  Serial.print(",");
  Serial.print(RollInput);
  Serial.print(",");
  Serial.print("Roll Error");
  Serial.print(",");
  Serial.print(RollError);
  Serial.print(",");
  Serial.print("Pitch Input");
  Serial.print(",");
  Serial.print(PitchInput);
  Serial.print(",");
  Serial.print("Pitch Error");
  Serial.print(",");
  Serial.print(PitchError);
  Serial.print(",");
  Serial.print("LoopTime");
  Serial.print(",");
  Serial.print(LoopDeltaTime);
  Serial.print(",");
  Serial.print(SettleErrorPos);
  Serial.print(",");
  Serial.print(SettleErrorNeg);
  Serial.println(system);

  delay(BNO055_SAMPLERATE_DELAY_MS);
}
```

The following code portrays the modified ISP control code, which was used during testing. The code integrated the additional hardware required for testing and allowed for the testing data to be logged onto a micro-SD card.

```
//Matthew Swanepoel
//218039131@stu.ukzn.ac.za
//MSc Mechatronics Research Project
//ISP & UAV Testing Code Including 2nd IMU and Data Logger

#include <Adafruit_BNO055.h>
#include <Adafruit_Sensor.h>
#include <Servo.h>
#include <Wire.h>
#include <Math.h>
#include <utility/imumaths.h>
#include <SPI.h>
#include <SD.h>

Servo RollServo;
Servo PitchServo;

float Q0;
float Q1;
float Q2;
float Q3;

float Q0T;
float Q1T;
float Q2T;
float Q3T;

double RollInput = 0;
double RollOutput;
double RollError=0;
double RollSignalCommand=135;
double TestRollOutput; //Roll Angle Reading From UAV IMU
double RollErrorOverwrite;
double DeltaRollError;
double GradRollError;
double RollErrorArea=0;
```

```
double PitchInput = 0; //Angle Setpoint
double PitchOutput; //Angle Reading From IMU & PID Input
double PitchError=0; //Setpoint to Input Difference
double PitchSignalCommand=135; //Initial Servo Orientation
double TestPitchOutput; //Pitch Angle Reading From UAV IMU
double PitchErrorOverwrite;
double DeltaPitchError;
double GradPitchError;
double PitchErrorArea=0;

//Timer Varibles
int PitchStartTime;
int PitchEndTime;
int PitchDeltaTime;

int RollStartTime;
int RollEndTime;
int RollDeltaTime;

int LoopStartTime;
int LoopEndTime;
int LoopDeltaTime;

float SettleErrorPos=0.05;
float SettleErrorNeg=-0.05;

//Roll Channel Tuning Parameters
int Kp_Roll=1.6809;
int Ki_Roll=0.000001513;
int Kd_Roll=2.186;

//Pitch Channel Tuning Parameters
double Kp_Pitch = 1.94609;
double Ki_Pitch = 0.00000440197;
double Kd_Pitch = 8.850;

const int ChipSelectPin=10;
File TestDataFile;
//Setting IMU Sample Rate
```

```
#define BNO055_SAMPLERATE_DELAY_MS (100)

Adafruit_BNO055 ISP_IMU = Adafruit_BNO055();
Adafruit_BNO055 UAV_IMU = Adafruit_BNO055(55, 0x29); //Declaring 2nd IMU with Altered Address
void setup()
{
 Serial.begin(115200);
 ISP_IMU.begin();
 delay(1000);
 UAV_IMU.begin();
 delay(1000);
 Wire.begin();
//Initialise SPI Communication
 SPI.begin();
 SD.begin(ChipSelectPin);

 ISP_IMU.setExtCrystalUse(true);
 UAV_IMU.setExtCrystalUse(true);
 RollServo.attach(6);
 PitchServo.attach(5);

 RollServo.write(RollSignalCommand);
 delay (20);
 PitchServo.write(PitchSignalCommand);
 delay (20);

 PitchStartTime=millis();
 RollStartTime=millis();
 LoopStartTime=millis();
}

void loop()
{

  uint8_t system, Gyro, Accel, Mag, GyroT, AccelT, MagT =0;

  ISP_IMU.getCalibration(&system, &Gyro, &Accel, &Mag); //Initialising ISP IMU
  UAV_IMU.getCalibration(&system, &GyroT, &AccelT, &MagT); //Initialising UAV IMU

  imu::Quaternion Quat = ISP_IMU.getQuat(); // Pulling raw Quaternion data from ISP IMU
```

```
imu::Quaternion quat = UAV_IMU.getQuat(); // Pulling raw Quaternion data from UAV IMU

Q0=Quat.w();  //Capturing & Organising Quaternion raw data from ISP
Q1=Quat.x();
Q2=Quat.y();
Q3=Quat.z();

Q0T=quat.w();  //Capturing & Organising Quaternion raw data from UAV
Q1T=quat.x();
Q2T=quat.y();
Q3T=quat.z();

//Computing Euler Angles from Quaternion Data
//Becasue the ISP has a fixed range of motion in both axes, Euler angles will be sufficient

//Computing the Roll output Euler angle from the Quaternion data (answer is in radians)
RollOutput=atan2(2*(Q0*Q1+Q2*Q3),1-2*((pow(Q1,2))+(pow(Q2,2))));

//Converting the Roll output Euler from radians to degrees
RollOutput=RollOutput*(180/PI);

//Computing the Pitch output Euler angle from the Quaternion data (answer is in radians)
PitchOutput=asin(2*(Q0*Q2-Q1*Q3));

//Converting the Pitch output Euler from radians to degrees
PitchOutput=PitchOutput*(180/PI);

//Computing UAV Orientation During Testing

TestRollOutput=atan2(2*(Q0T*Q1T+Q2T*Q3T),1-2*((pow(Q1T,2))+(pow(Q2T,2))));
TestRollOutput=TestRollOutput*(180/PI);

TestPitchOutput=asin(2*(Q0T*Q2T-Q1T*Q3T));
TestPitchOutput=TestPitchOutput*(180/PI);

PitchEndTime=PitchStartTime;
PitchStartTime=millis();
PitchDeltaTime=PitchStartTime-PitchEndTime;

PitchErrorOverwrite=PitchError;
```

```
  PitchError=PitchInput-PitchOutput;

  DeltaPitchError=PitchError-PitchErrorOverwrite;

  GradPitchError=DeltaPitchError/PitchDeltaTime;

  PitchErrorArea=PitchErrorArea+PitchError*PitchDeltaTime;

  PitchSignalCommand=PitchSignalCommand-
(Kp_Pitch*PitchError+Ki_Pitch*PitchErrorArea+Kd_Pitch*GradPitchError);

  if(abs(PitchOutput)<30)
  {
  PitchServo.write(PitchSignalCommand);
  }

  RollEndTime=RollStartTime;
  RollStartTime=millis();
  RollDeltaTime=RollStartTime-RollEndTime;

  RollErrorOverwrite=RollError;

  RollError=RollInput-RollOutput;

  DeltaRollError=RollError-RollErrorOverwrite;

  GradRollError=DeltaRollError/RollDeltaTime;

  RollErrorArea=RollErrorArea+RollError*RollDeltaTime;

  RollSignalCommand=RollSignalCommand-
(Kp_Roll*RollError+Ki_Roll*RollErrorArea+Kd_Roll*GradRollError);

  if(abs(RollOutput)<30)
  {
  RollServo.write(RollSignalCommand);
  }

  LoopEndTime=LoopStartTime;
```

```
  LoopStartTime=millis();
  LoopDeltaTime=LoopStartTime-LoopEndTime;


//Writing Raw IMU Data to SD
 TestDataFile=SD.open("TestData.txt", FILE_WRITE);

if(TestDataFile)
  {
// Writing Outputs to SD Card

TestDataFile.print(RollInput);
TestDataFile.print(",");
TestDataFile.print(RollError);
TestDataFile.print(",");
TestDataFile.print(PitchError);
TestDataFile.print(",");
TestDataFile.print(TestRollOutput);
TestDataFile.print(",");
TestDataFile.print(TestPitchOutput);
TestDataFile.print(",");
TestDataFile.print(LoopDeltaTime);
TestDataFile.println();
TestDataFile.close();
  }
  //Writing Outputs to Serial Monitor
  //Used to Verify Code Function Before Uploading to Microcontroller

  Serial.print(RollInput);
  Serial.print(",");
  Serial.print(RollError);
  Serial.print(",");
  Serial.print(PitchInput);
  Serial.print(",");
  Serial.print(PitchError);
// Testing UAV IMU on Serial Monitor
  Serial.print("TestRoll:");
  Serial.print(TestRollOutput);
  Serial.print(",");
  Serial.print("TestPitch:");
```

```
  Serial.print(TestPitchOutput);
  Serial.print(",");
  Serial.print("LoopTimer:");
  Serial.print(LoopDeltaTime);
  Serial.println(system);

  delay(BNO055_SAMPLERATE_DELAY_MS);
}
```

APPENDIX D: ENGINEERING DRAWINGS

Table D-1: Drawing Schedule

No.	Drawing Name	Drawing Number
1	ISP FINAL ASSEMBLY ORTHOGRAPHIC VIEWS	A1
2	ISP FINAL ASSEMBLY	A2
3	GIMBAL EXPLODED SUBASSEMBLY	SA1
4	FRONT LANDING GEAR MOUNT	P1
5	REAR LANDING GEAR MOUNT	P2
6	DROP ARM END CAP	P3
7	DROP ARM	P4
8	DROP ARM END CAP CONTROL SURFACE	P5
9	PITCH AXIS CONTROL ARM	P6
10	DROP ARM LID	P7
11	ROLL AXIS CONTROL ARM	P8
12	CRADLE EXPLODED SUBASSEMBLY	SA2
13	PAYLOAD CRADLE	P9
14	BNO055 HOUSING	P10
15	BNO055 HOUSING LID	P11
16	CRADLE BASE	P12
17	BATTERY HOUSING	P13
18	TPU VIBRATION DAMPENER	P14
19	TESTING SENSOR MOUNTING BRACKET	T1

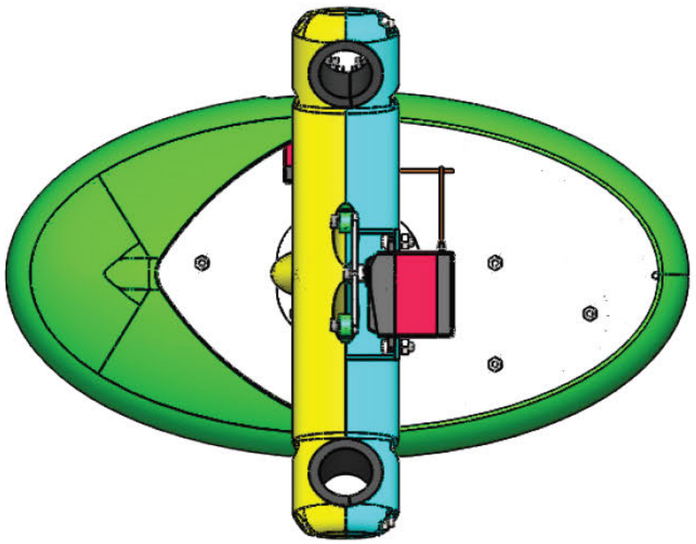

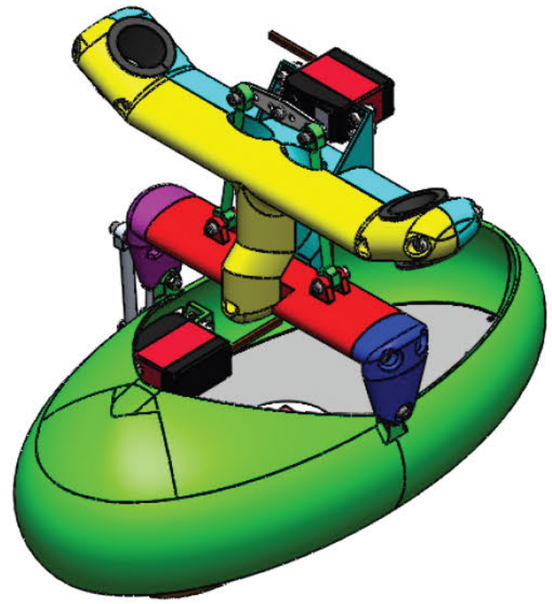

ISOMETRIC VIEW

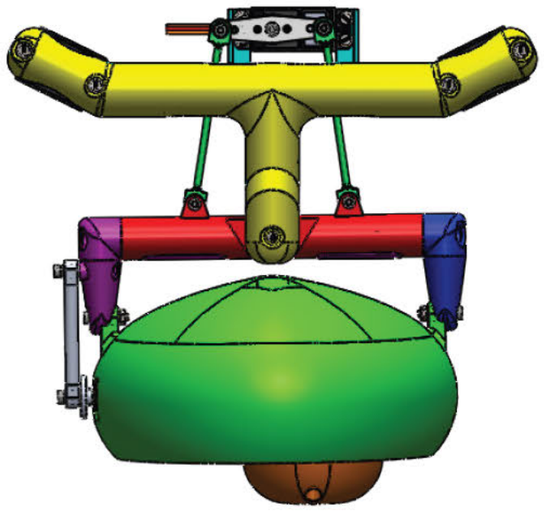

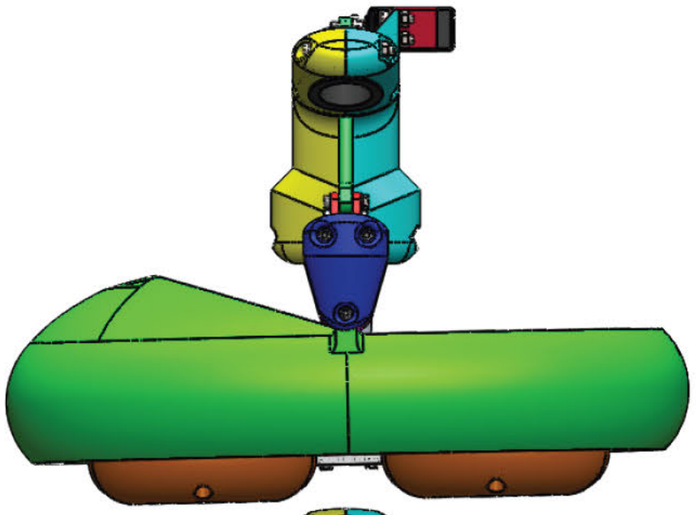

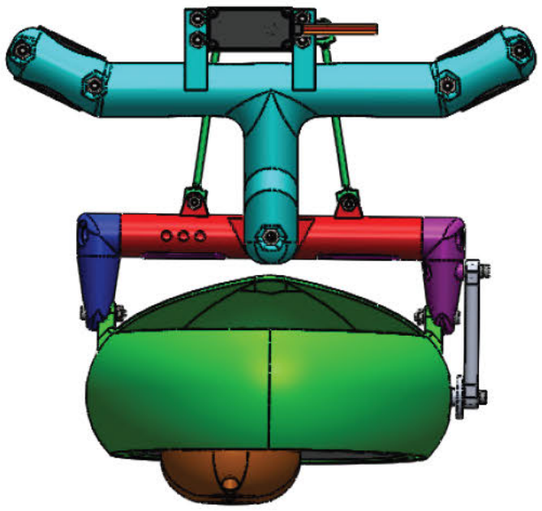

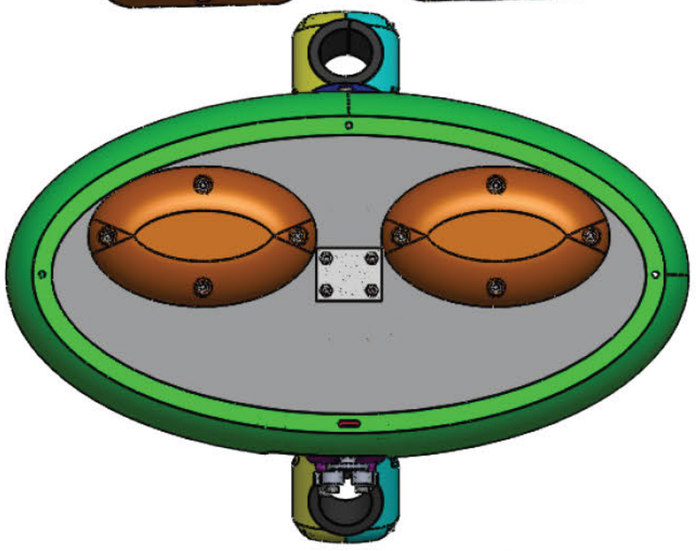

UNLESS OTHERWISE
STATED GENERAL
TOLERANCES: ±0.05 mm
ANGLES: ± 1 °

UNIVERSITY OF KWAZULU-NATAL

SCHOOL OF ENGINEERING

MECHANICAL ENGINEERING

MAT.: VARIOUS		No. REQ.: 1	SCALE: 1:3	UNITS: mm	PROJECT: MSC MECHATRONICS
	DATE	CHECKED	STUDENT NAME: MATTHEW SWANEPOEL		
PROJECT SUPERVISOR			STUDENT No.: 218039131		TITLE: ISP FINAL ASSEMBLY ORTHOGRAPHIC VIEWS
WORKSHOP TECHNICIAN			E-MAIL: 218039131@STU.UKZN.AC.ZA		
TECHNICAL OFFICER			TEL. No.: [redacted]		

No.: A1

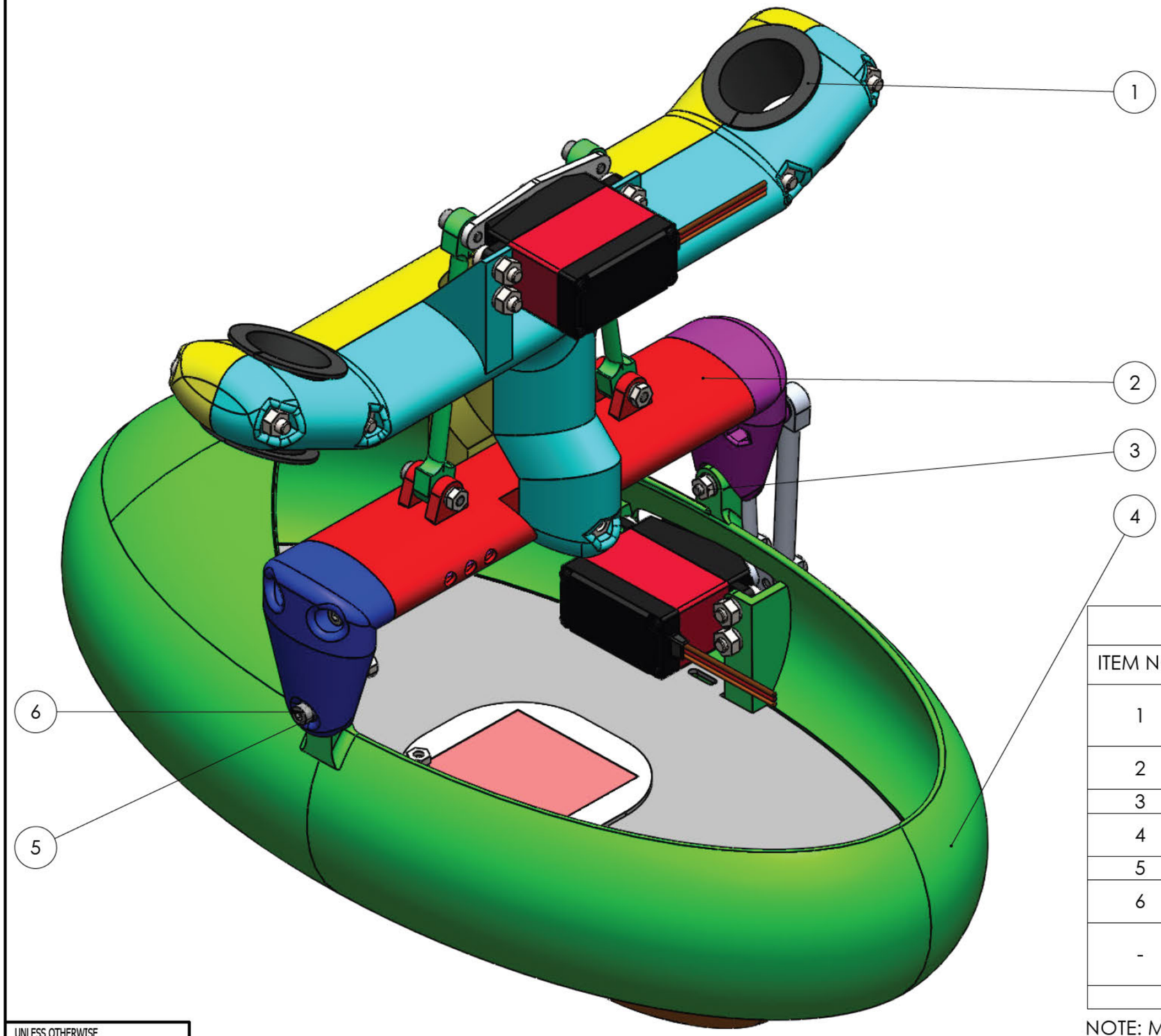

FINAL ASSEMBLY MASS DECMPOSITION

ITEM NO.	PART NAME	UNIT MASS (g)	QTY.	TOTAL MASS (g)
1	TPU VIBRATION DAMPENER	4.40	2	8.80
2	GIMBAL SUBASSEMBLY	243.00	1	243.00
3	M3 NUT	0.46	2	0.92
4	CRADLE SUBASSEMBLY	440.07	1	440.07
5	M3 WASHER	0.17	4	0.68
6	M3 CAP SCREW (3X20)	1.54	2	3.08
-	MISCELLANEOUS	-	-	13.31
TOTAL				709.86

NOTE: MISCELLANEOUS COMPONENTS INCLUDE WIRES, LEDs, SOLDER, AND HEAT SHRINK TUBING.

UNLESS OTHERWISE STATED GENERAL
TOLERANCES: ±0.05 mm
ANGLES: ± 1 °

UNIVERSITY OF KWAZULU-NATAL

SCHOOL OF ENGINEERING

MECHANICAL ENGINEERING

MAT.: VARIOUS		No. REQ.: 1	SCALE: 1:1.5	UNITS: mm
	DATE	CHECKED	STUDENT NAME: MATTHEW SWANEPOEL	
PROJECT SUPERVISOR			STUDENT No.: 218039131	
WORKSHOP TECHNICIAN			E-MAIL: 218039131@STU.UKZN.AC.ZA	
TECHNICAL OFFICER			TEL. No.: [redacted]	

PROJECT: MSC MECHATRONICS

No.: A2

TITLE: ISP FINAL ASSEMBLY

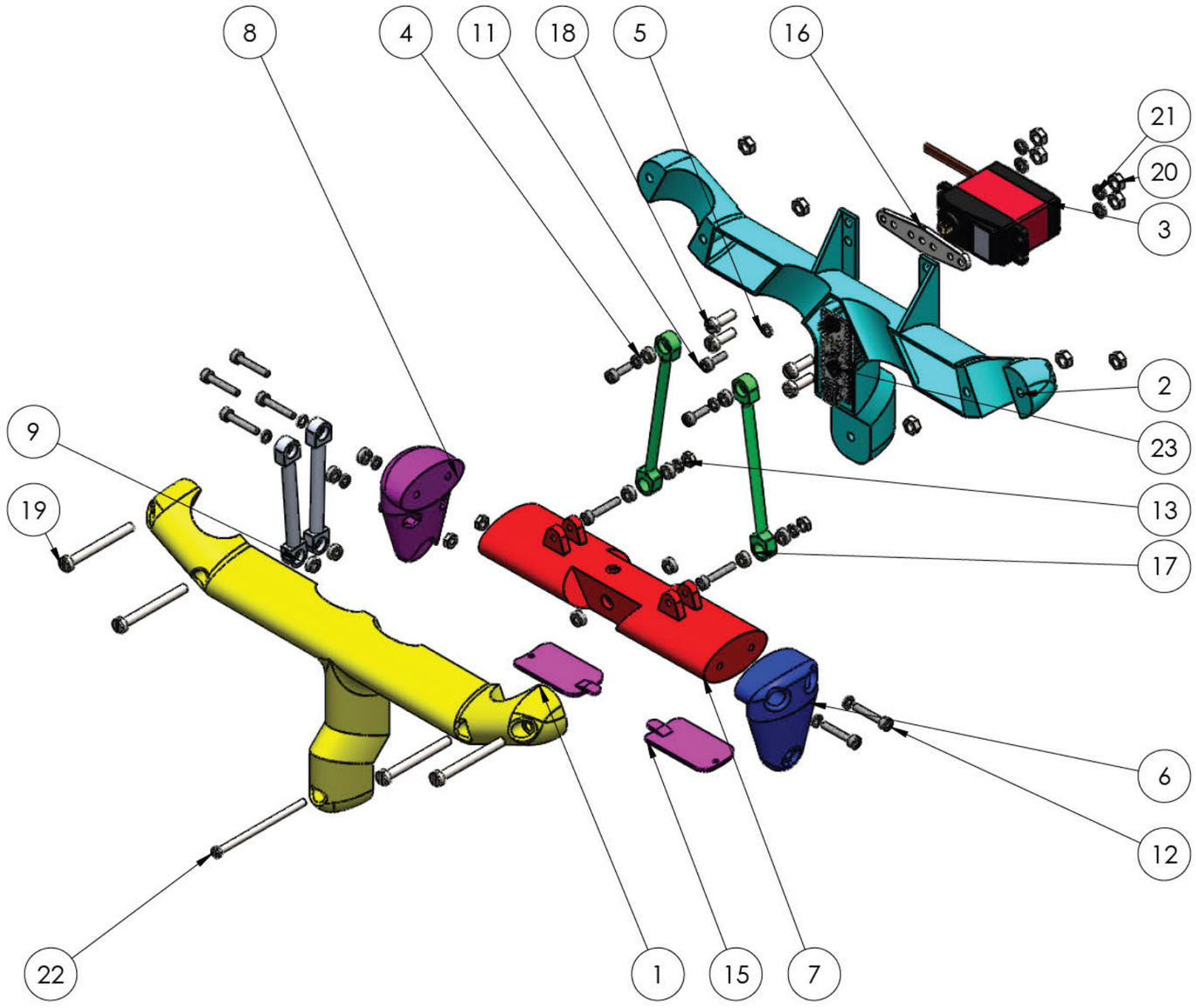

ITEM NO.	PART NAME	UNIT MASS (g)	QTY.	TOTAL MASS (g)
1	LANDING GEAR MOUNTING FRONT	41.81	1	41.81
2	LANDING GEAR MOUNTING REAR	44.92	1	44.92
3	DSSERVO 35KG SERVO MOTOR	33.55	1	33.55
4	683-RS BALL BEARING	0.74	12	8.88
5	M3 WASHER	0.17	15	2.55
6	PITCH AXIS DROP ARM END CAP	6.22	1	6.22
7	PITCH AXIS DROP ARM	24.51	1	24.51
8	DROP ARM END CAP CONTROL SURFACE	5.73	1	5.73
9	PITCH AXIS CONTROL ARM	2.44	2	4.88
11	M3 CAP SCREW (3X10)	1.10	3	3.30
12	M3 CAP SCREW (3X20)	1.54	8	12.32
13	M3 NUT	0.46	4	1.84
15	DROP ARM LID	1.63	2	3.26
16	ROLL SERVO HORN	1.42	1	1.42
17	ROLL AXIS CONTROL ARM	3.47	2	6.94
18	M4 SCREW (4x12)	2.03	4	8.12
19	M4 SCREW (4x40)	4.85	4	19.4
20	M4 NUT	0.76	9	6.84
21	M4 WASHER	0.24	4	0.96
22	M3 SCREW (3x55)	3.35	1	3.35
23	ARDUINO NANO	2.20	1	2.20
TOTAL				243.00

UNLESS OTHERWISE STATED GENERAL TOLERANCES: ±0.05 mm
ANGLES: ± 1 °

UNIVERSITY OF KWAZULU-NATAL

SCHOOL OF ENGINEERING

MECHANICAL ENGINEERING

MAT.: VARIOUS		No. REQ.: 1	SCALE: 1:2.4	UNITS: mm
	DATE	CHECKED	STUDENT NAME: MATTHEW SWANEPOEL	
PROJECT SUPERVISOR			STUDENT No.: 218039131	
WORKSHOP TECHNICIAN			E-MAIL: 218039131@STU.UKZN.AC.ZA	
TECHNICAL OFFICER			TEL. No.: [redacted]	

PROJECT: MSC MECHATRONICS

No.: SA1

TITLE: GIMBAL EXPLODED ASSEMBLY

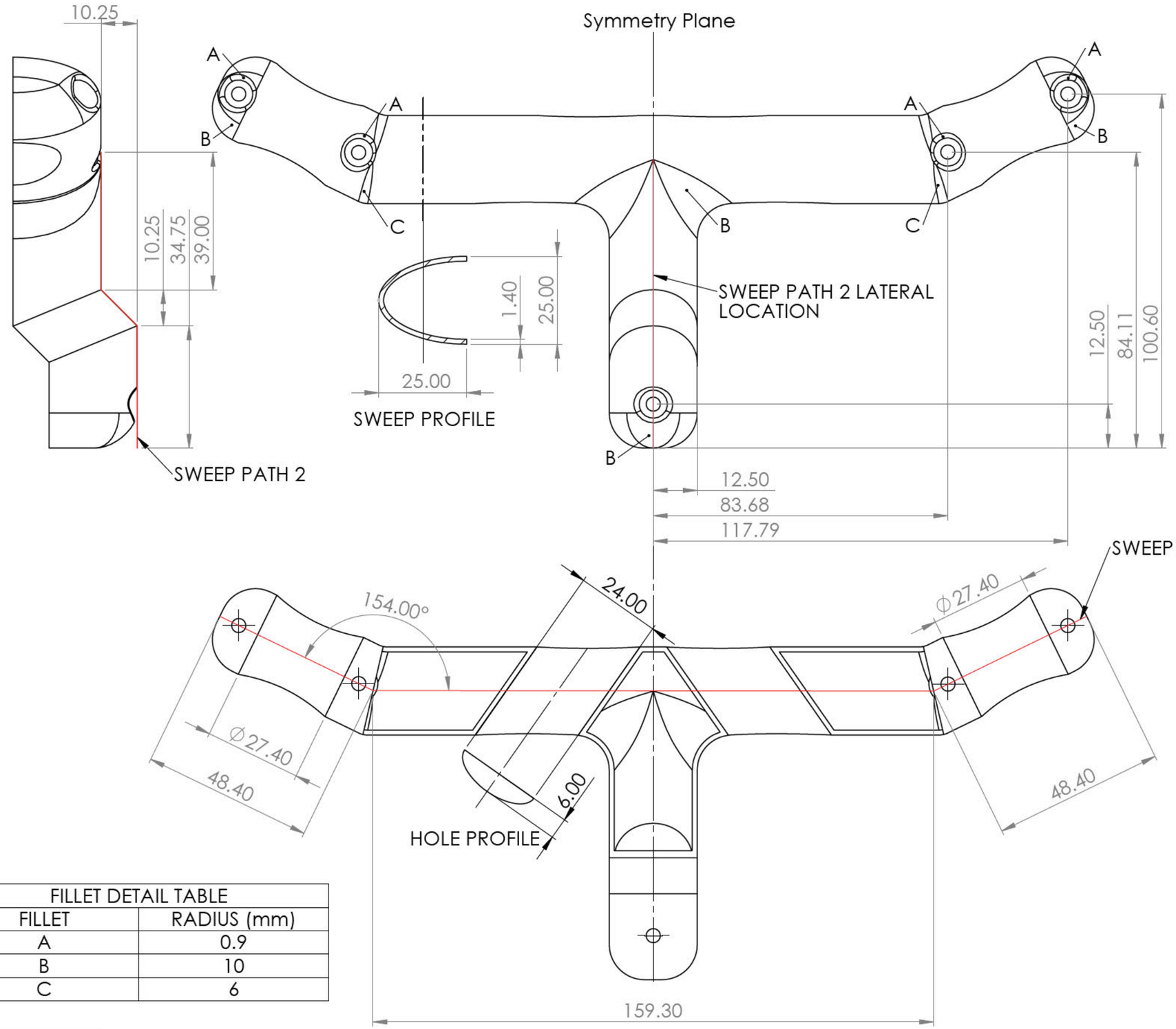

REAR VIEW SCALE 1:1.2

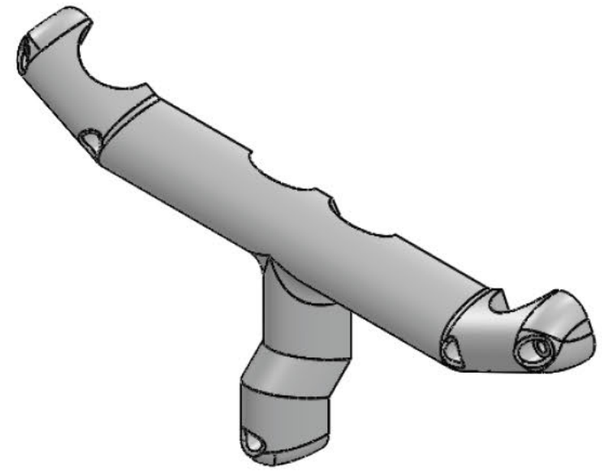

ISOMETRC VIEW SCALE 1:2

FILLET DETAIL TABLE	
FILLET	RADIUS (mm)
A	0.9
B	10
C	6

NOTES:

THE COMPONENT IS COMPRISED OF TWO INTERSECTING SWEPT PROFILES.

PROFILES ARE FIRST SWEPT ALONG THE INDICATED PATHS. HOLES, COUNTERBORES, AND FILLETS ARE APPLIED BEFORE SHELLING THE GEOMETRY WITH A SHELL THICKNESS OF **1.4mm**.

UNLESS OTHERWISE STATED GENERAL TOLERANCES: ±0.05 mm
ANGLES: ± 1 °

UNIVERSITY OF KWAZULU-NATAL

SCHOOL OF ENGINEERING

MECHANICAL ENGINEERING

MAT.: PLA		No. REQ.: 1	SCALE: 1:1.2	UNITS: mm	PROJECT: MSC MECHATRONICS
	DATE	CHECKED	STUDENT NAME: MATTHEW SWANEPOEL		No.: P1
PROJECT SUPERVISOR			STUDENT No.: 218039131		TITLE: FRONT LANDING GEAR MOUNT
WORKSHOP TECHNICIAN			E-MAIL: 218039131@STU.UKZN.AC.ZA		
TECHNICAL OFFICER			TEL. No.: [redacted]		

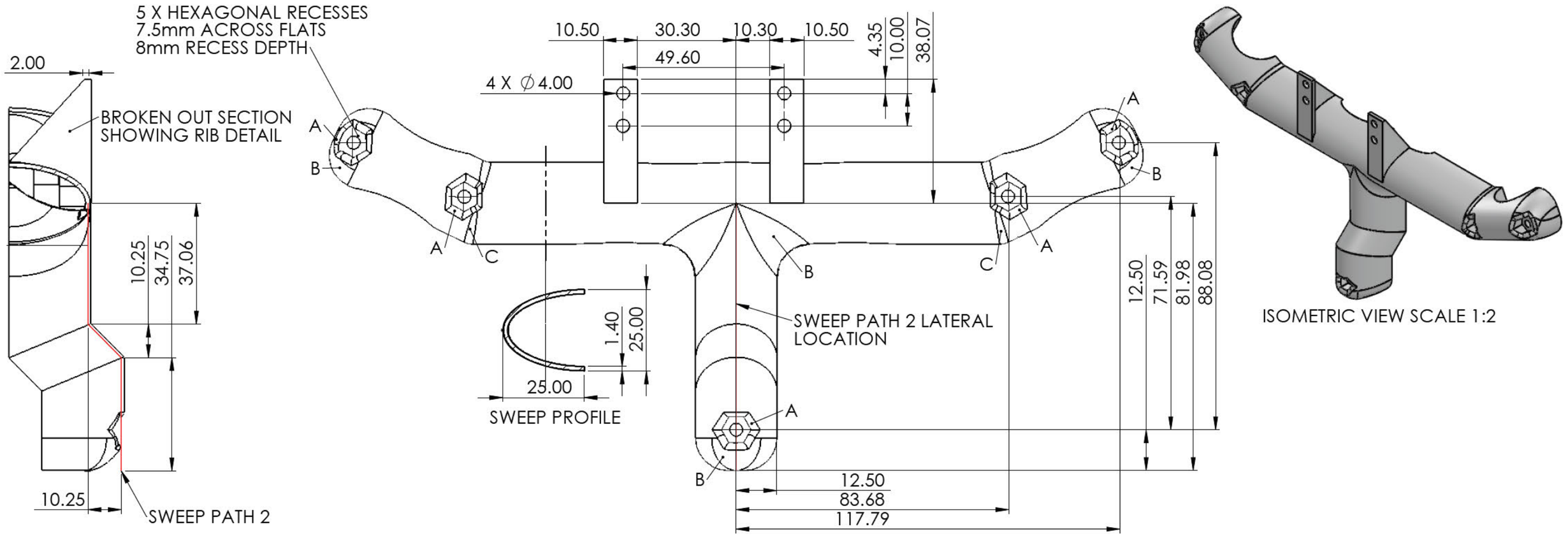

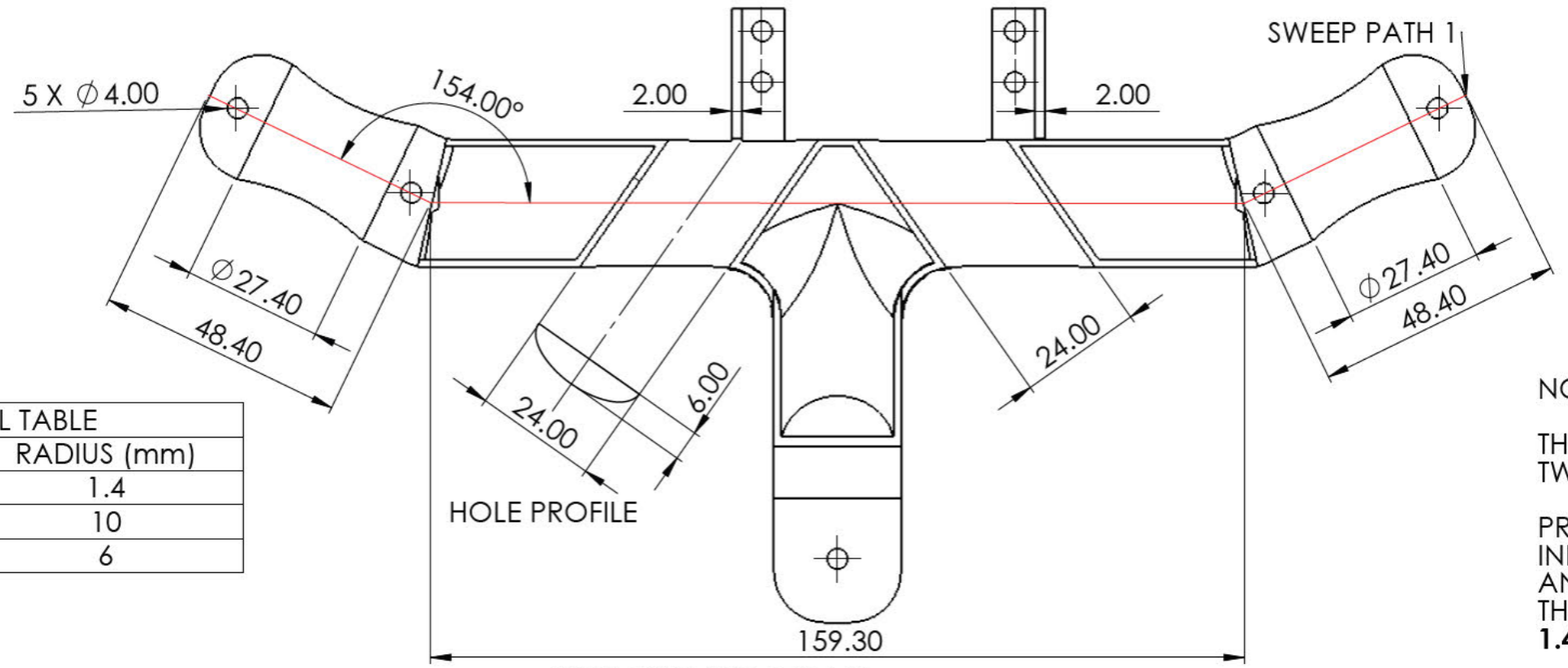

REAR VIEW SCALE 1:1.2

FILLET DETAIL TABLE	
FILLET	RADIUS (mm)
A	1.4
B	10
C	6

NOTES:

THE COMPONENT IS COMPRISED OF TWO INTERSECTING SWEPT PROFILES.

PROFILES ARE FIRST SWEPT ALONG THE INDICATED PATHS. HOLES, COUNTERBORES, AND FILLETS ARE APPLIED BEFORE SHELLING THE GEOMETRY WITH A SHELL THICKNESS OF **1.4mm**.

UNLESS OTHERWISE STATED GENERAL
TOLERANCES: ±0.05 mm
ANGLES: ± 1 °

UNIVERSITY OF KWAZULU-NATAL

SCHOOL OF ENGINEERING

MECHANICAL ENGINEERING

MAT.: PLA		No. REQ.: 1	SCALE: 1:1.2	UNITS: mm	PROJECT: MSC MECHATRONICS
	DATE	CHECKED	STUDENT NAME: MATTHEW SWANEPOEL		No.: P2
PROJECT SUPERVISOR			STUDENT No.: 218039131		TITLE: REAR LANDING GEAR MOUNT
WORKSHOP TECHNICIAN			E-MAIL: 218039131@STU.UKZN.AC.ZA		
TECHNICAL OFFICER			TEL. No.: [redacted]		

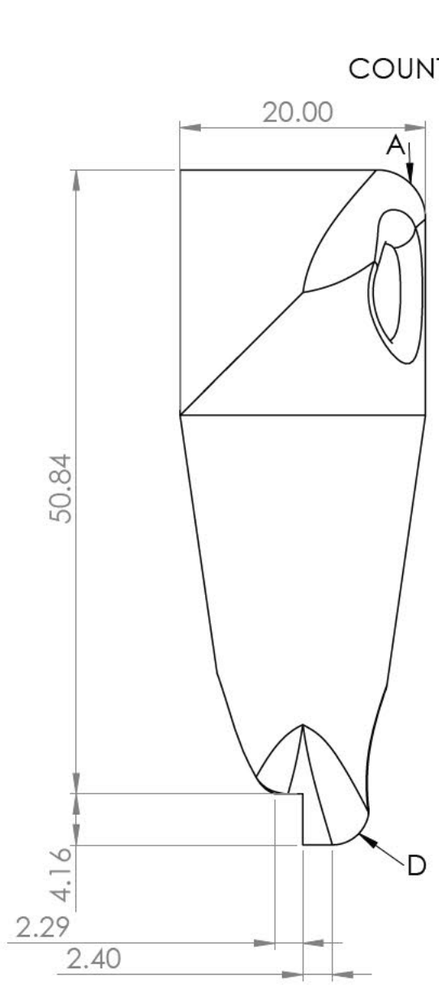

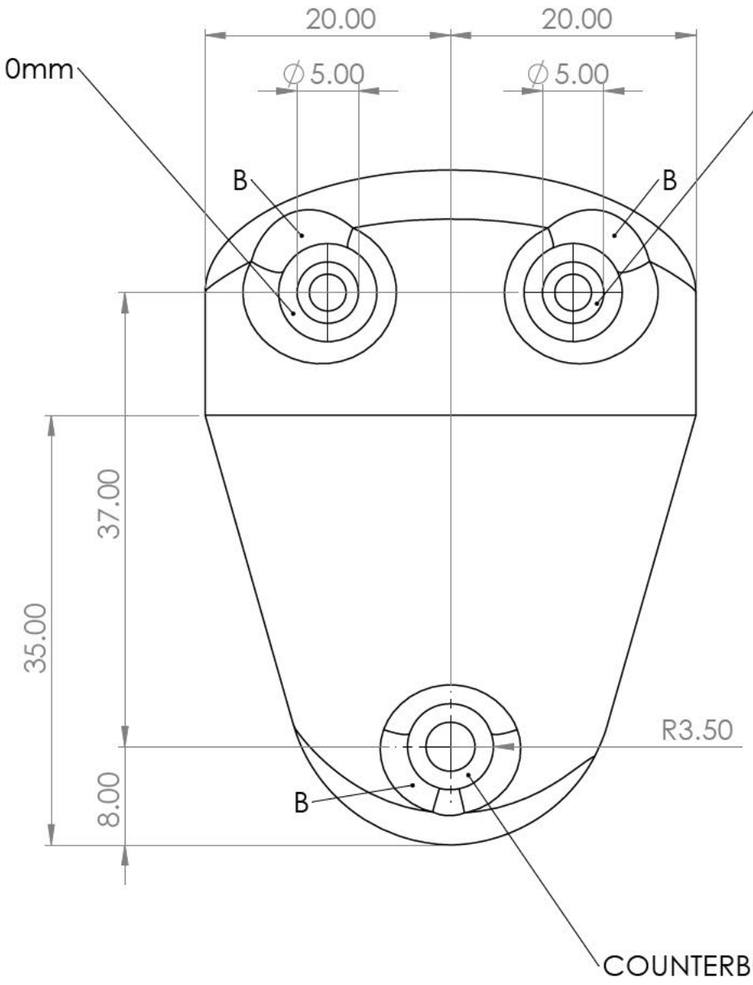

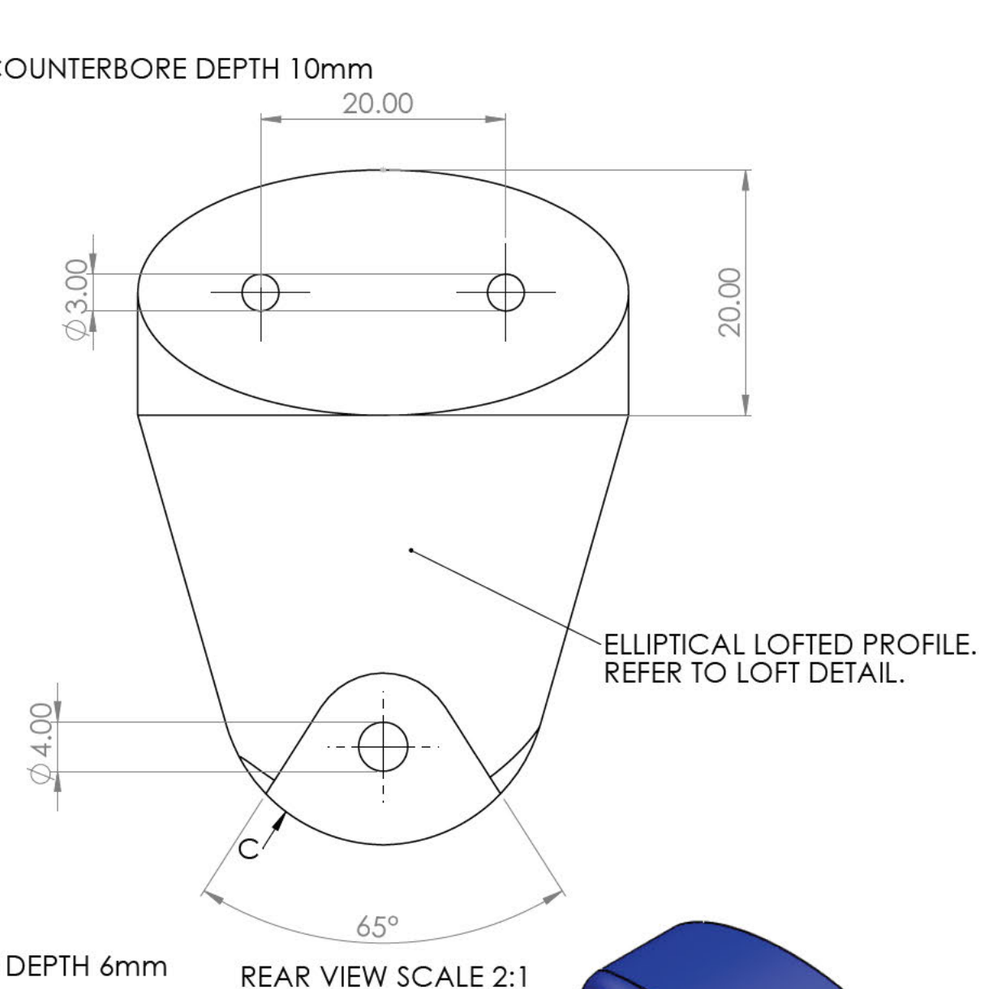

REAR VIEW SCALE 2:1

ISOMETRIC VIEW SCALE 1.5:1

FILLET DETAIL TABLE	
FILLET	RADIUS (mm)
A	4
B	1.8
C	13.5
D	3

LOFT DETAIL:

- BASE PROFILE DIMENTSIONS: 20mm X 10mm
- TERMINAL PROFILE DIMENSONS: 40mm X 20mm
- LOFT DISTANCE: 35mm

SHELL THICKNESS: 0.9mm

UNLESS OTHERWISE STATED GENERAL TOLERANCES: ±0.05 mm
ANGLES: ± 1 °

UNIVERSITY OF KWAZULU-NATAL

SCHOOL OF ENGINEERING

MECHANICAL ENGINEERING

MAT.: PLA		No. REQ.: 1	SCALE: 2:1	UNITS: mm	PROJECT: MSC MECHATRONICS
	DATE	CHECKED	STUDENT NAME: MATTHEW SWANEPOEL		No.: P3
PROJECT SUPERVISOR			STUDENT No.: 218039131		TITLE: DROP ARM END CAP
WORKSHOP TECHNICIAN			E-MAIL: 218039131@STU.UKZN.AC.ZA		
TECHNICAL OFFICER			TEL. No.: [redacted]		

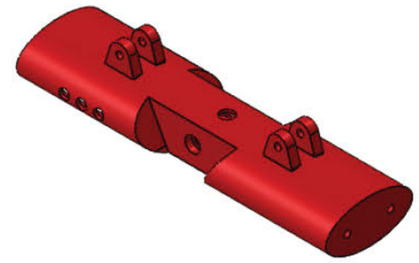

ISOMETRIC VIEW SCALE 1:2

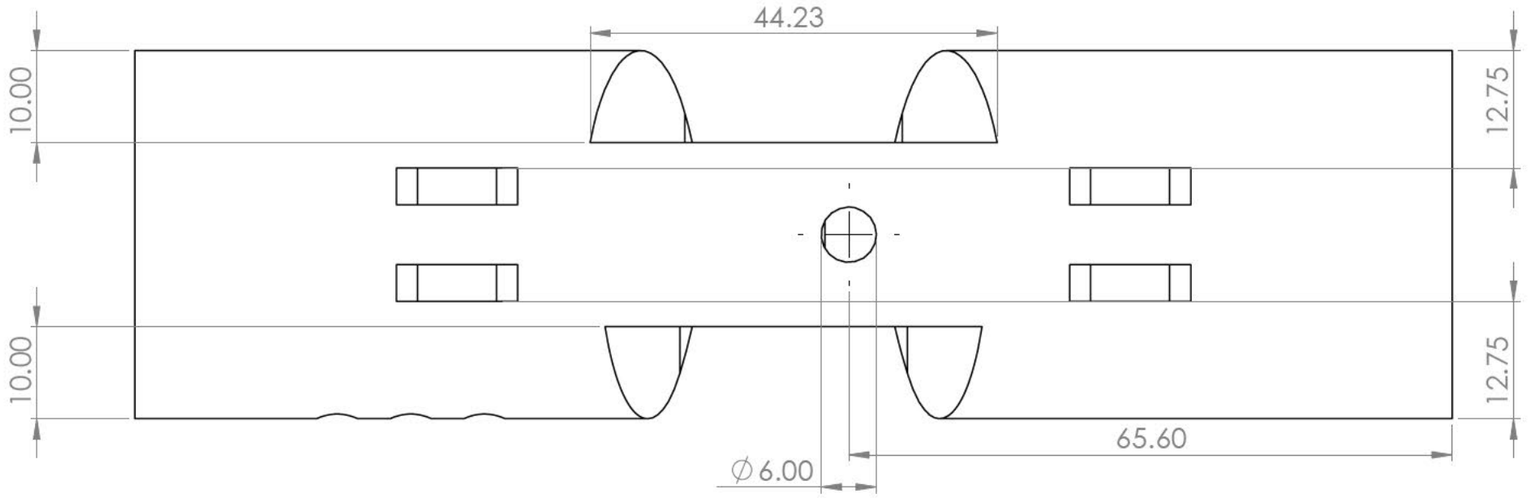

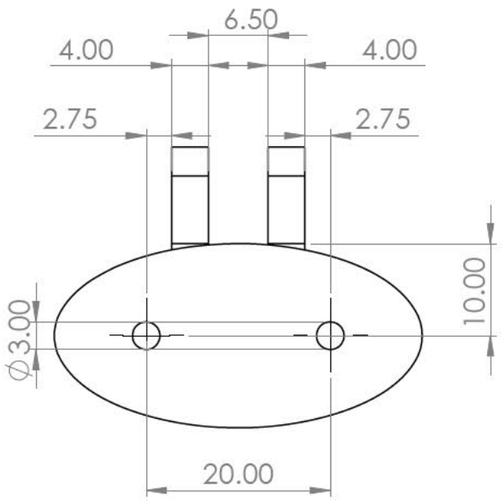

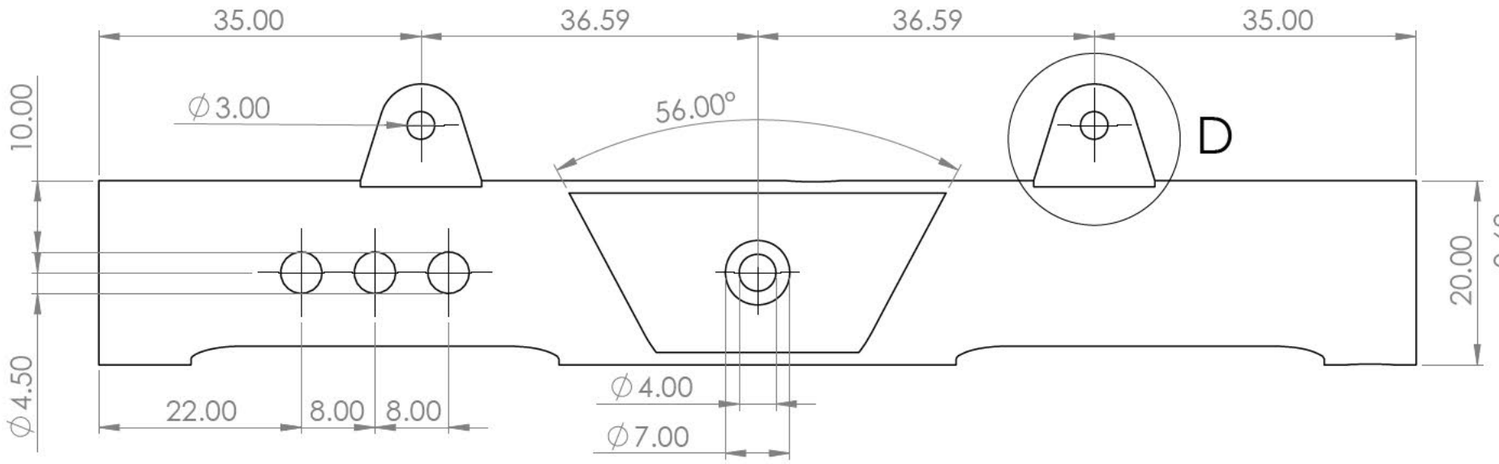

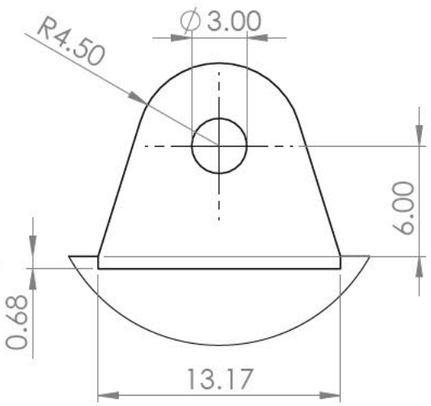

DETAIL D

SCALE 3 : 1

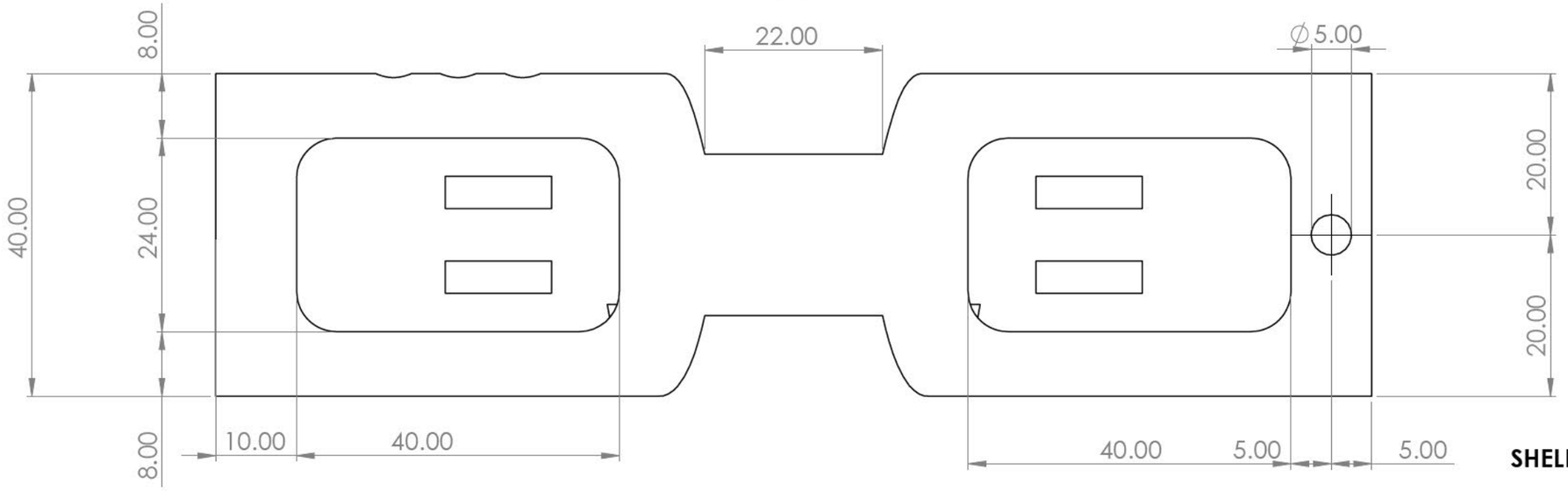

SHELL THICKNESS: 1.4**mm**

UNLESS OTHERWISE STATED GENERAL TOLERANCES: ±0.05 mm
ANGLES: ± 1 °

UNIVERSITY OF KWAZULU-NATAL

SCHOOL OF ENGINEERING

MECHANICAL ENGINEERING

MAT.: PLA		No. REQ.: 1	SCALE: 1.5:1	UNITS: mm	PROJECT: MSC MECHATRONICS
	DATE	CHECKED	STUDENT NAME: MATTHEW SWANEPOEL		No.: P4
PROJECT SUPERVISOR			STUDENT No.: 218039131		
WORKSHOP TECHNICIAN			E-MAIL: 218039131@STU.UKZN.AC.ZA		TITLE: DROP ARM
TECHNICAL OFFICER			TEL. No.: [redacted]		

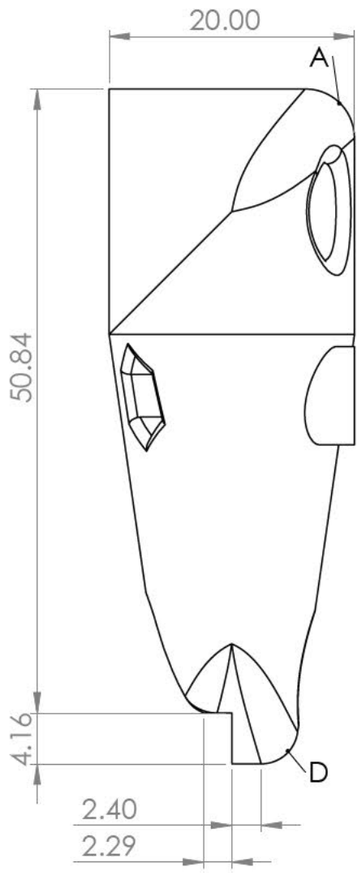

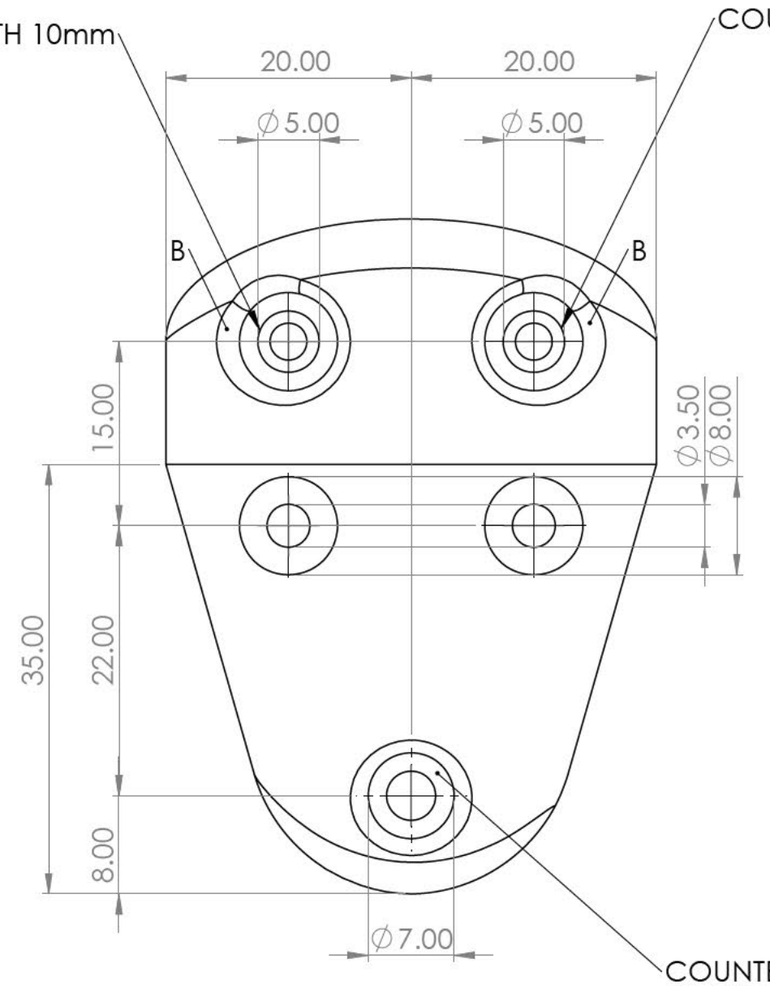

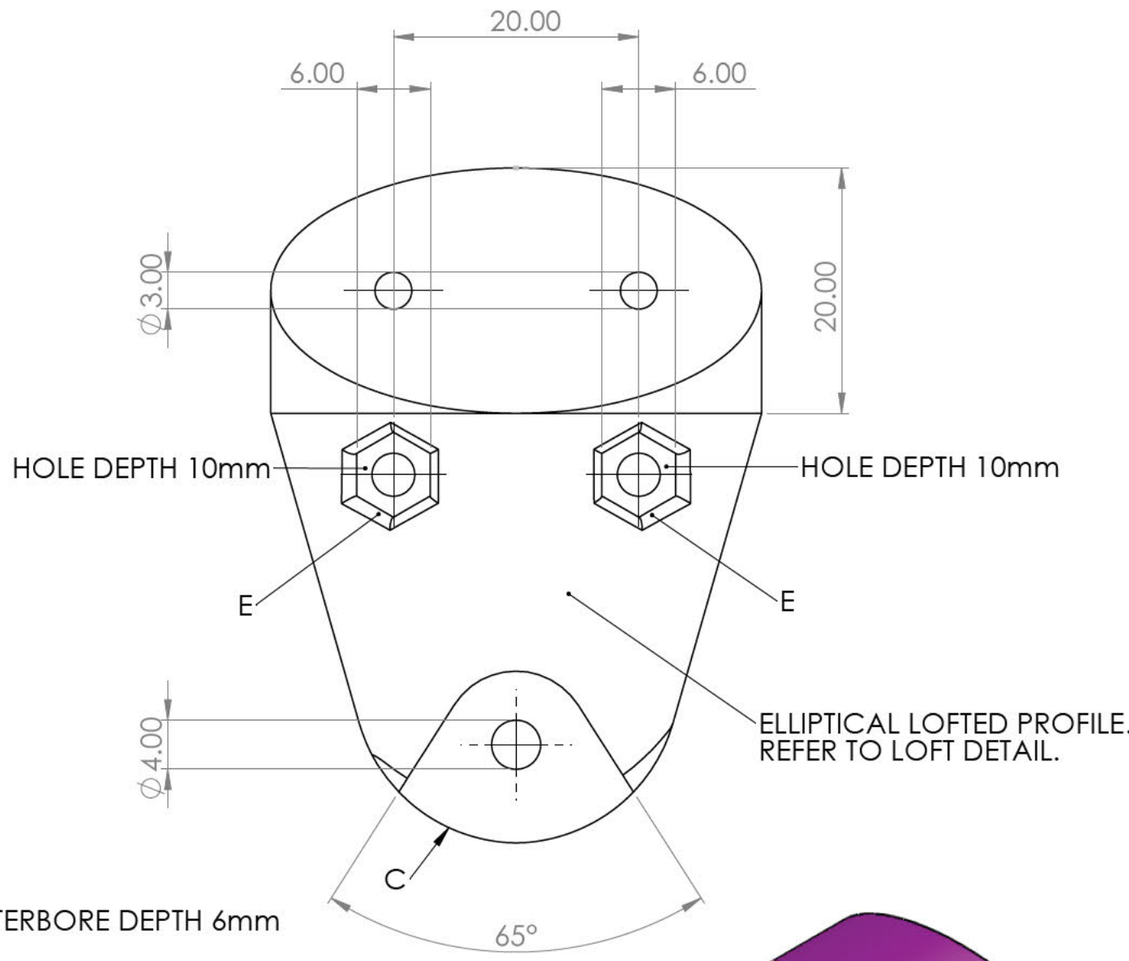

REAR VIEW SCALE 2:1

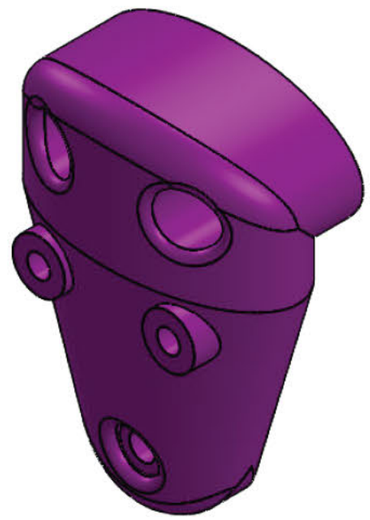

ISOMETRIC VIEW SCALE 1.5:1

FILLET DETAIL TABLE	
FILLET	RADIUS (mm)
A	4
B	1.8
C	13.5
D	3
E	0.8

LOFT DETAIL:

- BASE PROFILE DIMENTSIONS: 20mm X 10mm
- TERMINAL PROFILE DIMENSONS: 40mm X 20mm
- LOFT DISTANCE: 35mm

SHELL THICKNESS: 0.9mm

UNLESS OTHERWISE STATED GENERAL TOLERANCES: ±0.05 mm
ANGLES: ± 1 °

UNIVERSITY OF KWAZULU-NATAL

SCHOOL OF ENGINEERING

MECHANICAL ENGINEERING

MAT.: PLA		No. REQ.: 1	SCALE: 2:1	UNITS: mm	PROJECT: MSC MECHATRONICS
	DATE	CHECKED	STUDENT NAME: MATTHEW SWANEPOEL		No.: P5
PROJECT SUPERVISOR			STUDENT No.: 218039131		
WORKSHOP TECHNICIAN			E-MAIL: 218039131@STU.UKZN.AC.ZA		TITLE: DROP ARM END CAP CONTROL SURFACE
TECHNICAL OFFICER			TEL. No.: [redacted]		

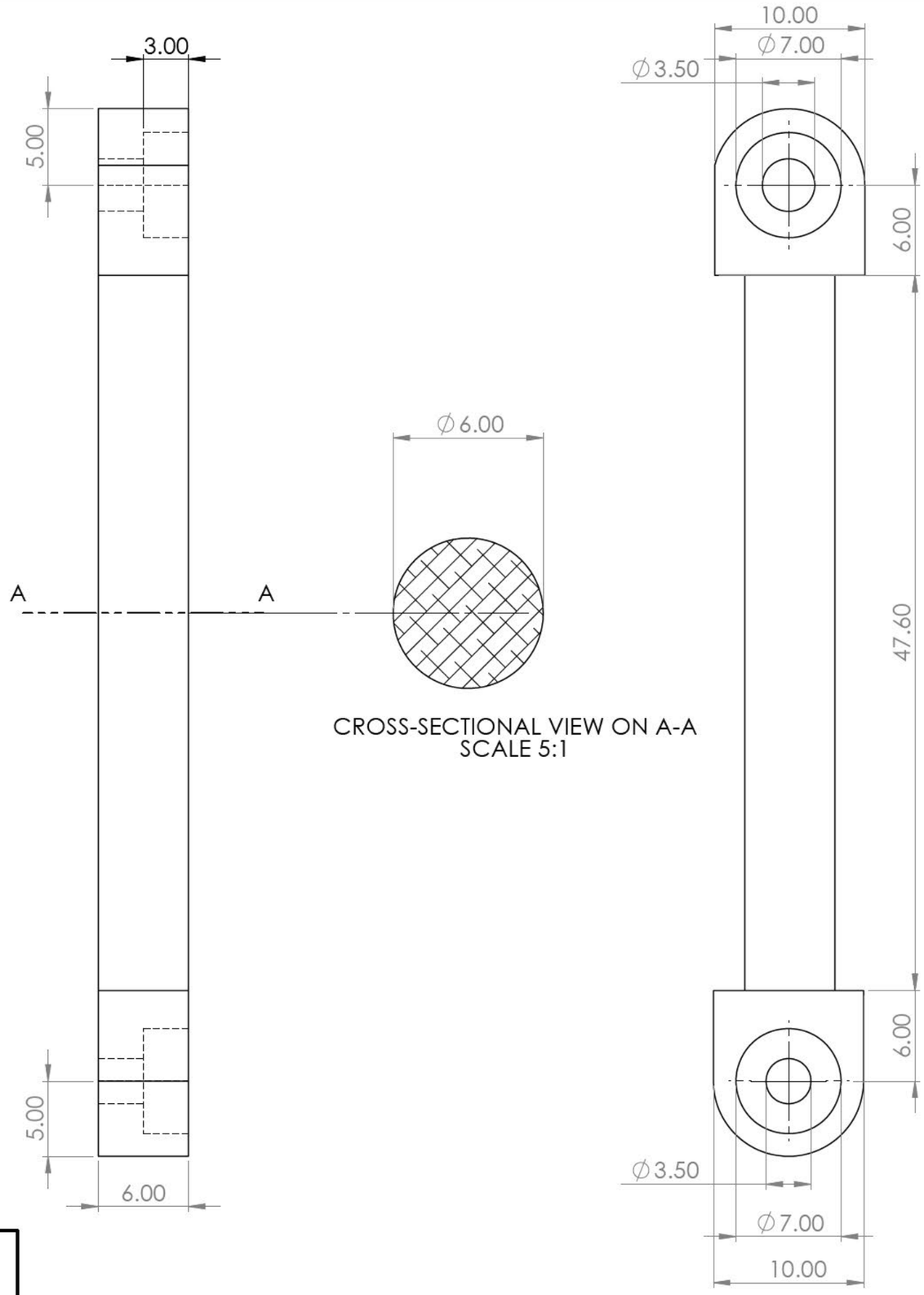

CROSS-SECTIONAL VIEW ON A-A
SCALE 5:1

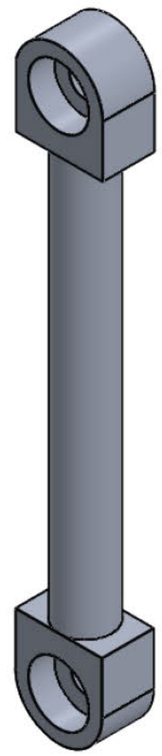

ISOMETRIC VIEW SCALE 2:1

UNLESS OTHERWISE
STATED GENERAL
TOLERANCES: ±0.05 mm
ANGLES: ± 1 °

UNIVERSITY OF KWAZULU-NATAL

SCHOOL OF ENGINEERING

MECHANICAL ENGINEERING

MAT.: PLA		No. REQ.: 2	SCALE: 3:1	UNITS: mm	PROJECT: MSC MECHATRONICS
	DATE	CHECKED	STUDENT NAME: MATTHEW SWANEPOEL		No.: P6
PROJECT SUPERVISOR			STUDENT No.: 218039131		TITLE: PITCH AXIS CONTROL ARM
WORKSHOP TECHNICIAN			E-MAIL: 218039131@STU.UKZN.AC.ZA		
TECHNICAL OFFICER			TEL. No.: [redacted]		

ISOMETRIC VIEW SCALE 2:1

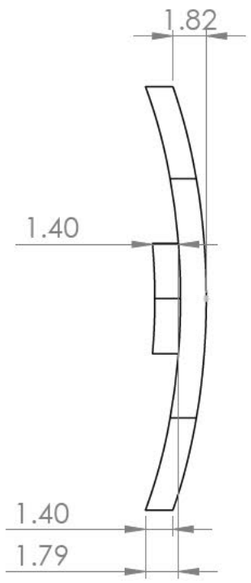

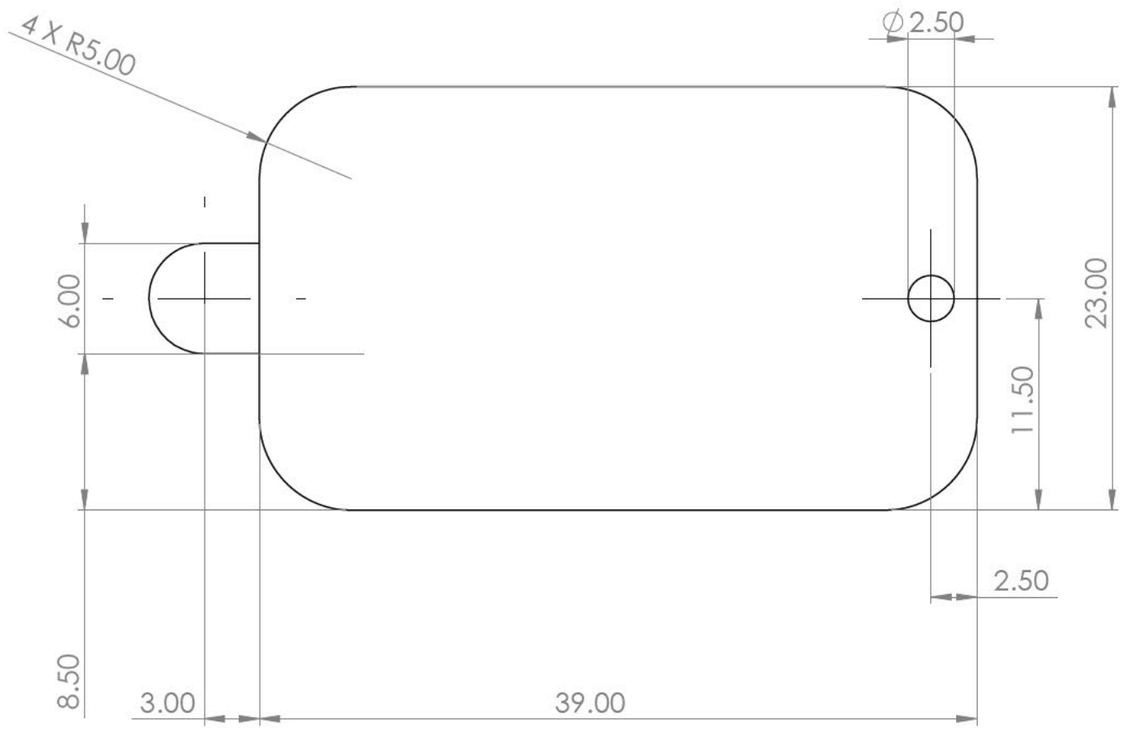

UNLESS OTHERWISE
STATED GENERAL
TOLERANCES: ±0.05 mm
ANGLES: ± 1 °

UNIVERSITY OF KWAZULU-NATAL

SCHOOL OF ENGINEERING

MECHANICAL ENGINEERING

MAT.: PLA		No. REQ.: 2	SCALE: 3:1	UNITS: mm	PROJECT: MSC MECHATRONICS
	DATE	CHECKED	STUDENT NAME: MATTHEW SWANEPOEL		No.: P7
PROJECT SUPERVISOR			STUDENT No.: 218039131		
WORKSHOP TECHNICIAN			E-MAIL: 218039131@STU.UKZN.AC.ZA		TITLE: DROP ARM LID
TECHNICAL OFFICER			TEL. No.: [redacted]		

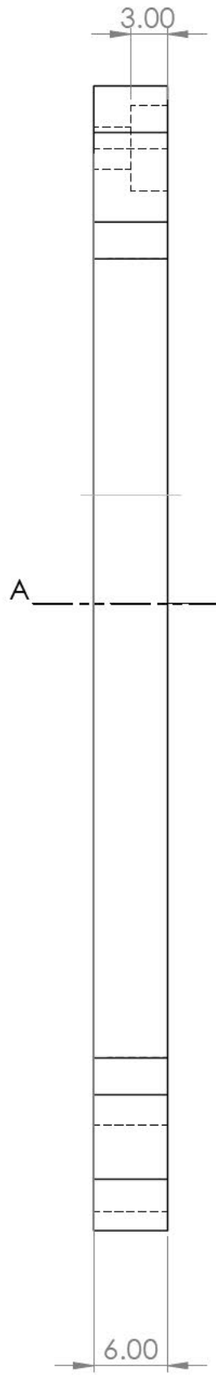

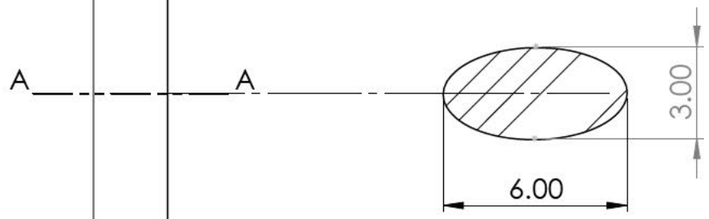

CROSS-SECTIONAL VIEWON A-A

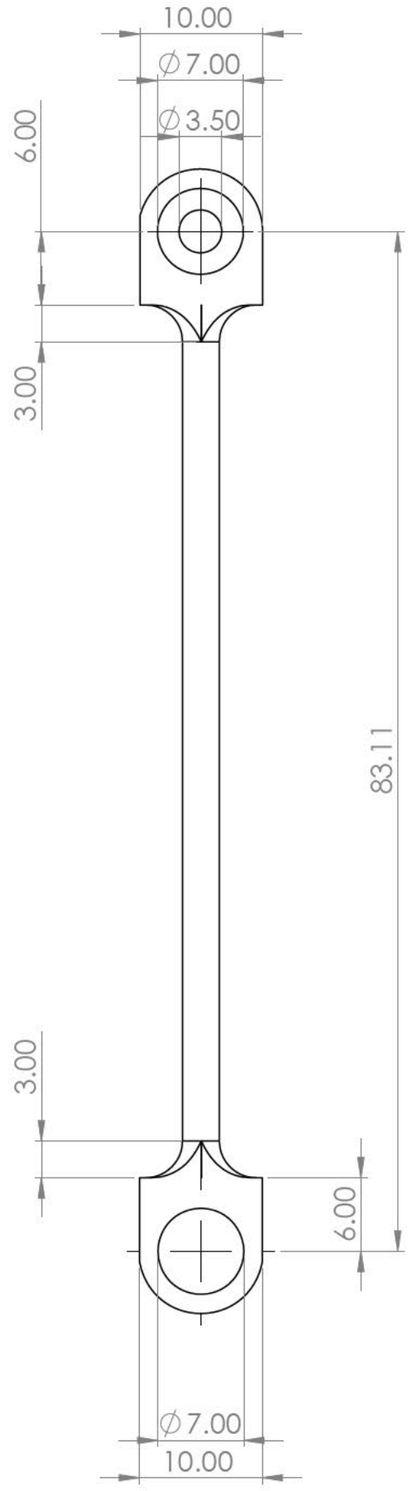

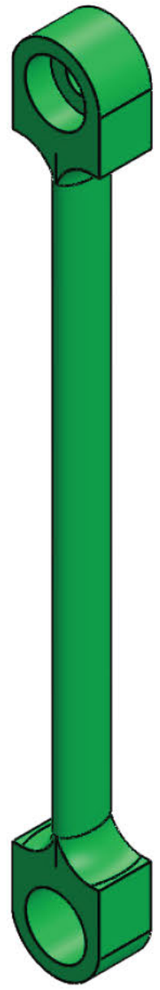

ISOMETRIC VIEW SCALE 2:1

UNLESS OTHERWISE
STATED GENERAL
TOLERANCES: ±0.05 mm
ANGLES: ± 1 °

UNIVERSITY OF KWAZULU-NATAL

SCHOOL OF ENGINEERING

MECHANICAL ENGINEERING

MAT.: PLA		No. REQ.: 2	SCALE: 2:1	UNITS: mm	PROJECT: MSC MECHATRONICS
	DATE	CHECKED	STUDENT NAME: MATTHEW SWANEPOEL		No.: P8
PROJECT SUPERVISOR			STUDENT No.: 218039131		TITLE: ROLL AXIS CONTROL ARM
WORKSHOP TECHNICIAN			E-MAIL: 218039131@STU.UKZN.AC.ZA		
TECHNICAL OFFICER			TEL. No.: [redacted]		

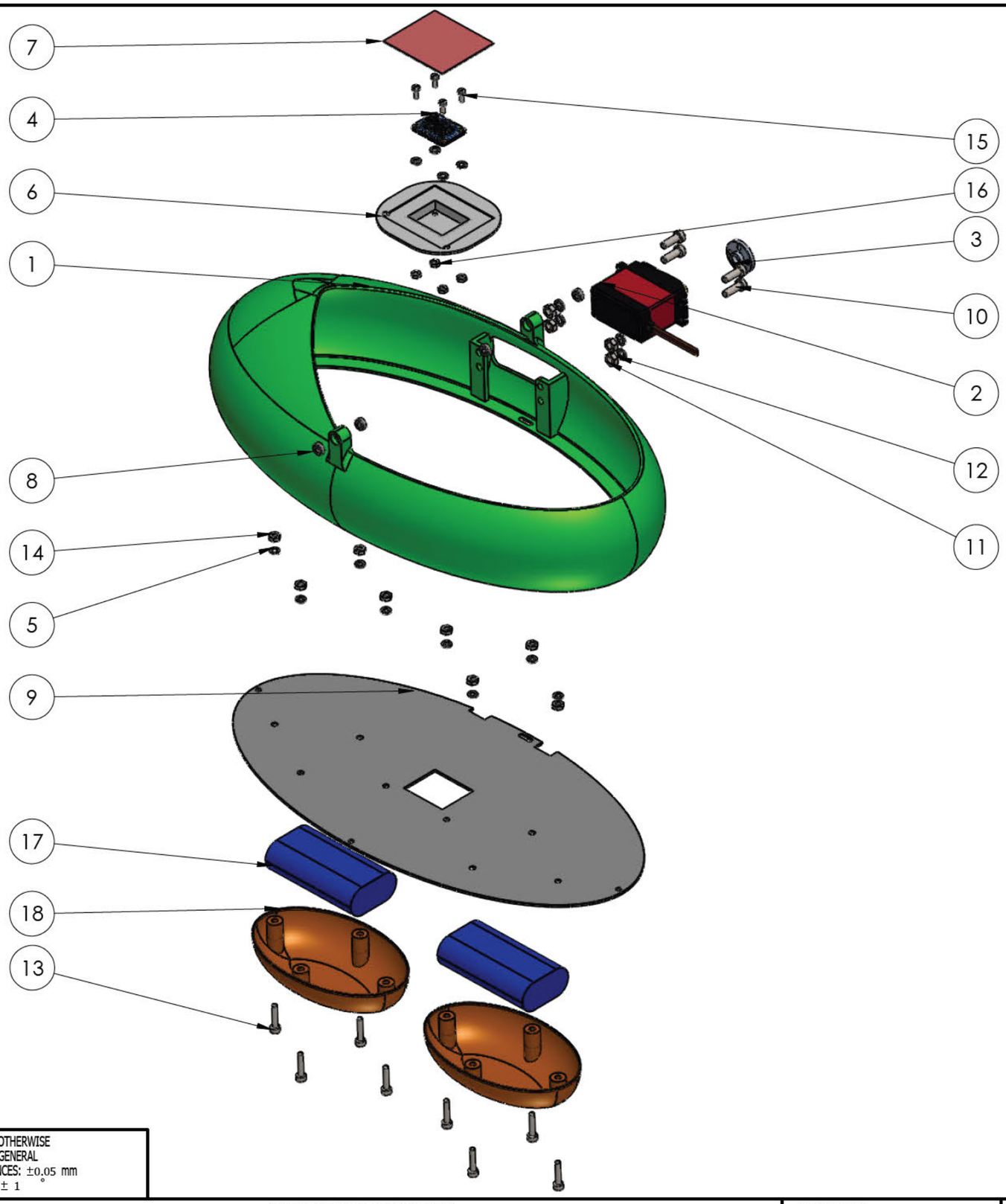

ITEM NO.	PART NAME	UNIT MASS (g)	QTY.	TOTAL MASS (g)
1	PAYLOAD CRADLE	102.26	1	102.26
2	DSSERVO 35KG SERVO MOTOR	33.55	1	33.55
3	ALUMINIUM SERVO HORN	2.10	1	2.10
4	ADAFRUIT BNO055	3.04	1	3.04
5	M3 WASHER	0.17	12	2.04
6	BNO055 HOUSING	7.62	1	7.62
7	BNO055 LID	1.49	2	2.98
8	683-RS BALL BEARING	0.74	4	2.96
9	CRADLE BASE	51.8	1	51.8
10	M4 SCREW (4x12)	2.03	4	8.12
11	M4 NUT	0.76	4	3.04
12	M4 WASHER	0.24	4	0.96
13	M3 CAP SCREW (3X15)	1.40	8	11.2
14	M3 NUT	0.46	8	3.68
15	M2.5 SCREW (2.5x6)	0.42	4	1.66
16	M2.5 NUT	0.27	4	1.08
17	7.4V 2600mAh LI-ION BATTERY	93.78	2	187.56
18	BATTERY HOUSING	8.69	2	17.38
TOTAL				440.07

UNLESS OTHERWISE STATED GENERAL
TOLERANCES: ±0.05 mm
ANGLES: ± 1 °

UNIVERSITY OF KWAZULU-NATAL

SCHOOL OF ENGINEERING

MECHANICAL ENGINEERING

MAT.: VARIOUS		No. REQ.: 1	SCALE: 1:2.6	UNITS: mm
	DATE	CHECKED	STUDENT NAME: MATTHEW SWANEPOEL	
PROJECT SUPERVISOR			STUDENT No.: 218039131	
WORKSHOP TECHNICIAN			E-MAIL: 218039131@STU.UKZN.AC.ZA	
TECHNICAL OFFICER			TEL. No.: [redacted]	

PROJECT: MSC MECHATRONICS

No.: SA2

TITLE: PAYLOAD CRADLE EXPLODED SUB-ASSEMBLY

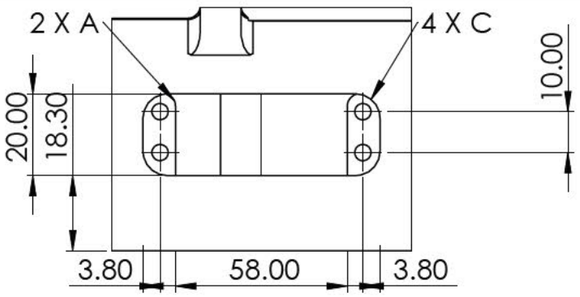

REAR VIEW CROPPED SECTION SCALE 1:1.5

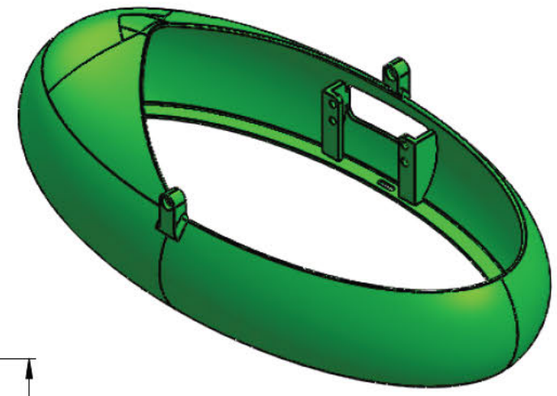

ISOMETRIC VIEW
SCALE 1:3

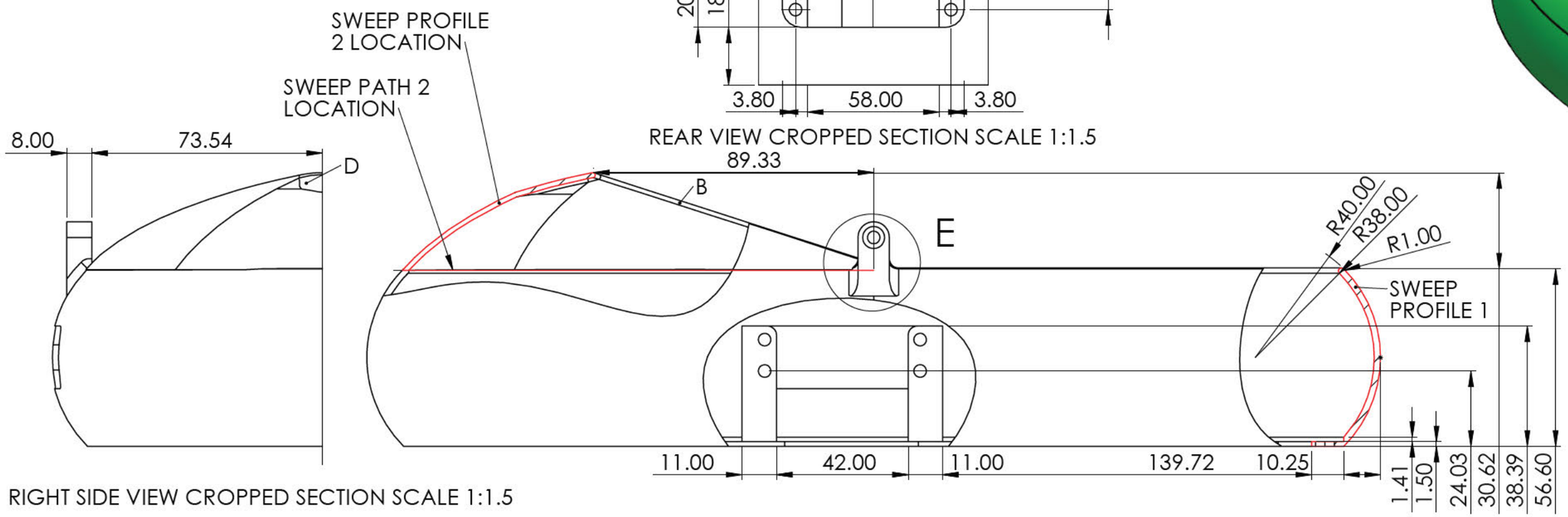

RIGHT SIDE VIEW CROPPED SECTION SCALE 1:1.5

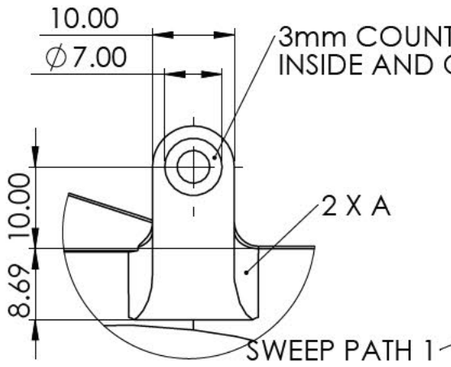

DETAIL E

SCALE 2 : 1.5

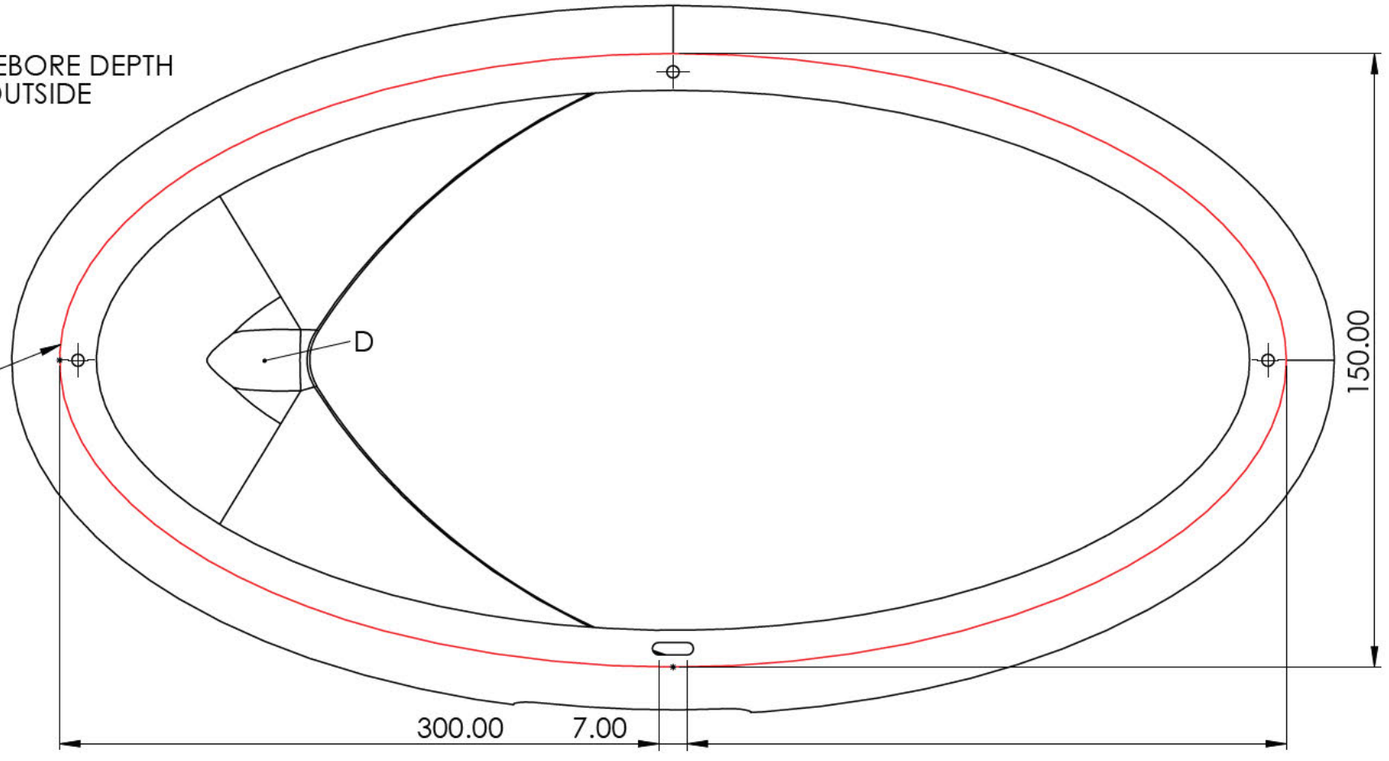

NOTES:

THE COMPONENT IS COMPRISED OF TWO SWEPT PROFILES.

PROFILES ARE FIRST SWEPT ALONG THE INDICATED PATHS. HOLES, COUNTERBORES, AND FILLETS ARE THEN APPLIED.

ALL HOLES 3mm UNLESS SPECIFIED OTHERWISE.

SWEEP PROFILE 2 IS A CONTINUATION OF SWEEP PROFILE 1 TO THE SPECIFIED HEIGHT AND 1.5mm WALL THICKNESS.

FILLET DETAIL TABLE	
FILLET	RADIUS (mm)
A	3
B	1
C	6
D	25

UNLESS OTHERWISE
STATED GENERAL
TOLERANCES: ±0.05 mm
ANGLES: ± 1 °

UNIVERSITY OF KWAZULU-NATAL

SCHOOL OF ENGINEERING

MECHANICAL ENGINEERING

MAT.: PLA		No. REQ.: 1	SCALE: 1:1.5	UNITS: mm	PROJECT: MSC MECHATRONICS
	DATE	CHECKED	STUDENT NAME: MATTHEW SWANEPOEL		No.: P9
PROJECT SUPERVISOR			STUDENT No.: 218039131		TITLE: PAYLOAD CRADLE
WORKSHOP TECHNICIAN			E-MAIL: 218039131@STU.UKZN.AC.ZA		
TECHNICAL OFFICER			TEL. No.: [redacted]		

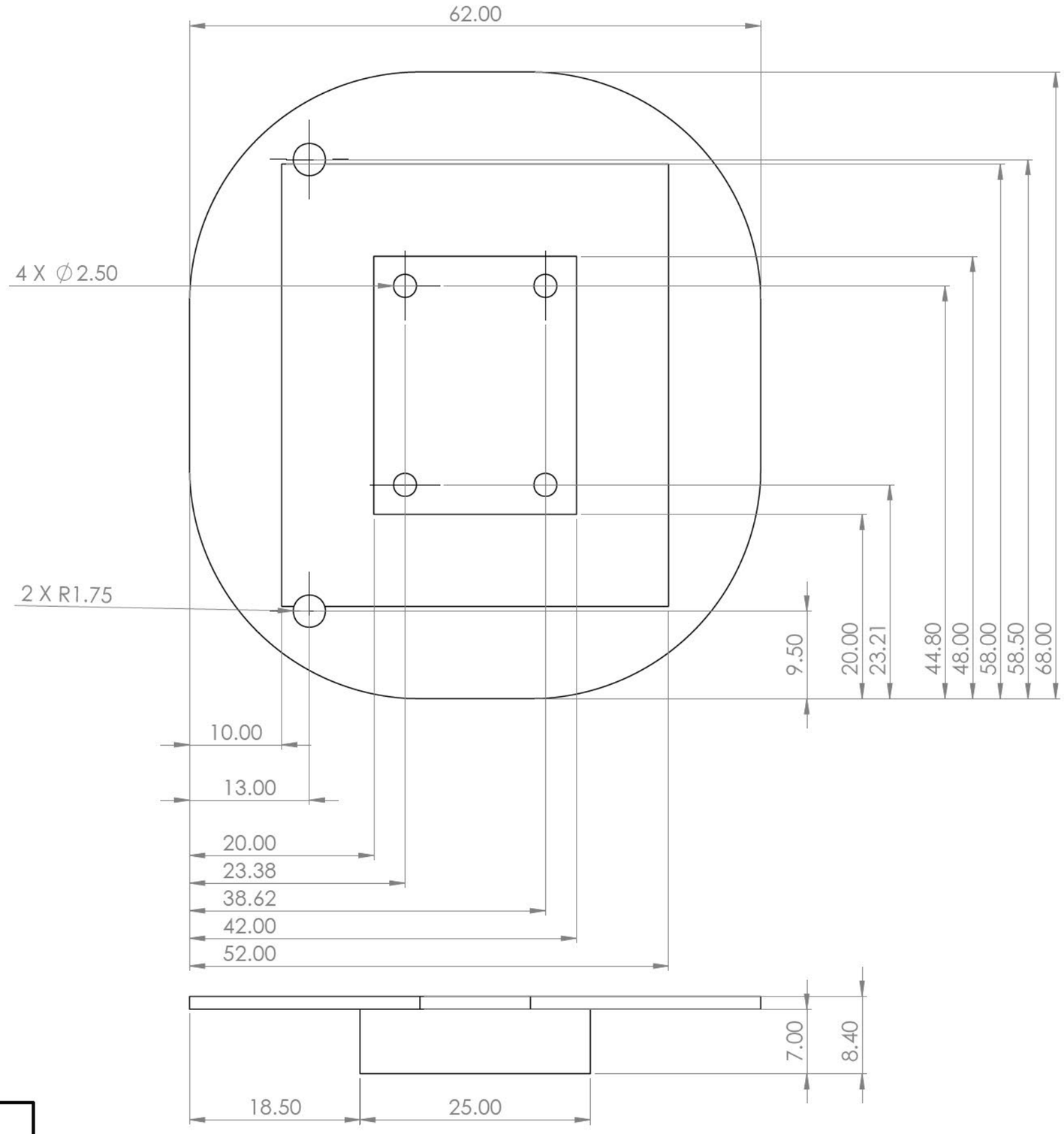

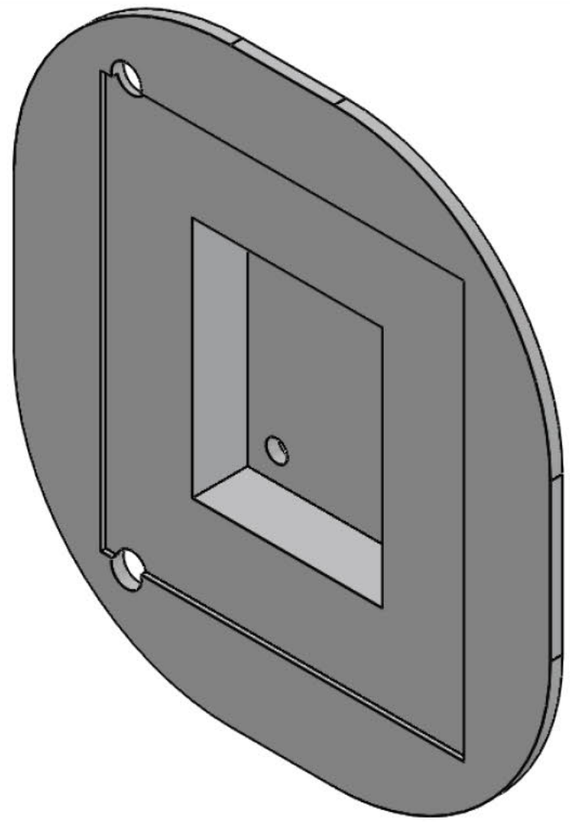

ISOMETRIC VIEW SCALE 2:1

UNLESS OTHERWISE
STATED GENERAL
TOLERANCES: ±0.05 mm
ANGLES: ± 1 °

UNIVERSITY OF KWAZULU-NATAL	MAT.: PLA	No. REQ.: 1	SCALE: 2:1	UNITS: mm	PROJECT: MSC MECHATRONICS
	DATE	CHECKED	STUDENT NAME: MATTHEW SWANEPOEL		No.: P10
SCHOOL OF ENGINEERING	PROJECT SUPERVISOR		STUDENT No.: 218039131		TITLE: BNO055 HOUSING
MECHANICAL ENGINEERING	WORKSHOP TECHNICIAN		E-MAIL: 218039131@STU.UKZN.AC.ZA		
	TECHNICAL OFFICER		TEL. No.: [redacted]		

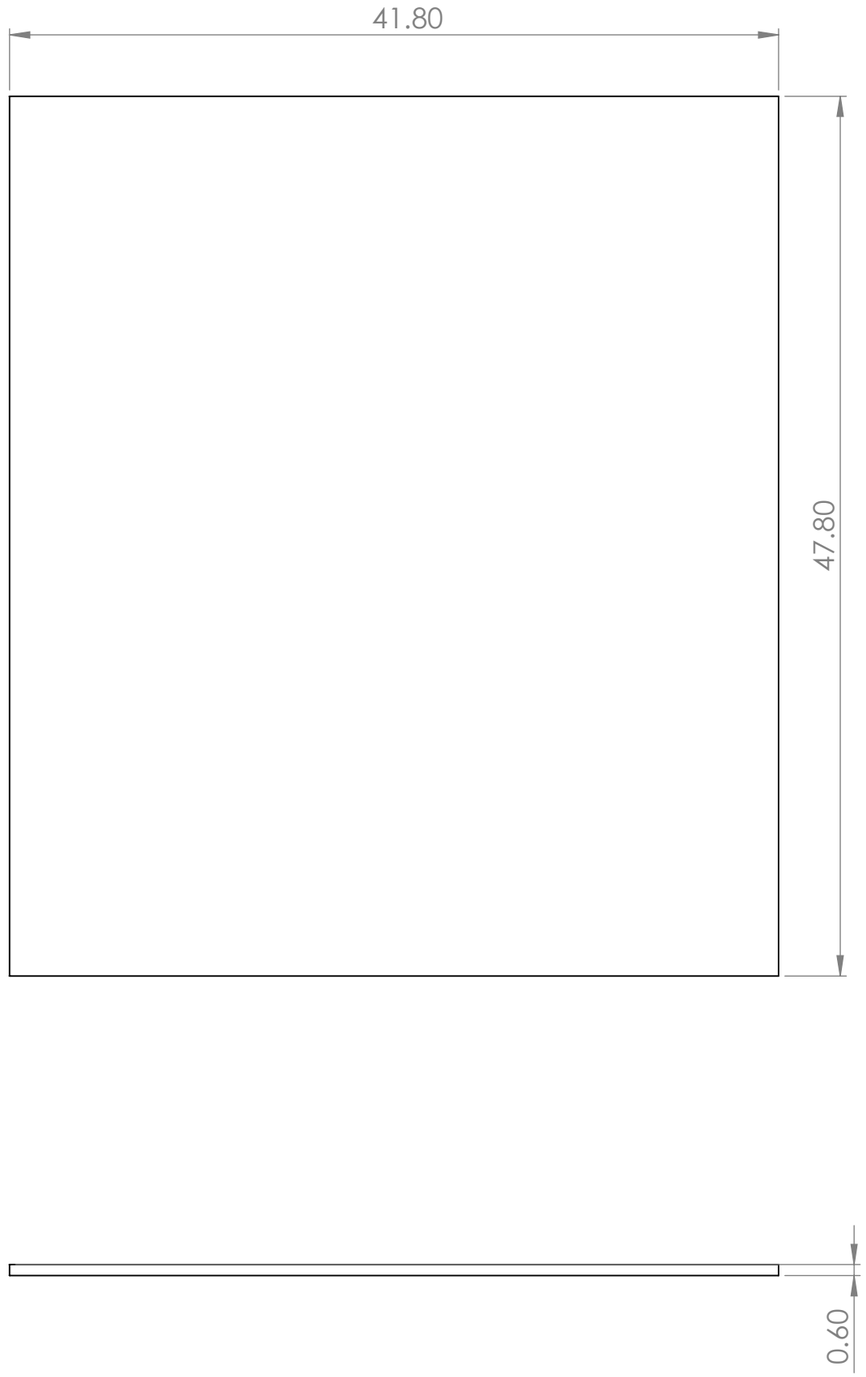

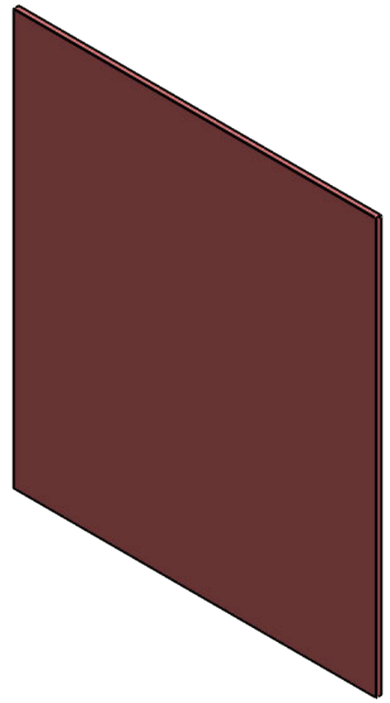

ISOMETRIC VIEW SCALE 2:1

UNLESS OTHERWISE
STATED GENERAL
TOLERANCES: ±0.05 mm
ANGLES: ± 1 °

UNIVERSITY OF KWAZULU-NATAL	MAT.: PLA		No. REQ.: 1	SCALE: 3:1 UNITS: mm	PROJECT: MSC MECHATRONICS
		DATE	CHECKED	STUDENT NAME: MATTHEW SWANEPOEL	No.: P11
SCHOOL OF ENGINEERING	PROJECT SUPERVISOR			STUDENT No.: 218039131	
	WORKSHOP TECHNICIAN			E-MAIL: 218039131@STU.UKZN.AC.ZA	TITLE: BNO055 HOUSING LID
MECHANICAL ENGINEERING	TECHNICAL OFFICER			TEL. No.: [redacted]	

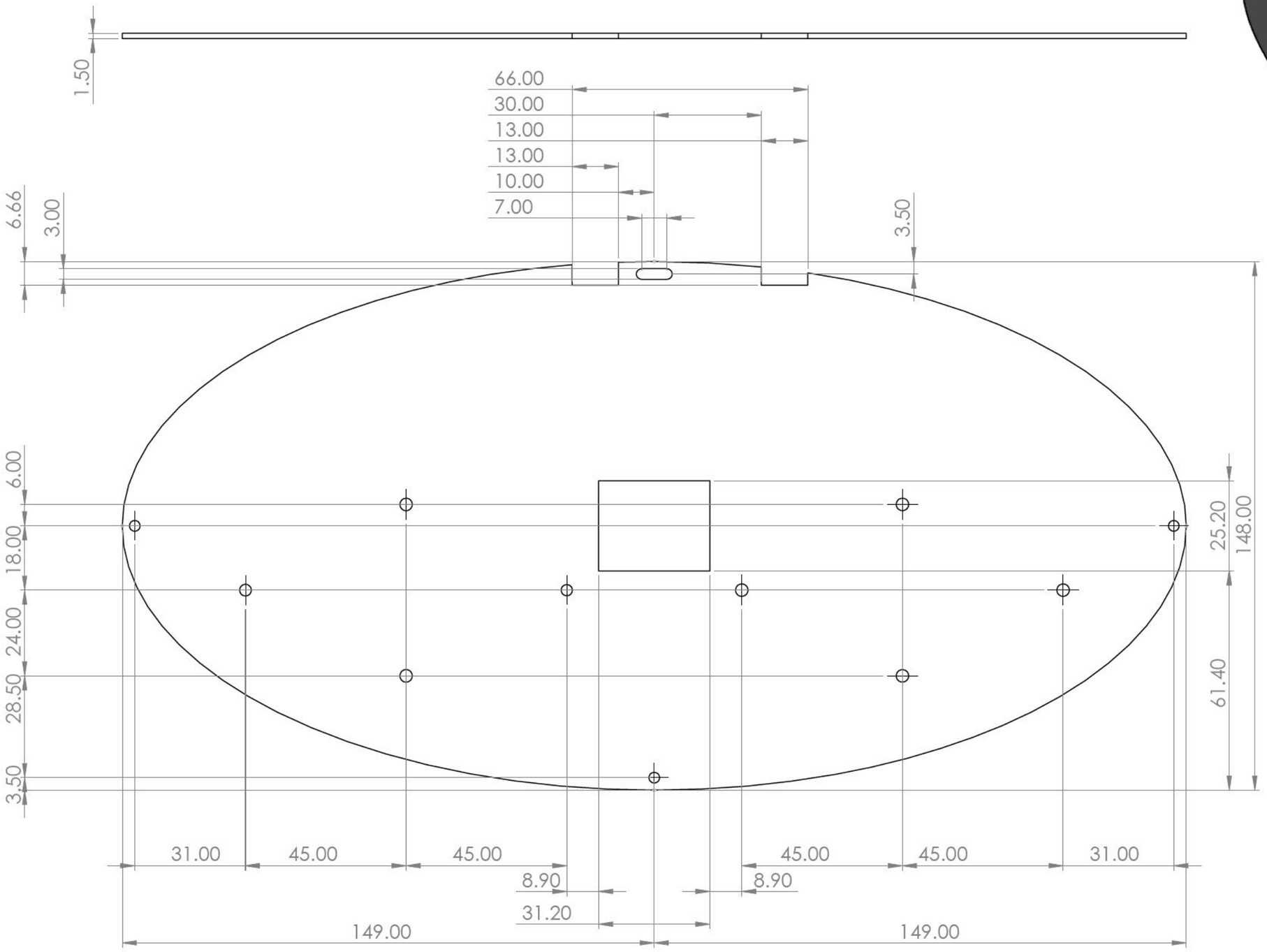

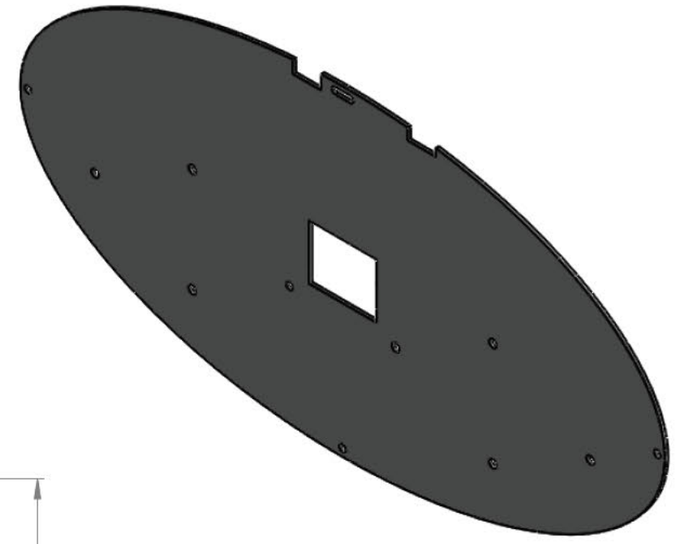

ISOMETRIC VIEW SCALE 1:2

UNLESS OTHERWISE
STATED GENERAL
TOLERANCES: ±0.05 mm
ANGLES: ± 1°

UNIVERSITY OF KWAZULU-NATAL

SCHOOL OF ENGINEERING

MECHANICAL ENGINEERING

MAT.: PLA		No. REQ.: 1	SCALE: 1:1.2	UNITS: mm	PROJECT: MSC MECHATRONICS
	DATE	CHECKED	STUDENT NAME: MATTHEW SWANEPOEL		No.: P12
PROJECT SUPERVISOR			STUDENT No.: 218039131		
WORKSHOP TECHNICIAN			E-MAIL: 218039131@STU.UKZN.AC.ZA		TITLE: CRADLE BASE
TECHNICAL OFFICER			TEL. No.: [redacted]		

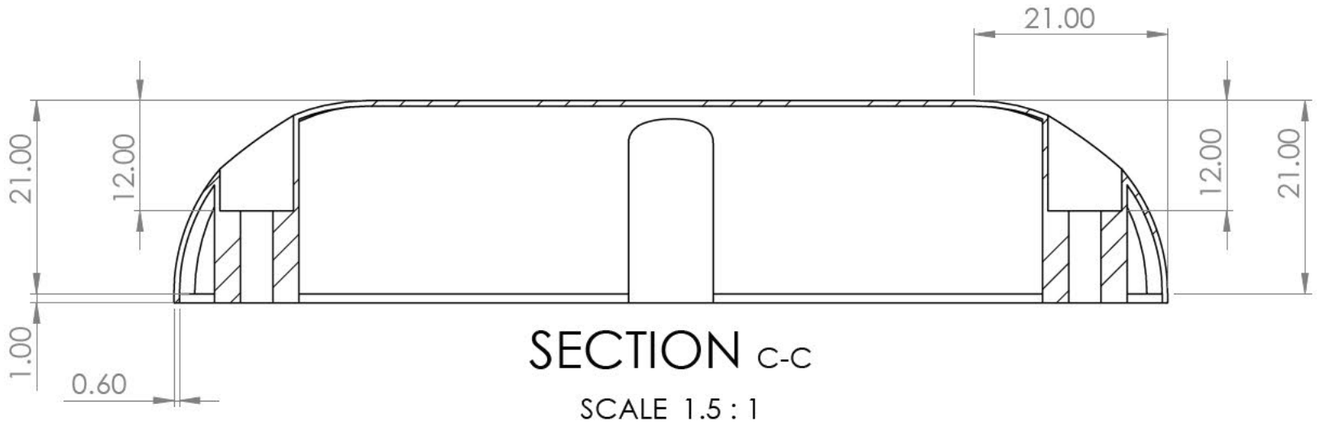

SECTION C-C

SCALE 1.5 : 1

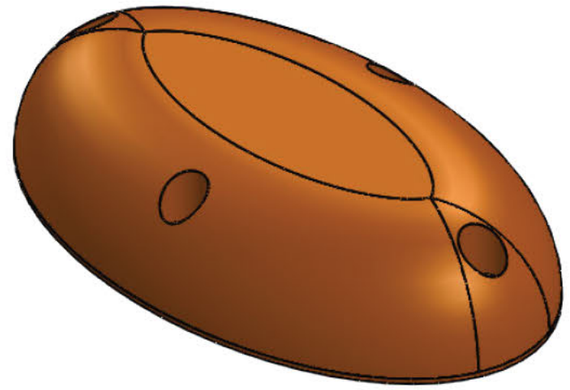

ISOMETRIC VIEW SCALE 1:1

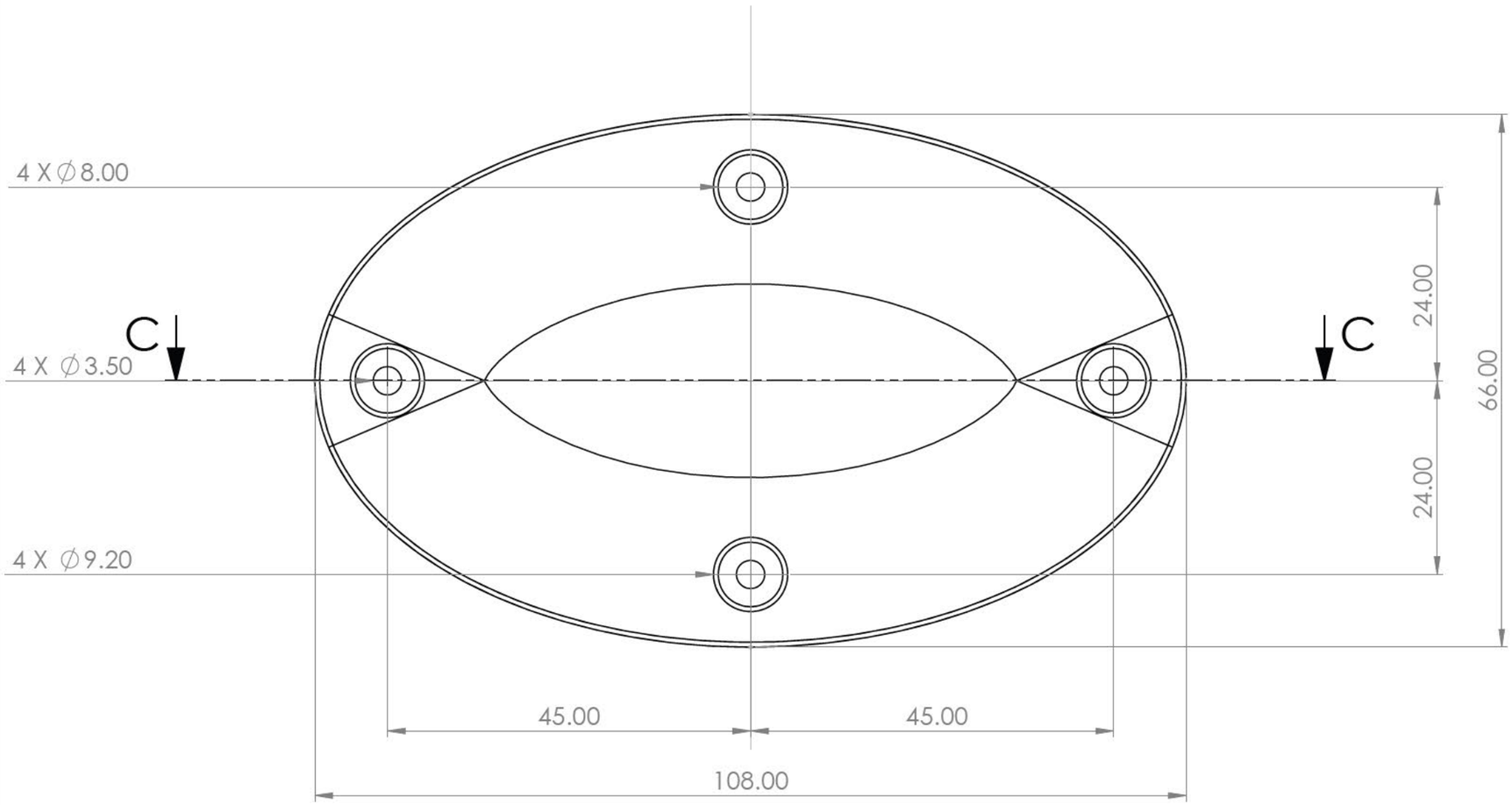

UNLESS OTHERWISE
STATED GENERAL
TOLERANCES: ±0.05 mm
ANGLES: ± 1 °

UNIVERSITY OF KWAZULU-NATAL	MAT.: PLA	No. REQ.: 2	SCALE: 1.5:1	UNITS: mm	PROJECT: MSC MECHATRONICS
SCHOOL OF ENGINEERING	DATE	CHECKED	STUDENT NAME: MATTHEW SWANEPOEL		No.: P13
MECHANICAL ENGINEERING	PROJECT SUPERVISOR		STUDENT No.: 218039131		TITLE: BATTERY HOUSING
	WORKSHOP TECHNICIAN		E-MAIL: 218039131@STU.UKZN.AC.ZA		
	TECHNICAL OFFICER		TEL. No.: [redacted]		

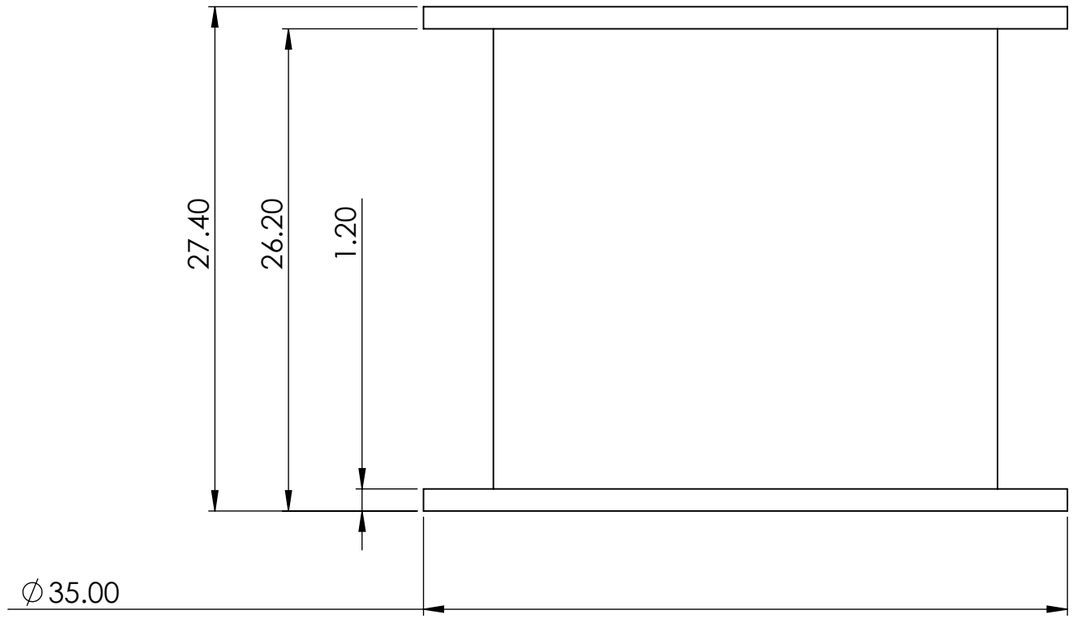

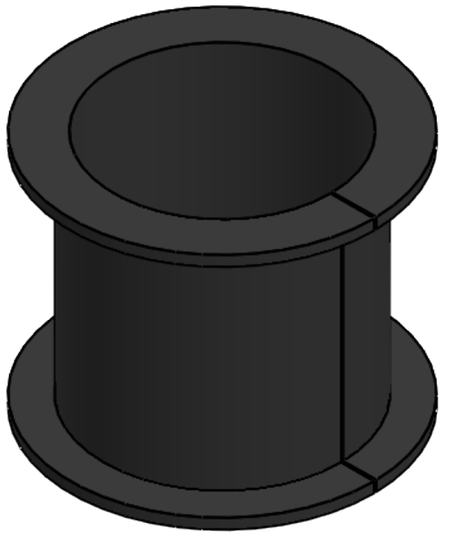

ISOMETRIC VIEW SCALE 2:1

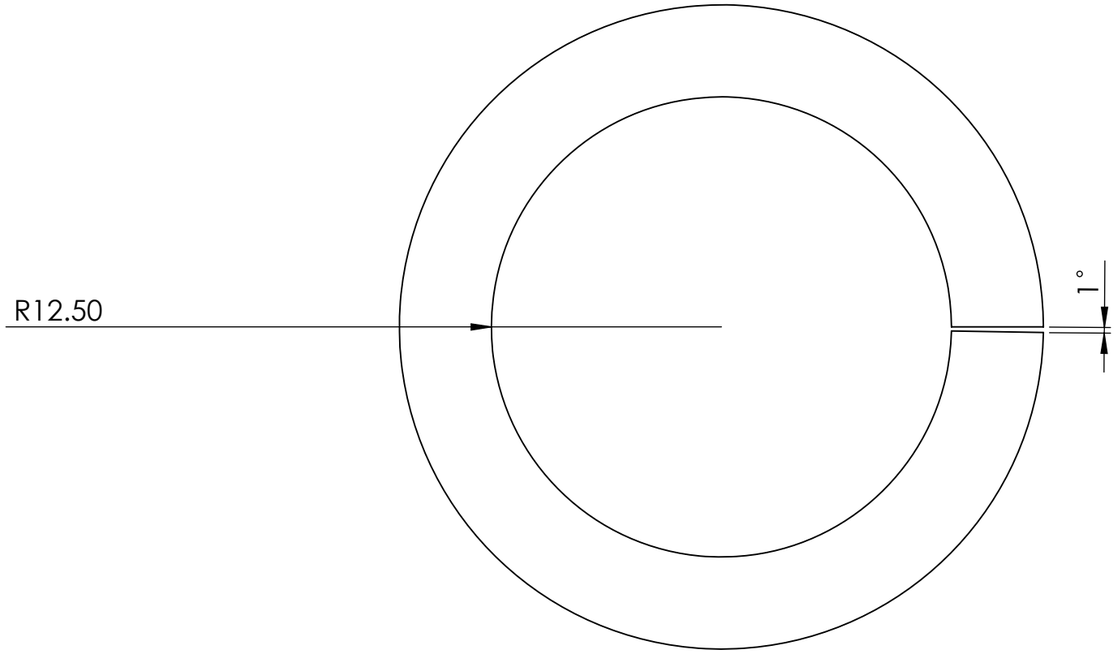

UNLESS OTHERWISE
STATED GENERAL
TOLERANCES: ±0.05 mm
ANGLES: ± 1 °

UNIVERSITY OF KWAZULU-NATAL

SCHOOL OF ENGINEERING

MECHANICAL ENGINEERING

MAT.: TPU		No. REQ.: 2	SCALE: 3:1	UNITS: mm	PROJECT: MSC MECHATRONICS
	DATE	CHECKED	STUDENT NAME: MATTHEW SWANEPOEL		No.: P14
PROJECT SUPERVISOR			STUDENT No.: 218039131		
WORKSHOP TECHNICIAN			E-MAIL: 218039131@STU.UKZN.AC.ZA		TITLE: TPU BUSH
TECHNICAL OFFICER			TEL. No.: [redacted]		

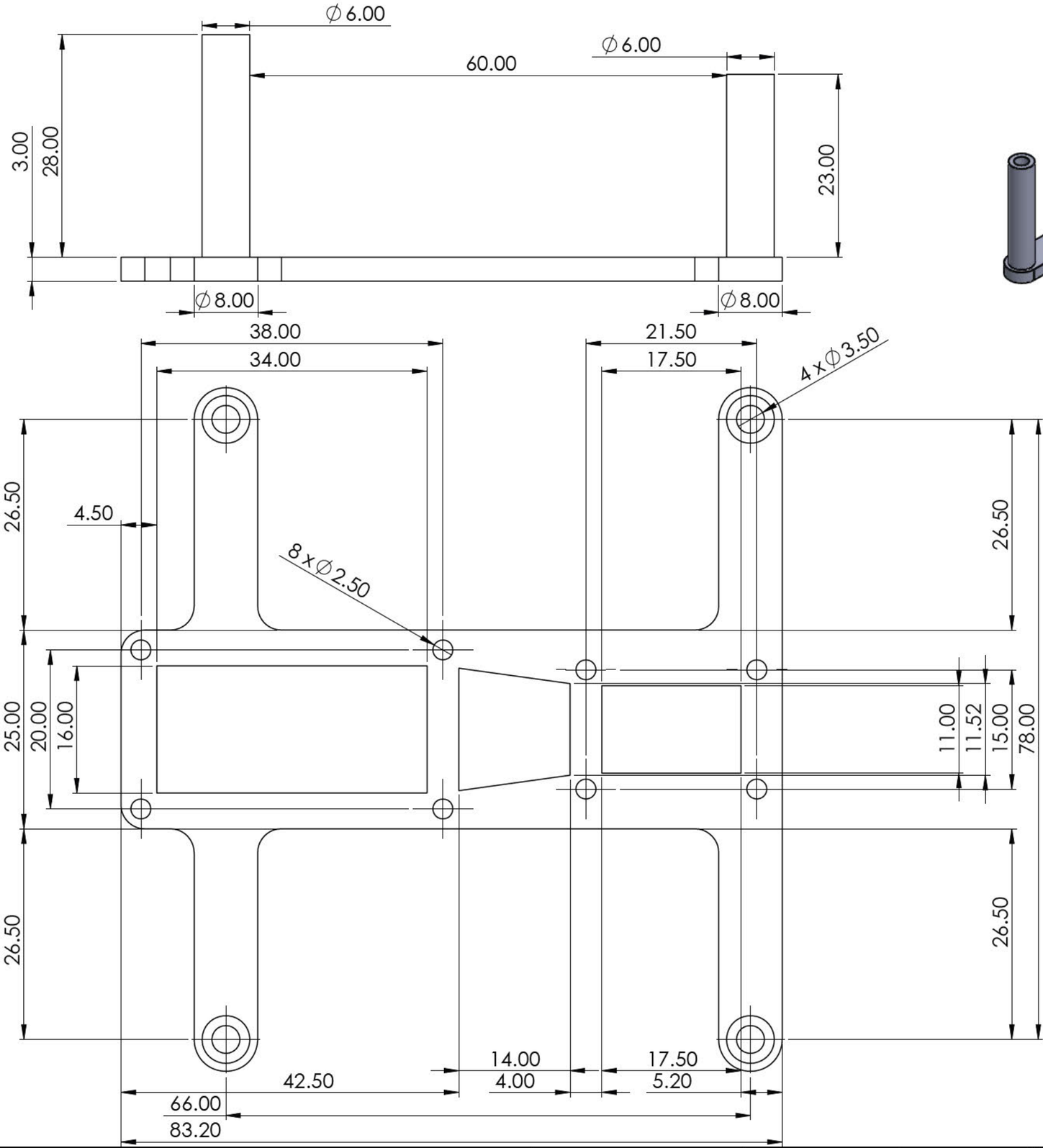

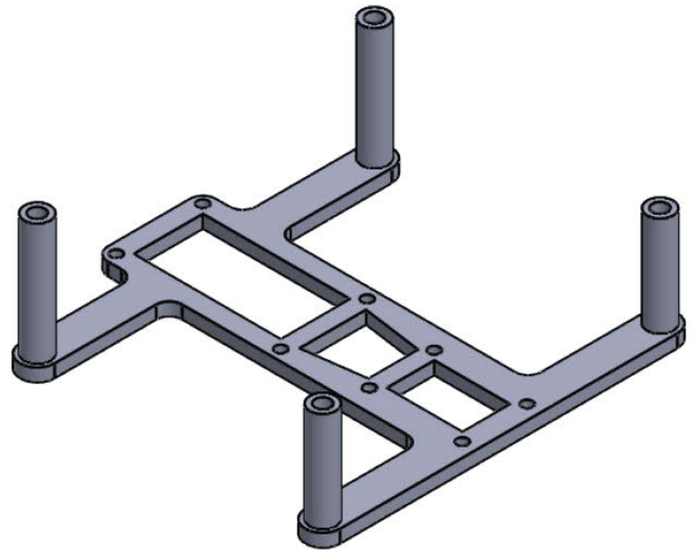

ISOMETRIC VIEW SCALE 1:1

NOTE:

ALL FILLETS 3mm

UNLESS OTHERWISE STATED GENERAL TOLERANCES: ±0.05 mm
ANGLES: ± 1 °

UNIVERSITY OF KWAZULU-NATAL

SCHOOL OF ENGINEERING

MECHANICAL ENGINEERING

MAT.: PLA		No. REQ.: 1	SCALE: 2:1	UNITS: mm	PROJECT: MSC MECHATRONICS
	DATE	CHECKED	STUDENT NAME: MATTHEW SWANEPOEL		No.: T1
PROJECT SUPERVISOR			STUDENT No.: 218039131		TITLE: TESTING SENSOR MOUNTING BRACKET
WORKSHOP TECHNICIAN			E-MAIL: 218039131@STU.UKZN.AC.ZA		
TECHNICAL OFFICER			TEL. No.: [redacted]		